PERFORMANCE OF POLYUREA RETROFITTED UNREINFORCED CONCRETE MASONRY WALLS UNDER BLAST LOADING

by

Laura Ciornei

Thesis submitted to the

Faculty of Graduate and Postdoctoral Studies

in partial fulfillment of the requirements for the degree of

Master of Applied Science

in Civil Engineering

Under the auspices of the Ottawa-Carleton Institute for Civil Engineering

uOttawa

University of Ottawa

August 2012

Abstract

Over the past two decades numerous structures have been subjected to blast loading due to deliberate or accidental explosions. This has resulted in loss of human lives and significant property damage. Historically, unreinforced masonry (URM) has provided a fast and inexpensive method for the construction of both load-bearing structural elements and non load-bearing non-structural elements (e.g. infill panels in concrete and steel frames or exterior facades for building enclosure). In spite of their many advantages, when subjected to blast loading, concrete masonry walls are not only vulnerable to collapse of the wall itself, but also to fragmentation. This leads to wall-debris projectiles travelling at high velocities, which are responsible for most of the casualties during a bomb blast. This thesis presents the results of experimental and analytical research on the effectiveness of using polyurea, a type of elastomer, for retrofitting unreinforced masonry walls when subjected to blast loading.

A total of four unreinforced masonry walls, were constructed and tested under various shock tube induced blast pressures at the University of Ottawa Shock Tube Testing Facility. Two walls were designed and built as non-load bearing infill walls, and the other two walls were designed and built as load bearing walls. The infill walls had a reduced top gap between the wall and the surrounding steel frame. For each category of walls, a polyurea-based retrofit was implemented. One of the two infill walls was sprayed with a layer of polyurea, and one of the two load-bearing walls had a retrofit system comprised of smooth steel wires sprayed with a layer of polyurea. All specimens were designed to represent the middle section of a wall with a length to height ratio greater or equal to three, therefore simulating one-way bending.

The results presented in this study indicate that the load capacity and the stiffness of masonry walls were significantly increased when the retrofits were incorporated. The use of polyurea efficiently controlled fragmentation. The experimental program also indicates that reducing the top edge gap between the masonry wall and the surrounding frame can increase the capacity of the wall substantially by activating the arching mechanism. Polyurea proved to be an excellent retrofit material for dissipating blast induced energy

while providing ductility to the system and changing the failure mode from brittle to ductile.

Numerical analysis using an equivalent single degree of freedom (SDOF) dynamic analysis was conducted for all the shock tube tests performed on the URM wall specimens. Displacement-resistance curves were developed for each wall and sequentially used in the SDOF model to predict mid-height displacements. The predicted displacements were compared with the experimentally recorded displacements. The results show that the analytical model provides reasonably accurate predictions of mid-height displacements.

Acknowledgements

This thesis would not have been possible without the encouragement, guidance, and support of my supervisors, Dr. Murat Saatcioglu and Dr. Timo Tikka, from the incipient to the final stages of working on this research project. I am fortunate and indebted to my fellow graduate students, Alan Lloyd and Eric Jacques, for their tremendous help during specimen testing in the laboratory and for always finding the time to guide me through this journey with precious advice. Also, thanks go out to the University of Ottawa structural engineering laboratory technical officer, Dr. Muslim Majeed, for his help during material properties testing.

I am extremely grateful to my wonderful family, in particular to my mother who always believed in my potential and positively influenced my life in spite of the physical distance. Also, I want to thank Dr. Nickolay Bukoreshtliev for offering me moral support and guidance, essential for completing this project.

Last, I want to acknowledge the financial support from OGS, University of Ottawa and Stantec Consulting that enabled me to focus on this project.

Table of Contents

List of Figures

List of Tables

Notations

Symbol		Definition
A	=	surface area exposed to blast waves
A_{steel}	=	total cross sectional area of steel reinforcement
b	=	waveform parameter
C	=	thrust force due to arching
C_R	=	reflected pressure coefficient
C_{steel}	=	compressive force in steel
d_{EXP}	=	displacement obtained from experimental data
d_{max}	=	maximum mid-height displacement
d_{SDOF}	=	displacement obtained from single degree of freedom analysis (SDOF)
d_{res}	=	residual mid-height displacement
E	=	modulus of elasticity
E_m	=	modulus of elasticity of masonry
E_{steel}	=	modulus of elasticity of steel
f_{mortar}	=	stress in the mortar
f'_m	=	ultimate compressive strength of masonry wall
f'_{mortar}	=	ultimate compressive strength of mortar
F	=	total lateral force
F_{al}	=	total resistance force from axial load arching
F_e	=	resistance at the point of crack initiation in the mortar joint
F_u	=	maximum flexural resistance
$F_{u(arching)}$	=	maximum arching resistance
g	=	gap between the wall and the surrounding frame
g_o	=	reduction in wall height due to axial shortening
H, h	=	wall height
H^d_{EXP}	=	heat of explosion
H^d_{TNT}	=	heat of explosion of TNT
i_r^-	=	negative reflected impulse

i_s^- = negative incident impulse

I_{cr} = moment of inertia of the cracked cross-section

I_e = moment of inertia of the gross uncracked cross-section

I_r = reflected impulse

I_{SO}^+ = positive phase incident impulse

I_{SO}^- = negative phase incident impulse

k_e = elastic stiffness

k_u = stiffness of the cracked section

$ku(t)$ = spring force

K_M = mass factor

K_L = load factor

K_{LM} = load-mass factor

L_D = shock tube driver length

L_W = wave length

L_W^- = negative phase wave length

m = mass of the structural system

M_e = uncracked sectional moment

M_O = moment about point O

M_u = cracked sectional moment

p = applied lateral pressure

P = total axial load

$P(t)$ = time dependent forcing function

P_D = shock tube driver pressure

P_O = atmospheric pressure

P_r = peak reflected pressure

P_r^+ = positive phase pressure

P_r^- = negative phase reflected pressure

P_{SO} = peak incident pressure

P_{SO}^+ = positive phase incident pressure

P_{SO}^- = negative phase incident pressure

R = distance from charge to recording station or standoff distance

R_h = horizontal support reaction

R_v = vertical support reaction

$R\big(u(t)\big)$ = time dependent resistance

s = length of membrane

t = masonry wall thickness

t_a = time of arrival

t_d^+ = positive phase duration

t_d^- = negative phase duration

t_{max} = time to maximum mid-height displacement

t_o = positive phase duration

t_o^- = negative phase duration

$u(t)$ = time dependent displacement of the system mass

$\ddot{u}(t)$ = time dependent acceleration of the system mass

U = shock front velocity

W = explosive charge weight

W_E = effective charge mass

W_{EXP} = mass of explosives

y = crack length

Z = scaled distance

α = degree of fixity at supports

α_i = angle of incidence

β = ratio of the curvature of the central section of the wall during crack development and the curvature of the central section at onset of crack

γ = factor equal to 0.9

Δ = displacement

Δ_{cr} = displacement at the point of crack initiation

Δ_e = displacement at the point of crack initiation in the mortar joint

Δ_g = initial displacement due to gap

Δ_{go} = displacement due to axial shortening

Δ_{max} = maximum deflection

Δ_u = displacement at maximum resistance

ϵ = strain

ϵ_m = strain in masonry

θ = support rotation

θ_{max} = maximum support rotation

λ = scaling factor

σ = stress

ϕ = displacement shape function

ϕ_{crG} = curvature of the central section of the wall during crack development

ϕ_{cr} = curvature of the central section of the wall at onset of crack

Acronym Definition

AFRL = Air Force Research Laboratory

ANFO = Ammonium Nitrate Fuel Oil

CMU = Concrete Masonry Unit

DIF = Dynamic Increase Factor

IMI = International Masonry Institute

LVDT = Linear Variable Displacement Transducer

PI = Pressure-Impulse

SDOF = Single Degree of Freedom

UFC = United Facility Criteria

URM = Unreinforced Masonry

CHAPTER 1

Introduction

1.1 General

As recent as ten years ago, many consulting engineering firms believed that little could be done to protect buildings from blast effects other than building a bunker-like structure or providing total isolation from the general public. During the past decade, extensive research has been carried out to develop innovative concepts of retrofitting buildings to withstand blast loads. These new concepts not only protect the buildings from the effects of blasts, but also are not excessively expensive, difficult to install nor do they alter the building's appearance (Crawford, 2006).

Protective designs for building components to minimize blast hazards include: increasing the stand-off distance, increasing strength, increasing ductility and increasing mass (ASCE, 1999). The first approach could be achieved by providing barriers to prevent the source of explosion from getting near the building. With an increase in stand-off distance, the quantity of explosives would have to increase in order to achieve the same damage level. Enhancing the wall strength so it can resist the actual blast load can be achieved in numerous ways, such as increasing the section depth, adding reinforcement such as steel bars or externally bonded FRP laminates and column jacketing. However, with increase in strength, the displacement ductility of the system could decrease. The structures would withstand greater loads, but would not be able to achieve high displacements. Increasing ductility enables structures to achieve higher displacements, and dissipate blast energy, without necessarily withstanding greater loads. Increasing mass can be an effective retrofit strategy for structures to withstand impulsive loading regimes. Another protective design would be to capture the debris caused by blast and prevent it from entering the building. This approach does not necessarily involve strengthening of the wall to improve its out-of-

plane flexural capacity, but it can provide displacement ductility to the system if the retrofit is applied on the building's elements.

Due to their many advantages, such as cost and ease of installation, Concrete Masonry Unit (CMU) walls are frequently used in construction either as non-load bearing (infill walls or building facade) or as structural load bearing walls. However, low blast pressures can cause wall fragmentation with pieces of debris flying at high speeds, which can lead to injuries and fatalities.

Unreinforced Masonry (URM) walls have low resistance to out-of-plane blast loading, with non-load bearing walls being most vulnerable, due to the lack of axial force that adds to the moment resistance. Interior URM walls are seldom used in new buildings due to the availability of other more convenient wall systems, but exterior URM walls are commonly used in the construction industry. On the other hand, older buildings were constructed with interior URM walls. Existing design codes require minimum steel reinforcement for interior masonry walls, but older buildings have no such requirement. URM infill walls are non-structural elements enclosed by steel or reinforced concrete frames. They are often separated from the structural elements to allow for service load deformations of structures. The gaps between URM and surrounding frame, usually located at the sides and top of wall, affect the blast performance significantly, leading to failure at very low pressures. Steel ties between the URM and surrounding frame are provided to prevent the wall from tipping over, but are not designed to resist shear forces generated by blast pressures. Protective designs for CMU walls can be accomplished in two ways. First approach is to strengthen the wall so it can withstand the actual shock wave, and the second approach is to prevent the debris from entering the occupant area. The strengthening method is most appropriate for load-bearing walls since they should not undergo large out-of-plane displacements that would jeopardize their load-bearing function. Debris reduction method is most suited for non-load bearing walls (i.e. infill walls) since they could act as sacrificial building elements intended for energy dissipation.

A convenient strengthening strategy for URM infill walls against blast loads is the activation of the arching mechanism. URM walls have very little resistance to blast

pressures. Providing end restraints promotes the formation of in-plane compression struts, which in turn generate arching action, which enhances flexural capacity even in the absence of reinforcement. In order to activate the arching mechanism, a cost effective and easy to implement measure is to decrease the top edge gap between the URM wall and the enclosing frame. The gap dimensions require a structural assessment in order to allow for serviceability deflections. As arching action develops, it is important to prevent out-of-plane translation (sliding) of the wall by providing mechanical shear restraints across the top and bottom of the masonry wall.

A strategy for reducing debris from fragmentation of URM infill walls is to apply a layer of spray-on polyurea on the tension side of the URM wall (interior face of a building's exterior wall). Polyurea, a type of elastomeric polymer derived from the reaction between an isocyanate and a resin blend component, has fast curing times, can be applied in extreme temperature and humidity conditions, and exhibits exceptional physical properties such as high tensile strength, hardness, tear strength, flexibility, chemical and water resistance (Broekaert, 2002).

A strategy for strengthening load-bearing walls involves adding a tension component that would increase the bending moment capacity of the section, such as a system comprised of smooth steel bars embedded in a layer of polyurea. This method not only increases the wall strength, but also reduces fragmentation. To provide anchorage, the smooth steel bars are welded to flat plates that can be easily bolted to the top and bottom of the surrounding frame. Polyurea is sprayed over the steel bars and mechanical shear restraints are placed at the top and bottom of the wall in order to prevent sliding.

The following sections present the objective and scope of the current research project. A brief summary of the blast loading mechanism and response of structures to shock waves are also discussed, followed by a literature review of previous research studies on polymer retrofit of concrete masonry walls.

1.2 Objective and Scope

The objective of the current research project is to develop blast retrofit methodologies for unreinforced concrete masonry walls that involve the use of spray-on polyurea. The

objective also includes the investigation of as-built and retrofitted URM walls under shock tube induced blast loading while developing analytical modelling techniques and design methodologies for such applications.

The scope of the current investigation consists of four parts:

1. Background study that includes the mechanics of blast phenomenon, structural response and the development of retrofit technologies as well as a literature review of the past experimental and analytical research on the use of polymer retrofit of concrete masonry walls subjected to blast loading.

2. The design and implementation of an experimental program and construction of four (4) unreinforced concrete masonry walls, two non load-bearing and two load-bearing walls; retrofitting one non-load bearing wall with spray-on polyurea and a load-bearing wall with a system comprised of smooth steel bars and a layer of polyurea; testing of specimens using University of Ottawa's Shock Tube to simulate blast loading.

3. Evaluation of test data and assessment of polymer (polyurea) performance as a retrofit material; development of a single-degree-of-freedom (SDOF) dynamic analysis model for the analysis of the URM wall specimens; comparison of the analytical model with experimental results.

4. Provide recommendation regarding the use of polymer retrofit methods for URM walls subjected to blast loading.

1.3 Mechanics of Blast Loading

To develop and evaluate a blast retrofit strategy, it is important to understand the mechanics of blast loading and structural response to such loading. A blast load is generated when an explosion sets in motion a surrounding mass of air, creating a high speed shock wave that travels in radial directions from the detonation point. A nearby building will be subjected to a short duration loading in the form of impulse (integral of force with respect to time). The intensity of such impulse will depend on the magnitude of the explosion, normally characterized by the amount of explosives, and the stand-off

distance, which is the distance between the building and the detonation point. The dynamic characteristics of an impulse will generate inertial forces in the building, directly proportional to the building mass. Buildings that are potential targets to blast loading are usually designed for wind and earthquake loads only; however, blast loads cause pressures that are hundred times greater than the wind loads, depending on the size of explosives, distance from the target, and the angle of incidence. Although blast loads have very high peak pressures, the durations are very short, which reduce the effects of such high pressures on structures.

Blast loads fall in two categories: Confined (inside the structure) and unconfined (outside the structure). Subcategories of the confined blast load include: fully vented, partially confined, and fully confined; whereas sub-categories of the unconfined blast loads include: free airburst, air burst, and surface burst. Take for example a cubicle filled with explosives, fully vented explosions occur when one or more sides of the cubicle are opened to the atmosphere. There is no pressure build up since the blast waves are immediately sent into the atmosphere. In the case of partially confined explosions, the cubicles will have one or more sides with frangible surfaces that can contain the blast load for a limited amount of time before being released into the atmosphere. The fully confined explosions occur in cubicles with non-frangible surfaces. Blast waves are being reflected, and amplified creating a gas pressure build-up.

Figure 1.1 shows unconfined blast loading described in three categories: free airburst, airburst and surface burst. Free airburst, or spherical burst, has the centre of detonation above the ground and the blast waves reach the structure before being reflected off the ground surface. Airburst loading occurs when the centre of detonation is above the ground. In this case the blast waves reflect off the ground surface before reaching the structure, as opposed to the spherical burst loading. Surface burst loading, also called hemispherical burst, occurs when the centre of detonation is on the ground and the waves reflect instantaneously.

During an explosion, gases are generated that are under extremely high pressure and temperature. These gases produce a sudden increase in pressure above the atmospheric

conditions (overpressure), forcing the surrounding air to expand and travel at supersonic speed. The expanding air is forced outwards, creating a layer of compressed air called the shock front. With time, the velocity of the shock front as well as the overpressure and temperature decrease. A vacuum is then formed (underpressure) that would cause the air to rush back and form a negative pressure region behind the shock front. This phenomenon is called rarefaction. During this phase, the pressure drops below atmospheric conditions, eventually returning to atmospheric setting as more time elapses.

1.3.1 Blast Wave Parameters

Blast wave parameters, used to define the blast loading, are identified as either primary or secondary. Primary parameters include the overpressure, duration, and impulse. The secondary parameters, which are obtained from the first three primary parameters, are the peak reflected pressure, peak dynamic pressure (or blast wind pressure), shock front velocity, and blast wave length.

Figure 1.2 shows the pressure profile of a blast wave. The duration in which the pressure is above atmospheric conditions (overpressure) is called the positive phase duration (t_d^+), whereas the duration when the pressure is below atmospheric conditions (underpressure) represents the negative phase duration (t_d^-). The time, t_a, represents the time it takes for the shock front to arrive at a recording station or simply the time of arrival. The pressure, P_{SO}, represents the overpressure, or the peak incident pressure recorded at the station that is above the atmospheric pressure, P_O. The underpressure is much lower than the overpressure and its effect is usually neglected for dynamic analysis of most structures.

The area under the pressure-time curve represents the impulse of the blast wave and it can be computed from Eqn. 1.1 and Eqn. 1.2 for positive phase and negative phase impulse respectively (Smith and Hetherington, 1994):

$$I_{SO}^{+} = \int_{t_a}^{t_a+t_d^+} \big(P_{SO}(t)\big)dt \qquad [1.1]$$

$$I_{SO}^{-} = \int_{t_a+t_d^+}^{t_a+t_d^++t_d^-} \big(P_{SO}(t)\big)dt \qquad [1.2]$$

The pressure-time profile can be described as an exponential function using the Friedlander equation, shown in Eqn. 1.3 (Smith and Hetherington, 1994):

$$P(t) = P_{SO}\left(1 - \frac{t}{t_d^+}\right)e^{-\frac{bt}{t_d^+}} \quad [1.3]$$

In Eqn. 1.3, b represents a waveform parameter that can be obtained from the following equation (Smith and Hetherington, 1994):

$$I_{SO}^+ = P_{SO}\, t_d^+ \left[\frac{1}{b} - \frac{1}{b^2}(1 - e^{-b})\right] \quad [1.4]$$

Reflection occurs when the shock waves encounter a denser medium than the initial medium where they were being propagated through. The air molecules forming the blast wave encounter the reflecting surface where they get further compressed by other incoming air molecules causing the overpressure to increase in magnitude. This magnified pressure is known as the reflected pressure, P_r. The magnification of the incident pressure depends on the angle of incidence between the plane shock front and the reflecting surface, $\propto_i$. Reflected pressures are more critical in design of blast resistant buildings since they are greater than the incident pressures by a magnification factor of at least 2. Wave reflection can be normal ($\propto_i = 90^0$), oblique ($\propto_i < 90^0$) or mach reflection. Mach reflection is created when the spherical shock waves reach the ground surface at a point directly under the center of detonation, are reflected and travel back to the center of detonation where they merge with other incoming waves forming a stronger shock front known as the Mach Stem (Figure 1.3). The point at which the Mach Stem, the incident shock front, and the reflected shock front are merging is called the triple point.

1.3.2 Scaling Laws

Due to the expensive nature of full scale testing, scaling laws are used in order to extrapolate small test data to tests that use larger quantities of explosives. Hopkinson-Cranz scaling law, also called the cube-root law, is most widely used and it states that "Self-similar blast waves are produced at identical scaled distances when two explosive charges of similar geometry and of the same type of explosive, but different sizes, are

detonated in the same atmosphere" (Baker, 1983). In other words, if an explosive of charge weight, W (with diameter, d), is detonated at a distance, R, from a specific recording station, the blast wave parameters: peak pressure, P_{SO}, duration of positive phase, t_d, and impulse, I_{SO}, would be similar to an explosive charge weight, W_1, with a diameter, λd, detonated at a distance, λR, from the same recording station, with the same peak pressure, P_{SO}, but with scaled duration, λt_d, and scaled impulse, λI_{SO}. The cube-root scaling law is illustrated in Figure 1.4.

The relationship between the two types of explosives is expressed in Eqn. 1.5:

$$W \propto d^3 and\ W_1 \propto d_1^3 \qquad [1.5]$$

Where d and d_1 are the diameters of the spherically shaped explosive charges. Rearranging the relationship in Eqn. 1.5 yields:

$$\frac{W}{W_1} = \left(\frac{d}{d_1}\right)^3 and\ \frac{d}{d_1} = \left(\frac{W}{W_1}\right)^{\frac{1}{3}} \qquad [1.6]$$

According to the cube-root scaling law, the incident pressure recorded at a specific station would be the same if the ratio of the characteristic diameters (cube-root of charge masses ratio) is the same as the ratio of standoff distances. This relationship can be expressed in the following manner:

$$\frac{R}{R_1} = \left(\frac{W}{W_1}\right)^{\frac{1}{3}} \Rightarrow \frac{R}{W^{1/3}} = \frac{R_1}{{W_1}^{1/3}} = constant = Z \qquad [1.7]$$

In Eqn. 1.7, the constant, Z, is known as the scaled distance, a constant of proportionality between standoff distance and charge weight. As the constant, Z, increases, the charge weight decreases resulting in a smaller incident pressure at the same standoff distance.

1.3.3 Trinitrotoluene (TNT) Equivalence

The amount of energy released during a detonation is called the magnitude of the explosion and it is expressed in terms of a TNT equivalence, the mass of TNT needed to produce the same effect of a given explosive, divided by the mass of the explosive tested. TNT is

chosen as a standard explosive for comparison purposes due to its availability, relative purity, safety of handling, and existence of test data.

TNT equivalence is described as

$$TNT\ Equivalence = \frac{W_E}{W_{EXP}} = \frac{H^d_{EXP}}{H^d_{TNT}} \quad [1.8]$$

where W_E is the effective charge mass or TNT equivalent mass (kg); W_{EXP} is the mass of explosive (kg); H^d_{EXP} is the heat of explosion (J/kg); H^d_{TNT} is the heat of explosion of TNT (J/kg).

Table 1.1 shows TNT equivalent masses for air blast of commonly used explosive materials (Hyde, 1992). TNT equivalent mass varies slightly for pressure and impulse. For simplicity, an average value can be used.

1.3.4 Blast Load Prediction

A widely accepted method of determining the values of the blast load parameters is using the Kingery-Bulmash charts reproduced in Figures 1.5, 1.6, 1.7, and 1.8. The charts have been developed from experimental and theoretical research for atmospheric conditions, based on TNT equivalent charge weights, for spherical and hemispherical detonations. The charts can be used to determine the peak reflected pressure, P_r; peak incident overpressure, P_{SO}; reflected impulse, I_r; incident impulse, I_{SO}; time of arrival, t_a; shock front velocity, U; duration of positive phase, t_d or t_O; and wave length, L_W. Separate curves, shown in Figures 1.5, 1.6, 1.7 and 1.8 are provided for each parameter as a value normalized by the cubic root of the mass of the explosive. Values for three of the blast parameters, peak incident pressure, P_r, the reflected pressure, P_r, and the shock front velocity, U, are not scaled. In order to determine the blast wave parameters from the Kingery-Bulmash charts, the scaled distance, Z, is first computed from equation:

$$Z = \frac{R}{W^{\frac{1}{3}}} \quad [1.9]$$

Where R is the standoff distance in meters (m) and W is the charge weight in kilograms (kg) of TNT. To determine the blast parameters for a different type of explosive material, the mass of explosive needs to be converted to an equivalent mass of TNT by using conversion factors such those listed in Table 1.1. The factors for pressure and impulse are often averaged to simplify calculations. Before determining the blast load parameters, it must be established whether the surface blast is spherical or hemispherical in nature.

Note that Figures 1.5 and 1.6 are used to determine blast wave parameters for positive phase only. Charts shown in Figures 1.7 and 1.8 have been provided to determine negative phase blast parameters of hemispherical and spherical TNT surface blast. The scaled distance, Z, computed from Eqn. 1.9, is used to directly obtain the following blast wave parameters: the reflected underpressure, P_r^-; incident underpressure, P_{SO}^-; negative reflected impulse, i_r^-; negative incident impulse, i_s^-; duration of negative phase, t_0^-; and negative phase wave length, L_W^-.

The values for the peak reflected pressure, P_r, and the peak reflected impulse, I_r, for both hemispherical and spherical TNT surface burst are given for normal reflection scenario only. When the angle of incidence, α, is smaller than 90^0, the peak reflected pressure can be computed from the following equation:

$$P_r = C_R \, P_{SO} \qquad [1.10]$$

where C_R is a reflected pressure coefficient and P_{SO} is the peak incident overpressure.

Figure 1.9 shows the relationship between the reflected pressure coefficient and the angle of incidence for different peak incident pressures. By knowing the angle of incidence, and interpolating for a specific incident pressure, the reflected pressure coefficient is obtained. The peak reflected pressure is then computed from Eqn. 1.10.

When the angle of incidence, α, is smaller than 90^0, the peak reflected impulse is interpolated from Figure 1.10 when the angle of incidence and the peak incident overpressure are known.

With the use of these simple tools, the blast wave parameters can be determined when the standoff distance and spherical TNT equivalent charge weight is known. One can also backtrack and obtain a standoff distance and a corresponding charge weight if the blast wave parameters are known.

1.4 Need for a Blast Retrofit Technique

Interior or exterior perimeter walls constructed of unreinforced masonry walls can be hazardous under blast loading. The wall fragmentation, pieces of debris flying at high speeds, can lead to injuries and fatalities. Unreinforced masonry (URM) walls have very low resistance to out-of-plane blast loading due to the brittle mode of failure as well as low flexural resistance. This becomes even more critical when the walls are non-load bearing, when there is no axial force to contribute to the bending moment resistance of the section. The interior URM perimeter walls are seldom used in new buildings due to other more convenient wall systems that are available, but the exterior URM walls are still common in construction practice. On the other hand, older buildings were constructed with interior URM walls that can be hazardous in case of blast loading. Existing design codes require minimum steel reinforcement for interior masonry walls, but older buildings have no such requirement. The need for developing retrofitting techniques for older buildings, that can improve the load carrying capacity, has risen because of the increased threat of terrorist attacks. These retrofit techniques should be able to resist blast and, in case the collapse of the wall is inevitable, be able to contain the wall debris within the system.

1.5 Protective Design for Masonry Walls

Protective designs for masonry walls to enhance blast resistance can be accomplished in two ways. The first approach is to enhance the wall strength and ductility to resist the actual impact from the blast load. The second approach is to capture the wall debris and prevent it from entering the building's occupied space and thereby preventing injuries. This second approach does not involve strengthening of the wall to improve its out-of-plane flexural capacity (Crawford et al., 2006).

Studies have been conducted that examine both approaches for improving blast resistance. These studies include: increasing thickness of the wall (adding mass to the wall system) by

using a back-up wall comprised of masonry, concrete or a steel framing system; reducing the span requirements by adding vertical steel members; application of Fiber Reinforced Polymers (FRP) composites on the interior surface of the wall to increase flexural resistance; installing sheet metal on the tension face of the wall etc (Crawford et al., 2006). By using these approaches, significant disruption to the building occupants is introduced in terms of installation time and also loss of usable floor space. Appearance becomes an issue when dealing with heritage buildings, especially buildings that are most likely to be a target for terrorist attacks. It is important that blast protection designs avoid creating a bunker-like appearance that compromises the architect's vision for the facility. Aesthetics is often a result of good design. Blast protection techniques should be installed so that the user of the facility is unaware of their existence.

1.6 Using Polymers for Blast Mitigation

Research has been conducted to retrofit masonry wall systems to resist blast loading, specifically, the retrofit of non-load bearing concrete masonry unit walls. In 1999 the Air Force Research Laboratory (AFRL) began experimenting with sprayed-on polymers. Although these polymers have very low stiffness, they showed good potential. The most suitable polymer for blast retrofitting, determined by the AFRL, was chosen to be a spray-on polyurea coating (Knox et al., 2000).

Polyurea is a type of elastomeric polymer derived from the reaction between an isocyanate component and a resin blend component. Polyurea coatings have fast curing time, can be applied in extreme variations of temperature and humidity conditions and exhibit exceptional physical properties such as high tensile strength, hardness, tear strength, flexibility, chemical and water resistance making it resilient to abrasion and weathering. The system is also compliant to the most stringent Volatile Organic Compounds (VOC) regulations (Broekaert, 2002).

Figure 1.11 shows the application process and finished look of polyurea coating. An architectural coat can be added to improve the aesthetics.

The physical and chemical properties make polyurea product suitable for truck bed liners, roof coatings, pipe protection, conveyor belts and many other applications (Broekaert,

2002). It was not until a little over ten years ago that researchers began investigating the potential of using polyurea as a blast mitigation technique. The following section provides an overview of the previous research performed on the use of polymers, particularly spray-on polyurea, as a blast retrofit technique.

1.6.1 Previous Research on Polymer Retrofit Concrete Masonry Walls

K. J. Knox, M. I. Hammons, T. T. Lewis, J. R. Porter, 2000

In 1999, the Air Force Research Laboratory (AFRL) performed a series of tests at Tyndall Airport Air Force Base (Tyndall AFB) with the goal of developing an inexpensive, light weight and easy to apply retrofit technique that would introduce "ductility and resilience into building walls" (Knox at al. 2000). Several (21) polymers were evaluated and based on results of material testing, an elastomeric polymer with a polyurea base was chosen as the retrofit material. The strength, flammability and cost were the principal selection criteria. Table 1.2 shows the average material properties of three groupings of polymers, extrusion, spray-on, and brush-on, along with a baseline polymer, the original truck bed liner, which is included for comparison. The stress-strain relationship for the polymer groupings are compared in Figure 1.12. The baseline polymer had excellent elongation properties, but the modulus of elasticity and rupture strength were lower than the extrusion or spray-on polymers. The extruded thermoplastics were stiffer and stronger than the other polymer applications. The extruded class of polymers was eliminated from consideration for application on existing structures; however this class remains suitable strengthening technique for new construction. The brush-on polymer proved weak and brittle with very long curing times. Of the spray-on polymers, polyurea was chosen by the researchers for the retrofit since it provided a balance between strength and elongation capabilities. Table 1.3 lists the properties of the selected polymer, polyurea. Spray-on polyurea has higher secant elastic modulus and tensile strength than the average spray-on applications given in Table 1.2, and elongation at rupture approaching the average of spray-on applications.

Single-degree-of-freedom (SDOF) dynamic modelling was used by Knox et al. (2000) to predict wall deflections at various explosive yields and standoffs. The SDOF involves developing a static resistance function from the details of the wall construction, transforming the wall properties into an equivalent SDOF model, and solving the equation

of motion to determine the response of a critical point in this case, a point in the center of the wall section. Figure 1.13 shows the composite resistance function used in the SDOF model for a typical 2.13 m (7 feet) high by 6.10 m (20 feet) long light weight shelter wall. It can be seen from the graph that the polymer membrane does not have a significant initial contribution in the strength increase; however, the strength contribution of the polymer increases exponentially as the other system components reach plastic stage or failure.

Initial tests were performed on lightweight composite structures and masonry walls that were retrofitted with spray-on polyurea material. The material was applied on both the interior and exterior wall surfaces. Both masonry and lightweight structures experienced large deflections during blast and the lightweight structure had severe ceiling crushing that required mitigation; however the debris was contained and did not enter the interior of the test cubicles. The proof-of-concept tests were deemed successful and they were then followed by three explosive tests on lightweight structures retrofitted with the polymer material. In the first explosive test two wall panels were subjected to blast and studied for performance of the retrofit material under high strain rates. In the second explosive test a single-wide construction trailer was tested with the polymer retrofit as well as additional strengthening techniques such as a thin steel tubing frame installed in attempt to reduce ceiling crushing. A continuous layer of spray-on polymer was assured by spraying the wall surface as well as the frame. The steel tubing frame had little impact on reducing the wall deflections. In the third test house trailers were designed for a higher explosive yield to "push the envelope of the retrofit technique". The thickness of the polymer retrofit as well as the stud spacing of the steel frame was varied (Knox et al. 2000). In the first two tests, the retrofit was successful at retaining the debris even when the wall panels sustained severe damage (Figures 1.14 and 1.15). In the third test, numerous tears were observed in the retrofit material, large enough to allow debris to enter the room and possibly harm the occupants (Figure 1.16). The tubular steel framing was successful at reducing the ceiling deflections compared to the initial tests. The researchers concluded that the polymer retrofit material would be a good addition to a comprehensive retrofit program.

J. D. Connell, 2002

After the lightweight structures program, the AFRL team shifted their research focus to the retrofit of concrete masonry unit (CMU) walls. A summary and discussion of their work on CMU walls is presented by Connell (2002). Three (3) CMU wall tests were conducted in 2001, using a spray-on polyurea retrofit. In the first two tests, a retrofitted wall and a control unreinforced CMU wall without any retrofit were tested. The first test used a low blast charge and a range of 15.24 m (50 feet) to show the control wall collapse while the retrofitted one experienced some damage while still standing (Figure 1.17).

The second test with a higher blast charge and a shorter stand-off distance of 13.11 m (43 feet) resulted in the complete collapse of both retrofitted and control wall specimens. The third test used the same charge as the second test, but at a stand-off distance of 19.81 m (65 feet). For this test, two walls were retrofitted using the spray-on polyurea: the first wall was sprayed on the inside face only, and the second wall was sprayed on both inside and outside surfaces. Both specimens survived the blast. The tests show the polymer retrofit to be effective in strengthening the unreinforced CMU walls; however Connell reported that challenges remain since the failure mode is not well understood and is highly dependent on the support conditions, peak load and duration.

J. S. Davidson, J. R. Porter, R. J. Dinan, M. I. Hammons and J. D. Connell, 2004

Based on initial tests by Knox et al. (2000), Davidson et al. (2004) conducted three full scale explosive tests to examine the effectiveness of the application of spray-on polymers for retrofitting unreinforced CMU walls. For the full scale explosive tests, several wall panels with or without retrofit were constructed and tested in reusable reaction structures, designed to withstand repeated blast loads (Figure 1.18). For each full scale test, two unreinforced CMU walls were constructed inside the reaction structure. Two “test cubicles” with one wall panel each were used only for the third full scale explosive test. The sprayed-on polymers were chosen based on their stiffness, ductility, fire resistance and cost. It was found that, although having a relatively low strength, the spray-on polymers possessed high ductility that enabled them to deform and contain the debris created during the blast event. After testing several types of polymers and applying them on either the inside face or both faces of the wall, the authors concluded that the retrofit can resist by

nearly 12 times the peak pressures resisted by unreinforced CMU walls. They also determined that the failure mechanisms are affected by support conditions, peak pressures and duration of the blast load. Spraying the walls on both faces, when compared to spraying only the inside face, was found to increase the wall strength and reduce the hazard to building occupants, but not enough to make it economically feasible. They also called for development of non-explosive laboratory tests to predict energy absorption of a given retrofit, further finite element (FE) modelling to simulate unretrofitted/retrofitted unreinforced CMU structures subjected to blast load, and the development of performance criteria for elastomeric coatings, engineering tools and guidelines.

E. L. McDowell, K. E. McKee and E. Sevin, 1956

McDowell et al. (1956) studied effects of arching on improving out-of-plane resistance of unreinforced masonry walls. They developed a theoretical relationship to determine the static load-deflection curves for masonry beams constructed with a solid cross section. The researchers observed an increase in capacity as the masonry wall was able to withstand much larger deflections than the ones predicted using conventional beam analysis. The additional strength was present only when the ends of walls were placed against rigid supports. They were able to experience three to six times the load-carrying capacity of simply supported walls, when only 1.5 times the capacity is expected from flexural theory by changing the support conditions from simply supported to fixed support conditions. The researchers explained that during flexure, the wall pushes against the top and bottom rigid supports, causing additional compressive stresses that increase the wall's bending moment capacity (Figure 1.19).

B. L. Gabrielsen, C. Wilton, 1973, and K. Kaplan, 1975

Gabrielsen et al. (1973 and 1975) conducted a series of blast tests on arched unreinforced masonry walls using shock-tunnel pressure waves to simulate blast load. The researchers established an increase factor of four to five times for arched walls as opposed to nonarched walls. They also noted that the presence of a gap in an arched wall will significantly decrease its capacity (Gabrielsen et al., 1975).

R. G. Drysdale, A. A. Hamid, L. R. Baker, 1994

Drysdale et al. (1994) developed a theoretical relationship based on the same approach as McDowell et al. (1956) for arching resistance of one-way action walls placed between rigid supports at the top and bottom. This method will be further explained in Chapter 4.

R. J. Dinan, J. W. Fisher, M. I. Hammons, and J. R. Porter, 2003

Dinan et al. (2003) used Drysdale et al. (1994) method as well as SDOF analysis to examine the effect of arching resistance for polymer retrofit CMU walls. The analysis results closely matched full-scale AFRL test data. The polymer retrofit membrane, in this case polyurea, was applied over the entire surface of the walls; however, during bending, the membrane did not get uniformly strained. The effective length of the membrane was established to be less than the total height of the wall and highly dependent on the anchoring of membrane to the masonry wall as well as how far the membrane strains pass the crack opening. For example, as a crack forms at a mortar bed joint, the membrane will strain above and below the crack. During AFRL blast tests it was observed that the length of polyurea membrane retrofit strained on each side of the mid-height crack opening was approximately half of the concrete masonry block height.

T. R. Slawson, D. R. Coltharp, S. T. Dennis, and R. Mosher, 1999

Slawson et al. (1999) described the use of a membrane catcher system for unreinforced CMU walls, designed to catch the debris and reduce casualties. The location of the membrane is on the inside face of the wall, attached to the floor and ceiling, but not to the wall itself. The material of choice can be aluminum sheets, steel sheet, fabrics etc. Slawson et al. (1999) describe the use in previous tests of anchored geofabrics to retrofit the CMU walls exposed to blast pressures. The membrane catcher system was not intended to strengthen the wall; its sole purpose was to capture flying debris caused by wall disintegration during blast. The geofabrics were deemed successful in retaining debris. Wall Analysis Code (WAC) SDOF analysis developed by the US Army Engineer Research and Development Center (ERDC) and DYNA-3D finite element software were used in attempt to compare with previously performed tests. The modelling results did not agree with the test results and were overestimating maximum deflections for the retrofitted walls.

The researchers suggested that further experimental data is required to validate numerical analysis and modelling procedures (Slawson et al. 1999).

D. L. Thornburg, 2004

AFRL performed tests at Tydall AFB in which two CMU walls were subjected to blast loading and spray-on polymers were used as retrofits. The construction of the two walls was identical, the application of the retrofit material being the only difference. The first CMU wall had the retrofit installed as a membrane polymer catcher system, without bond between the polymer and the wall, whereas the second CMU wall had the polymer retrofit sprayed directly on the wall. Unlike the spray-on retrofit wall, the wall that had incorporated the membrane only as a catcher system witnessed complete collapse during the test; however the performance was deemed acceptable for smaller blast loads.

Blast tests carried by Thornburg at AFRL, Tyndall Air Force Base, demonstrated the efficiency of low-stiffness polymers at reducing deflections and fragmentation of unreinforced CMU walls as well as increasing survival rates and reducing injuries from blasts. Numerous manufacturers provided samples to be tested in blast, but the expense of conducting full scale explosive tests lead to the use of non-explosive methods for testing such as the static flexure test, gas gun facility and drop tower to evaluate the potential of candidate material.

Thornburg tested 53 candidate polymeric and composite materials to determine material properties and behaviour using two series of tests. Static flexure tests were used in the first test series to determine the bond failure mechanism between the polymer and concrete substrate as well as the tensile strength, elongation and bond strength when the polymer material remained bonded to the concrete. Debonding was observed in three out of the four tests performed before the material reached failure. In the second test series, high-speed drop tower equipment was used to evaluate effectiveness of retrofits in shear as well as in dynamic energy absorption. By knowing the mass and velocity of the impact, the impact energy, total energy, strain energy absorption capacity and maximum load were determined. In the third series of tests, a gas gun facility was used and the polymer material was impacted with projectiles with velocities approaching 304.8 m/sec (1,000 ft/sec). This

test was performed to determine total energy absorbed as well as the ballistic limit for candidate materials. The polymer material was also sprayed on concrete blocks, subsequently tested in the gas gun facility to determine the energy absorption capacity. The coatings did not experience failure during testing nor did they experience local punching. Thornburg also performed uniaxial tension tests to determine stress-strain properties of each 53 candidate materials. The tests show that the stress-strain properties vary significantly (Thornburg, 2004).

S. Sudame, 2004

The work performed by Connell and Thornburg was further examined by Sudame (2004) through numerical modelling and by varying parameters of the polymer retrofit CMU wall to perform an input-sensitive study. The model was developed for one-way flexure with dimensions similar to those used in AFRL tests by Connell and Thornburg. Sudame selected 5% global damping coefficient after conducting frequency analyses. He also found that gravity loads have little effect on lateral displacements of the wall system after using relaxation methods of LS-DYNA.

Sudame modified parameters of the model to evaluate changes in the global response. Parameters considered in the analysis included: initial modulus of elasticity, yield strength, rupture strain, thickness of the polymer retrofit, bond strength between polymer and concrete surface, and bond strength at mortar joints. When Sudame systematically changed the modulus of elasticity of the polymer by multiplies of 10, no significant changes were recorded for displacement and velocities of the wall, but the increase of elastic modulus decreased the peak strains and increased the internal energy absorbed by the polymer. When the rupture strain was reduced from 10% to 2%, a significant reduction was recorded for the internal energy of the polymer. However, there was no impact on the displacement or velocities. When the thickness was increased from 1.6 mm (1/16 of an inch) to 6.4 mm (4/16 of an inch) in increments of 1.6 mm (1/16 of an inch), there was no significant change in displacements or velocities, but there was a significant increase in the strain energy and kinetic energy of the polymer. Overall, Sudame was able to obtain some correlation between test data and his computational models.

J. T. Baylot, B. Bullock, T. R. Slawson, and S. C. Woodson, 2005

Baylot et al. (2005) conducted a study on ¼- scale URM wall specimens that also included test specimens retrofitted with spray-on polyurea. The polyurea retrofit was applied for ungrouted, non-reinforced as well as partially grouted, lightly reinforced CMU walls. The polymer was sprayed on the surface of the wall, with a overlap of 50.8 mm at the top and bottom of the reaction structure. The results show the retrofit was successful at reducing hazards inside the structure. When the masonry walls were ungrouted and non-reinforced, although polyurea contained the debris, it separated from the reaction frame over a small length near each end of the bottom of the wall. For partially grouted, lightly reinforced walls, the polyurea retrofit was tested with and without steel clamping plates, installed at the top and bottom of the reaction structure on top of the polyurea overlap. When no steel clamping plates were used, the top of the wall disconnected from the reaction structure, rotated about the bottom support and fell into the occupant space. The steel clamping plates were considered to remedy this failure since the wall stayed in place. However, the polyurea experienced significant tears near the steel plate clamp connections.

J. S. Davidson, 2005

Davidson (2005) investigated the failure mechanisms of ungrouted CMU walls retrofitted with polyurea. Tests were performed to establish the limits of blast resistance effectiveness of the retrofit technique. It was found that the thin polymer coatings applied on the interior face of the wall can eliminate fragmentation and aid in preventing the collapse of the masonry wall. Wall behaviour during blast was characterized by immediate fracture of the face cells of some CMU blocks, stress concentrations in the mortar and CMU near the supports that potentially lead to tearing of the polymer material. The stress wave propagating through the wall fractured the weak parts of the wall. Compressive stresses caused by arching action were believed to have caused crushing of the front face shells. Tension on the inside of the wall caused tension failure of the polymer. Tensile failure of the polymer reinforcement, tearing and debonding of polymer near the supports were identified as failure modes. These failure modes could lead to global collapse of the wall. A strong bond between the polymer and the wall was crucial in the effectiveness of the wall system. Without this, the material resulted in tearing at the connection of the polymer coating to the host structure and collapse of the wall. Significant arching effects were

evident in some of the tests and they were found to be directly proportional to the strength of the mortar joints. The bond between the polymer and the wall is important in order to achieve composite action. When the polymer was not applied directly on the wall, such as the case of a catcher system, large peak displacements were recorded. The spray-on polymer bonded well to the masonry; however, as opposed to the catcher system, this method of application leads to concentrated strains at mortar joints and minimal strains to the rest of the polymer. An optimized balance between bond strength, strain energy absorption, and overlap strength may result in a more effective reinforcement system. Experiments show that in order to transfer the loads to the supports, only 152 mm (6 inches) of polymer spray overlap is sufficient. Finite element (FE) modelling was carried out to better understand the strain behaviour and failure mechanisms of the wall. Both the FE modelling results and the post-test analysis indicate that the upper-most mortar joints fracture in the early stages of flexure, resulting in relative displacement of the two courses of blocks causing high shear strains in the polymer.

The results from FE analysis correlated well with the experimental results. Strain rate was found to be less than 100/s from the flexural response, peak strains for polymers were about 20% at mortar lines where crack openings occurred between the CMU's, initial modulus of elasticity and yield stress were found to have little effect on the maximum displacement, however, the polymer thickness and elongation at rupture affected the latter. Although an effective balance should be maintained between stiffness and elongation ability, the elongation capacity is more important for this purpose than having a high stiffness. Davidson commented that a better balance between stiffness, shear tearing resistance, strength, and strain capacity should result in a more effective reinforcement. FE modelling results also indicate that a tight fit between the wall and the surrounding frame is needed for significant arching resistance to occur.

Experimental results performed on walls with window or door openings showed a larger area of front face shell crushing, a tendency for tearing to initiate at the corners of the door or window frame, as well as additional breaching into the occupant space; however, the overall effectiveness of the polymer remained high. Davidson noted that there are some concerns such as the polymers emitting toxic volatiles when sprayed; requirement for

protective clothing; high equipment costs and the level of difficulty in operating the equipment (Davidson, 2005).

L. G. Moradi, J. S. Davidson, and R. J. Dinan, 2008

Moradi et al. (2008) formulated resistance functions for membrane-retrofit unreinforced concrete masonry walls subjected to combined lateral pressure and axial force. The resistance functions were provided for unreinforced masonry walls with various degrees of fixity, with or without membrane retrofit as well as when the walls experienced arching action. The main assumption was that the effective mass or stiffness of the concrete masonry units were not affected by localized damage. The authors recommend that further research be performed on the bond between the polyurea and masonry as well as connection strength and detailing. Static pressure tests of full-size or reduced-size membrane retrofit walls for fine-tuning current analytical models were also recommended. Static tests would facilitate more detailed and accurate instrumentation of wall and retrofit assembly. They also call for comparative static and dynamic tests to gain a better understanding of the strain and crushing at the arching ends while the wall experiences large deflections.

L. G. Moradi, J. S. Davidson, and R. J. Dinan, 2009

Moradi et al. (2009) used the resistance functions formulations from Moradi et al. (2008) in a SDOF analysis of unreinforced masonry walls with polymer membrane retrofit subjected to blast loading. Numerical results were compared to the previous test data. The SDOF model did not correlate well with the experimental results and a possible explanation is that the model does not consider local damage of concrete after crushing.

J. E. Crawford, 2002

Unreinforced polymers can provide protection against blast, in particular for non load-bearing walls that can deform significantly without jeopardizing the integrity of the structure. These polymers such as polyurea and polyurethane can be further strengthened with continuous fibres that can provide additional energy dissipation to the point of fibre rupture. Crawford (2002) describes a retrofit system consisting of aramid laminates

secured to the wall with polyurethane adhesives and anchored to the surrounding frames with energy dissipating anchorages.

D. Piepenburg, R. Martinez, R. Del Frate, and K. Morrill (2002, 2003)

Piepenburg et al. (2002) used a hybrid urethane-urea polymer spray as well as aramid grid fabric to reinforce a non-load bearing CMU in-fill wall. Piepenburg at al. (2003) later used polyurea instead of the hybrid polymer in conjunction with the aramid grid fabric to retrofit load-bearing walls. The retrofits were successful in containing debris from the CMU wall.

C. F. Johnson, T. R. Slawson, T. K. Cummins, and J. L. Davis, 2004

Johnson et al. (2004) used spray-on polyurea combined with an open weave aramid fibre with different fibre lay-up applications. The capacity to blast loading was found to be 1.4 to 2.0 times higher than for masonry walls retrofitted with spray-on polyurea alone and 5.5 to7.5 higher for unretrofitted masonry walls.

The research shows that combining reinforcement with spray-on polymer can provide additional energy dissipation to the point of fibre rupture; however, the additional cost of fibres and placement should be weighted against the limited increase in blast resistance. This cost is justifiable for bearing walls where allowable displacements are limited.

J. Yi, M. C. Boyce, G. F. Lee, and E. Balizer, 2006

A previous study on polyurea and three polyurethanes conducted by Yi et al. (2006) provided a quantitative analysis of the stress-strain behaviour at low strain rates, smaller than 1/s, in comparison to the behaviour at high strain rates, higher than 1000/s. The polyurea displayed an increase in stiffness transitioning from a rubber-like material at low rates to a leather-like material at high rates. One of the polyurethanes displayed a transition from a rubber-like behaviour at low rates to a glass-like behaviour at high rates.

S. Sarva, S. Deschanel, M. C. Boyce, and W. Chen, 2007

Sarva et al. (2007) performed a study to further understand the strain-rate behaviour of polymers by examining strain rate data collected from tests, conducted through each decade, ranging from 0.001/s to 13,000/s. The locations and the nature of transition in the

polymers were precisely characterised. The rubber-leather transition was found to take place at a strain rate of about 1/s and the leather-glass transition around 1000/s.

Figure 1.20 shows the stress-strain behaviour of polyurea under compression at different strain rates. The behaviour is observed to be strain rate dependent and highly non-linear. The stress levels are seen to span from a few MPa to nearly 100 MPa depending on the values of true strain and strain rate.

1.6.2 Recommendations for Future Research

From literature review, the following are items that can be potentially investigated for future research projects:

1. Most of the past research on masonry walls has been performed for non-load bearing walls since they are most susceptible to fragmentation due to blast. However, load-bearing walls need more investigation since, in the case of collapse, other building members can be affected and the structure is at risk of experiencing progressive collapse. Polyurea material proved to be a good retrofit option for infill, non-load bearing walls, but due to its large deformation capabilities and low elastic modulus, cracking and extensive damage of concrete is inevitable. Although it can deflect and capture debris during blast event, it does not increase the out-of-plane capacity of the wall to resist the impact without losing its axial loading capacity. Future research can be performed on more innovative retrofit systems to increase wall stiffness, not just its ductility. For example, a retrofit consisting of steel and polyurea could provide additional capacity and in the event of crushing of concrete, the polyurea layer can act as a catcher system preventing debris from entering the occupant space;

2. Research shows the need for further investigation of the adherence of polyurea to the CMU wall. If steel is incorporated in the retrofit design, polyurea to steel is another interface to be evaluated for adhesion performance;

3. The retrofit connection performance is still not well understood and further research is required to come up with a design detailing procedure to provide a ductile behaviour, essential for the supports to avoid premature failure of the wall system;

4. The polymer overlap or development length at the top and bottom of surrounding reaction frame should be also investigated as well as the bond angle. A continuous overlap of polymer would behave differently than a polymer applied on a surface perpendicular to the wall;

5. The polymer thickness variation needs also further investigation since the available test data is limited;

6. The material properties of polyurea under high strain rates are not well understood, especially for compressive strength. For gapped infill walls, if the gap is filled with polyurea, it could promote arching if the compressive strength of the polyurea material will increase significantly under high strain rates. Under static loading conditions it will allow for serviceability deflections without turning a non-load bearing member into a load-bearing member;

7. Development of numerical analysis and modelling techniques that incorporate changes in stiffness and mass of the wall system due to local damage of concrete are needed;

8. The impact of a blast retrofit should be analysed for the building as a whole, not only for an individual member. Strengthening a member against blast can make it withstand the impact, but the energy could be dissipated by other building components that could cause even greater damage upon their failure;

9. Past research has concentrated on ensuring that fragmentation originating from walls does not enter in the occupant space. In reality, that is not the only concern since fragments can be generated from other sources as well.

This research study addresses items 1, 2, 5 and 6: a retrofit system comprised of steel and polyurea was used for load-bearing walls subjected to shock wave loading; the adherence

of polyurea to the concrete material as well as the composite action of polyurea and steel were monitored; two different thicknesses were used for the polyurea membrane retrofit; and the polyurea contribution to arching resistance was also investigated.

Table 1.1: Equivalent TNT Mass Factors (Hyde, 1992)

Explosive Type	Equivalent TNT Mass Factor	
	Pressure	Impulse
ANFO	0.82	0.82
Composition A-3	1.09	1.07
Composition B	1.11	0.98
Composition C-4	1.37	1.19
H-6	1.38	1.15
HBX-1	1.17	1.16
Octal (75/25)	1.06	1.06
Pentolite	1.42	1.00
RDX	1.14	1.09
TNT	1.00	1.00
Tritonal	1.07	0.96

Table 1.2: Average Tensile Strength Values for Tested Polymers (Knox et al., 2000)

Application (# tested)	Secant Modulus of Elasticity MPa (psi)	Elongation at Rupture (%)	Maximum Tensile Strength MPa (psi)
Extrusion (7)	1131 (164,000)	52	55.8 (8100)
Spray-on (13)	79 (11,400)	109	9.65 (1400)
Brush-on (1)	6.9 (1,000)	25	2.1 (300)
Baseline Polymer	6.9 (1,000)	94	5.5 (800)

Table 1.3: Properties of Selected Polymer- Polyurea (Knox et al., 2000)

Property	Measured Value
Initial Modulus of Elasticity	234 MPa (34,000 psi)
Secant Modulus of Elasticity	165 MPa (24,000 psi)
Elongation at Rupture	89 %
Stress at Rupture	13.9 MPa (2011 psi)
Maximum Tensile Strength	14.1 MPa (2039 psi)
Toxicity (according to manufacturer)	Nontoxic once cured

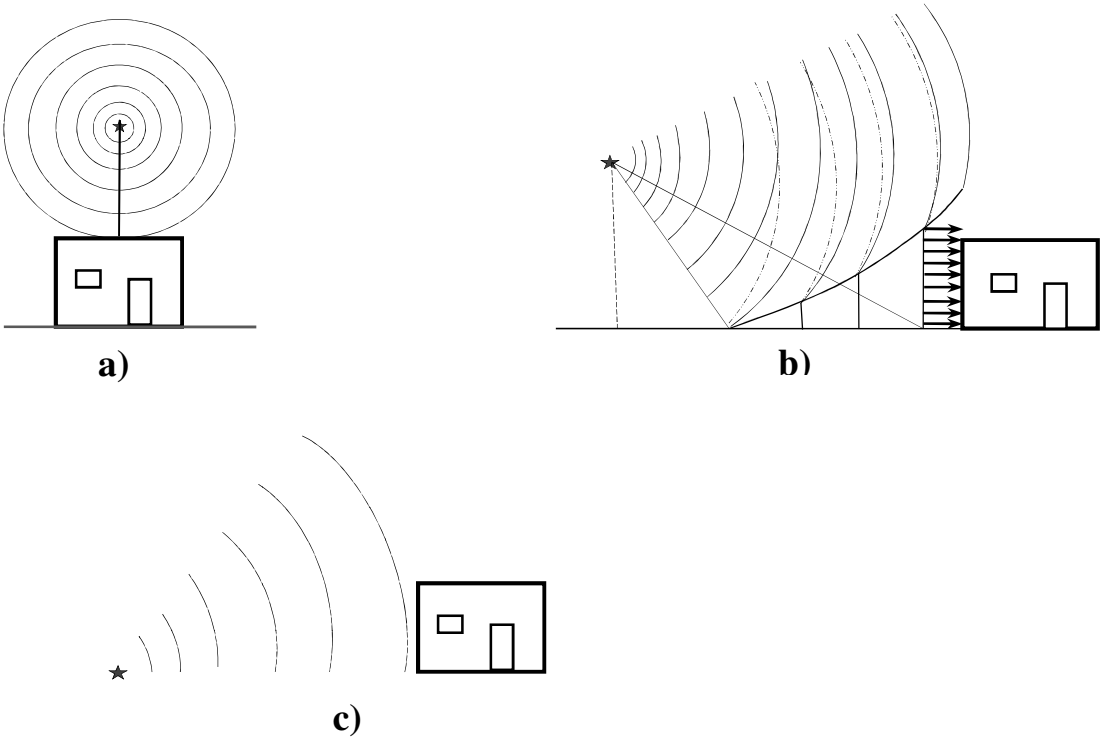

Figure 1.1: Blast Loading Category: a) Free Air Burst, b) Air Burst, c) Surface Burst

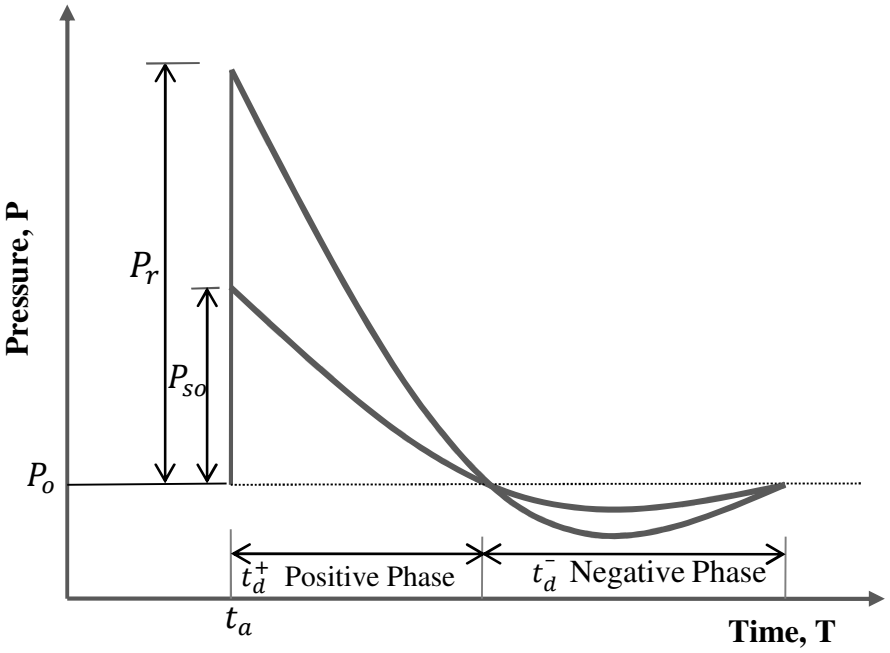

Figure 1.2: Blast Pressure Profile

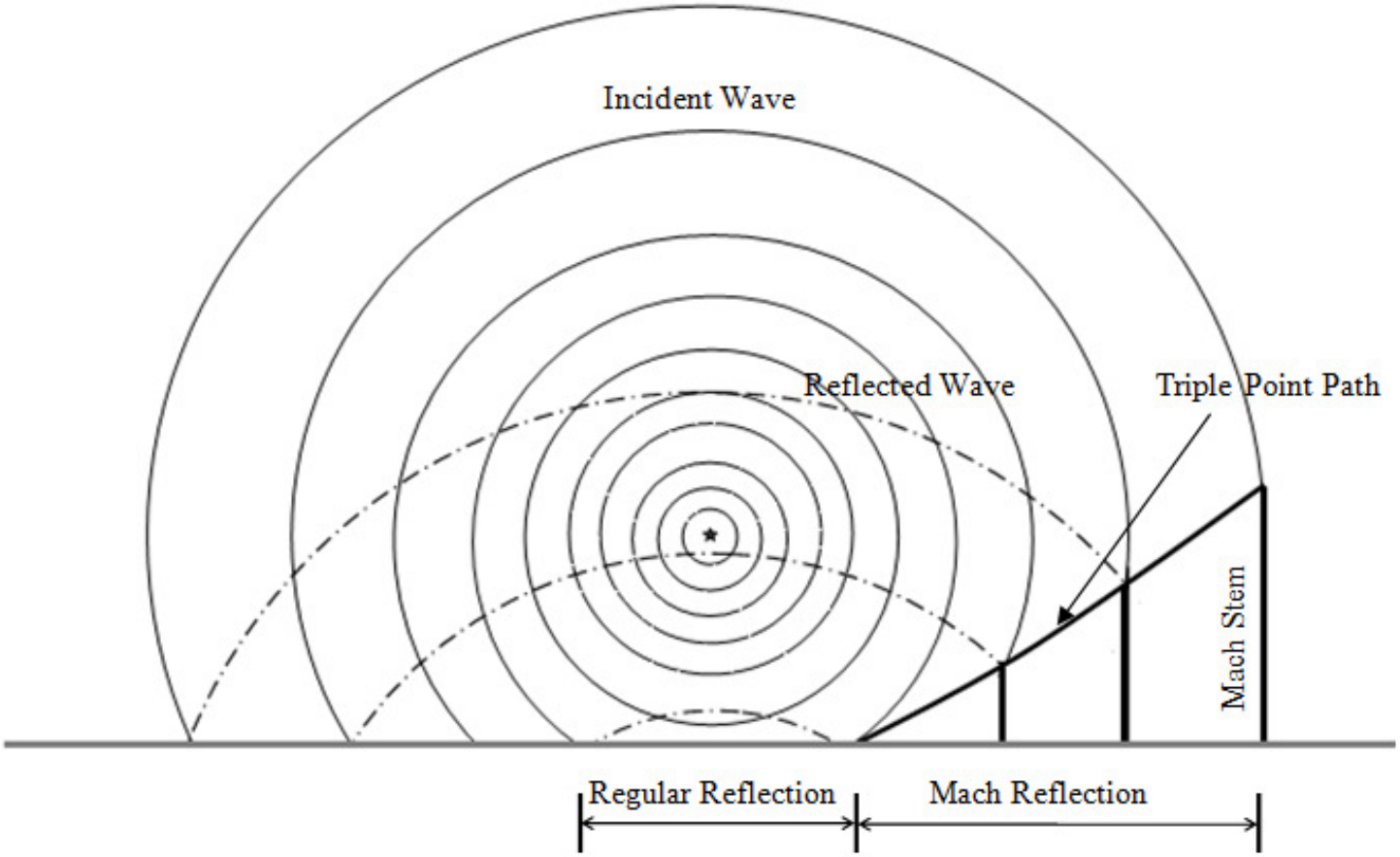

Figure 1.3: Mach Stem Creation

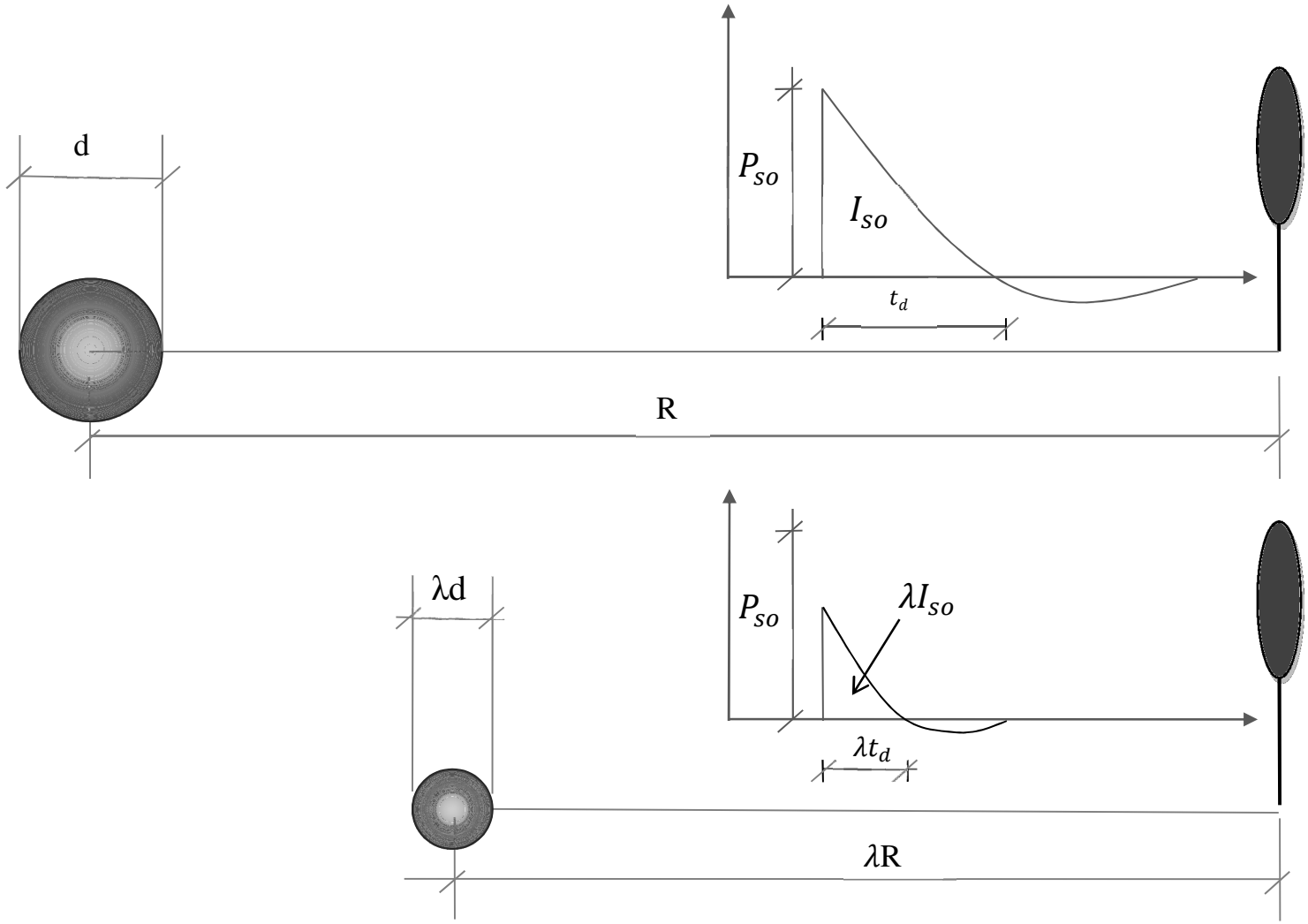

Figure 1.4: Hopkinson-Cranz Scaling Law

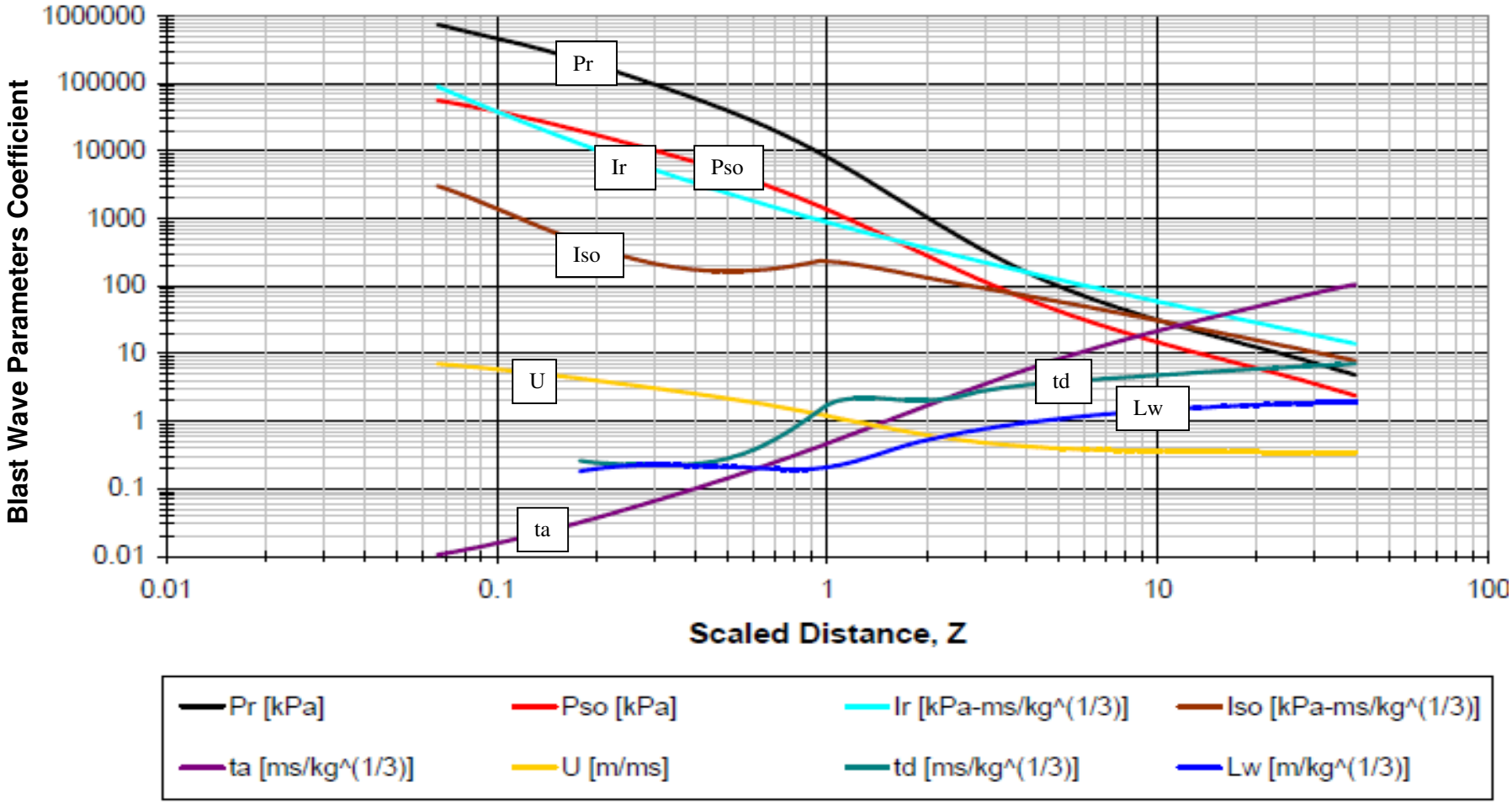

Figure 1.5: Positive Phase Blast Parameters for Hemispherical TNT Surface Blast (Adapted from UFC-3-340-02)

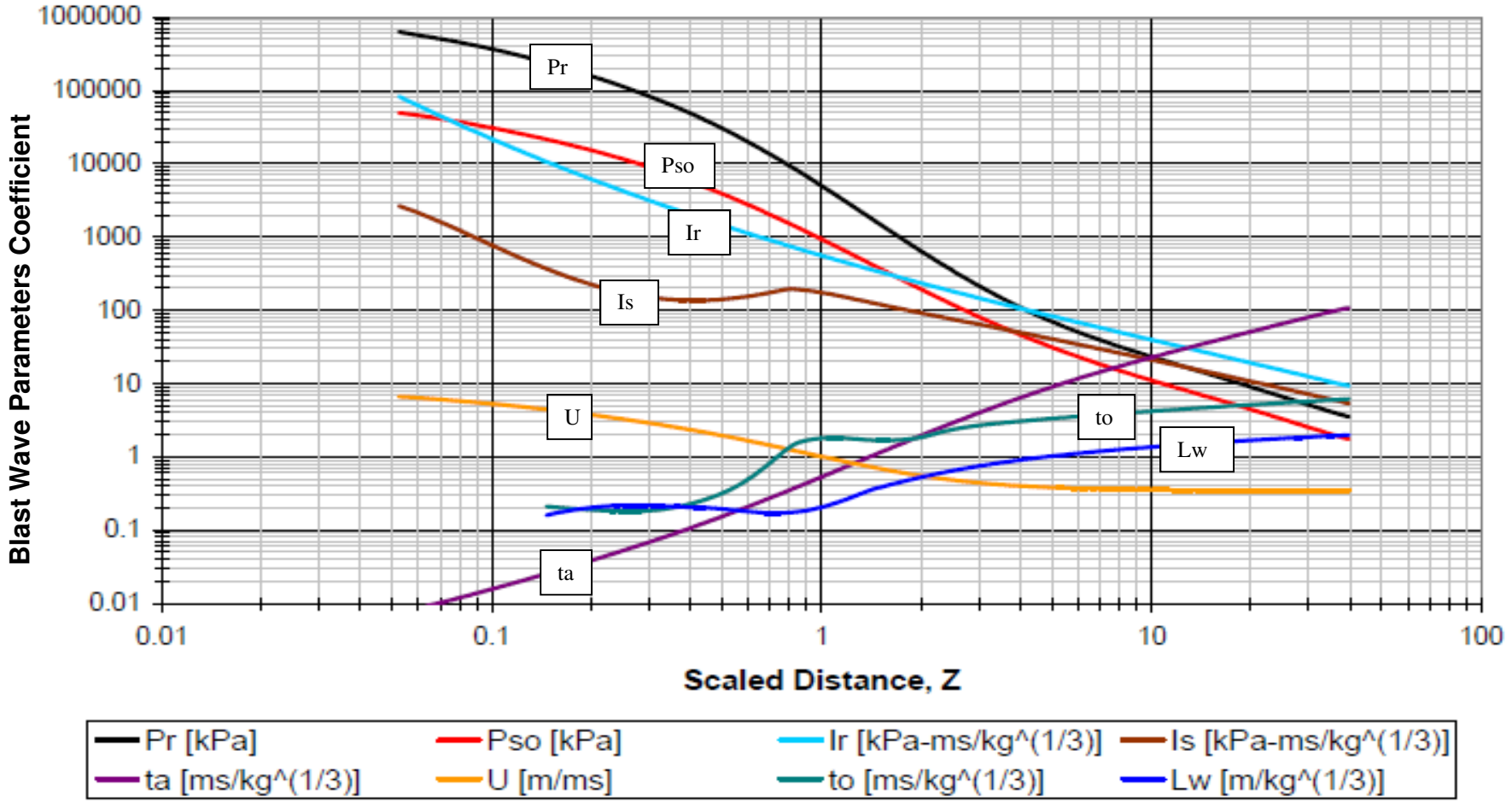

Figure 1.6: Positive Phase Blast Parameters for Spherical TNT Surface Blast (Adapted from UFC-3-340-02)

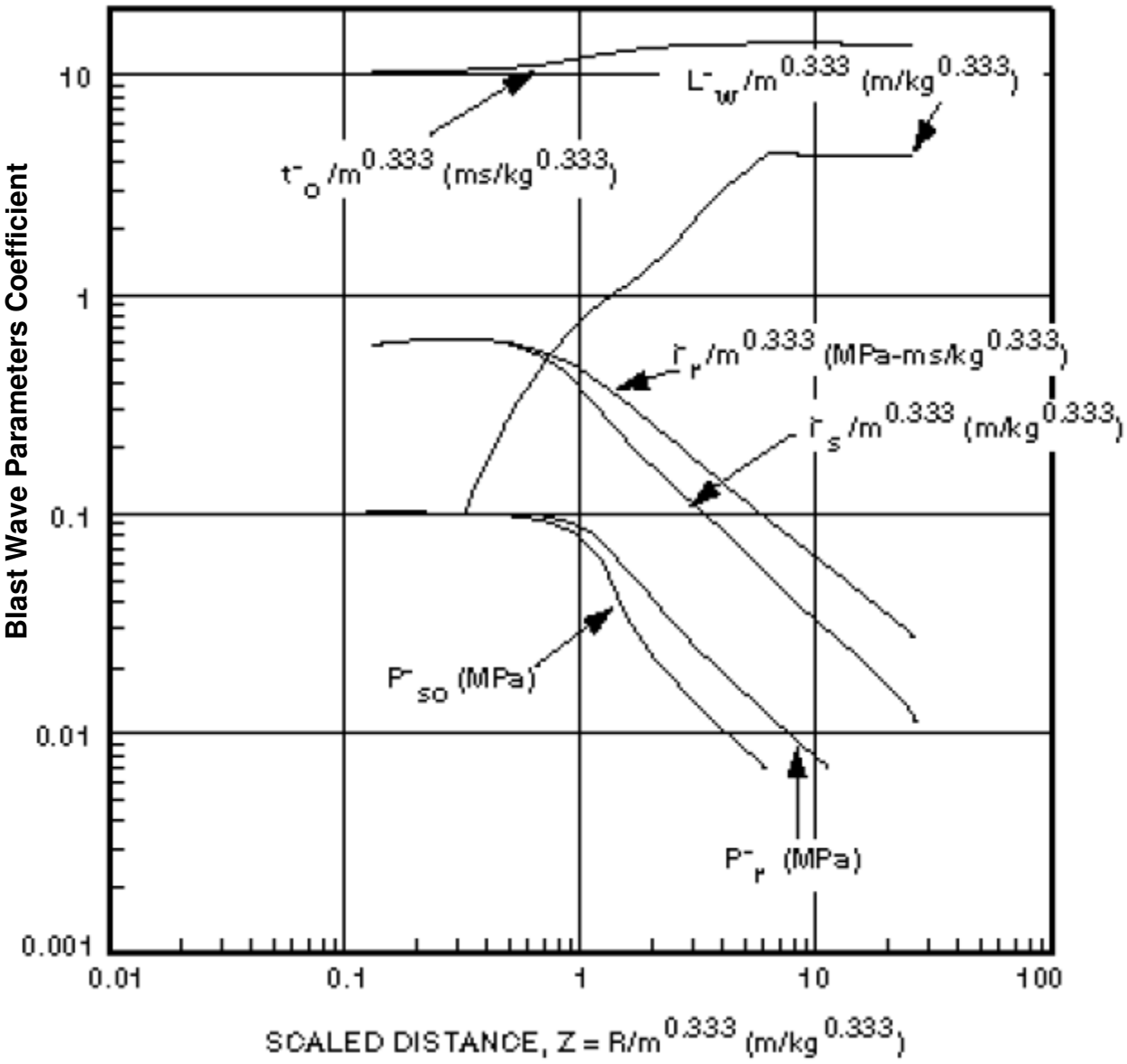

Figure 1.7: Negative Phase Blast Parameters for Hemispherical TNT Surface Blast (UFC-340-01)

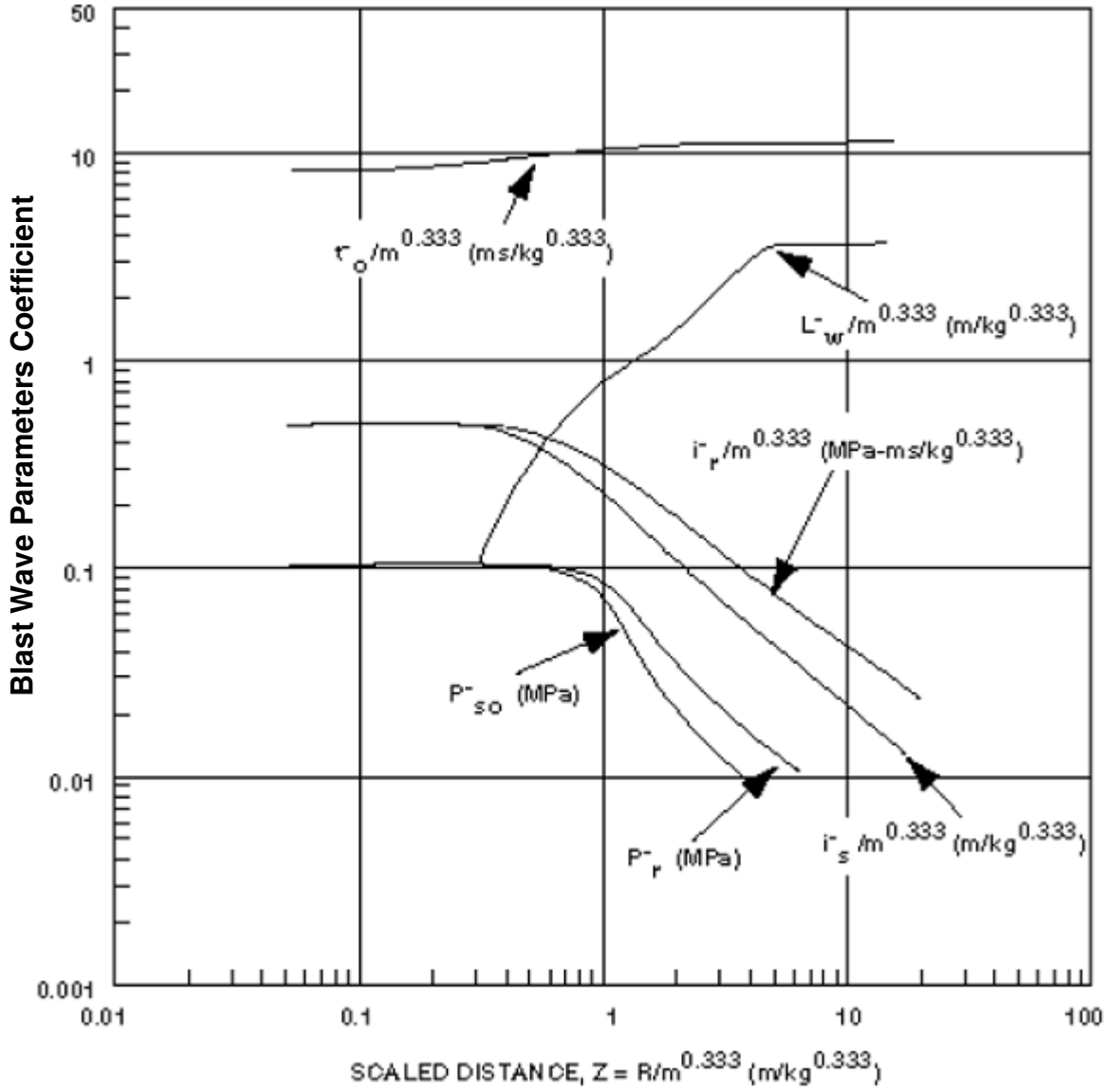

Figure 1.8: Negative Phase Blast Parameters for Spherical TNT Surface Blast (UFC-340-01)

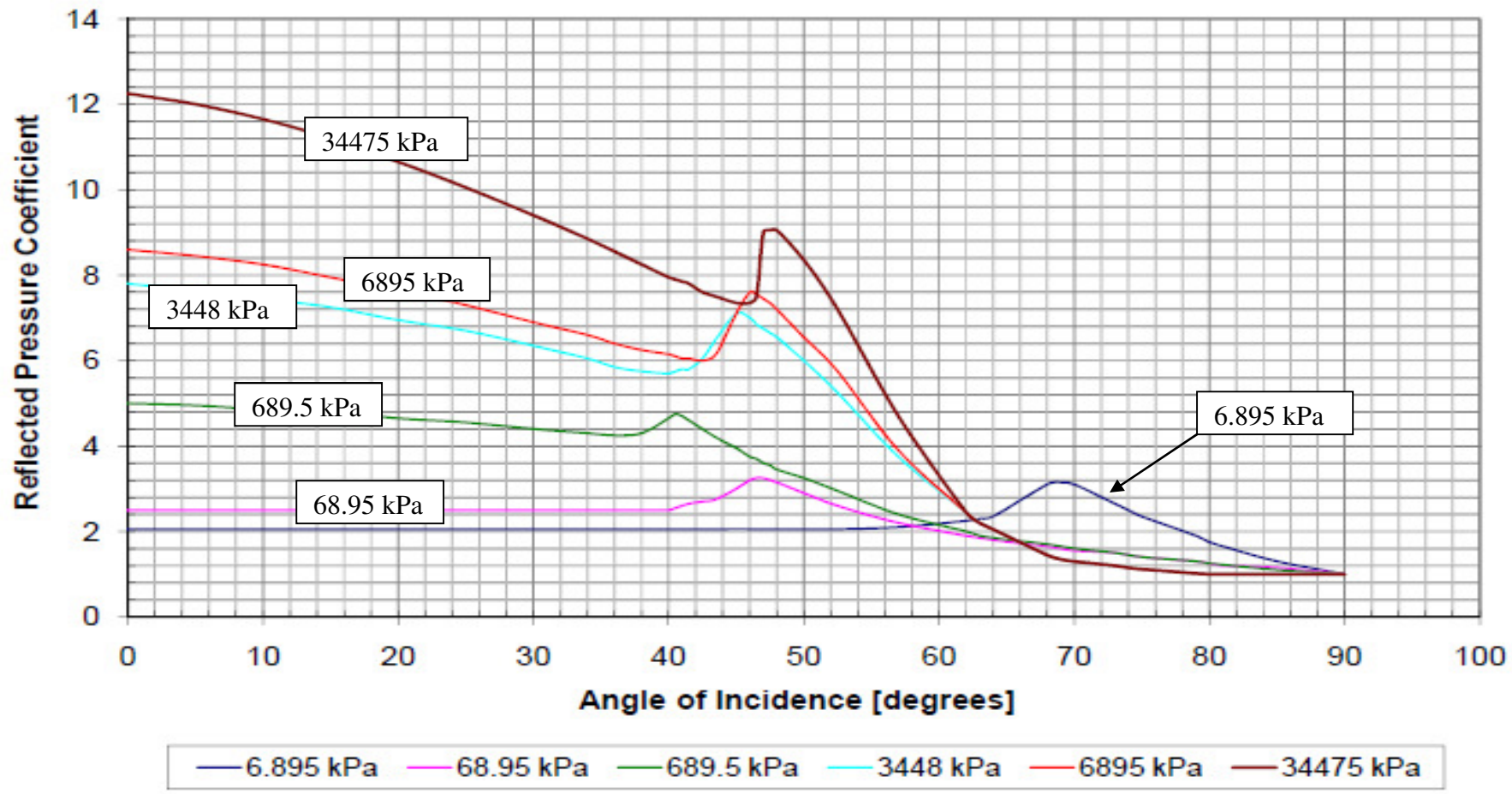

Figure 1.9: Reflected Pressure Coefficient versus Angle of Incidence (Adapted from UFC-3-340-02)

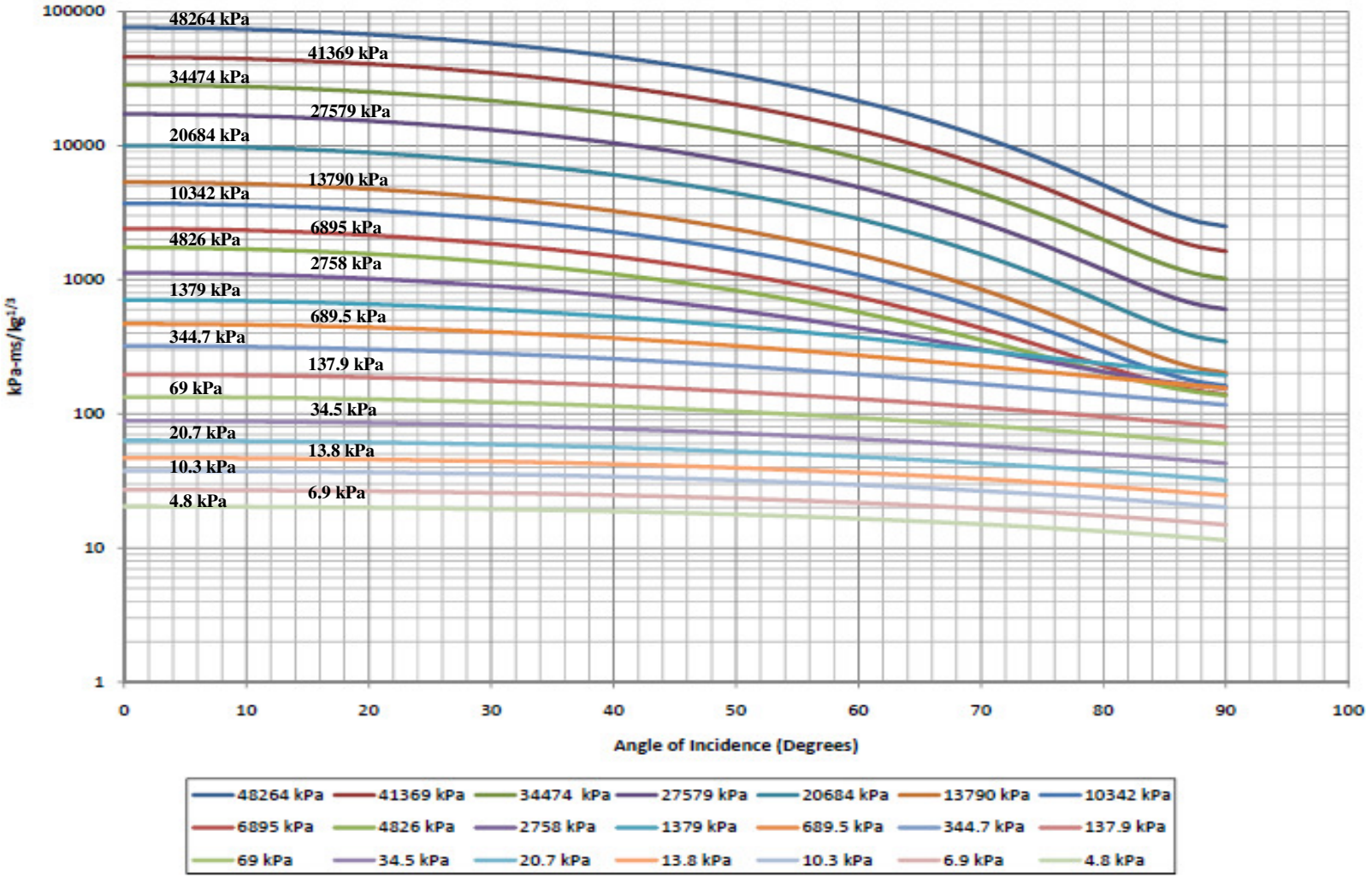

Figure 1.10: Normalized Reflected Impulse versus Angle of Incidence (Adapted from UFC-3-340-02)

a) b)

Figure 1.11: Polyurea Sprayed on Masonry Wall; a) Application; b) Appearance Coating (Crawford, 2006)

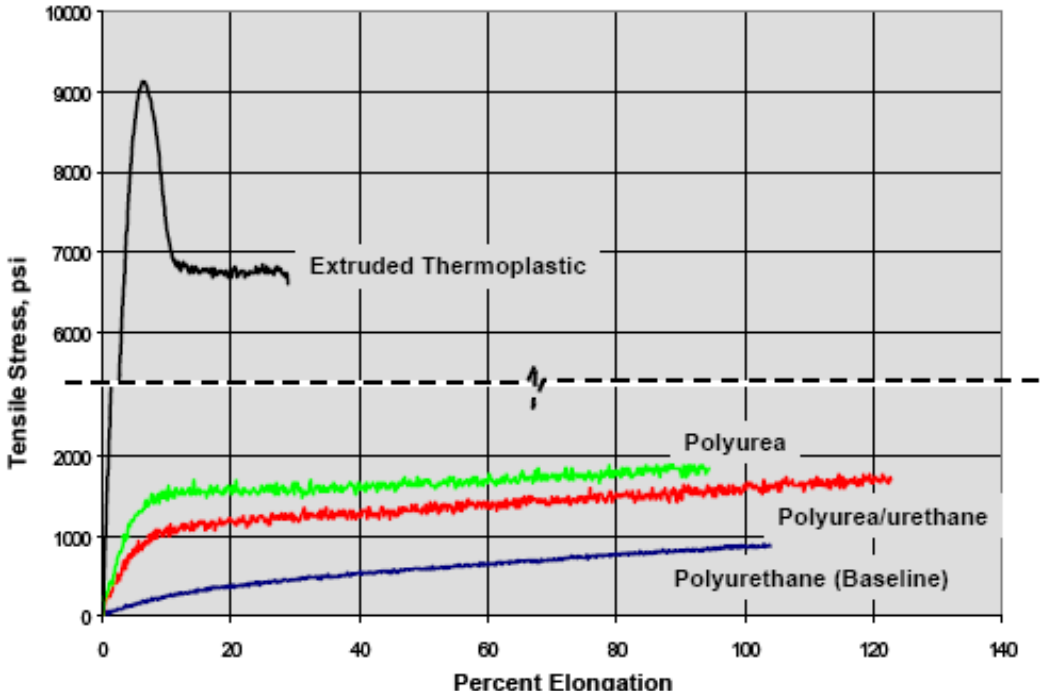

Figure 1.12: Typical Results from Polymer Tensile Testing (Knox et al., 2000)

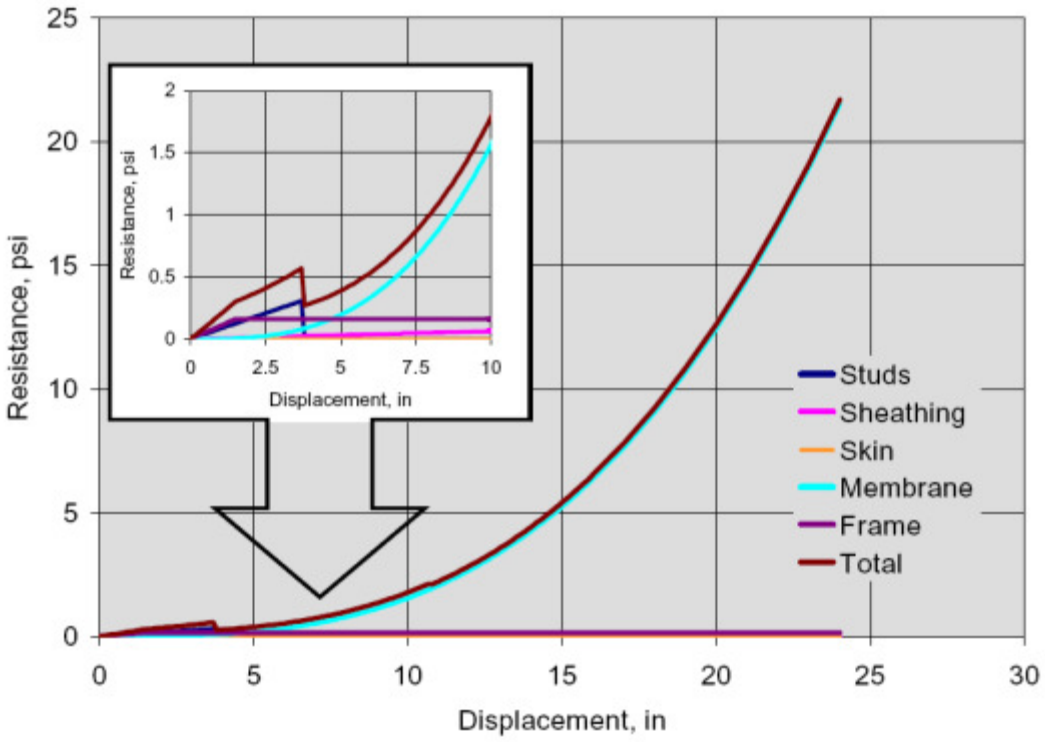

Figure 1.13: Composite Resistance Function for Lightweight Shelter Wall (Knox et al., 2000)

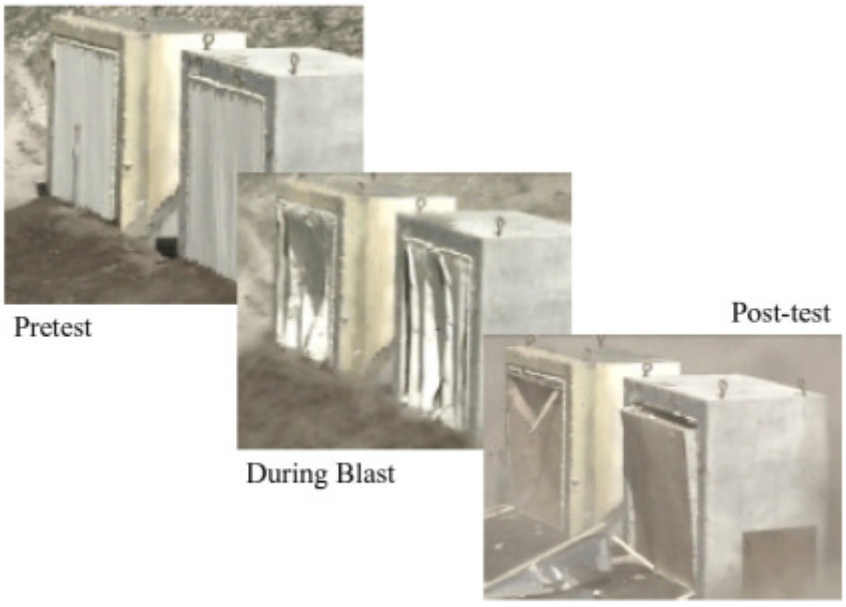

Figure 1.14: Component Wall Testing (Knox et al., 2000)

Figure 1.15: Single-Wide Trailer (Knox et al., 2000)

Figure 1.16: House Trailer Results (Knox et al., 2000)

a) **b)**

Figure 1.17: a) Test set-up; b) Visual Post Test Results (Connell, 2002)

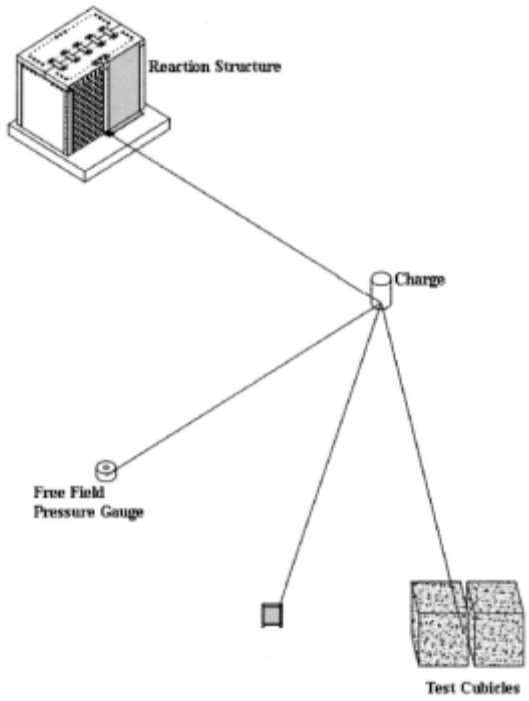

Figure 1.18: Test Setup (Davidson et al., 2004)

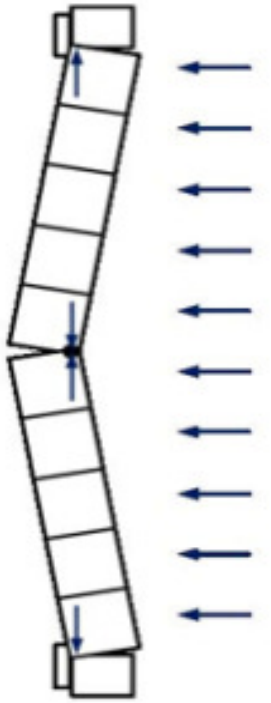

Figure 1.19: Arching Action Mechanism

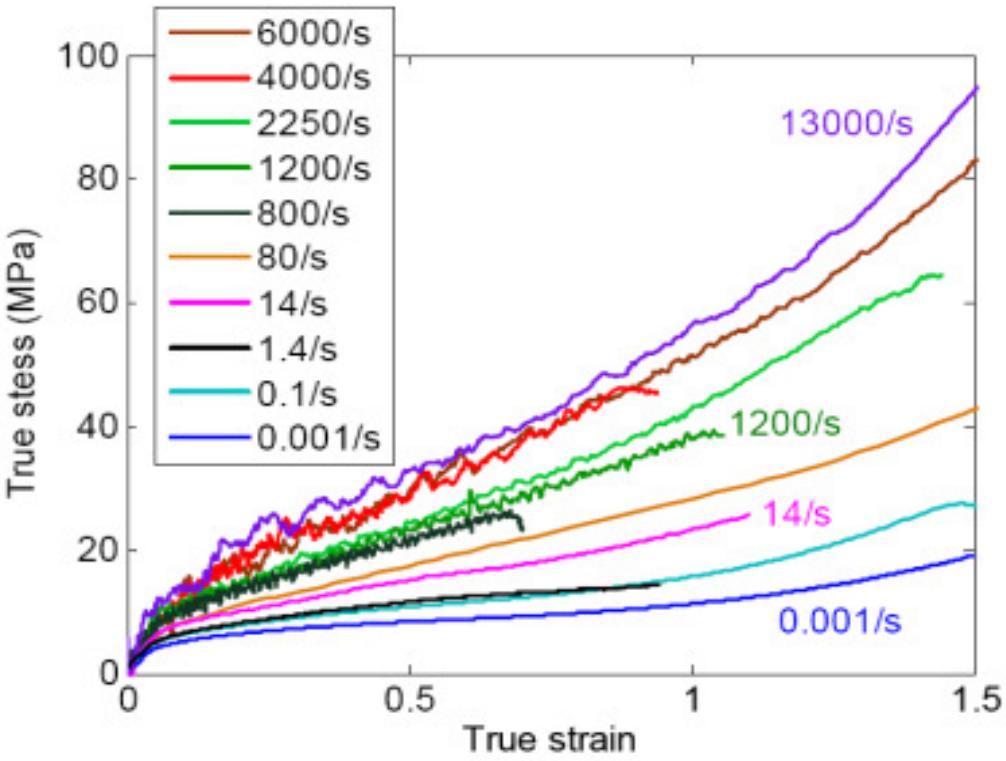

Figure 1.20: Stress-Strain Behaviour of Polyurea under Ranging Strain Rates (Sarva et al., 2007)

CHAPTER 2

Experimental Program

2.1 General

Four (4) unreinforced masonry (URM) walls were constructed for this study and tested under shock tube induced blast loading at the University of Ottawa Shock Tube Testing Facility. Two of the URM walls were designed and built as non load-bearing, infill walls. One of the infill walls was retrofitted with a layer of spray-on polyurea. The other two URM walls were designed and built as load-bearing walls meant to represent existing building construction. One of the load–bearing walls was retrofitted with a system comprised of non deformed steel wires with a layer of polyurea sprayed over the bars and concrete masonry surface. The specimens, representing the middle third section of a wall with a length to height ratio greater or equal to 3, were designed to simulate one-way action. Arching action was activated for all four URM wall specimens. This chapter describes the construction and testing regime for the above mentioned URM wall specimens.

2.2 University of Ottawa Shock Tube Facility

The University of Ottawa established a Blast Research Group within the Hazard Mitigation and Disaster Management Research Centre in the Civil Engineering Department, with the focus of conducting experimental tests using a shock tube. The shock tube facility, located in the Structural Engineering Laboratory of the University of Ottawa, is one of the very few facilities in the world where blast simulation tests can be performed on structural components. Experimental tests could be carried out on individual structural members such as beams, columns, slabs and walls as well as scaled models of bridges, dams and buildings.

During an explosion, a zone of compressed air is created that spherically expands as a shock wave from the centre of detonation. The University of Ottawa Shock Tube Facility can simulate the shock wave mechanism by using a compression chamber, also called a driver section that rapidly releases compressed air into an expansion chamber where it travels along its length until it interacts with the test specimen. The shock tube, shown in Figure 2.1 (a) and (b), consists of a driver section, a double diaphragm spool section with an aluminum diaphragm at each end, and an expansion chamber section that terminates in a rigid test frame. Operation of the shock tube involves simultaneously charging the driver and the spool sections to the desired pressures, then suddenly releasing the air in the spool section causing the aluminum diaphragm to rupture. The intensity and duration of the load are controlled by varying the driver section pressure and the driver section length, respectively. The benefits of using a shock tube over live explosives testing are: low cost of testing; predictability of shock wave parameters; ease of monitoring and instrumentation; as well as ease of operation and safety of operation (Lloyd et al., 2009).

2.3 Details of the Test Specimens

The following sections describe existing construction detailing of concrete masonry unit (CMU) walls, constructed inside a structural concrete or steel frame, as well as a detailed description of the specimens that were tested under shock tube induced blast loading for this particular experimental study.

2.3.1 Existing Construction

According to the International Masonry Institute (IMI), there are three types of CMU walls constructed inside a steel or concrete frame (IMI, 2010). Type I CMU wall, shown in Figure 2.2, has vertical gaps between the wall and the columns (Gap 1 and Gap 2) as well as a horizontal gap between the top of the masonry wall and the beam or slab (Gap 3). This scenario is representative of a non load-bearing wall where gaps allow both lateral drift at the columns as well as vertical deflection at the top. Type II CMU wall, shown in Figure 2.3, has gaps between the wall and the columns (Gap 1 and Gap 2), but no horizontal gap at the top between the wall and the beam (or slab). Type II represents a load-bearing shear wall that allows only lateral drift at the columns. Type III CMU wall is fully confined with the surrounding frame. The latter is currently under development and research is underway

to determine structural and construction requirements (IMI, 2010). Type I and II walls are able to resists out-of-plane loading through mechanical shear restraints at the top of the wall as well as dowels at the bottom (Figure 2.4). These anchors can have different configurations depending on the type of frame they connect to. Figure 2.4 shows the use of wide plates for shear transfer at the top of the wall, welded to the structural steel frame and bolted to the CMU. Vertically slotted holes are used to accommodate beam deflection for Type I non load-bearing CMU wall. Figure 2.5 shows the use of clip angles (Glanville et al., 1996) for Type I non load-bearing walls when the surrounding frame is made of concrete and drilled-in fasteners are installed to restraint the wall from out-of-plane movement. The Canadian Standards Association (CSA) Standard A370-04, prescribes a spacing of minimum ten times the wall thickness for a single-wythe wall or partition for horizontal lateral support anchors such as wide plates or clip angles (Clause 7.2.2 and 7.3.2). The vertical reinforcement (dowels) transfer tension tie-down forces as well as shear forces into the frame. An example of a column anchor configuration is shown in Figure 2.6. If the vertical reinforcement is not present, the anchors can be imbedded in the mortar joint. If horizontal joint reinforcements are present (Figure 2.4), they can be welded to the steel frame. CSA Standard A370-04 prescribes a minimum spacing for vertical lateral support anchors of four times the nominal thickness of the wall for single-wythe wall or partition (Clause 7.2.3 and 7.3.3).

2.3.2 Test Specimens

Four (4) unreinforced masonry (URM) walls, with a 2000 mm by 2000 mm surface area, were built for testing under shock waves. Table 2.1 provides a description of the test specimens with the corresponding retrofit. All walls were tested under simulated shock wave loading, with walls URM-3 and URM-4 tested under combined axial and shock wave loading. The simulated blast loading was applied using the University of Ottawa shock tube that creates the shock wave by rapidly releasing pressurised air from the driver section and the axial loading was applied using hydraulic jacks. The masonry walls were built using standard $100 \times 200 \times 400$ concrete blocks with 10 mm thick Type S mortar joints. Figure 2.7 and Table 2.2 show overall dimensions and properties of the standard $100 \times 200 \times 400$ concrete masonry unit block. The smallest available standard size was used for CMU blocks to assure failure of all the specimens, including the retrofitted walls, before

reaching the shock tube capacity. Figure 2.8 shows the construction process of the URM wall panels. General arrangement and details of the test specimen are shown in Figure 2.9 (a) and (b). Each wall was placed inside a 2388 mm by 2388 mm steel testing frame, fabricated from HSS 152×152×6.4 steel sections, and bolted to the shock tube end frame.

For both infill walls, URM-1 and URM-2, the top edge gap between the URM infill wall and the enclosing frame was reduced to 6 mm gap using structural steel filler in order to activate the arching mechanism. In existing construction, this gap is much greater (25mm to 40 mm); therefore, reducing the top edge gap to promote arching is a retrofit technique on its own. The load-bearing walls, URM-3 and URM-4, were constructed with no top edge gap. Two HSS 152×152×6.4, 2388 mm long, structural steel sections were installed across the top and bottom of all the specimens centered on the joint between the URM wall and the test frame (Figure 2.9 (b)), as mechanical shear restraints to prevent out-of-plane translation. Note that the structural elements used as mechanical shear restraints need only have sufficient capacity to withstand the applied out-of-plane forces. These mechanical shear restraints provide continuous lateral support as opposed to the anchors prescribed by CSA Standard A340-04 discussed in Section 2.3.1, that are designed to resist small lateral loads, not blast loads. Four HSS 76×76×6.4 sections, 457 mm long, were provided as end supports to secure the mechanical shear restraints to the shock tube as shown in Figure 2.9 (a) and (b). The top shear restraints were placed on top of steel brackets, whereas the bottom shear restraints were placed above the connecting rods. The mechanical shear restraints were intended to simulate existing construction practices for Type I and Type II CMU wall to beam connection as described in section 2.3.1. HSS sections were selected due to their immediate availability in the laboratory. No dowels were used since they could not be fitted inside the voids of the $100 \times 200 \times 400$ CMU blocks. However, the bottom mechanical shear restraint provided resistance to out-of-plane movement. The walls simulated one-way action; therefore there was no concern in providing wall to column anchoring system.

Figure 2.10 shows the general test setup for URM-1 infill wall specimen. The second wall (URM-2) was retrofitted with a layer of spray-on polyurea on the tension side of the wall as shown in Figure 2.9 (a) and (b). The shaded area represents the polyurea spray,

approximately 2000 mm wide by 2300 mm high, with an average thickness of 3 mm, recommended by the manufacturer as an optimum thickness for both blast protection as well as cost. Davidson (2005) recommends that the polyurea membrane be extended at least 152 mm beyond the limits of the masonry, therefore, for this experimental program, the spray was applied with a 152 mm overlap onto the top and bottom members of the steel testing frame. Figure 2.11 shows the application process of the polyurea retrofit as well as the specimen prior to testing. The construction and setup for the load-bearing wall URM-3 is similar to that of wall URM-1 (Figure 2.9 and 2.10); however, there is no gap between the URM wall and the top of surrounding steel frame.

The general arrangement and detailing for the retrofitted load-bearing wall (URM-4) is shown in Figure 2.12. The retrofit installation process and views of the specimen prior to testing are shown in Figure 2.13. The wall was constructed in a similar manner to the load-bearing wall, URM-3, however, twenty 6.3 mm non deformed steel wires were attached to the wall (Figure 2.13 (a)) with a 6 mm layer of polyurea sprayed on top (Figure 2.13 (b)). The steel wires, spaced horizontally at 100 mm, were welded to flat plates, and installed to the shock tube steel testing frame. The polyurea layer, sprayed on top of the steel wires and the masonry wall, assured composite action. The polymer thickness was doubled in order to ensure a continuous membrane over both the concrete block wall as well as the steel wires. The mechanical shear restraints were placed across the top and bottom of the wall to prevent sliding (Figure 2.13 (c) and (d)).

Axial load was applied to the load-bearing walls, URM-3 and URM-4, by using two hydraulic jacks located between the bottom of the testing frame and the rigid floor. The hydraulic jacks were located 686 mm from each side of the steel frame and 1016 mm apart from each other (Figure 2.9). The axial load level applied to each load-bearing wall was selected to be 10% of total axial capacity of the wall, translating to approximately 122 kN, 61 kN from each jack.

2.4 Polyurea Application

Polyurea retrofit spray (PAXCON PX-3350) was applied by Line-X of Ottawa certified staff. A day before the application, the wall was primed with a two-component aliphatic

urea product. The gap between the URM wall and the surrounding frame was filled with a latex type caulking material with no compressive strength. Prior to application, both the isocyanate and amine resin components were heated to temperatures of approximately 50ºC in order to achieve best mixing and polymerization results. The chemical reaction between the two components, with a volume mix ratio of 1:1, begins instantly at the end of the spray gun during application. Once applied, the spray has a tack free time of 9-12 seconds and a curing time of 24 hours. Polyurea is non-toxic once in place and cured, however during the application it requires special handling equipment such as protective clothing, gloves, masks and respirators.

Shortly after the application of the polyurea, the two HSS 152×152×6.4 mechanical shear restrains were installed across top and bottom of the frame. The polyurea retrofitted walls, URM-2 and URM-4, were tested 168 hours and 24 hours, respectively, after the application of the polyurea spray.

2.5 Material properties

The following section presents material properties results obtained from various experimental tests performed at the University of Ottawa Civil Engineering Structural Laboratory.

2.5.1 Ultimate Compressive Strength of the CMU Wall

An average 66 day ultimate compressive strength of 10 MPa was determined from prism tests. Four concrete block prisms were built from two standard $100 \times 200 \times 400$ CMU blocks, ungrouted, with a 10 mm Type S mortar joint and tested in uniaxial compression in accordance with CSA S304.1-04 (Figure 2.14 (a)). Concrete blocks were provided to build only four prisms, not five prisms as specified in CSA S304.1-04. The prisms failed by splitting of face shells as shown in Figures 2.14 (b), (c), and (d). Figure 2.15 shows the stress-strain data for the four prisms tested in compression. The strain values shown in Figure 2.15 are not the actual values since the test was only load-controlled. The ultimate compressive strength obtained from prism tests is representative for the overall wall specimen, also considering the interaction between the mortar joints and the CMU blocks.

2.5.2 Ultimate Compressive Strength of Mortar

An average 66 day ultimate compressive strength of 9.7 MPa was determined from compression tests performed on mortar cubes in accordance with CSA A179-04. Five 50 mm mortar cubes were casted in steel cube moulds. Typical shear fractures of the mortar samples are shown in Figure 2.16 (a), (b), and (c). Figure 2.17 shows the stress-strain characteristics for the 50 mm mortar cubes tested in uniaxial compression.

2.5.3 Tensile Strength of Polyurea

Table 2.3 summarises the mechanical properties of the polyurea material, properties provided by Line-X of Ottawa. Figure 2.18 shows the stress-strain characteristics for three polyurea coupons tested in tension at the University of Ottawa. The polyurea coupons were cut from 10 mm thick sheets. All coupons follow the same slopes; however, the rupture strains and strengths differ. Figure 2.19 shows the polyurea coupons after rupture. There is a slight disagreement in mechanical properties of polyurea between the manufacturer provided and the properties obtained through coupon testing at the University of Ottawa. For analysis purposes the stress-strain characteristic obtained from coupon testing at the University of Ottawa were used, since the coupons shown in Figure 2.18 follow the same slopes; however, the manufacturer provided rupture strain (Table 2.3) was used since the coupon tests show different rupture strains in Figure 2.18.

2.5.4 Tensile Strength of Non Deformed Steel Wires

Coupon tests were performed to determine the stress-strain characteristics of the 6.3 mm diameter non deformed steel wires that were used in the retrofitting the URM-4 wall specimen. Figure 2.20 shows the stress-strain curve for both tensile coupon tests.

2.6 Instrumentation and Data Acquisition

Five out-of-plane displacements measurements were taken along the centreline height of each wall using displacement gauges connected to both the wall and a support stand in a manner that would allow for rotation at both ends of the gauge. Figures 2.9 (a) and (b) show the location of the displacement gauges on the URM walls. For walls URM-1, URM-2, URM-3, wire transducers were used for in-plane displacement measurements; however, for wall specimen URM-4, linear variable displacement transducers (LVDT) were used.

The top part of the testing frame of the infill wall specimen, URM-1, was instrumented with four 350 ohm linear electric resistance strain gauges, 6 mm in length. The gauges were intended to record strains that would be caused by arching of the wall; however, the gauges did not record any strains. For wall specimens URM-2, URM-3 AND URM-4, two load cells were installed between the testing frame and the ceiling (strong floor). Steel shims were installed between bottom of testing frame and concrete floor. In the case of load-bearing walls, URM-3 and URM-4, shims were placed between the bottom of the testing frame and the hydraulic jacks. The frame was allowed to slide vertically in order to record any change in axial loading. The load cells were intended to record any axial loading that might be caused by arching of any of the walls as well as changes in load level for the load-bearing walls.

The non deformed steel wires that were part of the retrofit system of wall URM-4, were instrumented with six 350 ohm linear electric resistance strain gauges, 6 mm in length as shown in Figure 2.12. One strain gauge was attached at mid-height of the 5^{th} non deformed steel wire, and the other five gauges were installed along the height of the 10^{th} wire (counting from the left side of the wall).

Two pressure measurements, recorded using dynamic piezoelectric pressure sensors located near the compression, blast face of the specimen, were taken to record the reflected pressure time history for each test. An average value of the two pressure readings was used in the analysis. A digital oscilloscope reading at 100,000 Hz (samples per second) was used as the Data Acquisition Controller (DAC) during testing. In addition to specimen instrumentation, a high speed camera was used to record the wall response at a frame rate of 500 frames per second, synchronized to the recorded data histories.

2.7 Testing Plan

A total of four shock tube shots were carried on the URM-1 infill wall specimen and a total of ten shots for the polyurea retrofitted URM-2 infill wall. The URM-3 load-bearing wall was tested seven times and the URM-4 load-bearing wall was tested eight times. The shock tube driver pressure was increased by approximately 40 kPa increments to the point of wall failure. This pressure increase is only approximate and highly depended on the resistance

of the aluminum diaphragms. A poor quality diaphragm would lead to premature firing of the shock tube. The maximum reflected pressure recorded near the specimen is approximately 7 times smaller than the applied driver pressure. The duration of the blast load was kept constant (approximately 17 ms) by using the same driver length during all the shock tube tests, except the last shot performed on the URM-4 load-bearing wall specimen where the maximum driver length was used in order to achieve a positive phase duration of 50 ms. The effect of repeated loading on the strength of the specimens was considered negligible. Prior to each test and after the application of the load, all strain gauges, displacement gauges and load cells were set to record zero.

Table 2.1: Description of Test Specimens

WALL	DESCRIPTION	RETROFIT
URM-1	Non load-bearing, infill	- Reduce top edge gap to 6 mm - Provide mechanical shear restraints
URM-2	Polyurea retrofitted, non load-bearing, infill	- Reduce gap to 6 mm - Apply 3 mm layer of spray-on polyurea - Provide mechanical shear restraints
URM-3	Load-bearing	- Provide mechanical shear restraints
URM-4	Retrofitted, load-bearing	- Install twenty (20) 6.3 mm, non deformed steel wires, welded to flat plates and bolted to testing frame - Apply 6 mm layer of spray-on polyurea - Provide mechanical shear restraints

Table 2.2: Properties of Standard $100 \times 200 \times 400$ Concrete Masonry Unit (CMU)

Modular Size (mm)	100
Actual Overall Width (mm)	90
Minimum Faceshell Thickness (mm)	20
Minimum Web Thickness (mm)	20
Equivalent Thickness (mm)	66
Percentage Solid	74
Approximate Mass of Wall in Place (kg/m^2)	140

Table 2. 3 Mechanical Properties of Polyurea

Property	Measured Value
Modulus of Elasticity	386 Mpa
Tensile Strength	14 Mpa
Flexural Strength	18 Mpa
Elongation at Rupture	82%

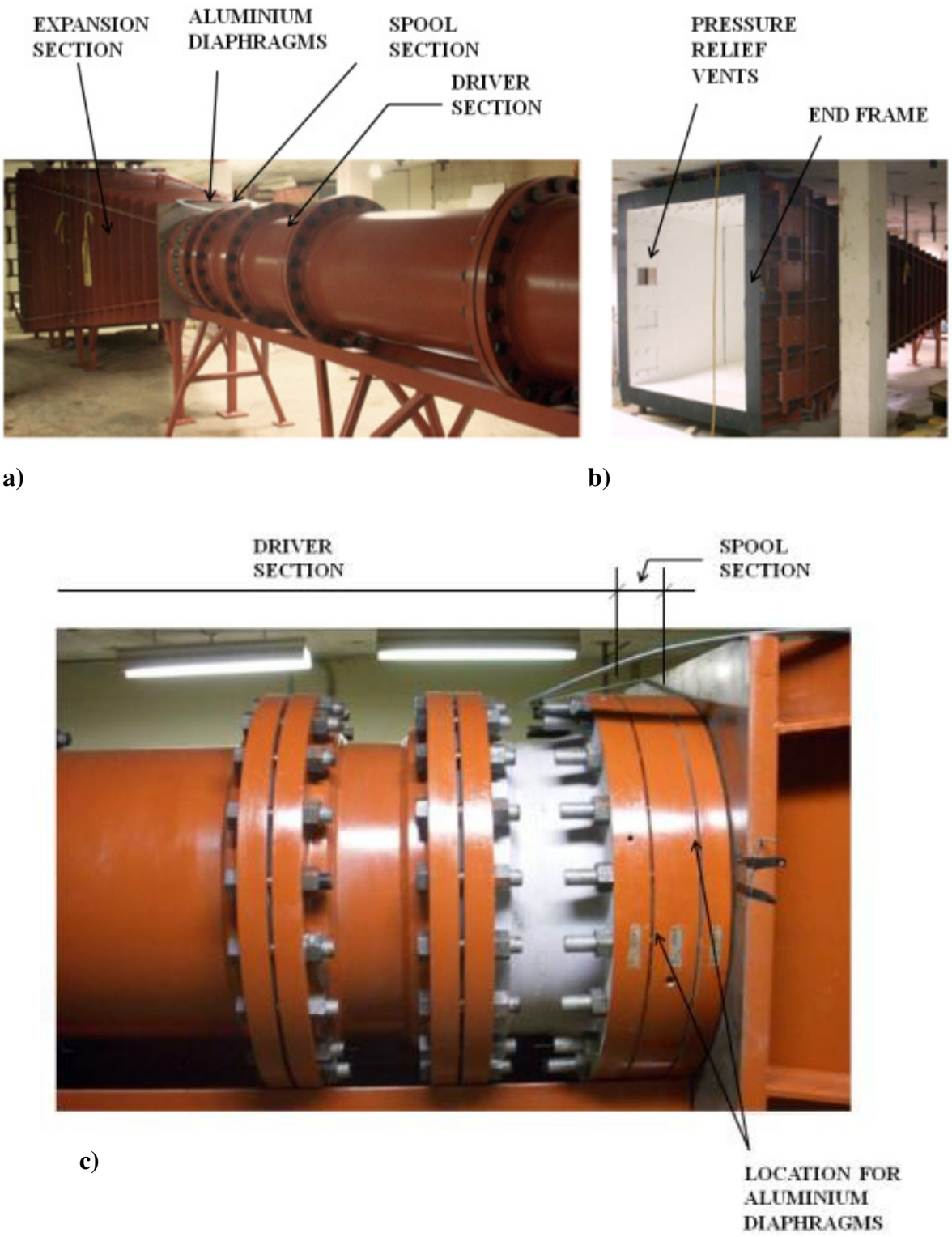

Figure 2.1: University of Ottawa Shock Tube Testing Facility: a) Shock Tube Driver Section and Expansion Chamber; b) Shock Tube End Frame; c) Spool Section

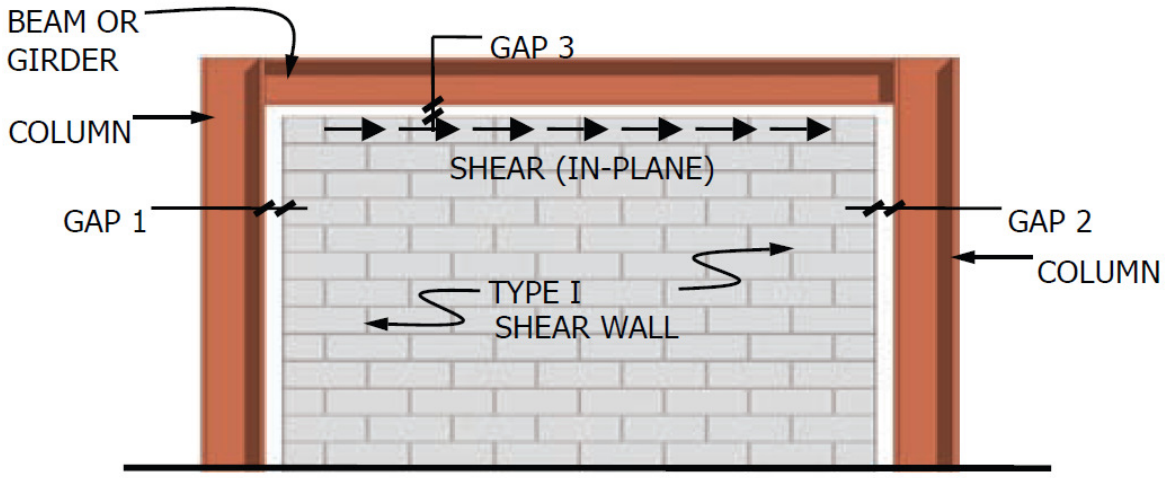

Figure 2.2 Type I Shear Wall (IMI, 2010)

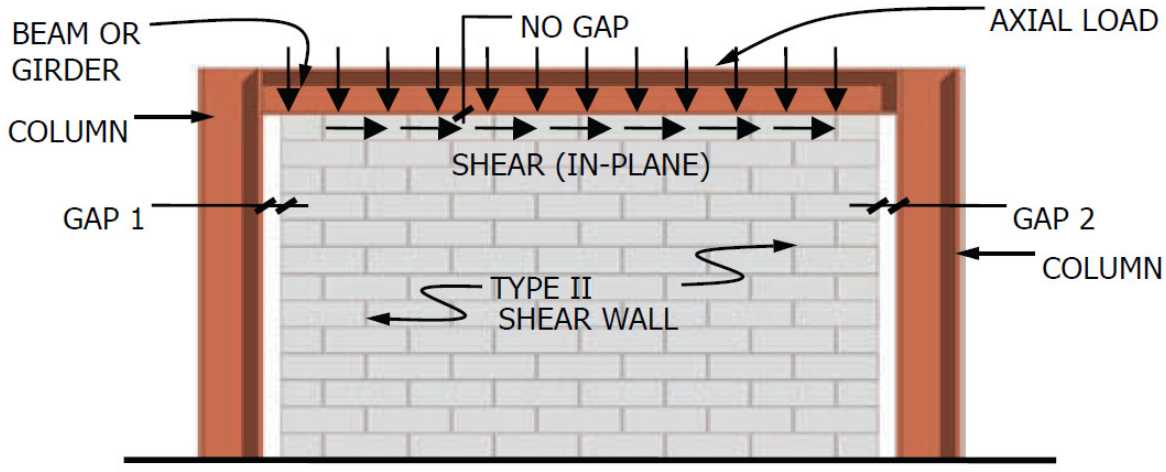

Figure 2.3 Type II Shear Wall (IMI, 2010)

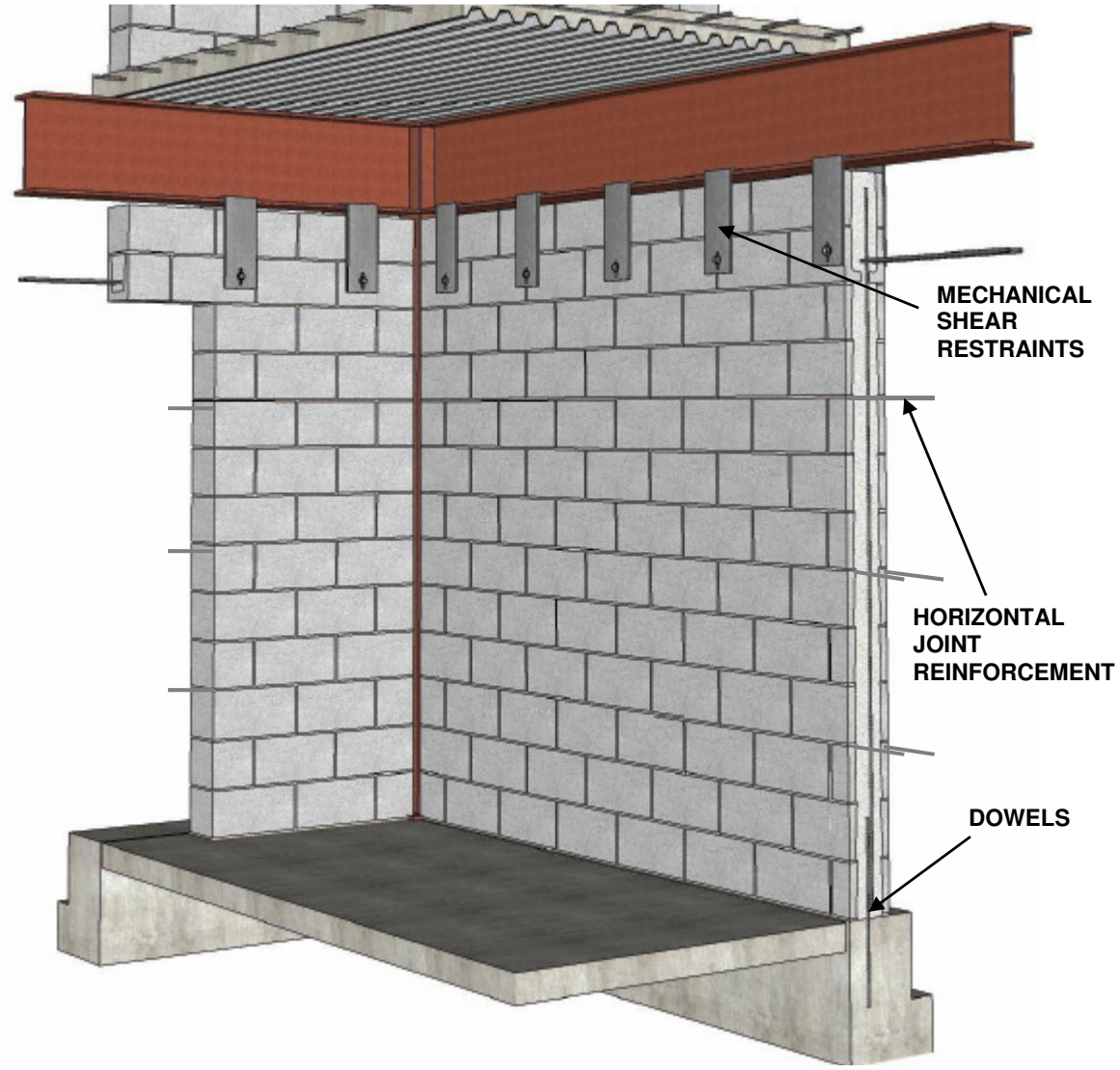

Figure 2.4: Foundation and Floor Detailing (IMI, 2010)

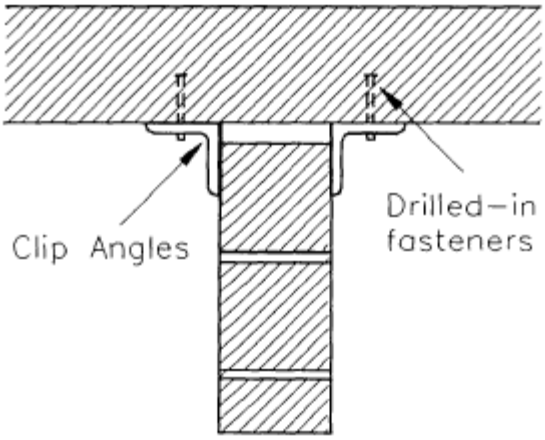

Figure 2.5: Lateral Support Anchors at the Top of Wall (Glanville et al., 1996)

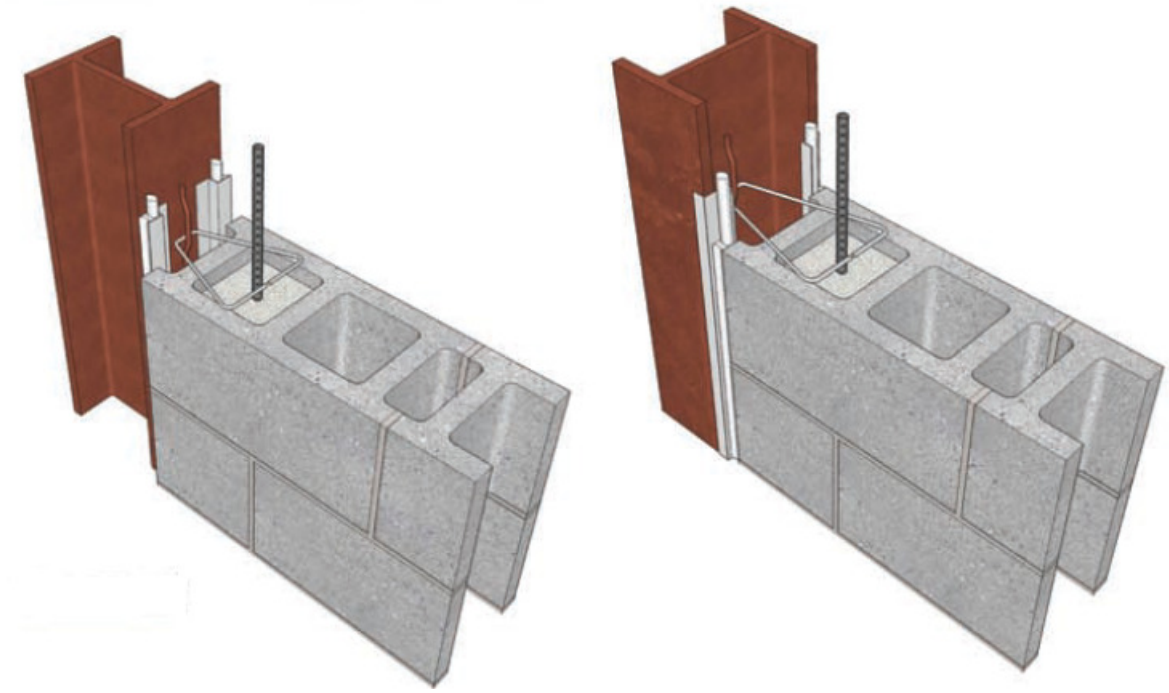

a) **b)**

Figure 2.6: Wall to Column Connection Details; a) Wall to Steel Column Flange Connection; b) Wall to Steel Column Web Connection (IMI, 2010)

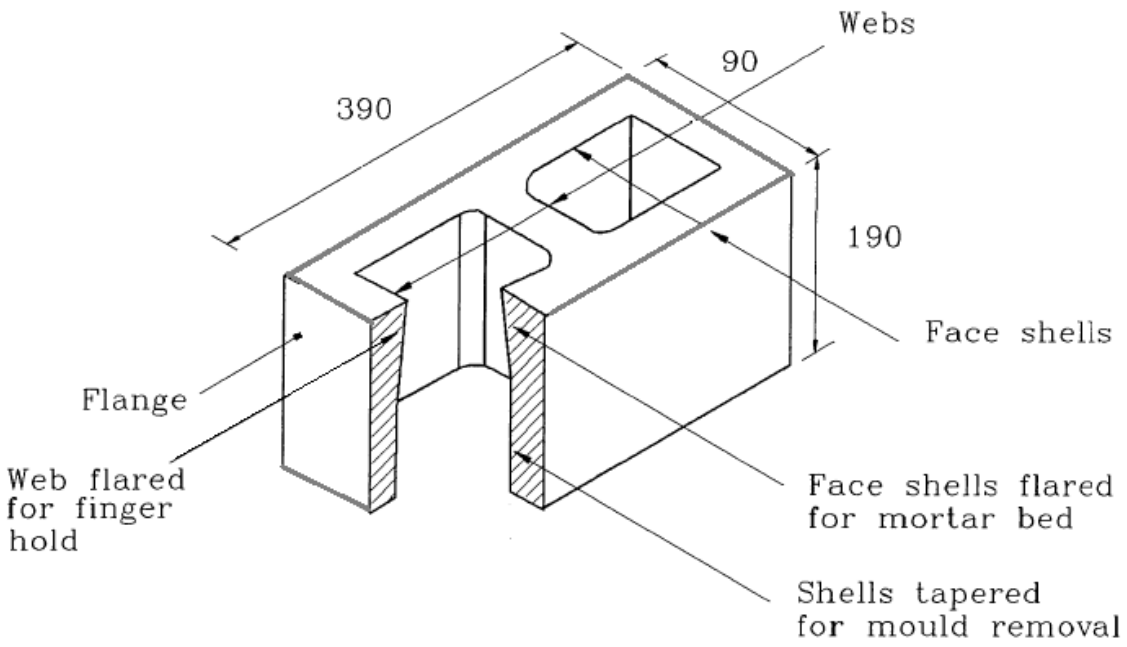

Figure 2.7: Standard 100 × 200 × 400 Concrete Masonry Unit Block (Glanville et al., 1996)

a) **b)**

Figure 2.8: Construction of URM Walls; a) Placing CMU Blocks on HSS Sections; b) During Construction Process

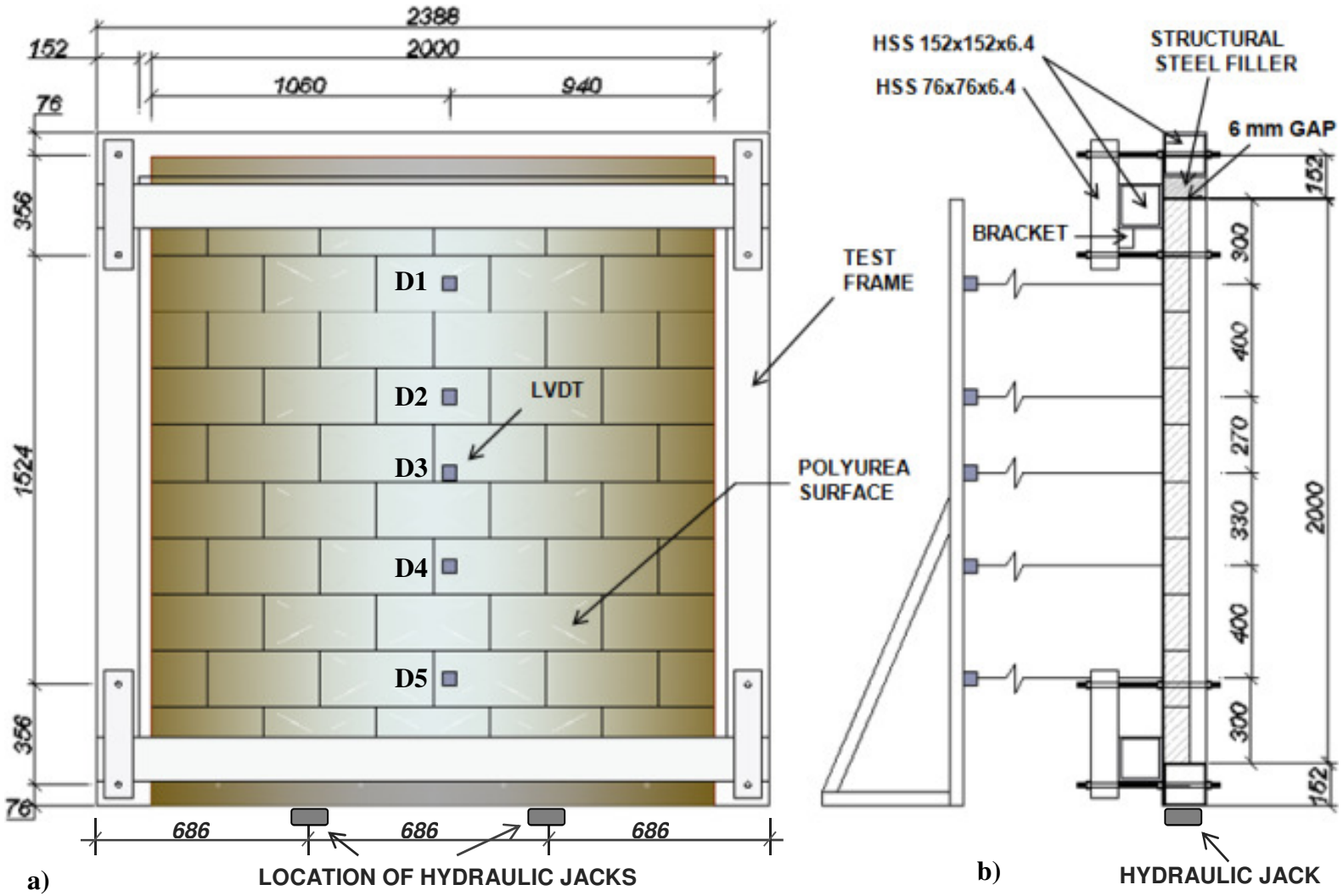

Figure 2.9: Detail of Test Specimen and Instrumentation (Dimensions in mm); a) Front View of URM Wall Placed in the Steel Test Frame; b) Elevation View of URM Wall

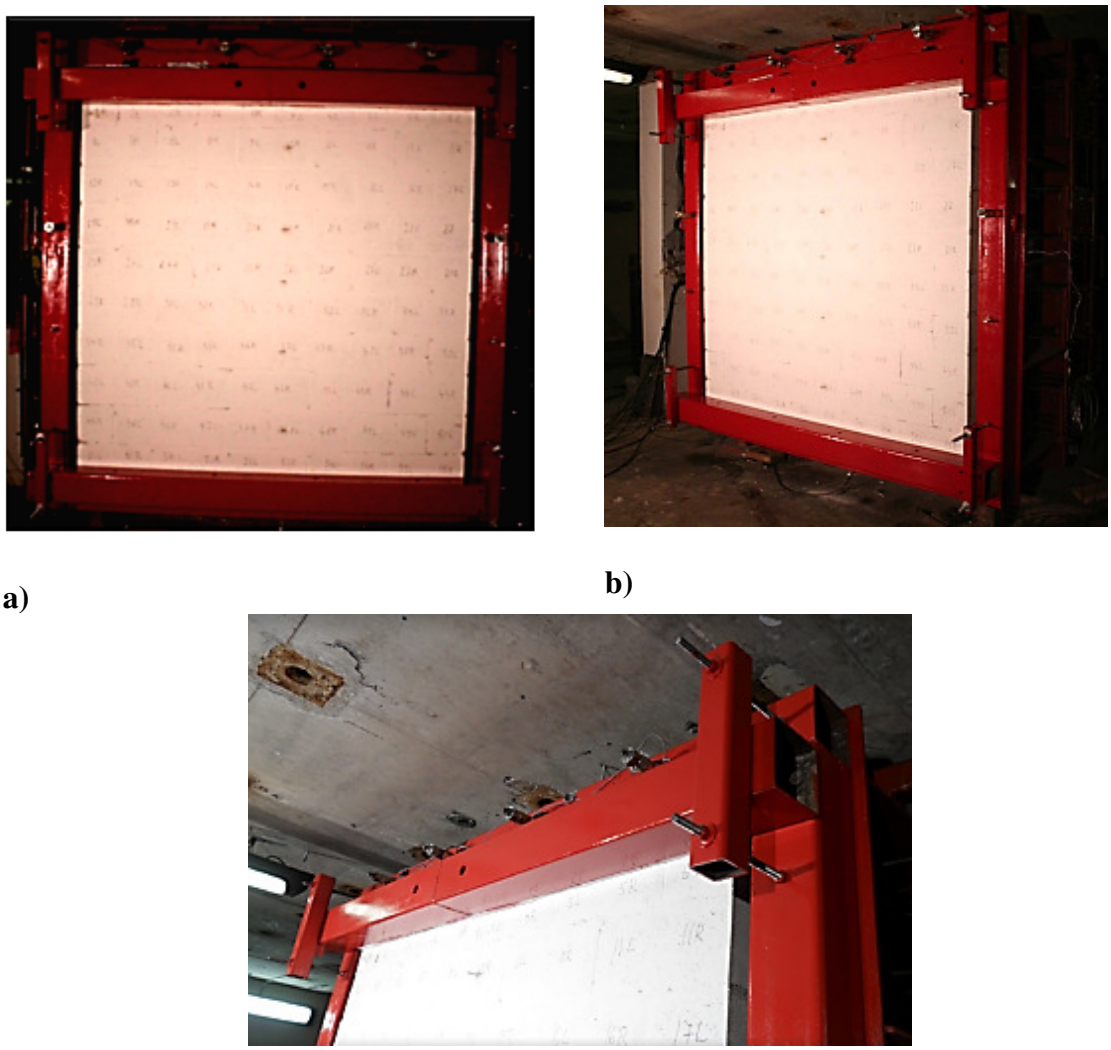

Figure 2.10 a) Front View of URM-1 Infill Wall Specimen; b) Specimen Attached to the Shock Tube; c) Specimen Top Support Showing the Mechanical Shear Restraints

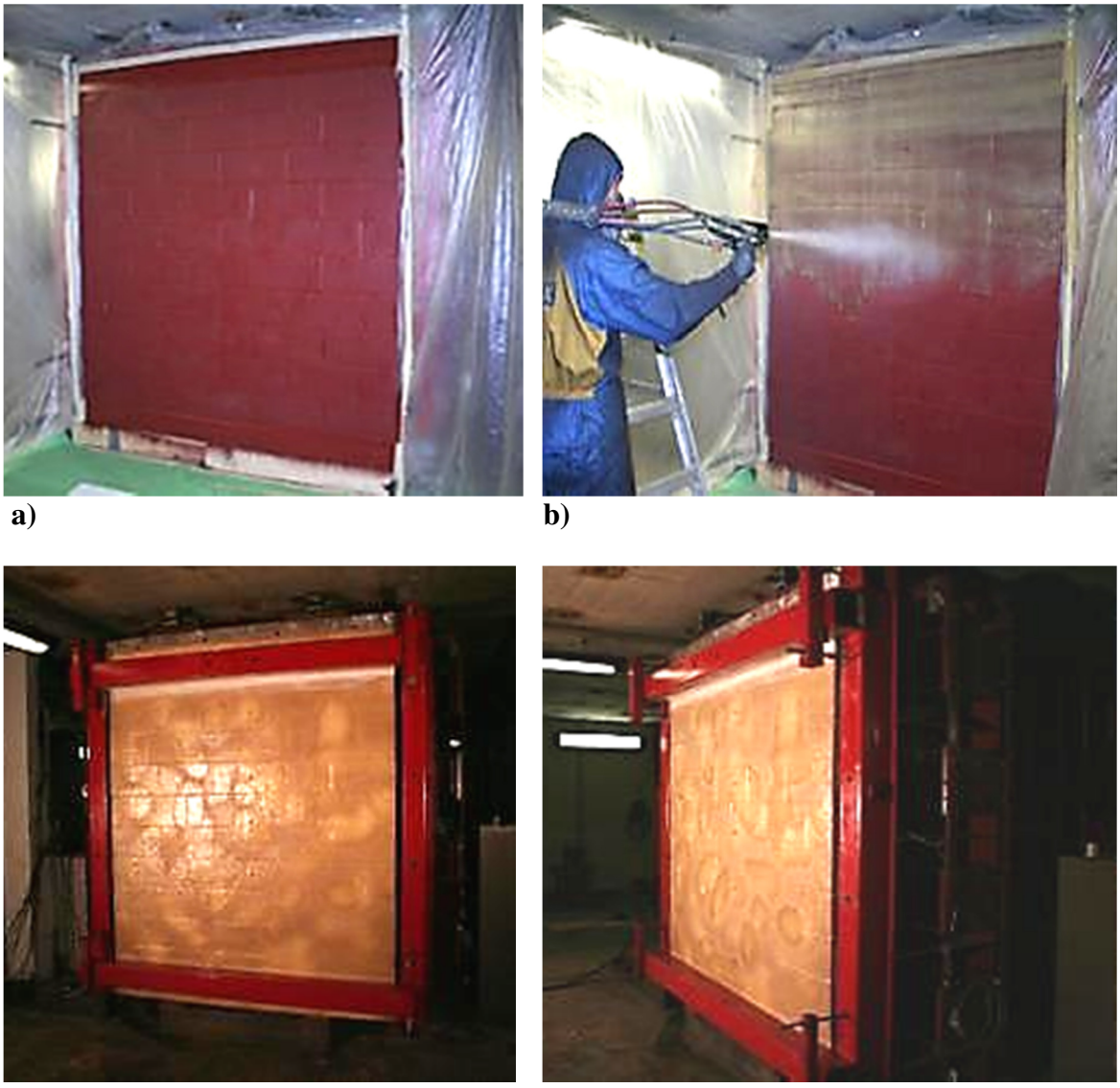

Figure 2.11: Polyurea Retrofitted Infill Wall Specimen (URM-2): a) Specimen after Application of Primer; b) Application of Spray-on Polyurea Retrofit; c) View of Specimen Prior to Testing; d) Side View of Specimen Prior to Testing

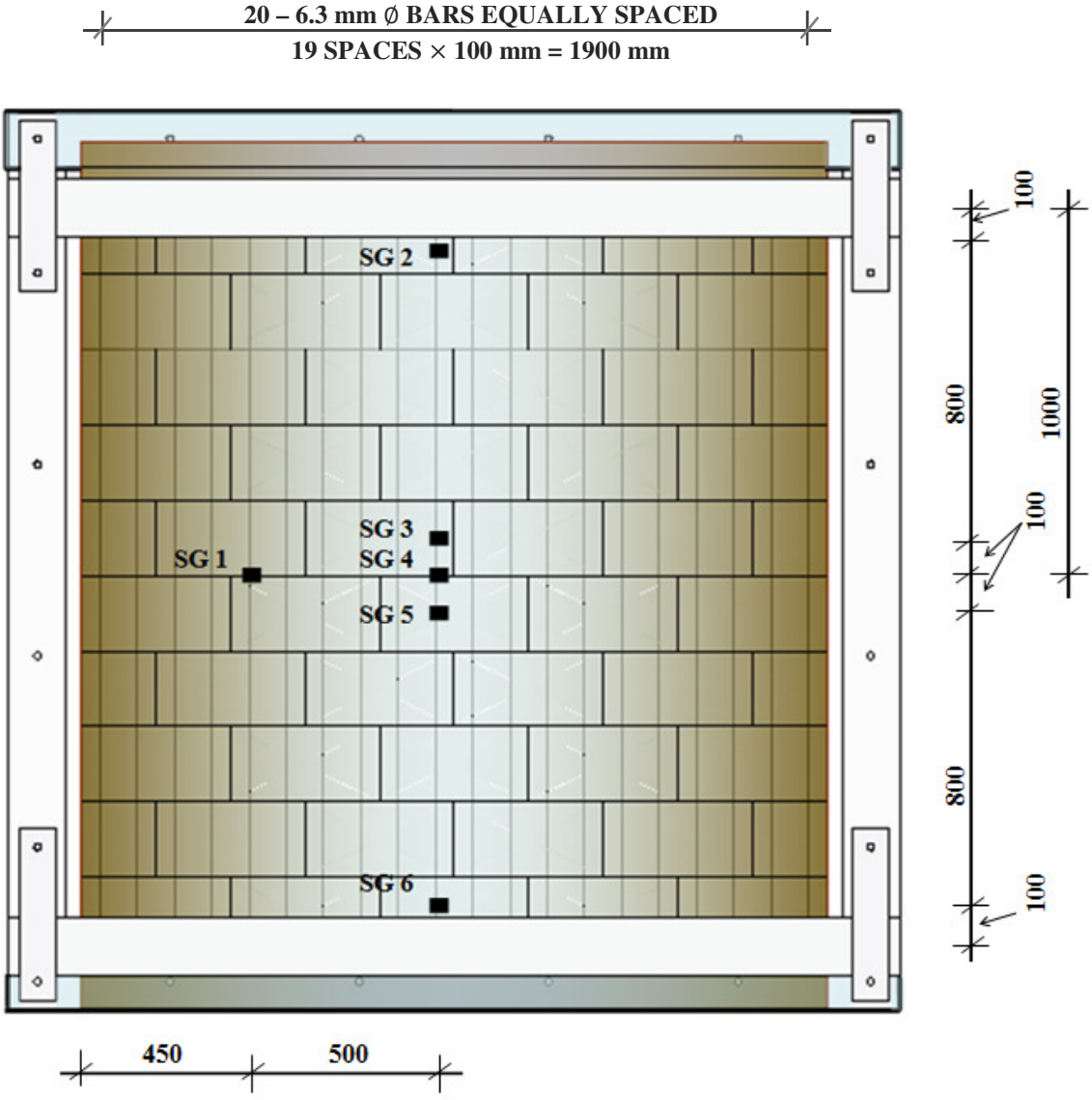

Figure 2.12: Retrofitted Load-Bearing Wall Specimen (URM-4) - Strain Gauge Location (Dimensions in mm)

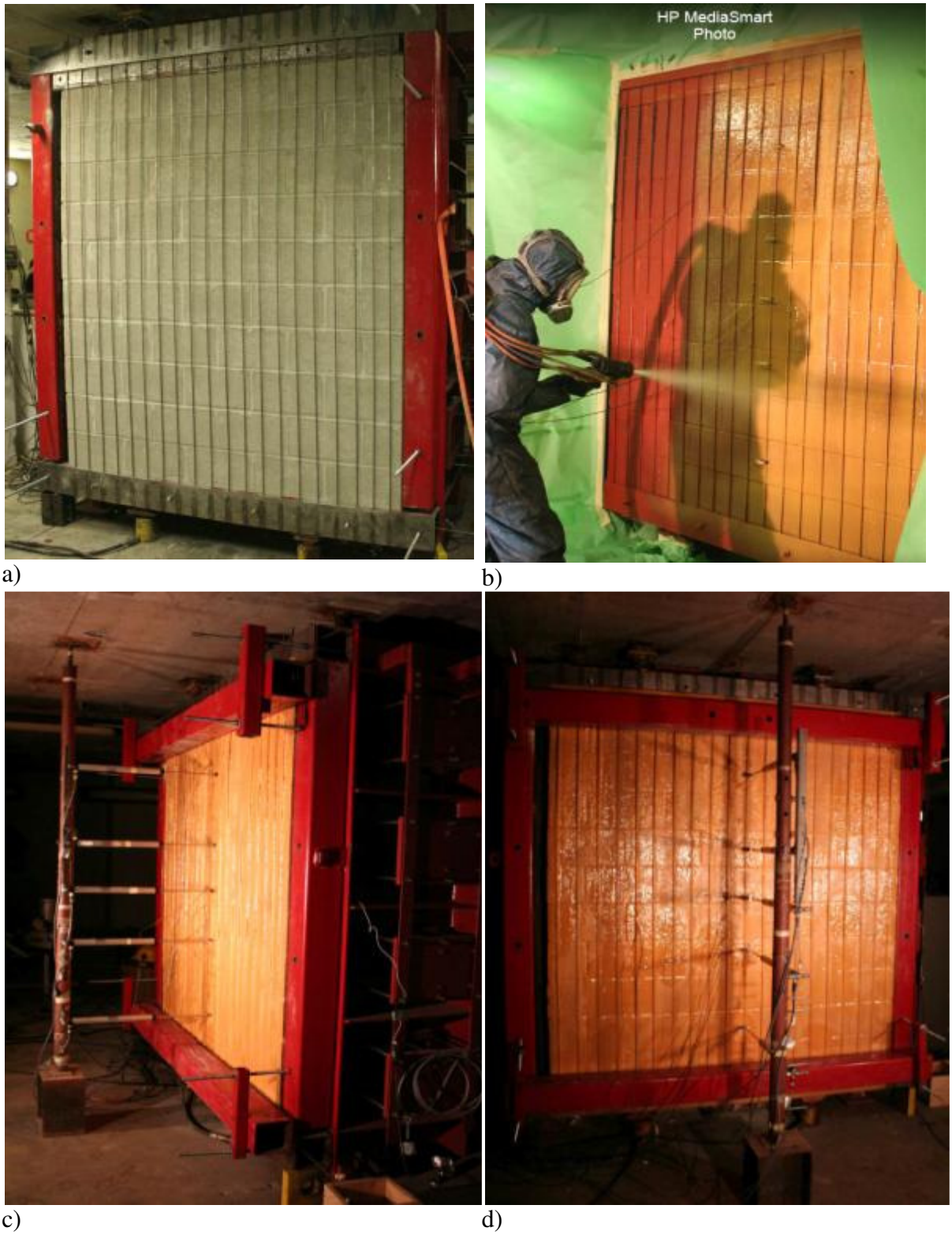

Figure 2.13: Retrofitted Load-bearing Wall Specimen: a) Installation of Non Deformed Steel Wires; b) Application of Polyurea Coating; c) Side View of Specimen Prior to Testing; d) Front View of Specimen Prior to Testing

a) **b)** **c)**

d)

Figure 2.14: Typical Failure Mode of Masonry Prisms in Compression (Different Views)

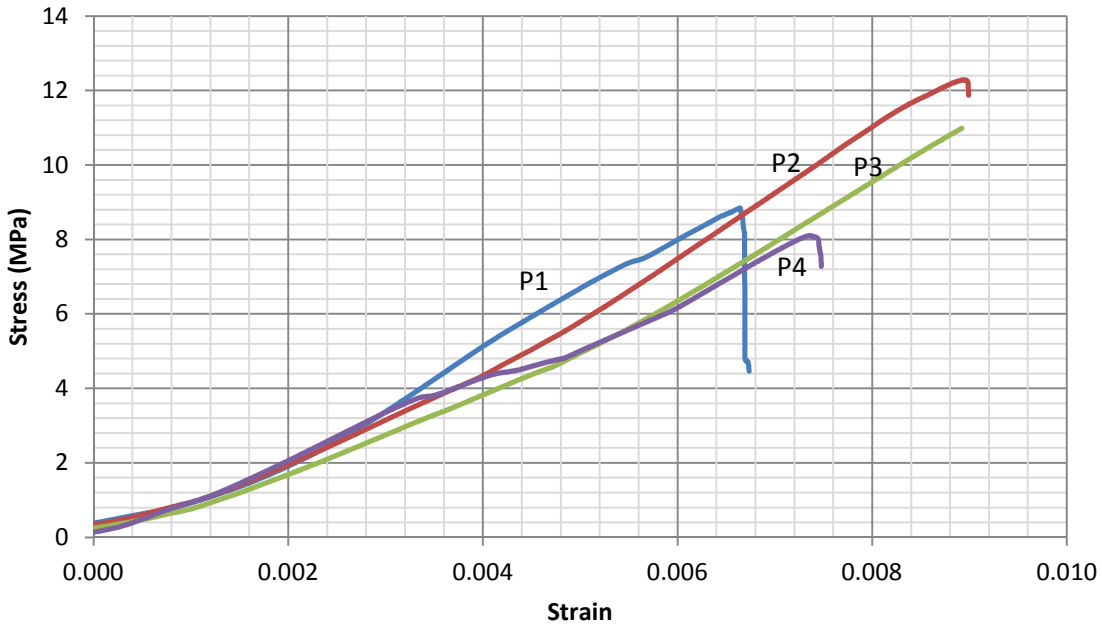

Figure 2.15: Stress-strain Data of Prism Tested in Compression (Test not Strain Controlled)

a) **b)** **c)**

Figure 2.16: Typical Failure Modes for Mortar Cubes Tested in Compression

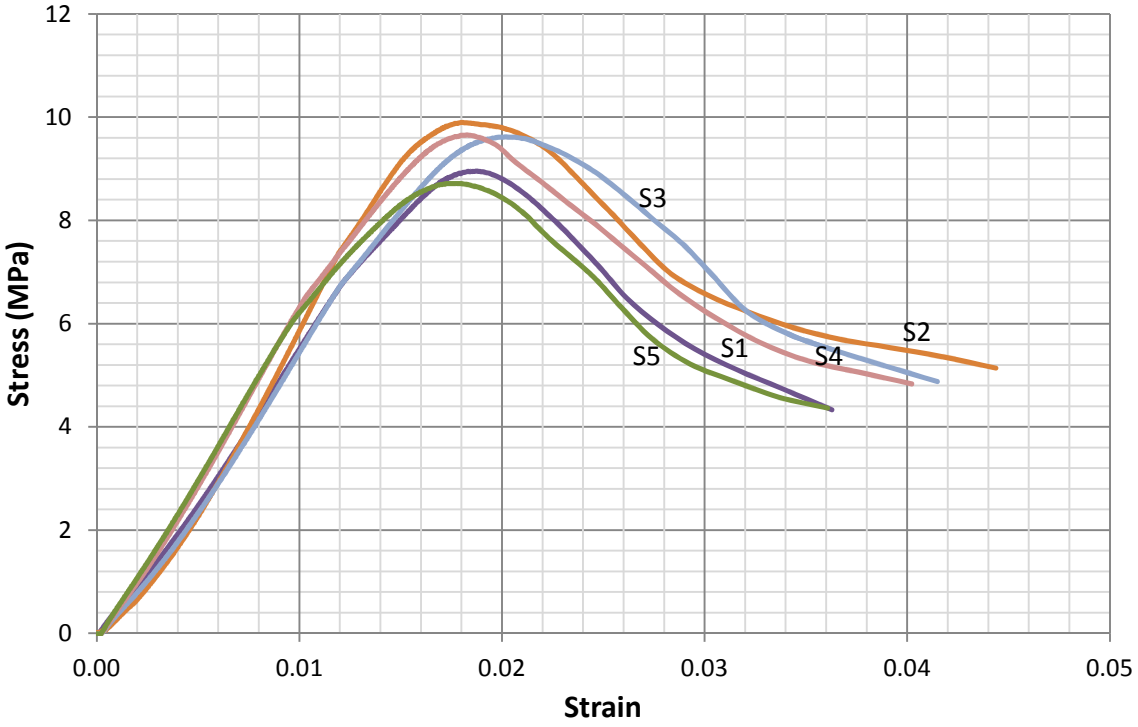

Figure 2.17: Stress-strain Data for 50 mm Mortar Cubes Tested in Compression

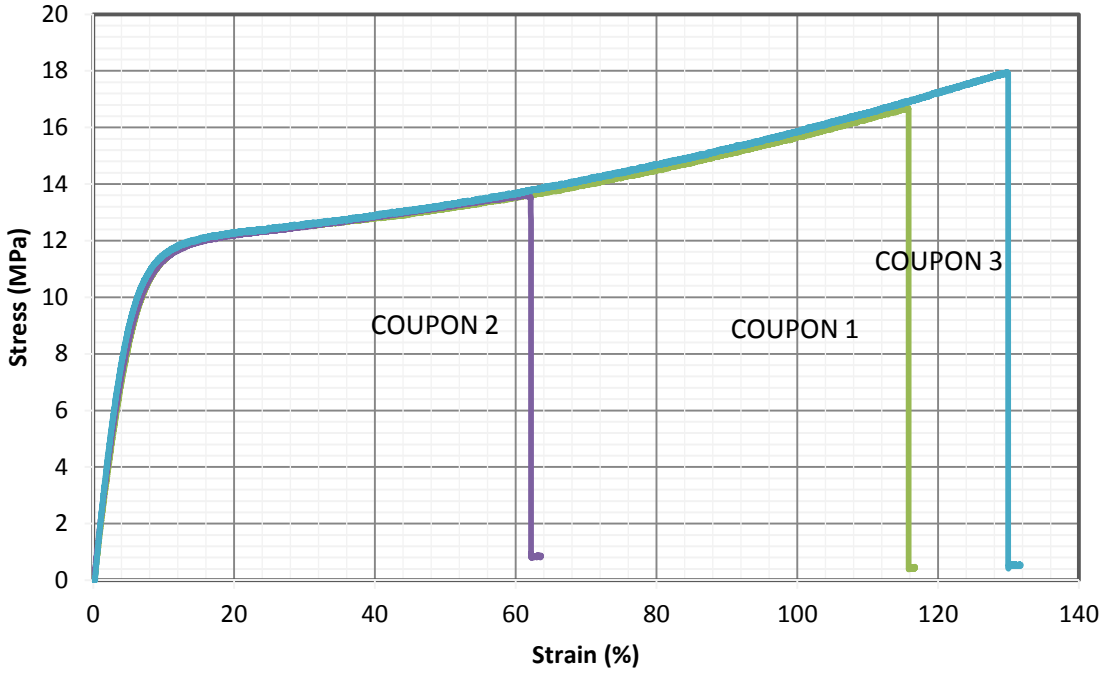

Figure 2.18: Stress-strain Data for Polyurea Tension Coupons Tests

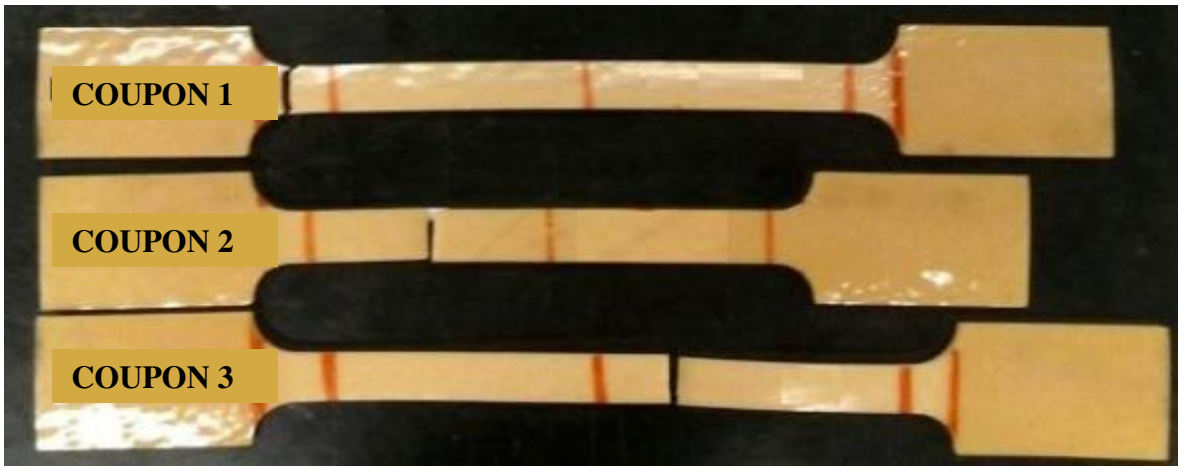

Figure 2.19: Polyurea Coupons after Rupture

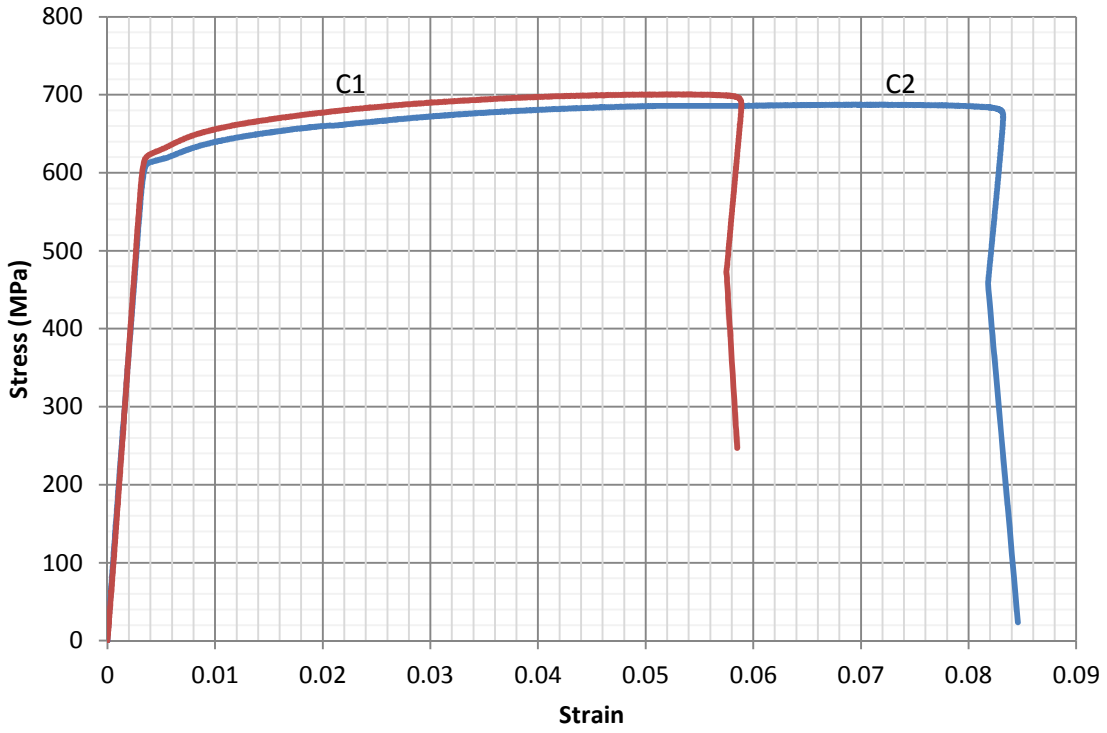

Figure 2.20: Stress-strain Data for 6.3 mm Non Deformed Steel Wires Tension Tests

CHAPTER 3

Experimental Results

3.1 General

This chapter presents results obtained from experimental work performed on four Unreinforced Masonry (URM) walls. Each wall was subjected to a series of pressure and impulse combinations in order to observe the wall response to shock wave loading. Shock waves were increased in magnitude until the global failure of the specimen was achieved. The magnitude of the shock wave reflected pressure was controlled by selecting the desired shock tube driver pressure and the duration of the positive phase was controlled by selecting the shock tube driver section length. The end of this chapter provides photos of specimens at different stages of testing, plots of pressure and impulse time histories as well as pressure and corresponding mid-height displacement time histories for each test. The tests are labelled using the "URM" abbreviation for "Unreinforced Masonry", followed by two numbers that represent the wall number and the test number, respectively. For example, test URM-3-4, designates the third wall and the fourth test. Axial load and pressure time histories are presented in Appendix A. Strain data is shown in Appendix B.

3.2 Boundary Conditions

The boundary conditions were intended to simulate pin-pin end conditions. Mechanical shear restraints were placed across the top and bottom of the wall in order to prevent out-of-plane sliding while allowing the wall to rotate freely at both ends.

3.3 Experimental Results

The testing regime as well the results of each test performed on the four URM walls are summarised in Table 3.1. The table includes information on the selected shock tube driver pressure (P_D), the shock tube driver length (L_D), the peak reflected pressure recorded near

the wall specimen (P_r), with the corresponding reflected impulse, (I_r), over the positive phase, the positive phase duration (t_d), the maximum mid-height displacement (d_{max}), the residual accumulated mid-height displacement (d_{res}), maximum support rotation (θ_{max}) and the time to reach maximum mid-height displacement (t_{max}). The shock tube driver pressures shown in Table 3.1 represent the measured pressures at the time the diaphragms ruptured and triggered the blast. The maximum support rotation (θ_{max}) was computed as the maximum mid-height displacement (d_{max}), divided by half the column height *(H/2)* and converted to degrees, considering maximum displacement occurred at mid-span. Maximum and residual displacements are summarised in Table 3.2. Figure 2.9 from Chapter 2 shows the location of gauges D1 through D5. The most accurate displacement gauge was the mid-height displacement gauge, D3. The other gauges are presented to give a qualitative measure of the displacement shape of each test.

The following sections describe each test procedure as well as post-test observations. Prior to each test, all gauge readings were set to record zero. To identify the location of damage on the tension side of the URM wall, the concrete block masonry courses were numbered from top to bottom, the wall units were numbered from left to right within the corresponding course, the mortar bed joints were numbered from top to bottom and the mortar head joints from left to right, within the corresponding course.

Figure 3.1 shows labelling pattern described above that can be applied to any of the four masonry wall specimens. Crack width played a major role in describing the specimens. URM-1 and URM-3 wall specimens were painted prior to testing in order to facilitate crack detection. The following qualitative terms were used to describe the crack width: "fine cracks" describes cracks that are barely visible, unable to detect without the white paint, smaller than 1.5 mm; "medium cracks" describes cracks that have a visible width that could be estimated between 1.5 mm to 3 mm; and "wide cracks" describes cracks with widths greater than 3 mm.

3.3.1 Masonry Wall URM-1

The masonry wall specimen URM-1 was designed and tested to represent an infill, unreinforced, non load-bearing wall. The general arrangement and details for this wall are

described in Chapter 2. To promote arching action, the retrofit technique for this wall involved reducing the top edge gap between the URM wall and the testing steel frame to 6 mm by using structural steel filler. No axial load was directly applied on the URM-1 wall specimen during any of the tests. The design promoted arching action, therefore it was expected the wall to start pushing on the steel testing frame. An attempt was made to record any strains resulting from arching. Strain gauges were installed on the steel testing frame; unfortunately, the gauges did not record any strains. A different approach was used for the other three walls (URM-2, URM-3 and URM-4). The testing frame surrounding the wall specimen was allowed to move up and down and displace vertically relative to the shock tube end frame. Load cells were installed on top of the steel testing frame to record axial loading, two jacks were used to apply initial axial loading in the case of a load-bearing wall and the top was shimmed against the strong ceiling slab.

A total of four shock waves were applied on the as-built wall URM specimen (URM-1-1, URM-1-2, URM-1-3 and URM-1-4) until it reached global collapse. The driver pressure of the shock tube was increased in approximately 40 kPa increments and the load duration was kept constant by using the same driver length of 1829 mm for all the tests. This created shock waves with peak reflected pressures and reflected impulses over relatively constant positive phase duration. Note that the driver pressure increase is only approximate and highly dependent on the resistance of the aluminum diaphragms. A slightly damaged diaphragm would lead to premature triggering of the shock tube, before the desired driver pressure is achieved. A summary of results for each test along with visual observations are provided below.

3.3.1.1 Test URM-1-1

For this test, a shock tube driver length of 1829 mm was selected and a shock tube driver pressure of 40 kPa was recorded at the time of diaphragm rupturing. This resulted in a peak reflected pressure of 6.1 kPa, a positive phase duration of 10 ms and a reflected impulse over the positive phase of 53.1 kPa-ms as shown in Figure 3.2 and listed in Table 3.1. The wall reached a maximum mid-height displacement of 9.1 mm with 0.52º of support rotation at 40 ms after the start of the shock wave loading. The recorded data showed a residual displacement of 6.2 mm. The reflected pressure and impulse time histories as well

as the reflected pressure and mid-height displacement time histories for the URM-1-1 test are shown in Figure 3.2 and Figure 3.3, respectively.

Figure 3.4 (a) shows URM-1 wall specimen after test URM-1-1 (Shot 1). The following visible damage was recorded: medium cracks between the 1st concrete masonry unit of the 1st course (top left unit) and the 1st mortar bed joint, medium cracks between the 1st concrete masonry unit of the 1st course (top left unit) and the 1st mortar head joint of the 1st course, medium cracks inside the 3rd mortar bed joint, fine cracks between the 3rd mortar bed joint and the 3rd concrete masonry unit of the 3rd course, fine cracks inside the 7th, 8th and 9th mortar bed joint, fine cracks between the 9th course and the 8th mortar bed joint.

3.3.1.2 Test URM-1-2

The shock tube driver pressure at time of diaphragms rupturing was 75.8 kPa. This resulted in a peak reflected pressure of 13.7 kPa, a positive phase duration of 11.4 ms and a reflected impulse over the positive phase of 150.9 kPa-ms as shown in Figure 3.5 and listed in Table 3.1. The wall reached a maximum mid-height displacement of 23.8 mm and a support rotation of 1.36º at 40 ms after the start of the shock wave loading. Since gauge readings are re-zeroed after each tests, the mid-height displacement gauge recorded 6 mm of residual displacement at this end of this test; however the accumulated mid-height residual displacement is 12 mm. The reflected pressure and impulse time histories as well as the reflected pressure and mid-height displacement time histories for the URM-1-2 test are shown in Figure 3.5 and Figure 3.6, respectively.

Figure 3.4 (b) shows URM-1 wall specimen after test URM-1-2 (Shot 2). The following damage was noted: medium cracks between the 1st concrete masonry unit of the 1st course (top left unit) and the 1st mortar bed joint, medium cracks between the 1st concrete masonry unit of the 1st course (top left unit) and the 1st mortar head joint of the 1st course, large cracks inside the 3rd mortar bed joint, fine cracks between the 3rd mortar bed joint and the 3rd concrete masonry unit of the 3rd course, fine cracks inside the 7th, 8th and 9th mortar bed joint, fine cracks between the 9th course and the 8th mortar bed joint, fine cracks inside the 4th head joint of the 8th course, fine cracks inside the 5th head joint of the 9th course.

3.3.1.3 Test URM-1-3

For the third test performed on the URM-1 wall specimen, the shock tube driver length was maintained at 1829 mm while the shock tube driver pressure was increased to 125.5 kPa. Figure 3.7 and Table 3.1 show a peak reflected pressure of 23.4 kPa, a positive phase duration of 13.5 ms and a reflected impulse over the positive phase of 179.3 kPa-ms recorded for the shot. The wall reached a maximum mid-height displacement of 56.5 mm and 3.24º support rotation at 92 ms after the start of the shock wave loading. The mid-height residual displacement recorded after this test was 1.9 mm with an accumulated mid-height residual displacement of 13.9 mm. The reflected pressure and impulse time histories as well as the reflected pressure and mid-height displacement time histories for the URM-1-3 test are shown in Figure 3.7 and Figure 3.8, respectively.

From video observations it was concluded that this test almost failed the specimen. In addition, the pressure and displacement time histories in Figure 3.8 show the displacement curve leveling out and suddenly increasing from about 45 mm to the maximum of 56.5 mm after 70 ms into the test. After approximately 1100 ms, the displacement curve returns to a residual displacement of 1.9 mm without failure of the wall. Figure 3.4 (c) shows the crack pattern observed after test URM-1-3 (Shot 3).

The following damage was documented for test URM-1-3: large cracks between the 1st concrete masonry unit of the 1st course (top left unit) and the 1st mortar bed joint, large cracks between the 1st concrete masonry unit of the 1st course (top left unit) and the 1st mortar head joint of the 1st course, large cracks inside the 3rd, 4th mortar bed joint, medium cracks inside the 5th mortar bed joint, fine cracks between the 3rd mortar bed joint and the 3rd concrete masonry unit of the 3rd course, fine cracks between the 4rd mortar bed joint and the 2rd concrete masonry unit of the 4rd course, fine cracks between the 5rd mortar bed joint and the 3rd and 4th units of the 5rd course, fine cracks inside the 7th, 8th and 9th mortar bed joint, fine cracks between 7th course and 7th mortar bed joint, fine cracks between 8th course and 7th mortar bed joint, fine cracks between the 9th course and the 8th mortar bed joint, fine cracks inside the 6th head joint of the 7th course, medium cracks inside the 4th head joint of the 8th course, fine cracks inside the 1st, 2nd, 3rd head joint of the 8th course, fine cracks

inside the 1st, 2nd, 3rd, 4th, 5th head joint of the 9th course, fine cracks in the first head joint of the 10th course.

3.3.1.4 Test URM-1-4

For the fourth test, the shock tube driver pressure was increased to 165.5 kPa, providing a recorded peak reflected pressure of 30.7 kPa, a positive phase duration of 13.9 ms and a reflected impulse over the positive phase of 265.1 kPa-ms, shown in Figure 3.9 and listed in Table 3.1. The reflected pressure and impulse time histories as well as the reflected pressure and mid-height displacement time histories for the URM-1-4 test are shown in Figure 3.9 and Figure 3.10, respectively.

This pressure impulse combination was intended to cause global failure of the specimen. Figure 3.4 (d) shows the rubble remains of the specimen after the fourth shot URM-1-4. The collapse progression of the wall, recorded with high speed video, shows the formation of a hinge in the middle, with the opening of the middle mortar joint, sequentially followed by the opening of other joints.

The displacement measurements indicate that the arching action was activated at loads prior to failure. This mechanism changed the failure mode of the wall specimen from a tilt-over collapse to a hinged-arched type collapse. A cantilevered URM infill wall, relying only on its self-weight, would simply fall over if there were no supports provided to resist its out-of-plane translation. By providing mechanical shear restraints and reducing the gap at the top of the URM wall, the arching action was activated, thus making the formation of the hinge in the middle of the wall possible.

Although there was some capacity added to the wall system by means of arching, the failure mode was still brittle in nature, with wall fragmentation and flying debris.

3.3.2 Masonry Wall URM-2

The masonry wall specimen URM-2 was designed and tested as a retrofitted, infill, unreinforced, non load-bearing wall. The specifications for this wall are presented in detail in Chapter 2. The top edge gap between the URM wall and the testing steel frame was reduced to 6 mm in a similar manner to the previous wall (URM-1) by using structural

steel filler. In order to facilitate the recording of axial loads resulting from arching action, the testing frame surrounding the wall specimen was allowed to displace vertically relatively to the shock tube end frame and load cells were installed on top of the steel testing frame, shimmed against the strong floor. A 3 mm layer of polyurea was applied by Line-X of Ottawa certified staff.

The polyurea retrofitted URM wall specimen was tested ten times until it reached global failure. The driver pressure of the shock tube was increased in about 40 kPa increments, from 40 to 320 kPa for shots 1 through 8, and increased by 80 kPa for the last two shots. The load duration was kept constant by using the same driver length of 1829 mm for each test.

A summary of results for each test along with visual observations are provided in the following sections.

3.3.2.1 Test URM-2-1

With the shock tube driver length at 1829 mm, a shock tube driver pressure of 41.4 kPa was used for the first test shot. This resulted in a recorded peak reflected pressure of 8.7 kPa, a positive phase duration of 14.6 ms and a reflected impulse over the positive phase of 68.2 kPa-ms as shown in Figure 3.11 and listed in Table 3.1. The wall reached a maximum mid-height displacement of 2.2 mm and 0.13º support rotation at 33 ms after the start of the shock wave loading. The reflected pressure and impulse time histories and the reflected pressure and mid-height displacement time histories for the URM-2-1 test are shown in Figure 3.11 and Figure 3.12, respectively.

After test investigation revealed no visible signs of damage in either the masonry wall or in the polyurea membrane. The recorded data showed a residual displacement of 2 mm, which indicates there was almost no rebound from the maximum displacement. This test was intended to simply verify if all gauges are working as expected. The recorded residual deflection is likely due to settling of the wall specimen.

3.3.2.2 Test URM-2-2

The shock tube driver pressure for the second shot of 82.7 kPa, resulted in a peak reflected pressure of 14.6 kPa, a positive phase duration of 12.5 ms and a reflected impulse over the

positive phase of 128.7 kPa-ms (Figure 3.13 and Table 3.1). The wall reached a maximum mid-height displacement of 6.4 mm and corresponding 0.37º support rotation at 37 ms after the start of the shock wave loading with a rebound of only 0.6 mm. The reflected pressure and impulse time histories as well as the reflected pressure and mid-height displacement time histories for the URM-2-2 test are shown in Figure 3.13 and Figure 3.14, respectively.

No visible signs of damage were observed. The recorded data showed an accumulated mid-height residual displacement of 7.8 mm, 2 mm from the first shot and 5.8 mm from this second shot.

3.3.2.3 Test URM-2-3

The selected shock tube driver length and the shock tube driver pressure at diaphragm rupturing were 1828.8 mm and 118.6 kPa, respectively. This resulted in a peak reflected pressure of 23 kPa, a positive phase duration of 12.8 ms and a reflected impulse over the positive phase of 188.5 kPa-ms as shown in Figure 3.15 and listed in Table 3.1. The wall reached a maximum mid-height displacement of 10.3 mm with a corresponding rotation of 0.59º at 40 ms after the start of the shock wave loading. The recorded data showed an accumulated mid-height residual displacement of 11.1 mm, 7.8 mm from the previous tests and an additional 3.3 mm from this shot. The reflected pressure and impulse time histories as well as the reflected pressure and mid-height displacement time histories for the URM-2-3 test are shown in Figure 3.15 and Figure 3.16, respectively.

No visible signs of damage were observed. Since the polyurea is sprayed on top of the wall, potential cracks on the tension side of the wall would not be visible.

3.3.2.4 Test URM-2-4

The shock tube driver pressure for the fourth shot performed on the URM-2 wall specimen of 173.7 kPa resulted in a peak reflected pressure of 32 kPa, a positive phase duration of 13.1 ms and a reflected impulse over the positive phase of 294.5 kPa-ms (Figure 3.17 and Table 3.1). The wall reached a maximum mid-height displacement of 23 mm (1.32º support rotation) at 41 ms after the start of the shock wave loading. The recorded data showed an accumulated mid-height residual displacement of 12.1mm, with 11.1 mm from previous tests and 1 mm from this shot alone. The reflected pressure and impulse time

histories as well as the reflected pressure and mid-height displacement time histories for the URM-2-4 test are shown in Figure 3.17 and Figure 3.18, respectively.

No visible signs of damage were recorded.

3.3.2.5 Test URM-2-5

A shock tube driver pressure at the point of diaphragm rupture of 207.5 kPa, resulted in a peak reflected pressure of 37.5 kPa, a positive phase duration of 14.1 ms and a reflected impulse over the positive phase of 338.5 kPa-ms as shown in Figure 3.19 and Table 3.1. The wall achieved a maximum mid-height displacement of 36.9 mm with a corresponding support rotation of 2.11º at 44 ms after the start of the shock wave loading. The recorded data showed a residual mid-height displacement of 3.43 mm with an accumulated mid-height residual displacement of 15.5 mm. The reflected pressure and impulse time histories as well as the reflected pressure and mid-height displacement time histories for the URM-2-5 test are shown in Figure 3.19 and Figure 3.20, respectively.

No visible signs of damage got recorded. Figure 3.20 shows a 9 mm rebound in the mid-height displacement time history; therefore it is likely that cracking on the blast face of the wall occurred. Monitoring crack development on the blast face of the wall is a difficult task due to poor visibility.

3.3.2.6 Test URM-2-6

For this test, the shock tube driver length was kept constant at 1829 mm and the shock tube driver pressure was increased to 249.6 kPa. This resulted in a peak reflected pressure of 42.1 kPa, a positive phase duration of 14.5 ms and a reflected impulse over the positive phase of 406.3 kPa-ms as shown in Figure 3.21 and listed in Table 3.1. The wall reached a maximum mid-height displacement of 50 mm and 2.86º support rotation at 47 ms after the start of the shock wave loading. The recorded data showed a residual mid-height displacement of 0.76 mm and an accumulated mid-height residual displacement of 16.3 mm. The reflected pressure and impulse time histories as well as the reflected pressure and mid-height displacement time histories for the URM-2-6 test are shown in Figure 3.21 and Figure 3.22, respectively.

No visible signs of damage were observed.

3.3.2.7 Test URM-2-7

A constant shock tube driver length of 1828.8 mm and a shock tube driver pressure of 291 kPa, resulted in a peak reflected pressure of 46.1 kPa, a positive phase duration of 14.5 ms and a reflected impulse over the positive phase of 433.8 kPa-ms as shown in Figure 3.23 and listed in Table 3.1. The wall reached a maximum mid-height displacement of 69.2 mm (3.96º support rotation) at 48 ms after the start of the shock wave loading. The recorded data showed a residual displacement of 1.05 and an accumulated mid-height residual displacement of 17.3 mm. The reflected pressure and impulse time histories as well as the reflected pressure and mid-height displacement time histories for the URM-2-7 test are shown in Figure 3.23 and Figure 3.24, respectively.

No visible signs of damage were noted.

3.3.2.8 Test URM-2-8

For the eight test, a the shock tube driver pressure of 324.1 kPa, lead to a peak reflected pressure of 53.9 kPa over a positive phase duration of 14.7 ms and a reflected impulse over the positive phase of 483.3 kPa-ms as shown in Figure 3.25 and Table 3.1. The wall reached a maximum mid-height displacement of 88.4 mm with a corresponding support rotation of 5.07º at 51 ms after the start of the shock wave loading. The recorded data showed an accumulated mid-height residual displacement of 22.7 mm, 17.3 mm being from the previous tests and 5.41 mm from this shot. The reflected pressure and impulse time histories as well as the reflected pressure and mid-height displacement time histories for the URM-2-8 test are shown in Figure 3.25 and Figure 3.26, respectively.

Debonding of polyurea membrane from the URM wall was observed at mid-height of wall, just above and below the middle bed joint (Figure 3.27).

3.3.2.9 Test URM-2-9

For this tests, a shock tube driver length of 1829 mm and a shock tube driver pressure of 448.8 kPa, resulted in a peak reflected pressure of 84.4 kPa, a positive phase duration of 16.5 ms and a reflected impulse over the positive phase of 597.2 kPa-ms as shown in

Figure 3.28 and listed in Table 3.1. The wall reached a maximum mid-height displacement of 158.9 mm with a corresponding rotation of 9.1º at 63 ms after the start of the shock wave loading. The recorded data showed an accumulated mid-height residual displacement of 30.4 mm, 22.7 mm being from previous tests. The reflected pressure and impulse time histories as well as the reflected pressure and mid-height displacement time histories for the URM-2-9 test are shown in Figure 3.28 and Figure 3.29, respectively.

Local failure of the specimen, involving a small tear in the polyurea membrane initiated from the left side of the wall, at the fourth mortar bed joint (Figure 3.30). Extensive debonding of membrane from the URM wall was also observed in the middle of the wall, spanning approximately 300 mm above and below the middle mortar bed joint. On the blast face of the wall, crushing of the 5th mortar joint was observed.

3.3.2.10 Test URM-2-10

This shot with a driver pressure of 551 kPa, caused the global failure of the specimen, involving an extensive tear in the polyurea membrane, tear initiated in the previous test, URM-2-9, from the left side of the wall, at the fourth mortar bed joint (Figure 3.31). Extensive debonding of membrane from the URM wall was also observed at mid-height of wall, spanning approximately 300 mm above and below the middle mortar bed joint. The extensive tear in polyurea membrane created an opening that allowed for some debris to escape into the assumed occupant area. Although the driver pressure was increased from 449 kPa to 551 kPa, while maintaining the same shock tube driver length of 1828.8 mm, the reflected pressure was less than the previous shot, since the polyurea membrane ripped and allowed the air to escape. A peak reflected pressure of 78.1 kPa, a positive phase duration of 17.3 ms and a reflected impulse over the positive phase of 723.4 kPa-ms were recorded and are shown in Figure 3.32 and listed in Table 3.1. The reflected pressure and impulse time histories as well as the reflected pressure and mid-height displacement time histories for the URM-2-10 test are shown in Figure 3.32 and Figure 3.33, respectively.

The polyurea membrane was extremely effective at containing the debris during the first 9 tests and for the last test the number of projectiles was reduced significantly when compared to wall URM-1. The wall did not experience a dangerous collapse. Unlike the

URM-1 wall specimen, test URM-1-4, when the whole wall collapsed in a brittle manner (Figure 3.4 (d)), the gauges show the wall deflecting 253.5 mm (14.52º support rotation) at 72 ms after the start of the shock wave loading and the remains of the wall returning to a 29.1 mm residual displacement (accumulated mid-height residual of 59.5 mm).

Visual observations indicate that the thickness of the polymer was less at the point of tear initiation than along the other edges of the wall. This indicates that care should be taken in the application process of the polyurea to assure a uniform application in order to reduce stress concentrations in the material.

3.3.3 Masonry Wall URM-3

The masonry wall specimen URM-3 was designed and tested as an unreinforced, load-bearing wall. The construction details for this wall are presented in Chapter 2. In order to facilitate the recording of axial loads, the testing frame around the wall specimen was allowed to move up and down and displace vertically and load cells were installed on top of the steel testing frame, shimmed against the strong floor. The wall had full contact with the top and bottom of the surrounding steel frame and axial load was applied by two hydraulic jacks placed 508 mm left and right of the vertical center line of the wall. The total axial load applied was approximately 123 kN (10% of the total load carrying capacity of the wall).

A total of seven shock waves were applied on the URM-3 wall specimen until it reached global failure. The driver section of the shock tube was increased by approximately 40 kPa increments and the load duration was kept constant by using the same driver length of 1829 mm.

A summary of results for each test along with visual observations are provided below.

3.3.3.1 Test URM-3-1

A shock tube driver length of 1829 mm and a shock tube driver pressure of 34.5 kPa, resulted in a peak reflected pressure of 6.1 kPa, a positive phase duration of 9.4 ms and a reflected impulse over the positive phase of 49 kPa-ms as shown in Figure 3.34 and listed in Table 3.1. The wall reached a maximum mid-height displacement of 1.1 mm with a

0.06º support rotation at 25 ms after the start of the shock wave loading. The reflected pressure and impulse time histories as well as the reflected pressure and mid-height displacement time histories for the URM-3-1 test are shown in Figure 3.34 and Figure 3.35, respectively.

After test investigation reveals no visible signs of damage. The recorded data showed a mid-height residual displacement of 0.4 mm. This test was intended to merely verify if all gauges are working as expected.

3.3.3.2 Test URM-3-2

For the second shot performed on the URM-3 wall specimen, a shock tube driver length of 1829 mm and a shock tube driver pressure of 79.3 kPa resulted in a peak reflected pressure of 13.2 kPa, a positive phase duration of 12.7 ms and a reflected impulse over the positive phase of 121.9 kPa-ms as shown in Figure 3.36 and listed in Table 3.1. The wall reached a maximum mid-height displacement of 8.2 mm and a support rotation of 0.47º at 32 ms duration after the start of the shock wave loading. The recorded data showed an accumulated mid-height residual displacement of 1.6 mm, with 0.4 mm from tests URM-3-1. The reflected pressure and impulse time histories as well as the reflected pressure and mid-height displacement time histories for the URM-3-2 test are shown in Figure 3.36 and Figure 3.37, respectively.

After test visual investigations revealed minor visible signs of damage. A fine crack formed on the tension face of the wall, at the middle mortar bed joint extending approximately 130 mm in length starting from left side of the wall.

3.3.3.3 Test URM-3-3

For the third shot, a shock tube driver pressure of 121.4 kPa resulted in a peak reflected pressure of 24.7 kPa, a positive phase duration of 13.5 ms and a reflected impulse over the positive phase of 193.3 kPa-ms as shown in Figure 3.38 and listed in Table 3.1. The wall reached a maximum mid-height displacement of 16.6 mm and a corresponding support rotation of 0.95º at 35 ms after the start of the shock wave loading. The recorded data showed an accumulated mid-height residual displacement of 3.2 mm, 1.6 mm from previous tests. The reflected pressure and impulse time histories as well as the reflected

pressure and mid-height displacement time histories for the URM-3-3 test are shown in Figure 3.38 and Figure 3.39, respectively.

The following visible damage was documented: fine cracks along the 4th mortar bed joint that initiated above the 2nd, 3rd, 4th and 5th mortar head joints of the 5th course, and a medium crack along the 5th mortar bed joint that initiated above all the mortar head joints of the 6th course.

3.3.3.4 Test URM-3-4

For this test, a shock tube driver length of 1829 mm and a shock tube driver pressure of 166.9 kPa, resulted in a peak reflected pressure of 28 kPa, a positive phase duration of 13.6 ms and a reflected impulse over the positive phase of 271.9 kPa-ms as shown in Figure 3.40 and listed in Table 3.1. The wall reached a maximum mid-height displacement of 28.6 mm (1.64° support rotation) at 37 ms after the start of the shock wave loading. The recorded data showed an accumulated mid-height residual displacement of 5.3 mm, 3.2 mm from previous tests and 2.1 mm from this test. The reflected pressure and impulse time histories as well as the reflected pressure and mid-height displacement time histories for the URM-3-4 test are shown in Figure 3.40 and Figure 3.41, respectively.

Figure 3.42 (a) and Figure 3.42 (b) show specimen URM-3 after test URM-3-4 (Shot 4). The following damage was documented: medium crack between 1st mortar head joint and the 2nd concrete block unit of the 1st course, medium crack between 1st mortar bed joint and the 1st concrete unit of the second course, fine crack formed inside the 1st mortar bed joint approximately 200 mm in length from the right side of the wall (just below the 6th concrete unit of the 1st course), fine cracks inside the 4th mortar bed joint located above all the mortar head joints of the 5th course, medium crack inside the 5th mortar bed joint, approximately 600 mm in length from the left side of the wall, and fine cracks inside 5th mortar bed joint located above 2nd, 3rd, 4th head joints of the 6th course.

3.3.3.5 Test URM-3-5

The shock tube driver length and the shock tube driver pressure used for this test were 1828.8 mm and 212.4 kPa, respectively. This resulted in a peak reflected pressure of 37.7 kPa, a positive phase duration of 13.7 ms and a reflected impulse over the positive phase of

309.2 kPa-ms as shown in Figure 3.43 and listed in Table 3.1. The wall reached a maximum mid-height displacement of 45 mm and a support rotation of 2.58º at 40 ms after the start of the shock wave loading. The recorded data showed a residual mid-height displacement of 3.47 mm and an accumulated mid-height residual displacement of 8.7 mm. The reflected pressure and impulse time histories as well as the reflected pressure and mid-height displacement time histories for the URM-3-5 test are shown in Figure 3.43 and Figure 3.44, respectively.

Figure 3.42 (c) shows specimen URM-3 after test URM-3-5 (Shot 5). Previously formed cracks got extended and their size got wider. The following damage was documented: a wide crack between 1st mortar head joint and the 2nd concrete block unit of the 1st course (in previous test this crack was medium in size), wide crack between 1st mortar bed joint and the 1st concrete unit of the second course (same crack was medium in size after previous test), fine crack formed inside the 1st mortar bed joint approximately 200 mm in length from the right side of the wall (just below the 6th concrete unit of the 1st course), fine cracks inside the 4th mortar bed joint located above all the mortar head joints of the 5th course, fine crack inside 4th mortar head joint of the 5th course, fine crack inside 1st mortar head joint of the 6th course, and medium crack along the whole length of the 5th mortar bed joint (in previous test the cracked length was approximately 600 mm).

3.3.3.6 Test URM-3-6

The shock tube driver length and the shock tube driver pressure were selected to be 1828.8 mm and 248.2 kPa, respectively. This resulted in a peak reflected pressure of 39 kPa, a positive phase duration of 12.9 ms and a reflected impulse over the positive phase of 290.8 kPa-ms as shown in Figure 3.45 and listed in Table 3.1. The wall reached a maximum mid-height displacement of 41.7 mm (2.39º) at 41 ms after the start of the shock wave loading. The reflected pressure and impulse time histories as well as the reflected pressure and mid-height displacement time histories for the URM-3-6 test are shown in Figure 3.45 and Figure 3.46, respectively.

The following damage was documented: wide crack between 1st mortar head joint and the 2nd concrete block unit of the 1st course, wide crack between 1st mortar bed joint and the 1st

concrete unit of the second course, fine crack formed inside the 1st mortar bed joint approximately 200 mm in length from the right side of the wall (just below the 6th concrete unit of the 1st course), fine cracks inside the 4th mortar bed joint located above all the mortar head joints of the 5th course, fine crack inside 4th mortar head joint of the 5th course, fine crack inside 1st mortar head joint of the 6th course, medium crack along the whole length of the 5th mortar bed joint, fine crack inside 6th mortar bed joint, approximately 1200 mm from the left side of the wall, fine crack inside 7th mortar bed joint above the 7th block of the 8th course. The recorded data showed an accumulated mid-height residual displacement of 8.7 mm.

3.3.3.7 Test URM-3-7

This shot with a shock tube driver pressure of 288.2 kPa and a driver length of 1829 mm, caused global failure of the specimen. A peak reflected pressure of 51 kPa, a positive phase duration of 12.9 ms and a reflected impulse over the positive phase of 414.6 kPa-ms were recorded and are shown in Figure 3.47 and listed in Table 3.1. The reflected pressure and impulse time histories as well as the reflected pressure and mid-height displacement time histories for the URM-3-7 test are shown in Figure 3.47 and Figure 3.48, respectively.

Figure 3.42 (d) shows the remains of the specimen after shot URM-3-7. The collapse progression of the wall, recorded with high speed video, shows the formation of a hinge in the middle, with the opening of the middle mortar joint, sequentially followed by the opening of other joints.

The failure mode was brittle in nature, with fragmentation of concrete blocks and flying debris.

3.3.4 Masonry Wall URM-4

The masonry wall specimen URM-4 was designed and tested as a retrofitted, unreinforced, load-bearing wall. The general arrangement and details for this wall are described in Chapter 2. In order to facilitate the recording of axial loads, the testing frame surrounding the wall specimen was allowed to displace vertically relatively to the shock tube end frame and load cells were installed on top of the steel testing frame, shimmed against the strong floor. The wall had a tight contact with the surrounding steel frame and axial load was

applied by two hydraulic jacks placed 508 mm left and right of the vertical center line of the wall. The total axial load applied was approximately 123 kN (10% of the total load carrying capacity of the wall). The retrofit system was installed as follows: first, the steel bars were welded one by one to the steel flat plates at a 100 mm horizontal spacing; second, the bars attached to the plates were bolted to the steel testing frame; third, a 6mm layer of polyurea was sprayed over the tension face of the wall by Line-X of Ottawa certified staff team.

A total of eight shock waves were applied on the retrofitted load-bearing URM wall specimen until it reached global failure. The driver section pressure of the shock tube was increased and the load duration was kept constant for the first seven tests by using the same driver length of 1829 mm. For the first test, URM-4-1, similar reflected pressure-impulse combination to shots URM-1-3, URM-2-3, and URM-3-3, was used in order to facilitate direct comparison. Shot URM-4-2, had similar reflected pressure-impulse combination with shot URM-1-4 that failed URM-1 wall specimen, URM-2-4, and URM-3-4. The third and fourth shot, URM-4-3, and URM-4-4, respectively had a similar reflected pressure-impulse combination to shot URM-3-7, shot that failed URM-3 specimen. The firth shot, URM-4-5, has similar pressure-impulse combination to shot URM-2-10, shot that failed the URM-2 specimen. For the last three shots, the driver pressure was increased until failure of the URM-4 specimen was achieved. The last shot, intended to cause maximum damage, used the longest driver length available (4877 mm) in order to increase the load duration from 17 ms to 50 ms.

A summary of results for each test along with visual observations are provided below.

3.3.4.1 Test URM-4-1

The first shot used a shock tube driver length of 1829 mm, and a shock tube driver pressure of 123.4 kPa. This resulted in a peak reflected pressure of 24.6 kPa, a positive phase duration of 14.1 ms and a reflected impulse over the positive phase of 258.8 kPa-ms as shown in Figure 3.49 and listed in Table 3.1. The wall reached a maximum mid-height displacement of 8.8 mm and 0.50º support rotation at 17 ms after the start of the shock wave loading. The recorded data showed no mid-height residual displacement. The

reflected pressure and impulse time histories as well as the reflected pressure and mid-height displacement time histories for the URM-4-1 test are shown in Figure 3.49 and Figure 3.50, respectively.

No distinct signs of damage were recorded. Due to the presence of the polyurea and steel wire retrofit system, any potential cracks on the tension face of the wall would not be visible.

3.3.4.2 Test URM-4-2

The second test used a constant shock tube driver length of 1829 mm and a shock tube driver pressure of 165.5 kPa in order to generate a peak reflected pressure of 32.2 kPa over a 14.2 ms positive phase duration and a reflected impulse over the positive phase of 350.3 kPa-ms as shown in Figure 3.51 and listed in Table 3.1. The wall reached a maximum mid-height displacement of 13.1 mm (0.75º) at 16 ms after the start of the shock wave loading. The wall had a recorded mid-height residual displacement of 0.2 mm. The reflected pressure and impulse time histories as well as the reflected pressure and mid-height displacement time histories for the URM-4-2 test are shown in Figure 3.51 and Figure 3.52, respectively.

No visible signs of damage were recorded.

3.3.4.3 Test URM-4-3

A shock tube driver length of 1829 mm and the shock tube driver pressure of 244.8 kPa, resulted in a peak reflected pressure of 47.5 kPa, a positive phase duration of 14.6 ms and a reflected impulse over the positive phase of 462 kPa-ms as shown in Figure 3.53 and listed in Table 3.1. The wall reached a maximum mid-height displacement of 18.4 mm (1.05º support rotation) at 19 ms after the start of the shock wave loading. The recorded data showed an accumulated mid-height residual displacement of 0.8 mm. The reflected pressure and impulse time histories as well as the reflected pressure and mid-height displacement time histories for the URM-4-3 test are shown in Figure 3.53 and Figure 3.54, respectively.

No visible signs of damage were recorded.

3.3.4.4 Test URM-4-4

The shock tube driver length and the shock tube driver pressure were selected to be 1828.8 mm and 291.7 kPa, respectively. This resulted in a peak reflected pressure of 51.3 kPa, a positive phase duration of 16.4 ms and a reflected impulse over the positive phase of 536.2 kPa-ms as shown in Figure 3.55 and listed in Table 3.1. The wall reached a maximum mid-height displacement of 23.8 mm (1.36º support rotation) at 21 ms after the start of the shock wave loading. The recorded data showed an accumulated mid-height residual displacement of 2.6 mm. The reflected pressure and impulse time histories as well as the reflected pressure and mid-height displacement time histories for the URM-4-4 test are shown in Figure 3.55 and Figure 3.56, respectively.

No visible signs of damage were recorded.

3.3.4.5 Test URM-4-5

For this test, a shock tube driver length and the shock tube driver pressure were selected to be 1828.8 mm and 426.1 kPa, respectively, that resulted in a peak reflected pressure of 69.7 kPa, a positive phase duration of 16.7 ms and a reflected impulse over the positive phase of 675.8 kPa-ms as shown in Figure 3.57 and listed in Table 3.1. The wall reached a maximum mid-height displacement of 36.4 mm with a 2.09º support rotation at 22 ms after the start of the shock wave loading. The recorded data showed an accumulated mid-height residual displacement of 7 mm. The reflected pressure and impulse time histories as well as the reflected pressure and mid-height displacement time histories for the URM-4-5 test are shown in Figure 3.57 and Figure 3.58, respectively.

No visible signs of damage were recorded.

3.3.4.6 Test URM-4-6

A shock tube driver length of 1829 mm and a shock tube driver pressure of 555 kPa, resulted in a peak reflected pressure of 107.7 kPa, a positive phase duration of 18 ms and a reflected impulse over the positive phase of 891.9 kPa-ms as shown in Figure 3.59 and listed in Table 3.1. The wall reached a maximum mid-height displacement of 55.1 mm with a corresponding support rotation of 3.16º at 25 ms after the start of the shock wave

loading. The recorded data showed an accumulated mid-height residual displacement of 11.1 mm. The reflected pressure and impulse time histories as well as the reflected pressure and mid-height displacement time histories for the URM-4-6 test are shown in Figure 3.59 and Figure 3.60, respectively.

Figure 3.61 shows specimen URM-4 after test URM-4-6 (Shot 6). Crushing of the middle mortar joint was observed on the compression face (blast face) as well as the formation of a crack near the middle mortar joint on the compression face as shown in Figure 3.61 (b).

3.3.4.7 Test URM-4-7

The shock tube driver length and the shock tube driver pressure were selected to be 1828.8 mm and 748.1 kPa, respectively. This resulted in a peak reflected pressure of 125.7 kPa, a positive phase duration of 23.3 ms and a reflected impulse over the positive phase of 1157.5 kPa-ms as shown in Figure 3.62 and listed in Table 3.1. The wall reached a maximum mid-height displacement of 88.1 mm (5.04º support rotation) at 29 ms after the start of the shock wave loading. The recorded data showed an accumulated mid-height residual displacement of 28.7 mm. The reflected pressure and impulse time histories as well as the reflected pressure and mid-height displacement time histories for the URM-4-7 test are shown in Figure 3.62 and Figure 3.63, respectively.

Excessive deformations (Figure 3.64 (a)) and splitting of the middle course shells on the compression side of the masonry wall occurred (Figure 3.64 (b)). Although the wall underwent excessive deformations and loss of mass, it was able to retain its load-bearing capabilities.

3.3.4.8 Test URM-4-8

This shot was intended to cause maximum damage to the masonry wall. The shock tube driver length and the shock tube driver pressure were selected to be 4876.8 mm and 683.3 kPa, respectively. This resulted in a peak reflected pressure of 97.3 kPa, a positive phase duration of 58.5 ms and a reflected impulse over the positive phase of 1995 kPa-ms as shown in Figure 3.65 and listed in Table 3.1. The wall reached a maximum mid-height displacement of 261 mm (14.95º support rotation) at 45 ms after the start of the shock wave loading. The recorded data showed an accumulated mid-height residual displacement

of 140.5 mm, with 28.7 mm mid-height residual displacement from previous shots and with 111.89 mm mid-height residual displacement from this test alone. The reflected pressure and impulse time histories as well as the reflected pressure and mid-height displacement time histories for the URM-4-8 test are shown in Figure 3.65 and Figure 3.66, respectively.

Although the wall could not hold any axial loading, it failed in a ductile manner (Figure 3.67) and the retrofit worked extremely efficient for eliminating flying debris caused by fragmentation.

3.4 Arching Action

Arching action was identified as an increase in measured axial force with the increase of the reflected pressure for every shock tube test performed on each wall specimen. Axial load time history data is provided in Appendix A for all the shock tube tests. For example, the axial load time history for test URM-2-6 (Figure 3.68) shows that the axial load time history follows a similar pattern as the pressure time history. The sudden increase in magnitude is due to the wall deflecting and pushing on the top and bottom rigid supports. The shape of the axial loading time history provides qualitative proof of the occurrence of arching action, but not a quantitative measure. The specimens were installed inside the steel testing frame, and the load cells were placed above the steel testing frame, shimmed to the strong floor. The testing frame was attached to the shock tube end frame in a manner that would allow for relative vertical translation. This vertical translation was enabled by releasing the tension in the bolts connecting the test frame to the shock tube end frame; however, it is likely some of the axial load was transferred to the rods, thus leading to inaccurate load cell readings.

3.5 Discussion and Comparison of Experimental Results

The specimen URM-1 failed in a brittle manner, with significant amount of debris that scattered for a distance of up to 3.8 m away from the shock tube test frame (Figure 3.4 (d)). High speed video recording shows the failure mechanism involved the formation of a hinge at the middle mortar bed joint location, followed by the opening of the same middle mortar bed joint, sequentially followed by the opening of the other mortar bed joints, and, finally,

the collapse of the wall. The arching action, enabled by the reduction in top edge gap between the wall and the surrounding test frame as well as the installation of the mechanical shear restraints at the top and bottom of the wall, changed the failure mode from a tilt-over to a hinged-arched type failure mode. However, the failure of the wall was still brittle in nature with fragmentation and flying debris. Cracks initiated in the early stages of testing, initially across the middle mortar bed joint, sequentially at the other mortar bed joint location, and last at the mortar head joint location. Cracks formed inside the mortar joints, as well as between the concrete blocks and the mortar joint. There were no cracks that occurred inside the concrete masonry block units. The wall collapsed before any crushing of the concrete took place at mid-height of the compression face of the wall. There was evidence of crushing of the middle mortar joint. It appears arching occurred and provided lateral load capacity to the wall specimen with compression struts forming as the wall deflected and started pushing on the top and bottom rigid supports. The mechanical shear restraints successfully prevented the wall from sliding or simply tilting over. Since the installed strain gauges did not record any strains for URM-1 specimen, the occurrence of arching action could not be verified by test data.

Test specimen URM-2 failed in a ductile manner with little flying debris (Figure 3.31) when compared to URM-1. The polyurea retrofit not only reduced the amount and size of debris, it also added ductility and increased strength of the wall as in can be seen in the test results. Strength increase is due to the polyurea membrane not being uniformly strained. A uniformly strained, 2 m long, polyurea membrane would not be subjected to high stresses since the strains are small. However, in the case of URM-2 wall specimen, as it deflected, stress and strain in polyurea layer developed first at and near the horizontal mortar joints, with the highest stresses and strains occurring at the mid height, and there would be little or no stresses or strains where the polyurea was bonded to the concrete blocks. These regions were identified from post-experiment observations as regions where polyurea debonded from the URM block face. The higher localized stresses and strains at locations adjacent to horizontal mortar joints, yield higher bending moment resistance that in turn adds capacity to the specimen. Debonding of the polyurea membrane from the concrete masonry wall initiated at mid-height, above and below the mortar bed joint, during test URM-2-8. The specimen experienced a local tear in polyurea membrane during test URM-2-9. This tear

was extended and created an approximate 400 mm long opening during test URM-2-10 that allowed for little debris to escape into the assumed occupant area.

A comparison of maximum mid-height displacements between URM-1 and URM-2 is provided in Figure 3.69. To facilitate direct comparison, similar load increments and a constant driver length of 1829 mm were used for all the shock tube tests performed on URM-1 and URM-2 wall specimens that translated into a constant positive phase loading duration of approximately 17 ms. The polyurea retrofit significantly increased ductility, since the URM-2 wall specimen was able to deflect at mid-height 158.9 mm as opposed to URM-1 that deflected at mid-height only 56.5 mm, before global failure of the specimen. There is also significant increase in strength, since the retrofitted wall, URM-2, had local failure at a reflected pressure of 84 kPa, 2.6 times higher than the reflected pressure of 32 kPa that caused failure of URM-1.

Wall specimen, URM-3, failed in a brittle manner, similar to that of URM-1 wall specimen but at a higher blast load. The debris fell approximately 2.8 m away from the testing frame (Figure 3.42 (d)). The failure mechanism involved formation of a hinge at mid-height of the wall, followed by the opening of the middle mortar bed joint, sequentially followed by the other mortar bed joints. The reflected pressure that caused failure of URM-3 wall specimen (51 kPa) was 1.7 times higher than the reflected pressure that caused failure of URM-1 wall specimen (31 kPa), as listed in Table 3.1. The increase in capacity is due to the presence of axial loading that added to the sectional moment capacity as well as arching action.

The retrofit used for specimen URM-4 changed the failure mode from a brittle (URM-3) to a ductile failure mode (Figure 3.67). The smooth steel wires reinforcement, sprayed over with polyurea, increased the ultimate resistance to out-of-plane loading from 39 kPa for URM-3 to 125.7 kPa for URM-4 (Table 3.1). There was no observed damage to the specimen until test URM-4-7, with a reflected pressure of 125.7 kPa, which caused splitting of the mid-height concrete masonry unit face shells on the blast face. At the end of test URM-4-7, there was no change in axial load capacity since the hydraulic jacks were reading the same pressure as they were before the test. The reflected pressure that cause

local splitting of the compression side mid-height face shells (125.7 kPa), was 2.5 times higher than the reflected pressure that caused global failure of URM-3 wall specimen (51 kPa), with the same loading duration (Table 3.1). By increasing the driver length for test URM-4-8 from 1829 mm to 4877 mm, the maximum length available, and using a very high driver pressure of 683 kPa, the maximum damage level was obtained. This shot represents the maximum limits of the shock tube capabilities for both driver length and driver pressure. Post-test observations show fracturing of the steel reinforcement caused by high tensile forces, as well as splitting of the compression side face shells as shown in post-test photos (Figure 3.67). Although the wall did not retaining its axial loading capacity after test URM-4-8, the failure mode was ductile in nature with no flying debris caused by fragmentation, all of debris was contained.

A comparison of maximum mid-height displacements between URM-3 and URM-4 is provided in Figure 3.70. Most of the shock tube tests had similar load increments and the same loading duration to facilitate direct comparison of results, except the last shot. The retrofit significantly increased the ductility of the system, since URM-4 wall was able to achieve a mid-height deflection of 88.1 mm in comparison with URM-3 specimen that deflected at mid-height 41.7 mm, before global failure occurred. The increase in strength is also shown since the retrofitted wall, URM-4, had local failure in form of splitting of compression face shells at mid-height of wall, at a reflected pressure of 126 kPa, 2.5 times higher than the reflected pressure of 51 kPa that caused failure of URM-3 wall specimen.

Figure 3.71 shows mid-height displacement time history comparison for all the URM wall specimens subjected to a similar reflected pressure time history using 1829 mm driver length and a driver pressure of about 120 kPa. The polyurea retrofitted walls, URM-2 and URM-4, had significantly lower measured mid-height displacement when compared to URM-1 and URM-3. The polyurea retrofit system decreased the mid-height displacement of the non-load bearing, infill wall by a factor of 5.5, whereas for the load-bearing wall, the steel and polyurea retrofit system decreased the mid-height displacement only by a factor of 2. This is partly due to the higher resistance of the load-bearing wall as compared to the non-load bearing, infill wall. The applied axial load increases the bending moment capacity

of the section. Since the infill wall is more vulnerable, less stable, than the load-bearing wall, the retrofit system has a higher effect.

3.6 Summary of the Experimental Results

The following is a summary of the experimental findings:

- Results indicate that reducing the top edge gap between the URM wall and the surrounding frame can increase capacity of URM wall by activating the arching mechanism.
- Arching mechanism and the addition of mechanical shear restraints changed the failure mode of the URM-1 wall specimen from a tilt-over to a hinged-arched type collapse.
- Polyurea retrofit significantly increased the blast resistance of both infill and load-bearing masonry wall specimens. In addition to increasing strength and ductility, fragmentation and flying debris due to disintegration of concrete masonry units are also reduced.
- The increase in wall capacity is due to the polyurea membrane not being uniformly strained along the entire height of the URM wall. As the wall deflected, the polyurea layer developed stresses and strains at and near the mortar joints, with the highest levels at the mid height. These regions were identified from post-experimental observations as regions where polyurea debonded from both the URM wall sides.
- Polyurea proved excellent at dissipating the energy by changing the failure mode from a brittle to a ductile mode.

Table 3.1: Summary of Test Results

	P_D (kPa)	L_D (mm)	P_r (kPa)	I_r (kPa-ms)	t_d (ms)	d_{max} (mm)	d_{res} (mm)	θ_{max} (degrees)	t_{max} (ms)
URM-1-1	40	1828.8	6.1	53.1	10	9.1	6.2	0.5214	40
URM-1-2	75.8	1828.8	13.7	150.9	11.4	23.8	12	1.3636	40
URM-1-3	125.5	1828.8	23.4	179.3	13.5	56.5	13.9	3.2372	92
URM-1-4	165.5	1828.8	30.7	265.1	13.9	N/A	N/A	N/A	N/A
URM-2-1	41.4	1828.8	8.7	68.2	10.9	2.2	2	0.1261	33
URM-2-2	82.7	1828.8	14.6	128.7	12.5	6.4	7.8	0.3667	37
URM-2-3	118.6	1828.8	23	188.5	12.8	10.3	11.1	0.5901	40
URM-2-4	173.7	1828.8	32	294.5	13.1	23	12.1	1.3178	41
URM-2-5	207.5	1828.8	37.5	338.5	14.1	36.9	15.5	2.1142	44
URM-2-6	249.6	1828.8	42.1	406.3	14.5	50	16.3	2.8648	47
URM-2-7	291	1828.8	46.1	433.8	14.5	69.2	17.3	3.9649	48
URM-2-8	324.1	1828.8	53.9	483.3	14.7	88.4	22.7	5.0649	51
URM-2-9	448.8	1828.8	84.4	597.2	16.5	158.9	30.4	9.1043	63
URM-2-10	550.9	1828.8	78.1	723.4	17.3	253.5	59.5	14.5245	72
URM-3-1	34.5	1828.8	6.1	49	9.4	1.1	0.4	0.0630	25
URM-3-2	79.3	1828.8	13.2	121.9	12.7	8.2	1.6	0.4698	32
URM-3-3	121.4	1828.8	24.7	193.3	13.5	16.6	3.2	0.9511	35
URM-3-4	166.9	1828.8	28	271.9	13.6	28.6	5.3	1.6387	37
URM-3-5	212.4	1828.8	37.7	309.2	13.7	45	8.7	2.5783	40
URM-3-6	248.2	1828.8	39	290.8	12.9	41.7	8.7	2.3892	41
URM-3-7	288.2	1828.8	51	414.6	14.5	N/A	N/A	N/A	N/A
URM-4-1	123.4	1828.8	24.6	258.8	14.1	8.8	0	0.5042	17
URM-4-2	165.5	1828.8	32.2	350.3	14.2	13.1	0.2	0.7506	16
URM-4-3	244.8	1828.8	47.5	462	14.6	18.4	0.8	1.0542	19
URM-4-4	291.7	1828.8	51.3	536.2	16.4	23.8	2.6	1.3636	21
URM-4-5	426.1	1828.8	69.7	675.8	16.7	36.4	7	2.0856	22
URM-4-6	555	1828.8	107.7	891.9	18	55.1	11.1	3.1570	25
URM-4-7	748.1	1828.8	125.7	1157.5	23.3	88.1	28.7	5.0478	29
URM-4-8	683.3	4876.8	97.3	1995	58.5	261	140.5	14.9542	45

Table 3.2: Experimentally Recorded Maximum and Residual Displacements

	Maximum Displacements (mm)					Residual Displacements (mm)				
	D1	D2	D3	D4	D5	D1	D2	D3	D4	D5
URM-1-1	5.31	10.46	9.07	7.96	2.05	1.19	2.91	6.19	5.60	1.93
URM-1-2	13.61	30.75	23.76	19.32	6.63	4.18	7.61	5.75	3.72	5.85
URM-1-3	16.23	41.65	56.53	39.34	13.08	-15.70	-7.00	1.94	0.58	7.23
URM-1-4	N/A	N/A	N/A	N/A	N/A	N/A	N/A	N/A	N/A	N/A
URM-2-1	0.36	3.04	2.18	2.58	0.33	0.03	2.70	2.01	2.24	0.24
URM-2-2	1.60	6.67	6.37	4.79	1.78	1.24	2.58	5.76	3.85	1.49
URM-2-3	4.35	10.55	10.30	10.36	3.92	2.93	2.93	3.35	4.12	3.60
URM-2-4	9.09	20.59	22.95	20.27	9.12	1.87	2.93	1.02	2.06	7.43
URM-2-5	14.18	31.08	36.92	29.27	11.88	2.40	2.75	3.43	2.55	5.11
URM-2-6	22.74	43.26	49.92	33.45	17.80	3.64	2.96	0.76	-2.45	3.51
URM-2-7	25.40	55.99	69.18	54.08	33.07	-0.71	-0.03	1.05	1.51	4.10
URM-2-8	24.84	71.73	88.38	64.48	14.83	-0.89	0.58	5.41	-0.85	-4.28
URM-2-9	45.36	127.49	158.89	124.95	39.99	-5.21	2.70	7.71	8.64	4.52
URM-2-10	85.15	217.93	253.46	186.73	59.15	4.03	23.69	29.03	22.42	-0.74
URM-3-1	0.24	0.74	1.13	0.98	0.18	-0.41	0.06	0.44	0.67	-0.06
URM-3-2	3.02	7.44	8.19	5.49	1.27	2.19	1.60	1.20	1.34	0.91
URM-3-3	5.68	13.53	16.58	11.81	1.27	1.48	3.32	1.58	0.92	0.66
URM-3-4	8.82	20.97	28.56	23.10	3.62	1.66	0.68	2.08	2.35	2.30
URM-3-5	15.51	35.18	45.01	34.24	14.62	3.43	3.81	3.47	2.20	6.40
URM-3-6	13.56	31.37	41.67	34.27	14.86	1.60	1.05	-0.06	2.84	6.28
URM-3-7	N/A	N/A	N/A	N/A	N/A	N/A	N/A	N/A	N/A	N/A
URM-4-1	5.36	8.03	8.83	8.68	6.05	0.16	-0.03	-0.25	-0.10	-0.23
URM-4-2	6.97	11.67	13.12	12.64	8.23	0.16	0.18	0.16	0.06	-0.23
URM-4-3	9.18	16.05	18.39	17.36	10.63	0.77	0.76	0.64	0.55	0.10
URM-4-4	10.95	20.94	23.83	21.90	12.17	1.51	1.77	1.84	1.87	1.35
URM-4-5	15.67	31.44	36.38	32.57	16.68	3.27	3.95	4.35	3.83	3.29
URM-4-6	21.96	47.34	55.06	47.62	22.54	2.79	3.70	4.16	3.83	2.86
URM-4-7	32.14	77.47	88.09	71.54	29.94	6.97	15.70	17.50	13.41	6.28
URM-4-8	7.77	2.13	261.01	3.95	7.17	0.13	-0.05	111.89	0.23	-0.16

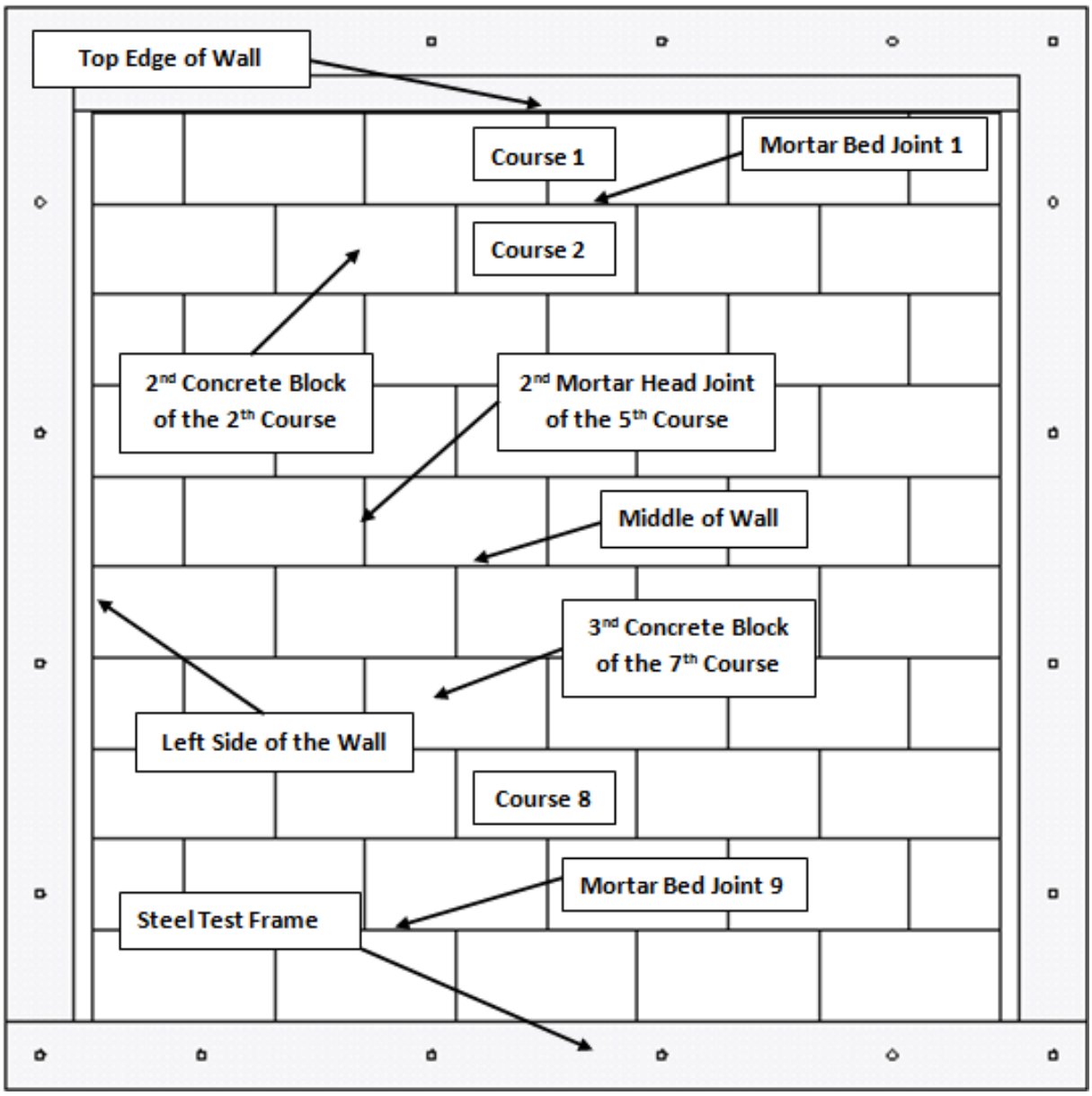

Figure 3.1: Masonry Wall Labelling Diagram

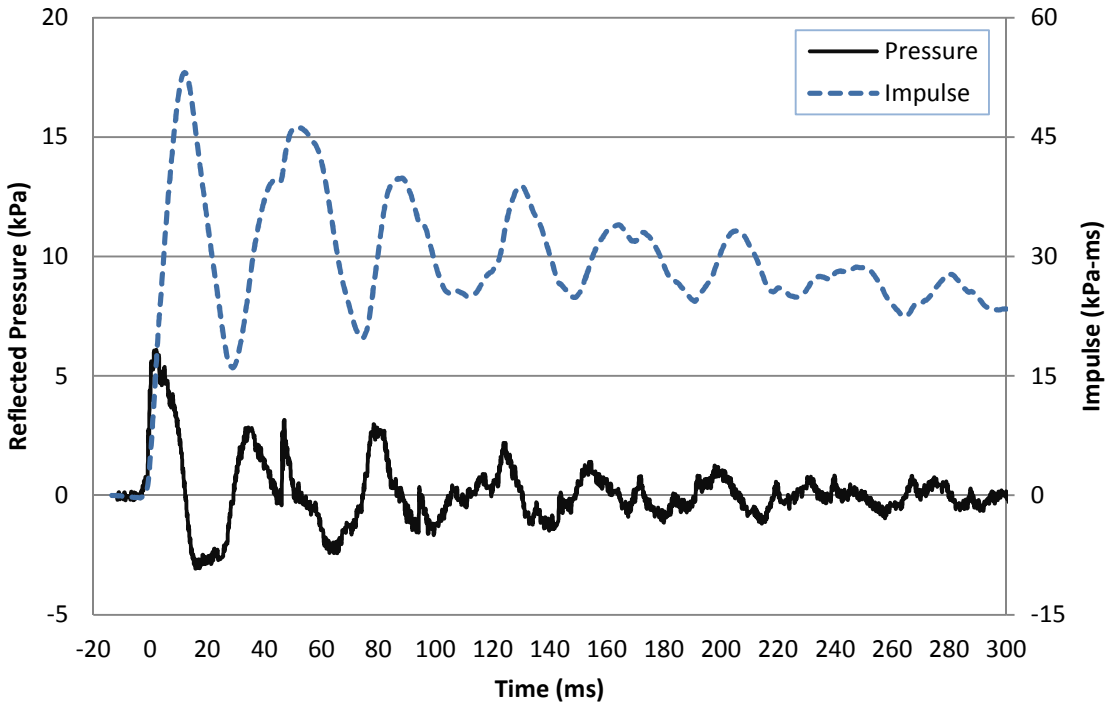

Figure 3.2: Reflected Pressure and Impulse Time History for Test URM-1-1

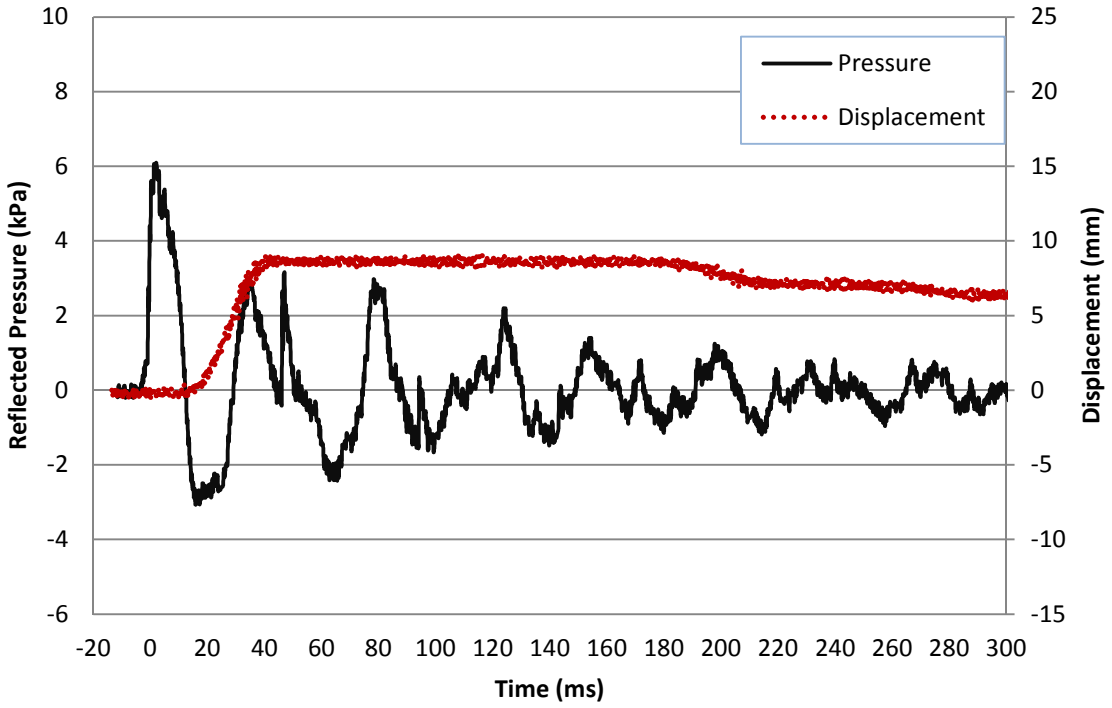

Figure 3.3: Reflected Pressure and Mid-Height Displacement Time History for Test URM-1-1

a) 

b) 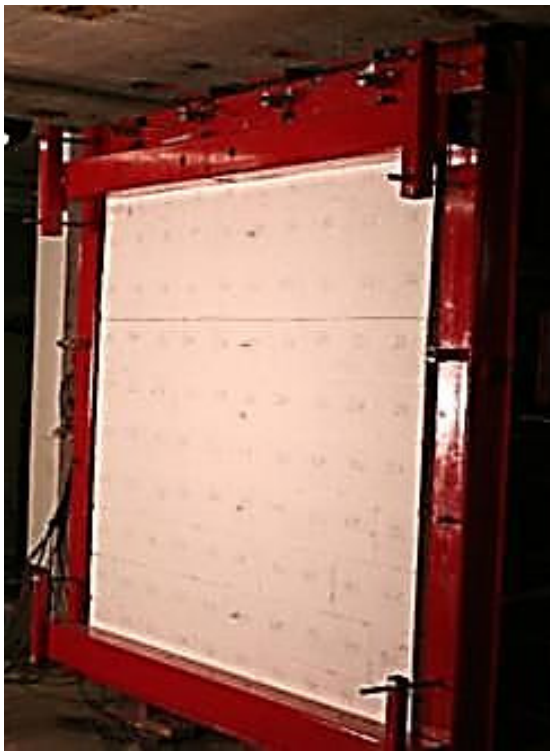

c) 

d) 

Figure 3.4: URM-1 Wall After Various Stages of Testing: a) After Shot 1; b) After Shot 2; c) After Shot 3; d) After Shot 4

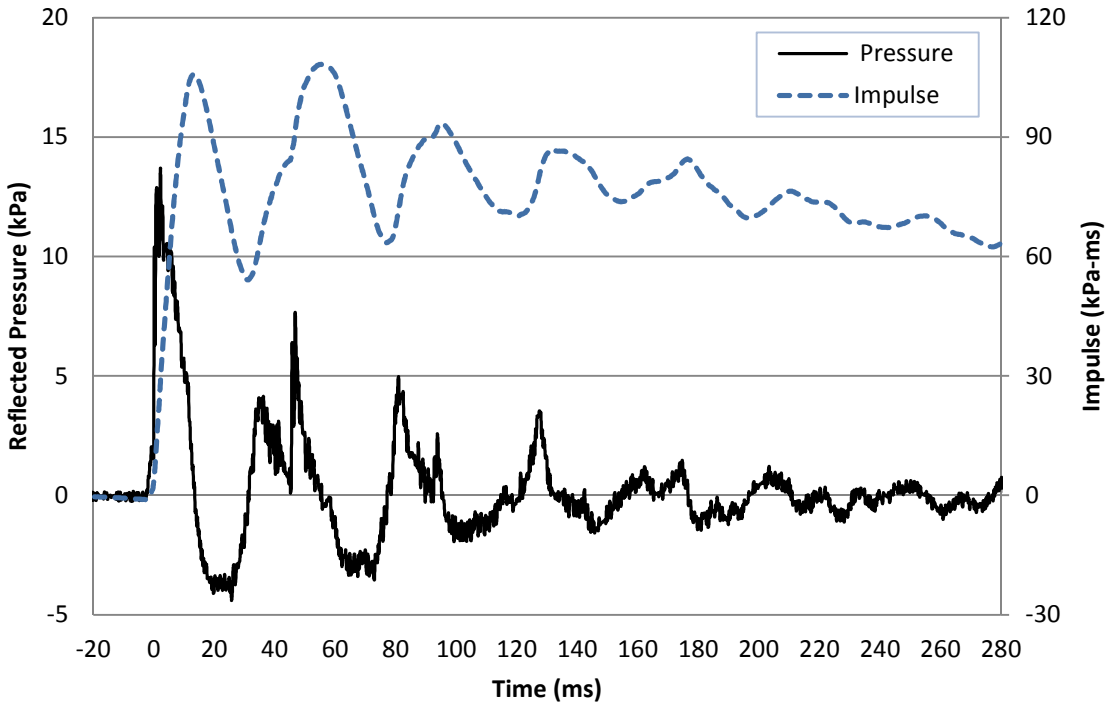

Figure 3.5: Reflected Pressure and Impulse Time History for Test URM-1-2

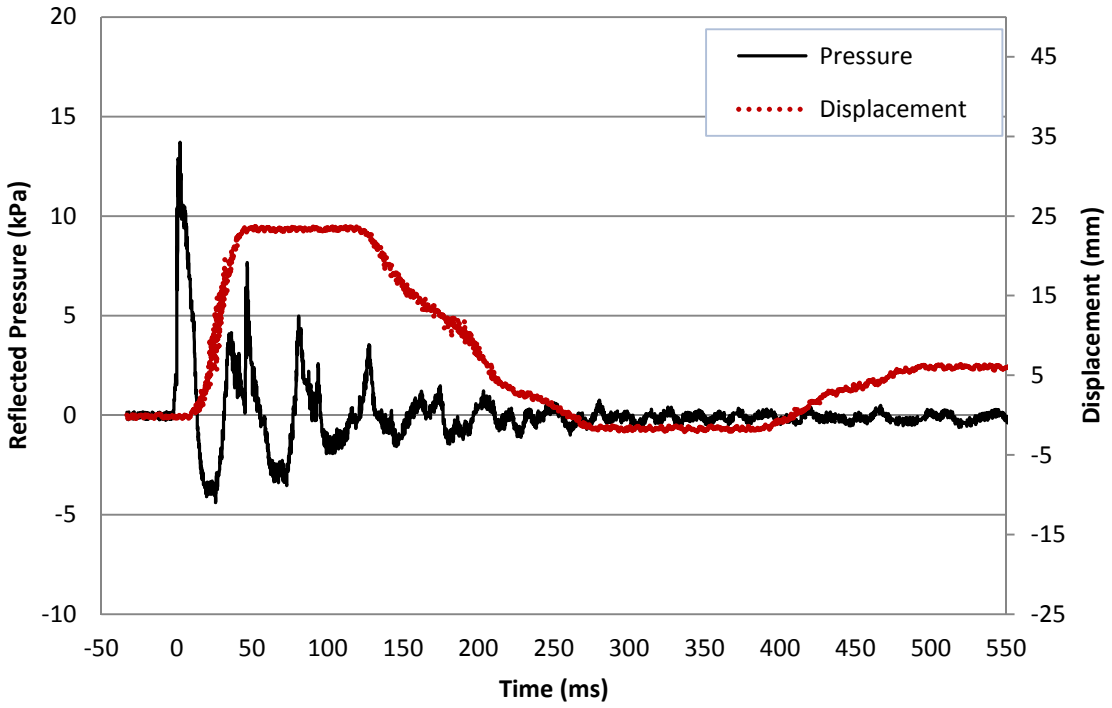

Figure 3.6: Reflected Pressure and Mid-Height Displacement Time History for Test URM-1-2

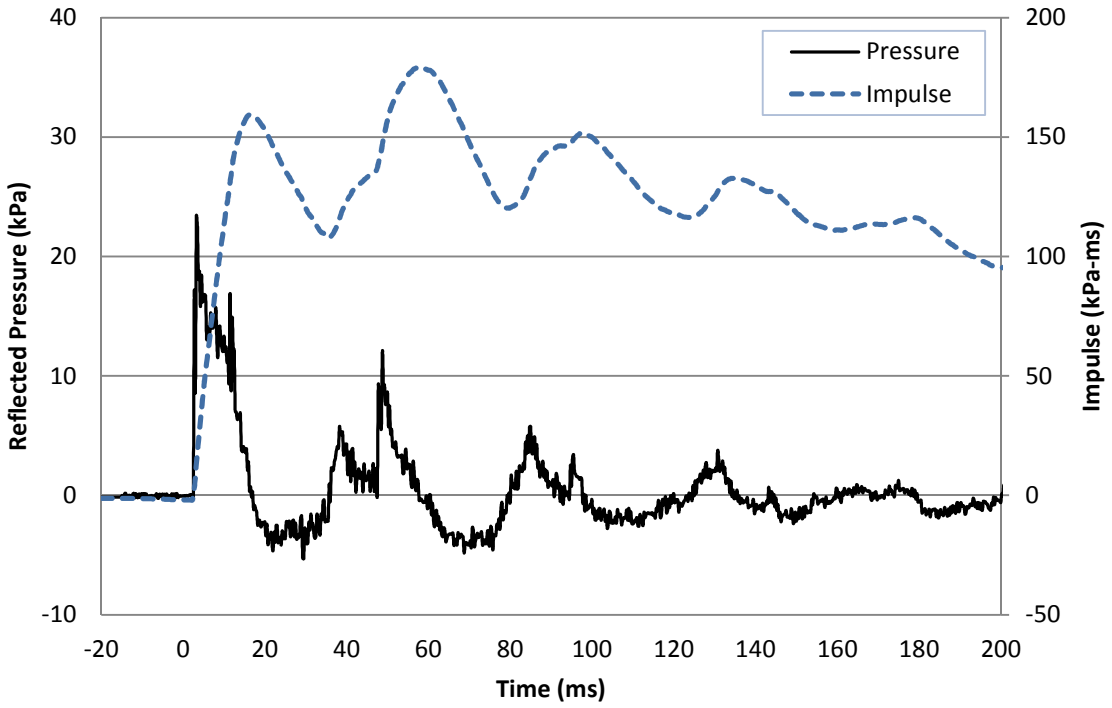

Figure 3.7: Reflected Pressure and Impulse Time History for Test URM-1-3

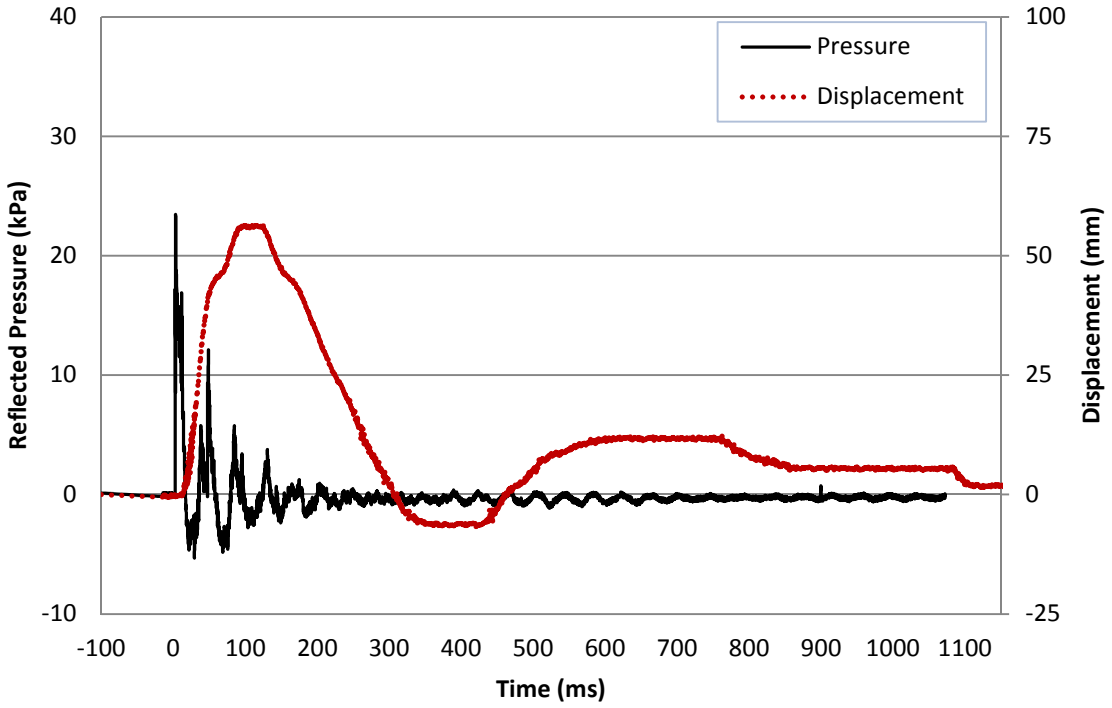

Figure 3.8: Reflected Pressure and Mid-Height Displacement Time History for Test URM-1-3

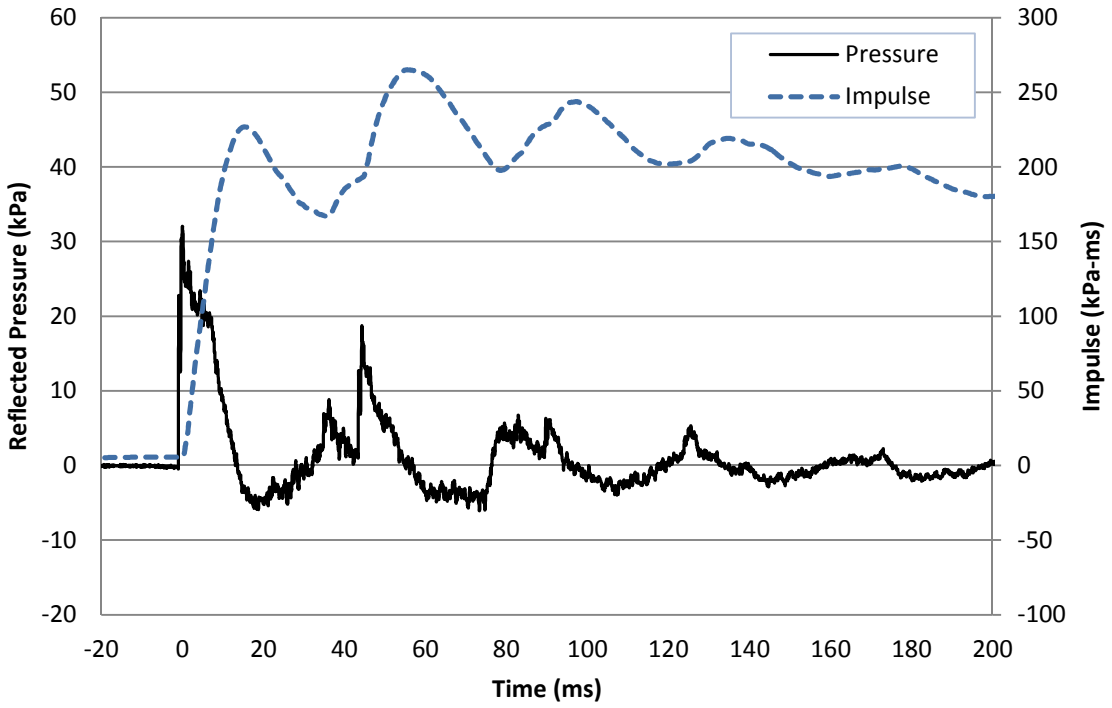

Figure 3.9: Reflected Pressure and Impulse Time History for Test URM-1-4

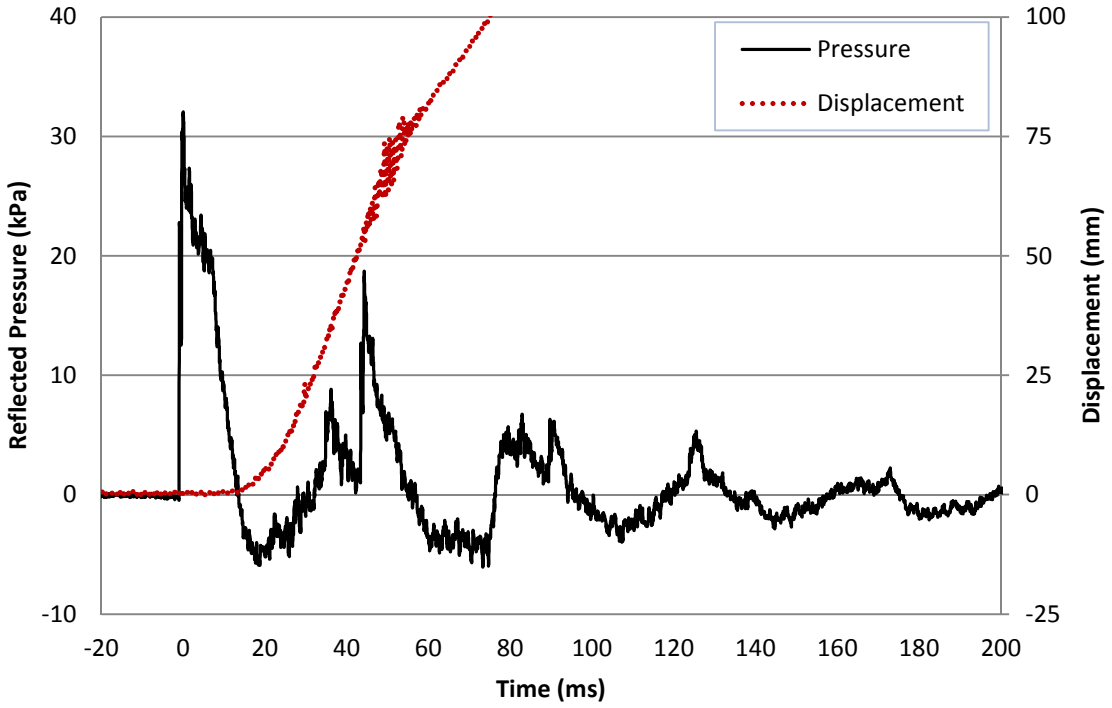

Figure 3.10: Reflected Pressure and Mid-Height Displacement Time History for Test URM-1-4

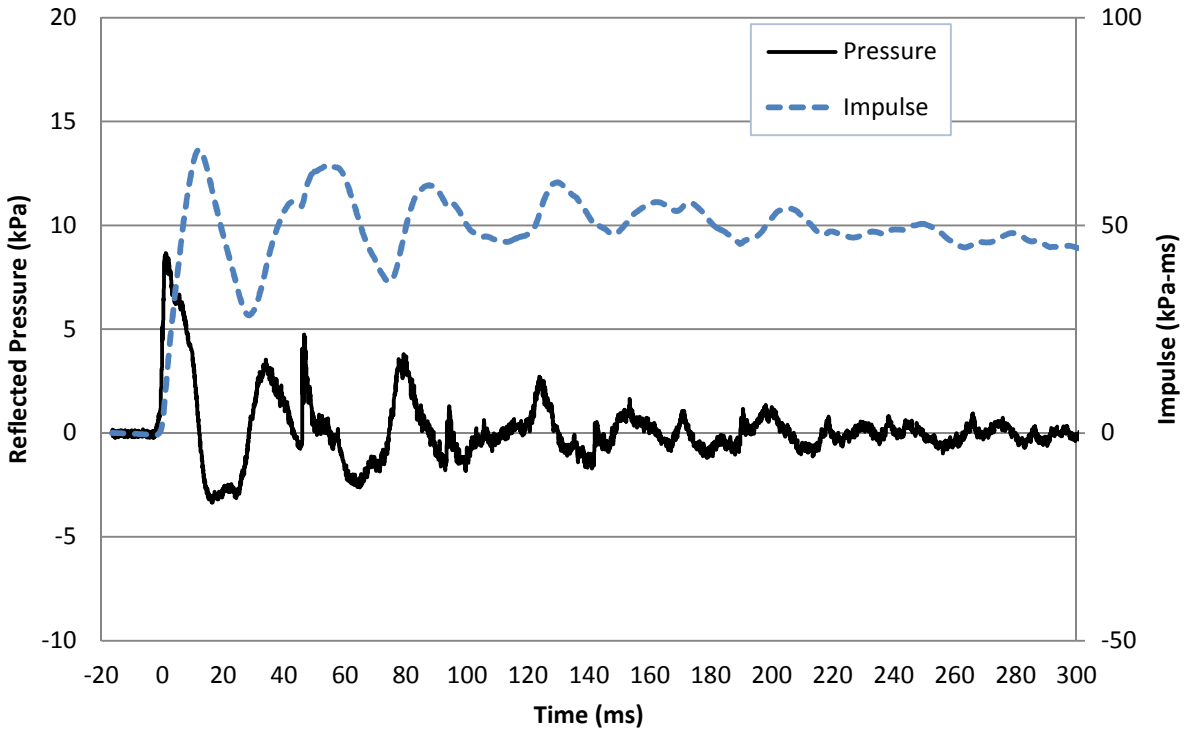

Figure 3.11: Reflected Pressure and Impulse Time History for Test URM-2-1

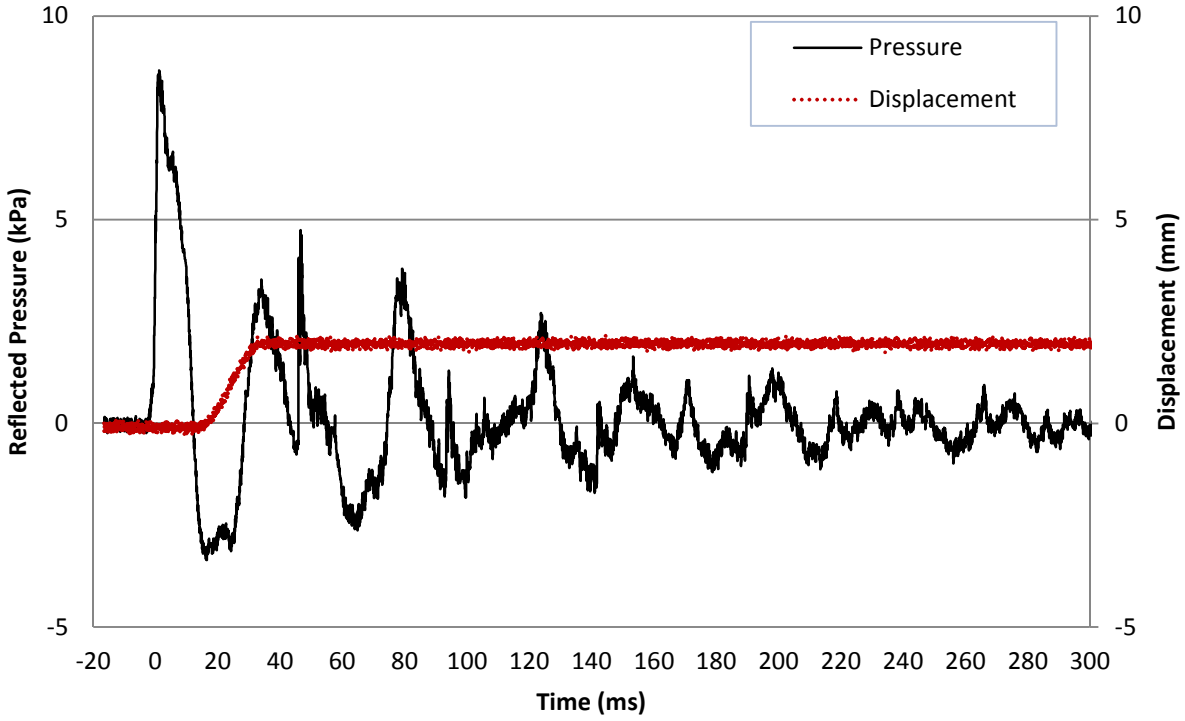

Figure 3.12: Reflected Pressure and Mid-Height Displacement Time History for Test URM-2-1

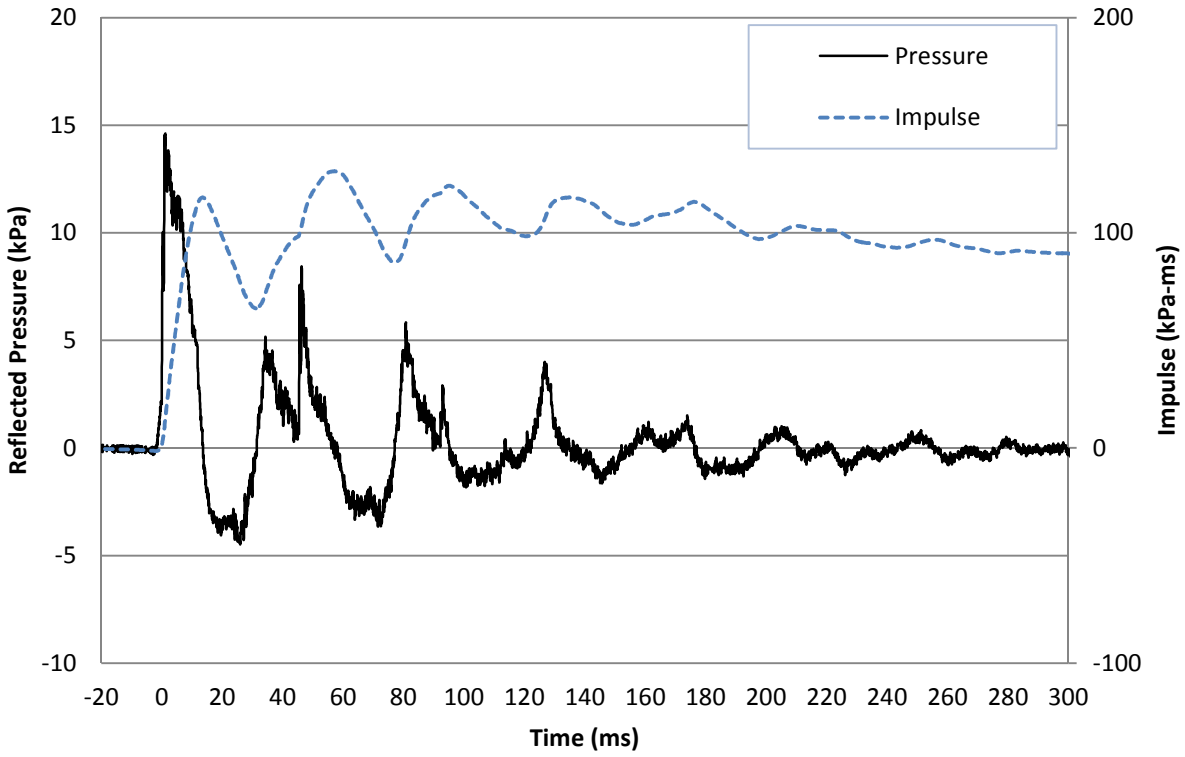

Figure 3.13: Reflected Pressure and Impulse Time History for Test URM-2-2

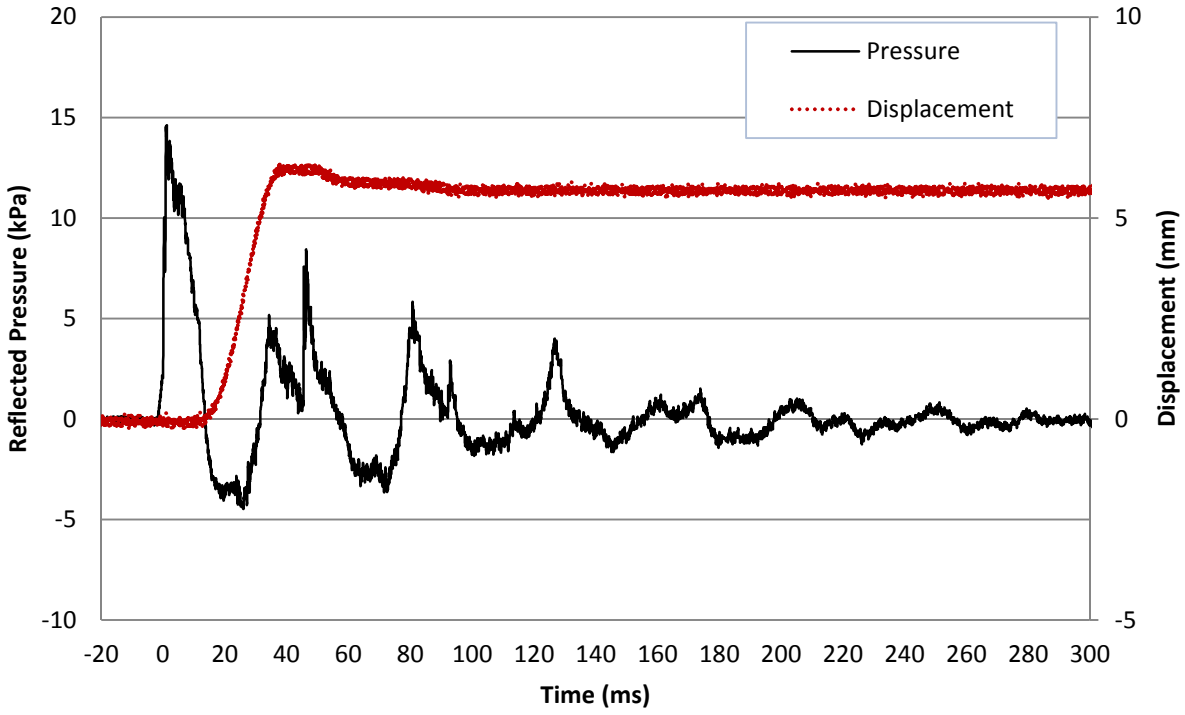

Figure 3.14: Reflected Pressure and Mid-Height Displacement Time History for Test URM-2-2

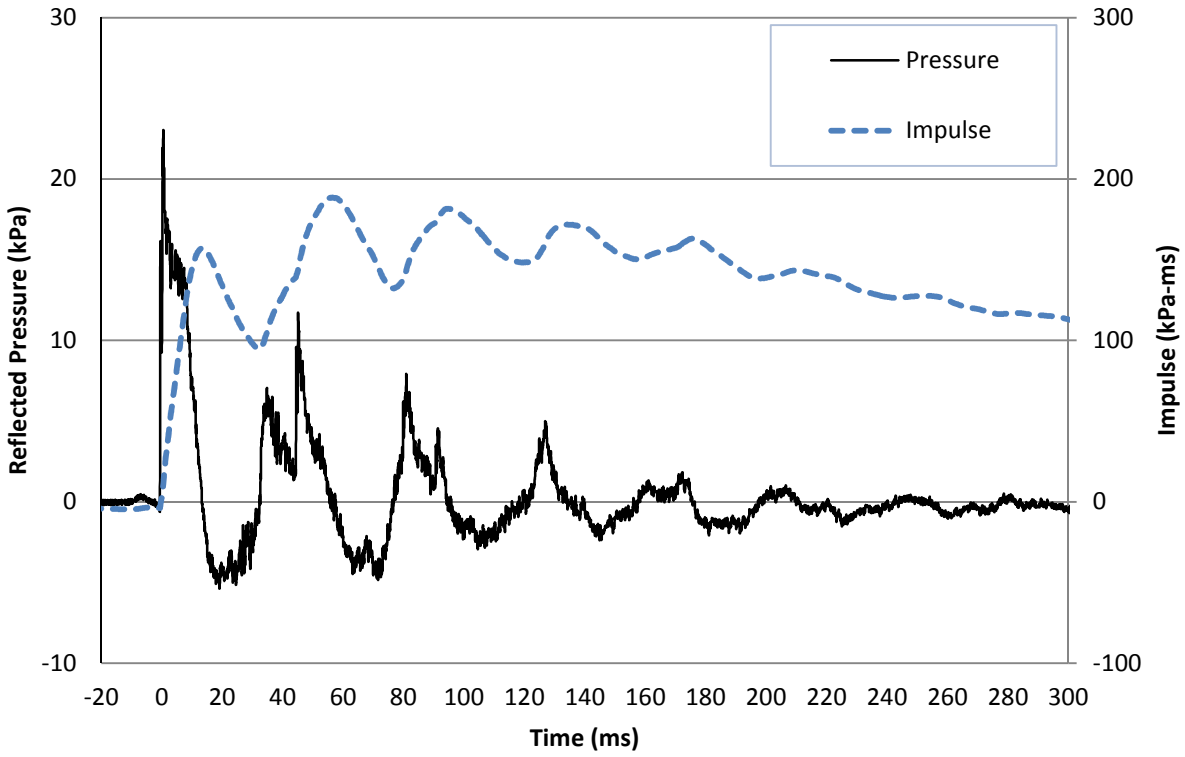

Figure 3.15: Reflected Pressure and Impulse Time History for Test URM-2-3

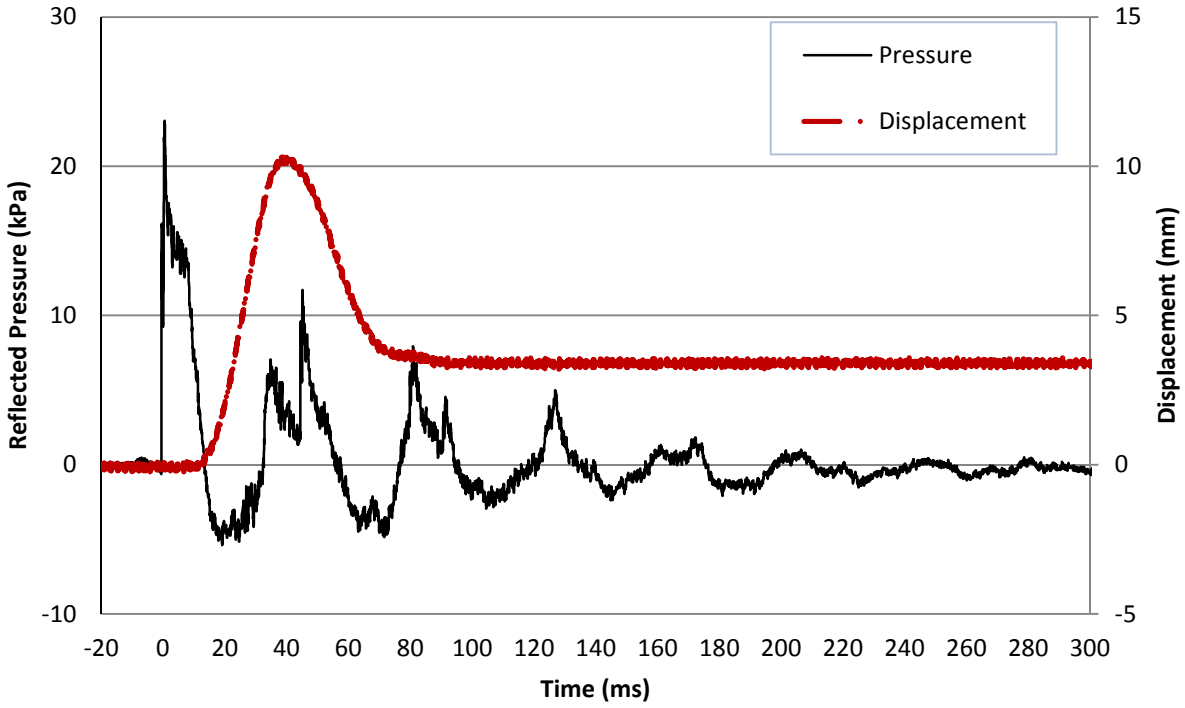

Figure 3.16: Reflected Pressure and Mid-Height Displacement Time History for Test URM-2-3

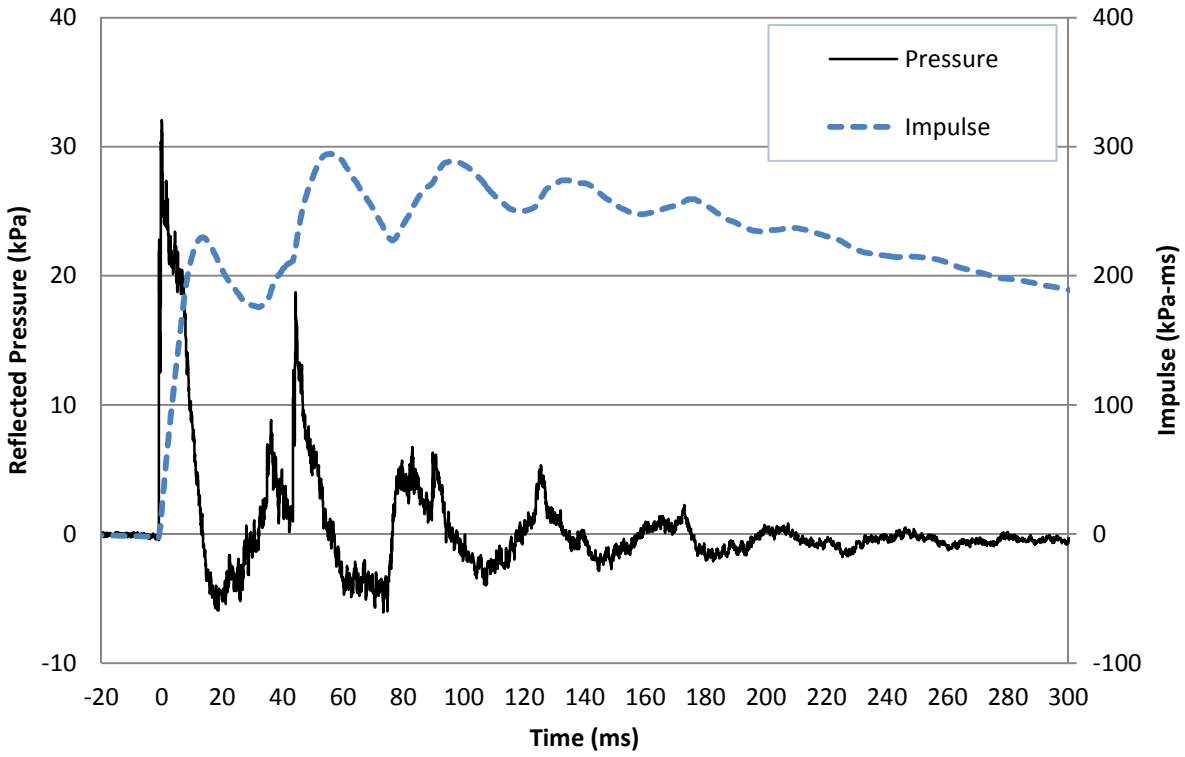

Figure 3.17: Reflected Pressure and Impulse Time History for Test URM-2-4

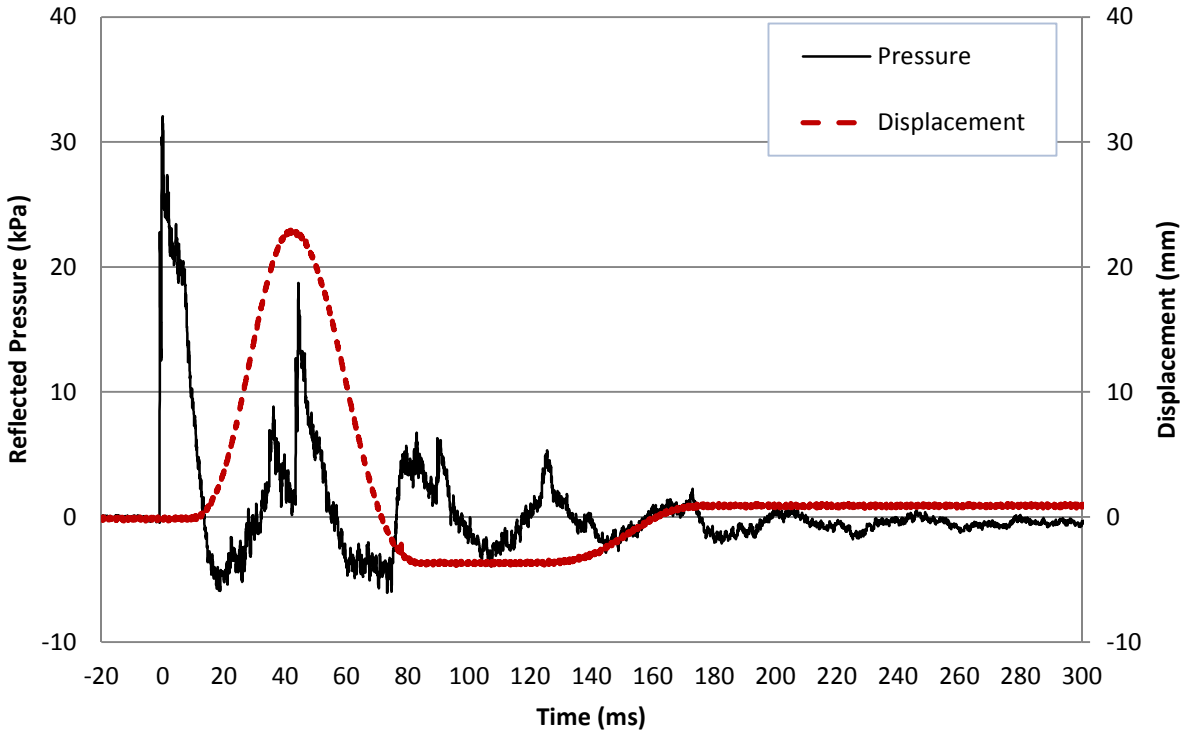

Figure 3.18: Reflected Pressure and Mid-Height Displacement Time History for Test URM-2-4

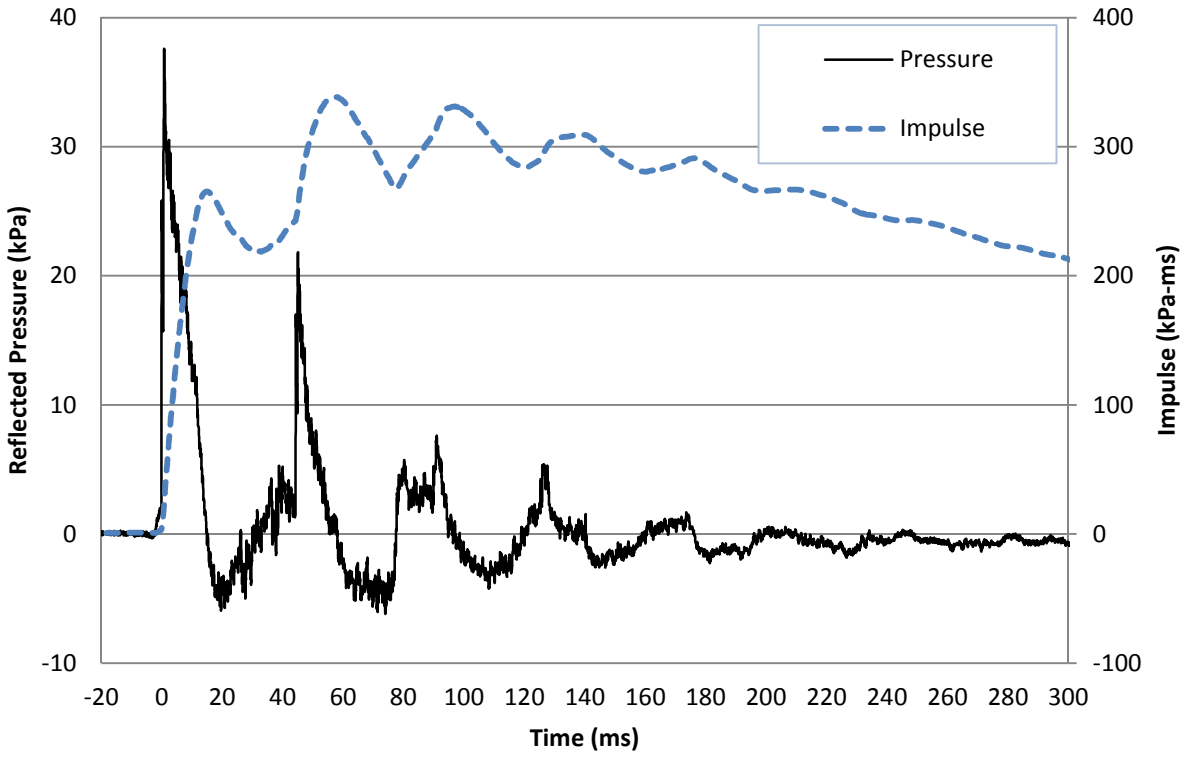

Figure 3.19: Reflected Pressure and Impulse Time History for Test URM-2-5

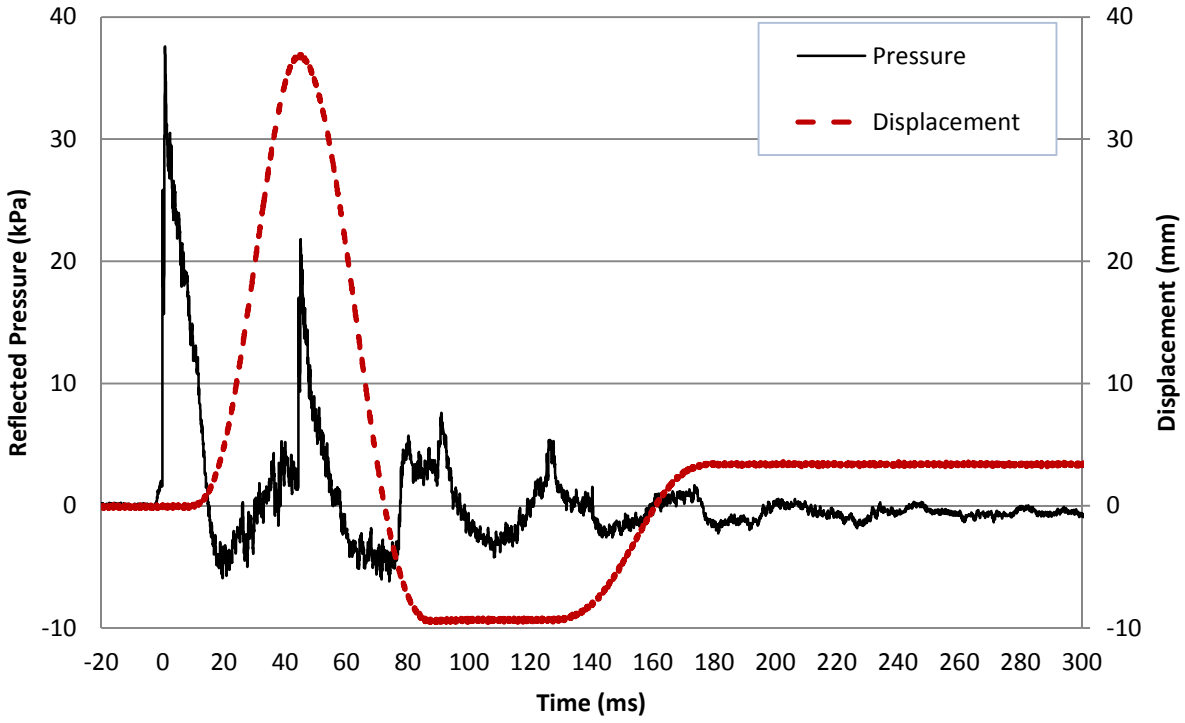

Figure 3.20: Reflected Pressure and Mid-Height Displacement Time History for Test URM-2-5

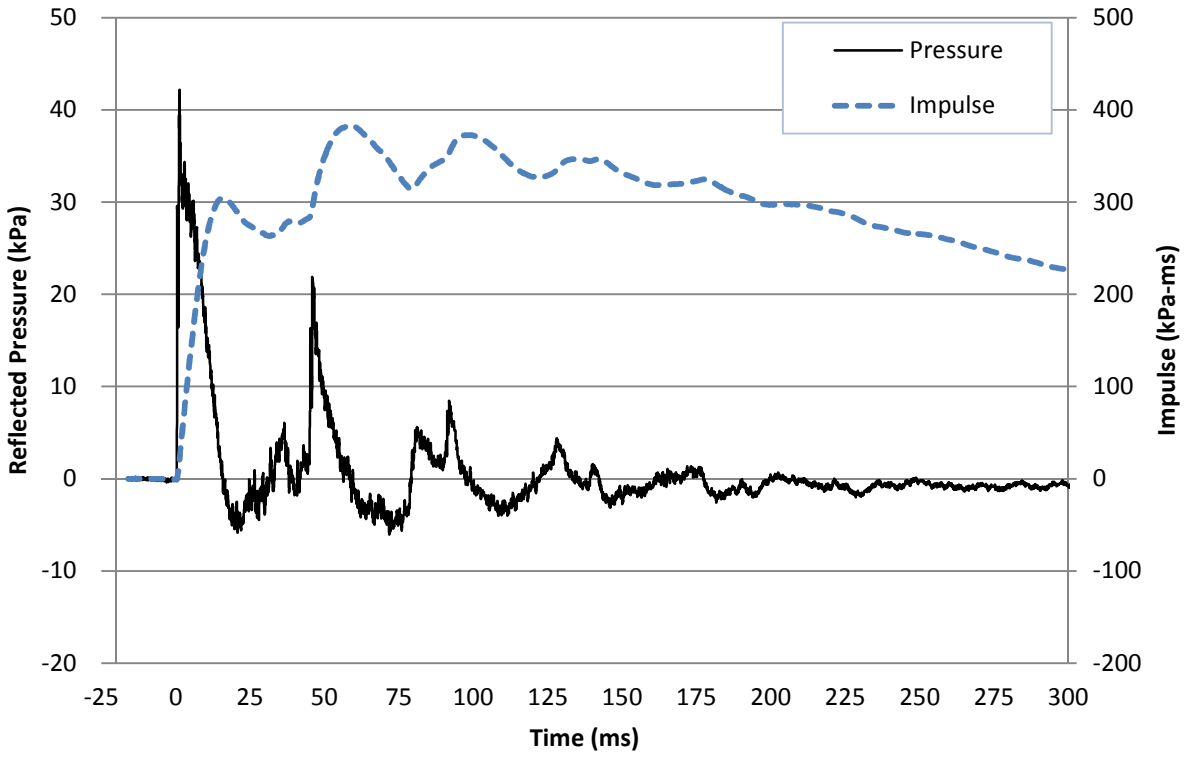

Figure 3.21: Reflected Pressure and Impulse Time History for Test URM-2-6

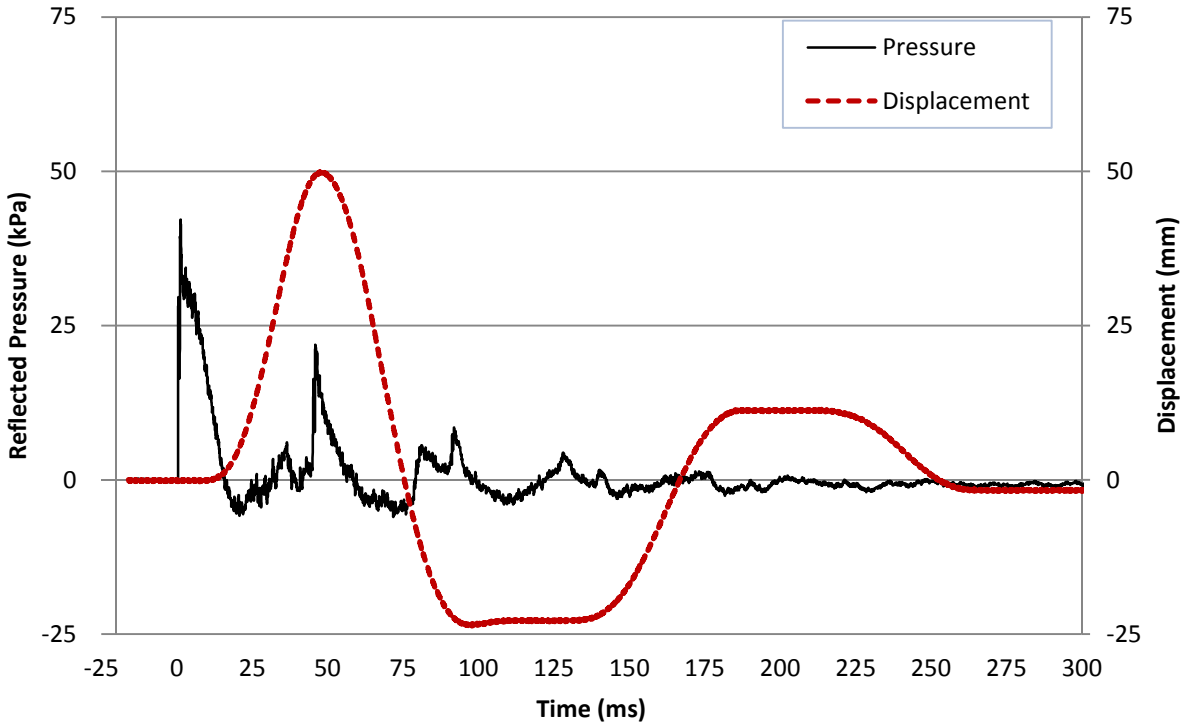

Figure 3.22: Reflected Pressure and Mid-Height Displacement Time History for Test URM-2-6

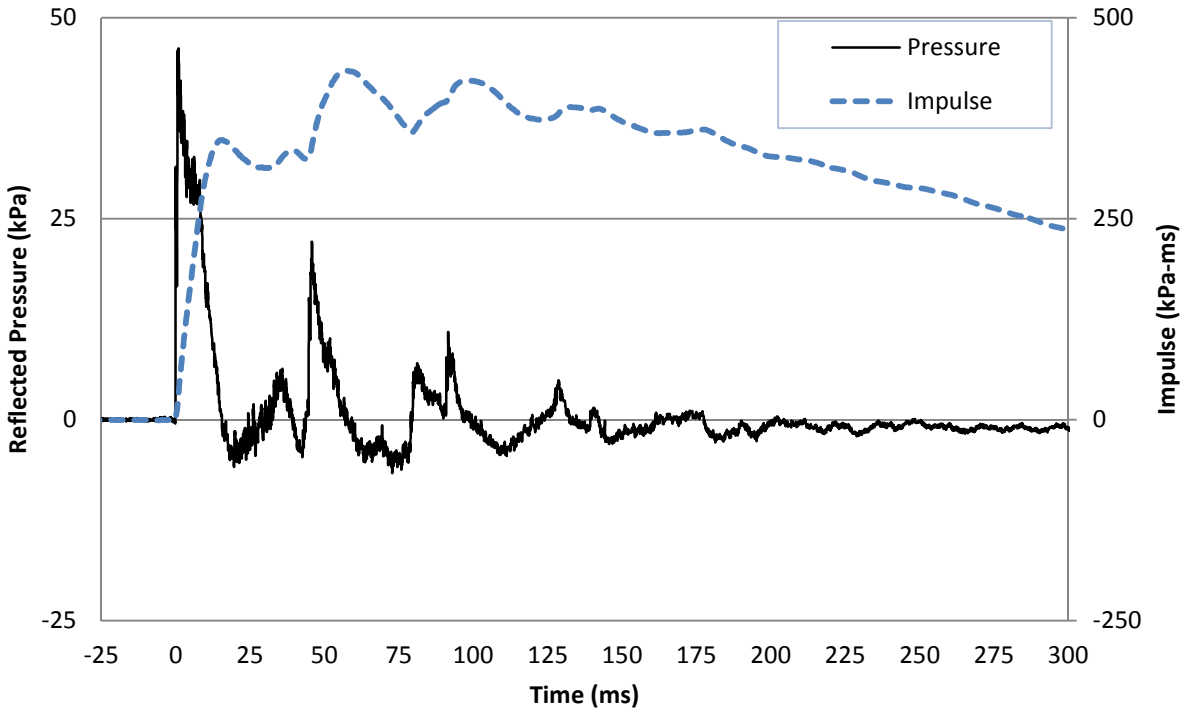

Figure 3.23: Reflected Pressure and Impulse Time History for Test URM-2-7

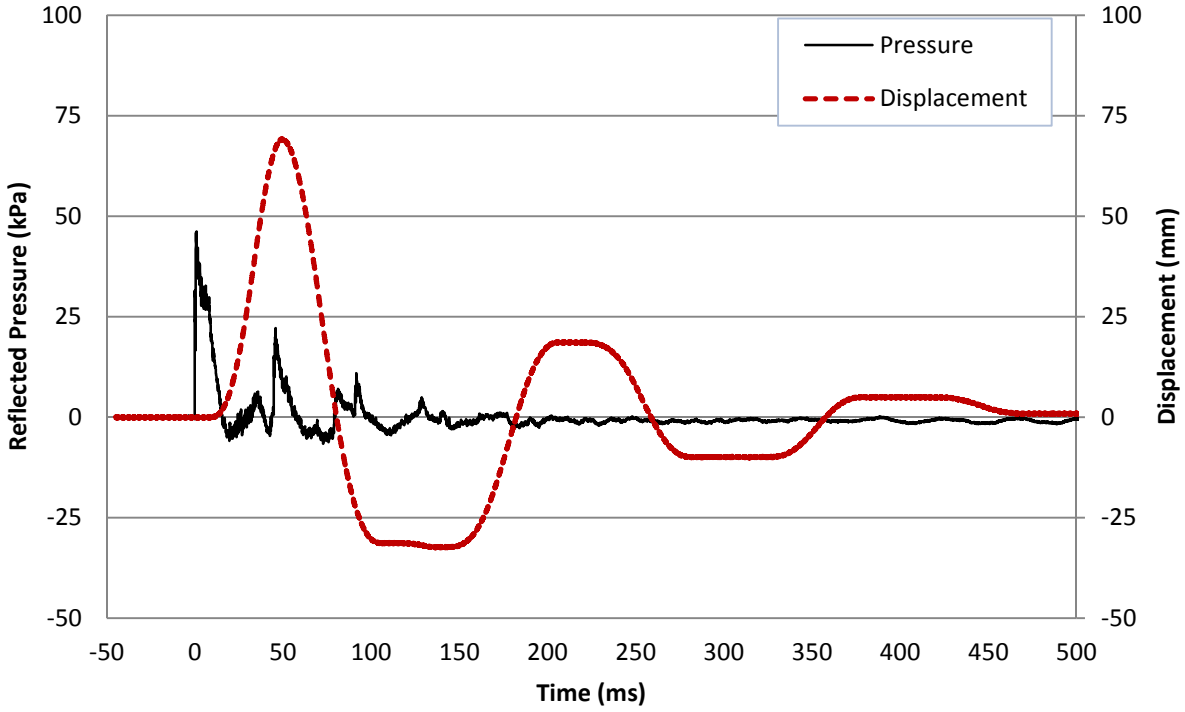

Figure 3.24: Reflected Pressure and Mid-Height Displacement Time History for Test URM-2-7

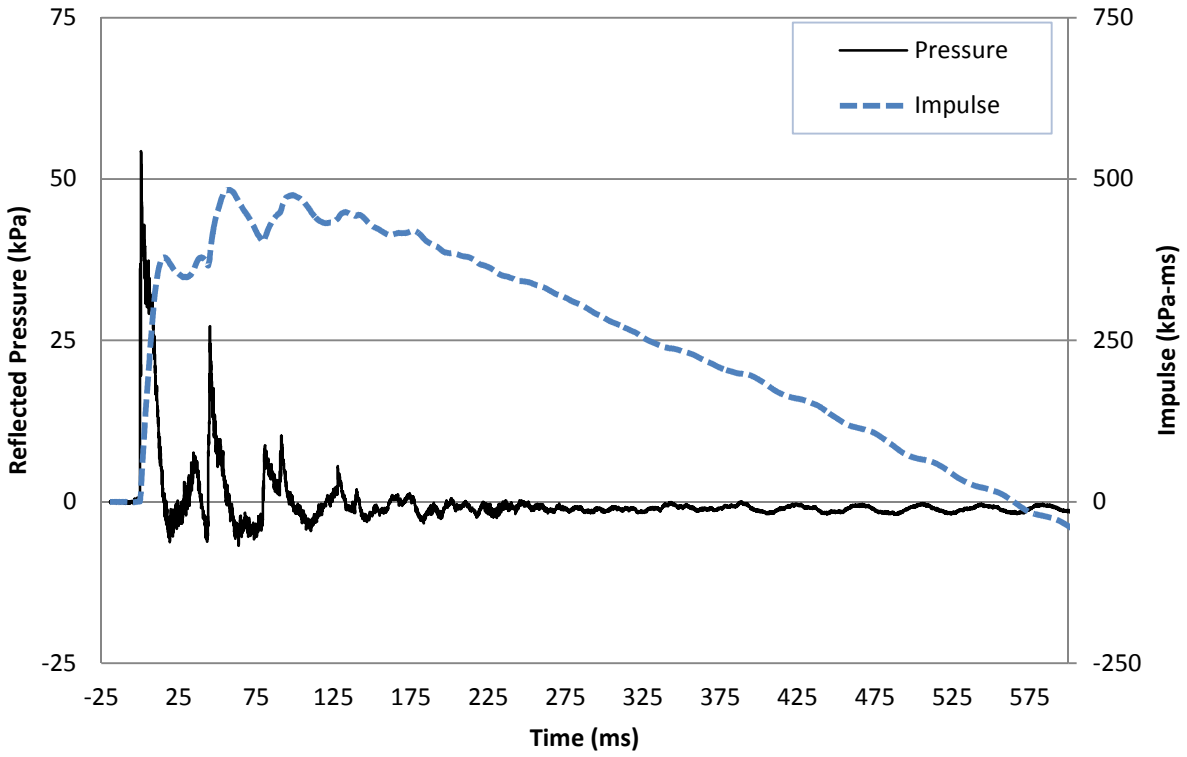

Figure 3.25: Reflected Pressure and Impulse Time History for Test URM-2-8

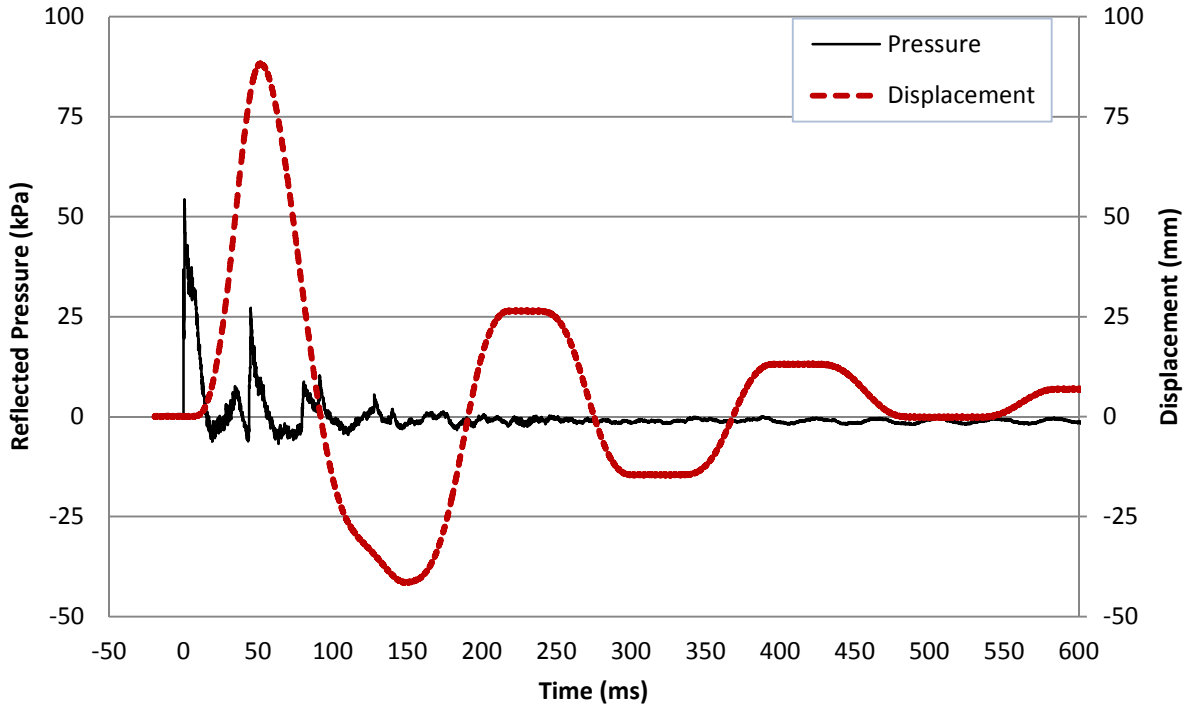

Figure 3.26: Reflected Pressure and Mid-Height Displacement Time History for Test URM-2-8

a)  b) 

Figure 3.27: Retrofitted Infill Wall URM-2; a) After Shot 8; b) Delamination Observed after Shot 8

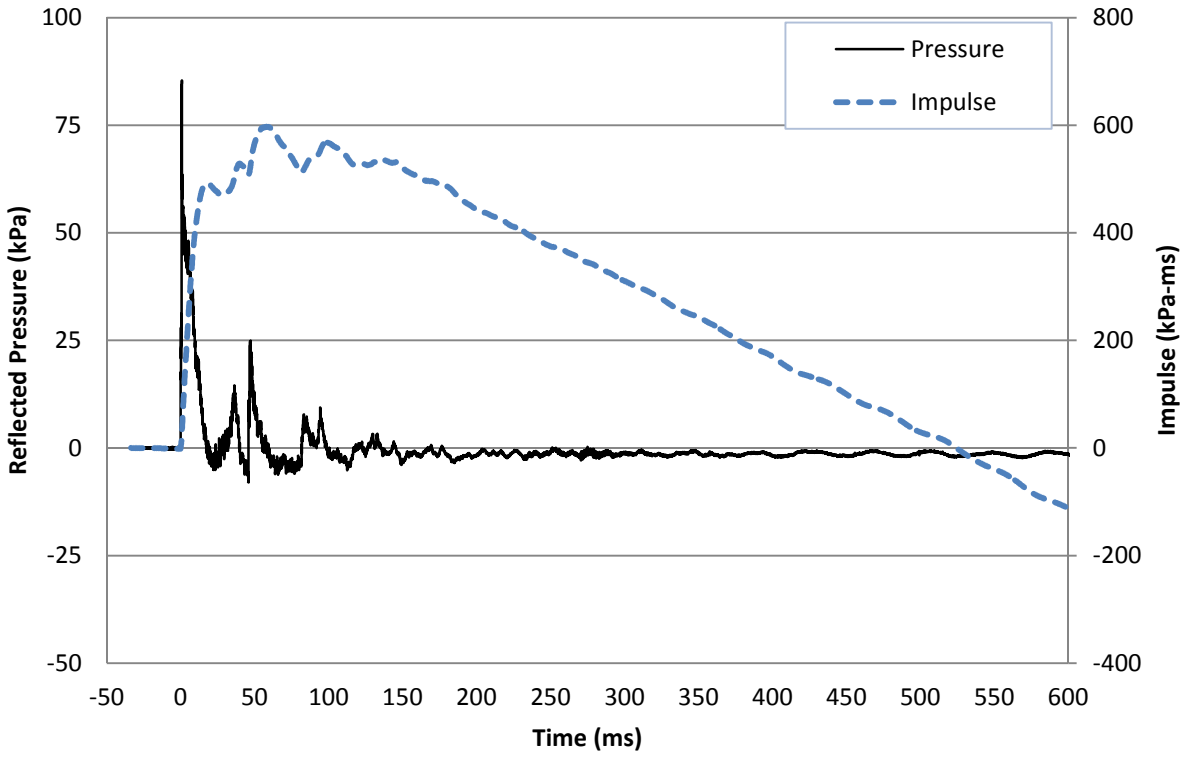

Figure 3.28: Reflected Pressure and Impulse Time History for Test URM-2-9

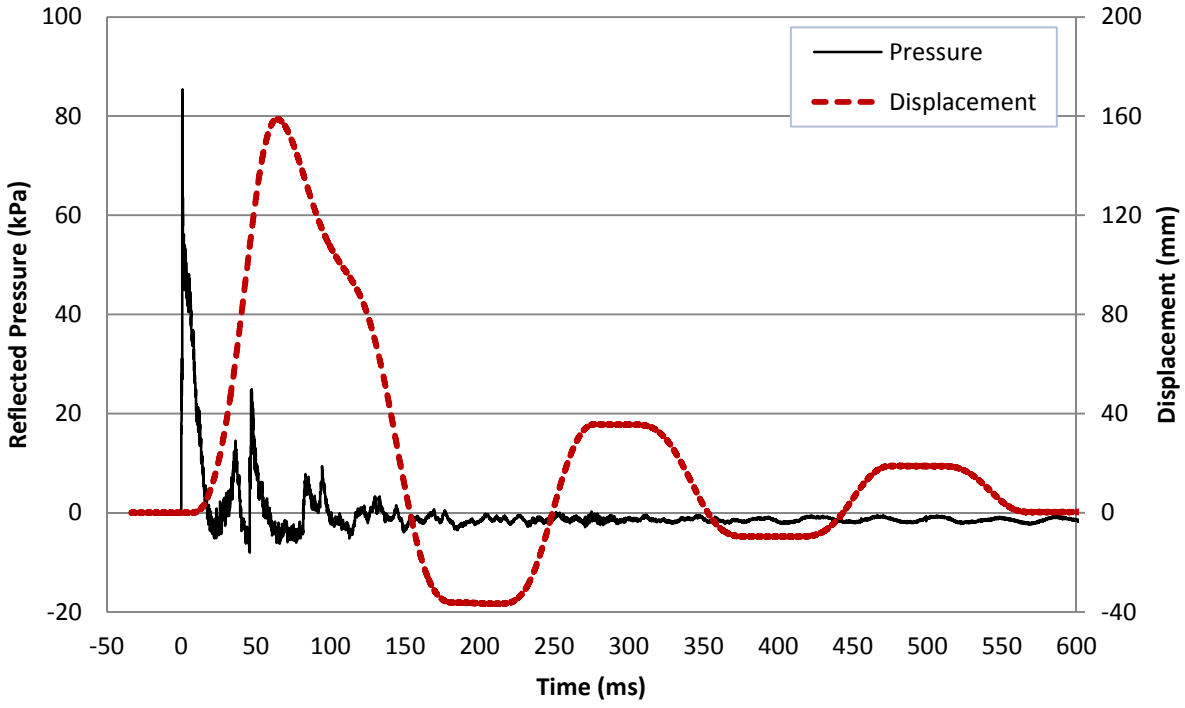

Figure 3.29: Reflected Pressure and Mid-Height Displacement Time History for Test URM-2-9

Figure 3.30: Retrofitted Infill Wall URM-2 after Shot 9: a) Local Failure Involving a Small Tear in Polyurea Membrane; b) Marked Location of Tear in Polyurea; c) Debonding at the Supports; d) Extensive Debonding at Mid-Height

a) 

b) 

c) 

d) 

Figure 3.31: Retrofitted Infill Wall URM-2 after Shot 10: a) Extended Tear in Polyurea; b) Compression Face of the Wall; c) Extended Debonding at Supports; d) Scattered Debris after Global Failure of Specimen

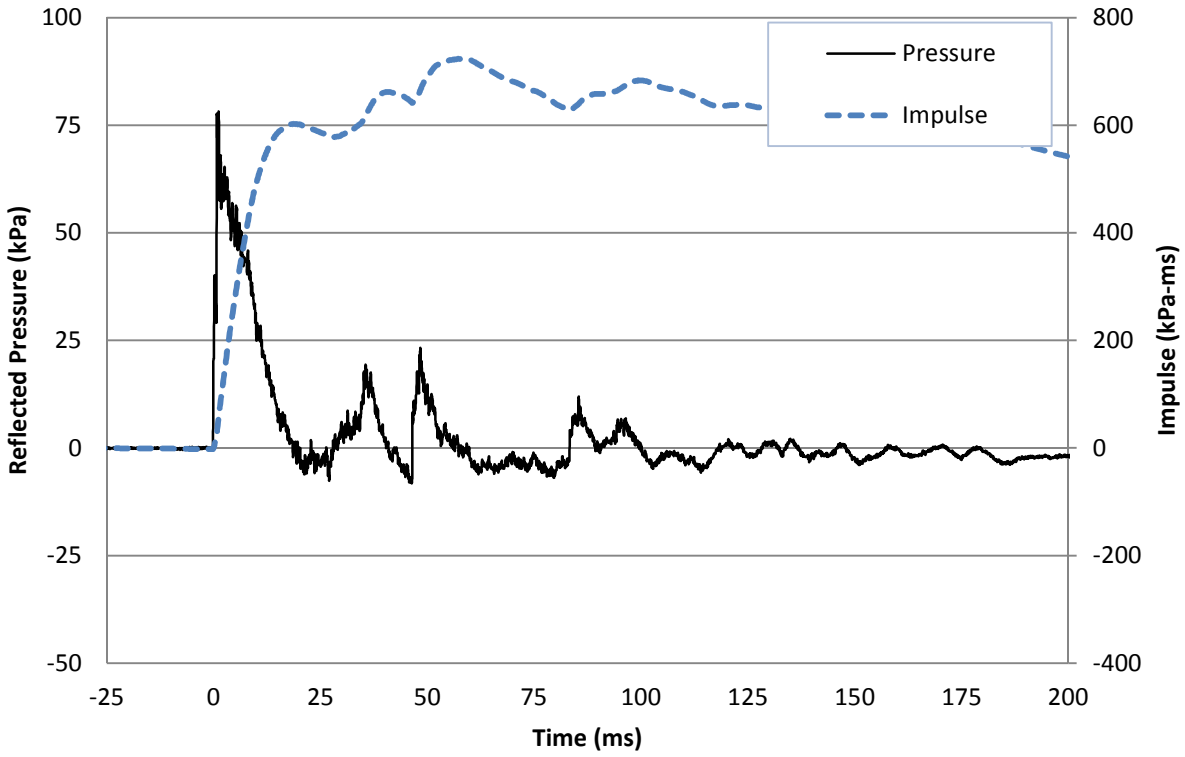

Figure 3.32: Reflected Pressure and Impulse Time History for Test URM-2-10

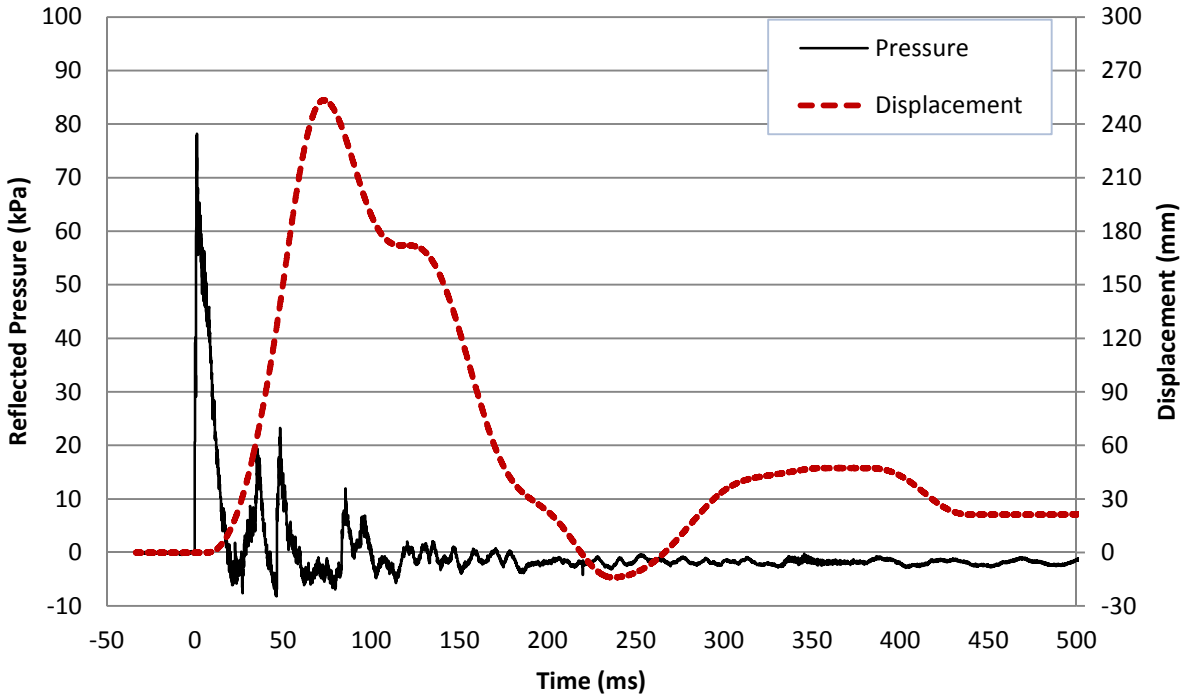

Figure 3.33: Reflected Pressure and Mid-Height Displacement Time History for Test URM-2-10

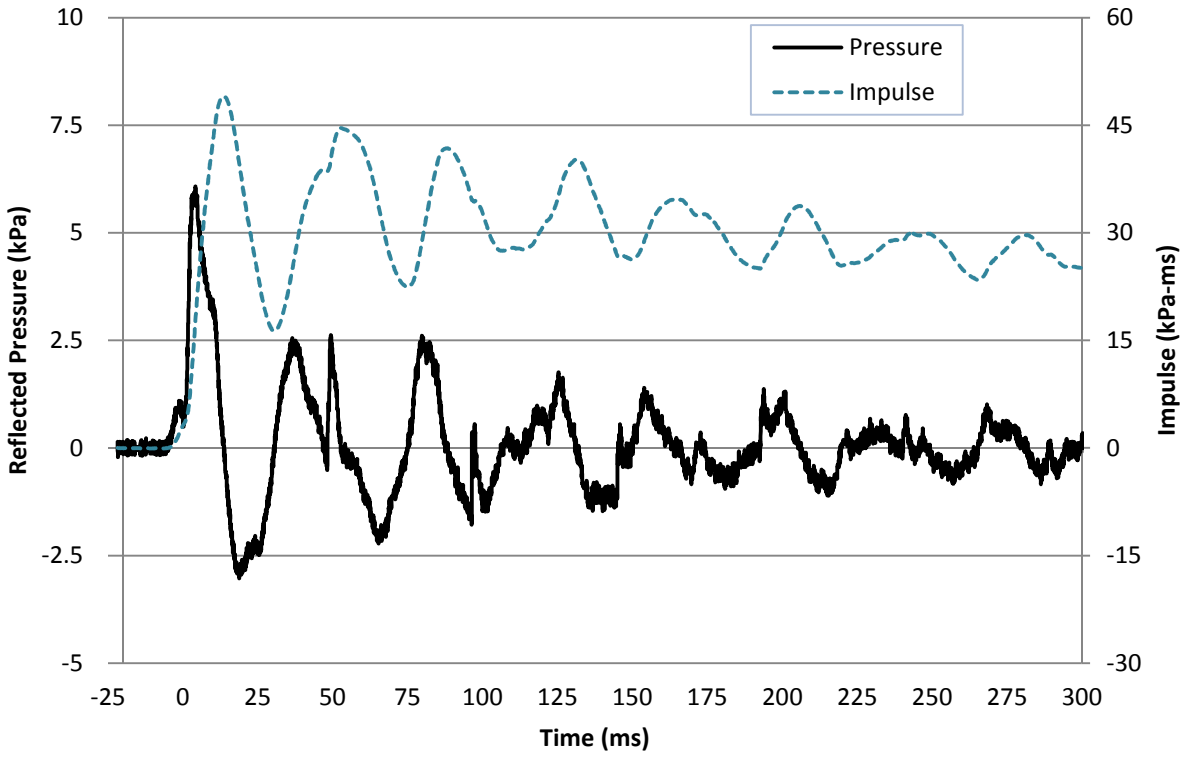

Figure 3.34: Reflected Pressure and Impulse Time History for Test URM-3-1

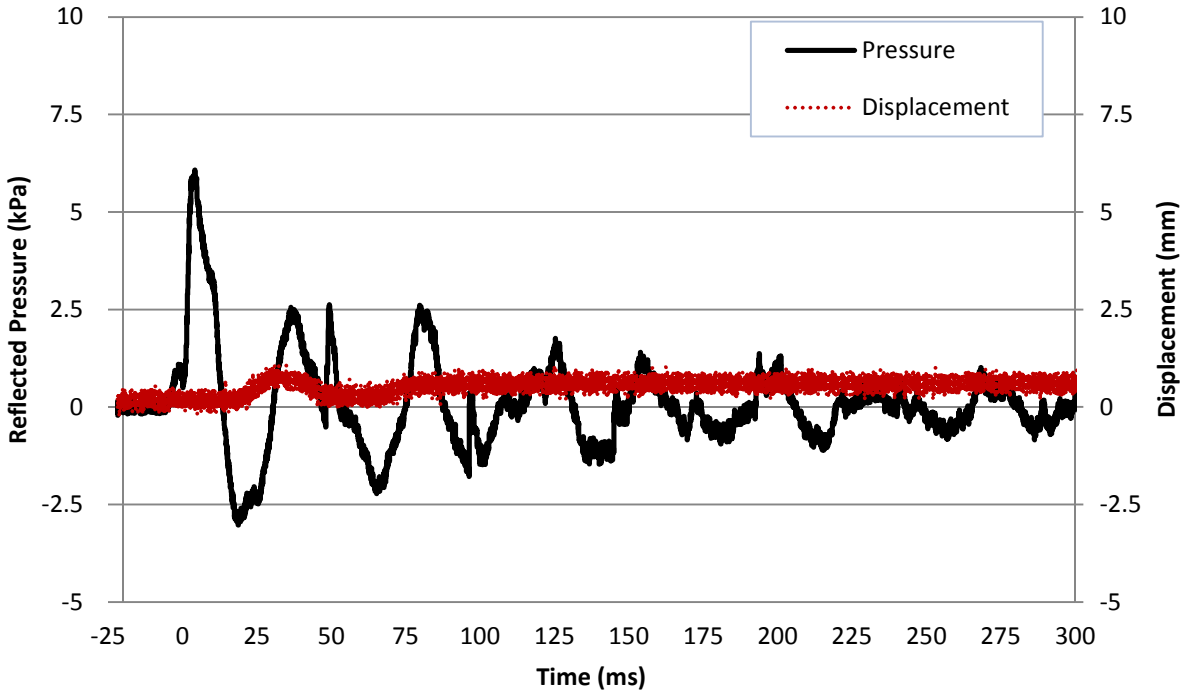

Figure 3.35: Reflected Pressure and Mid-Height Displacement Time History for Test URM-3-1

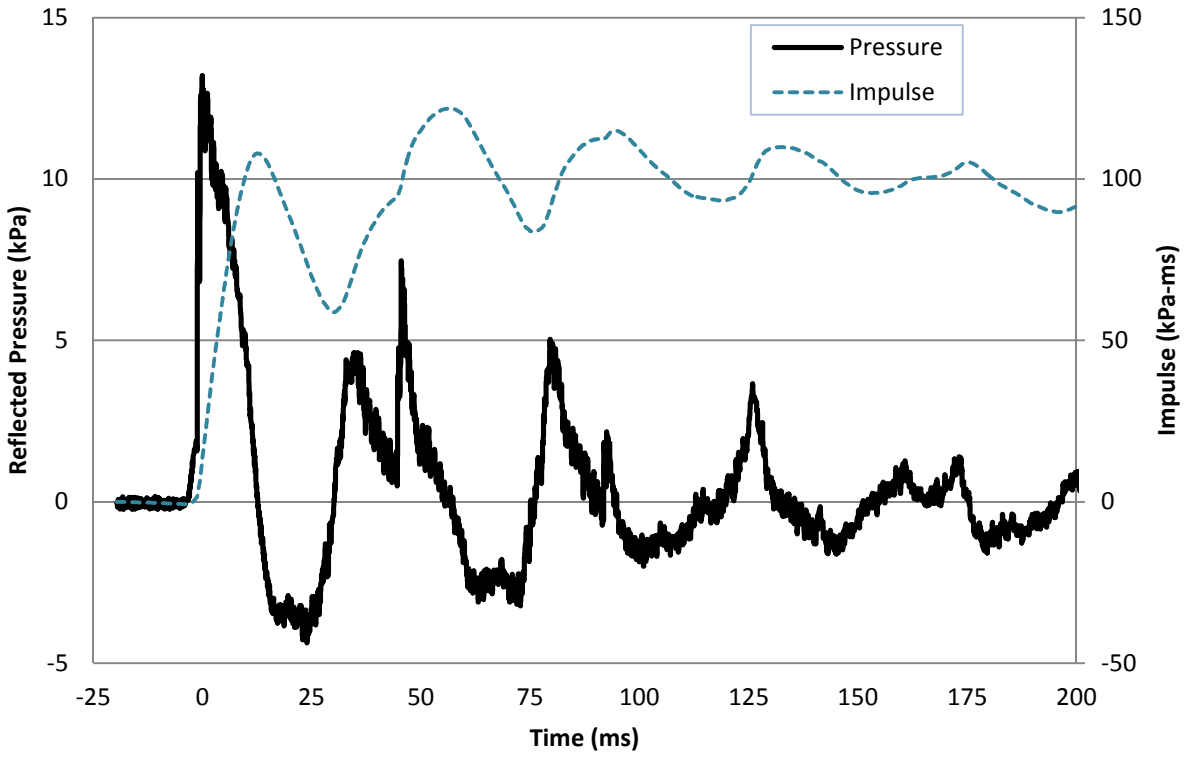

Figure 3.36: Reflected Pressure and Impulse Time History for Test URM-3-2

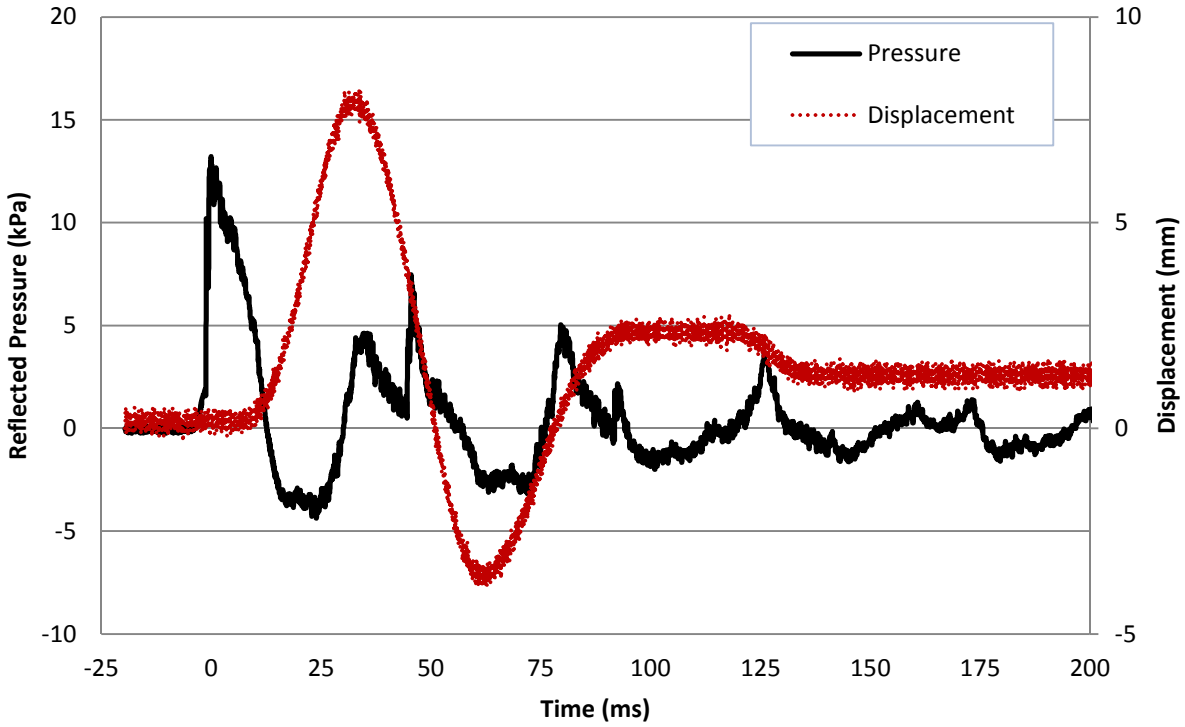

Figure 3.37: Reflected Pressure and Mid-Height Displacement Time History for Test URM-3-2

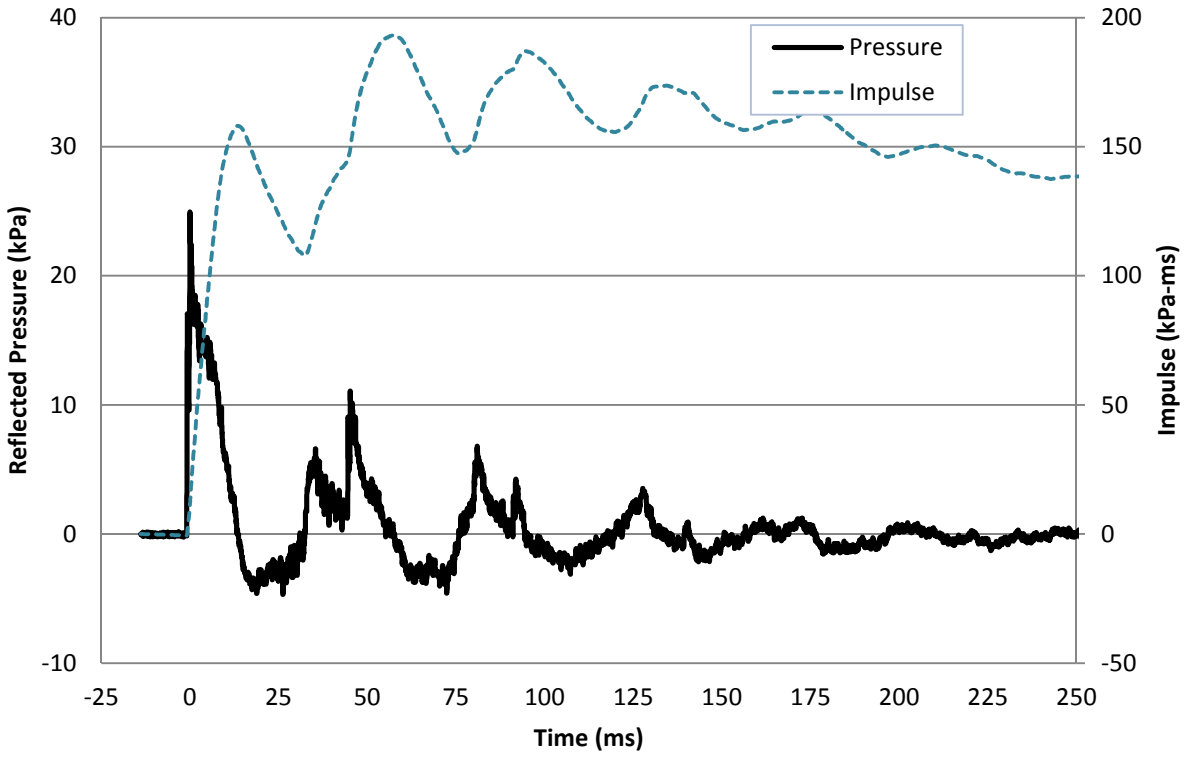

Figure 3.38: Reflected Pressure and Impulse Time History for Test URM-3-3

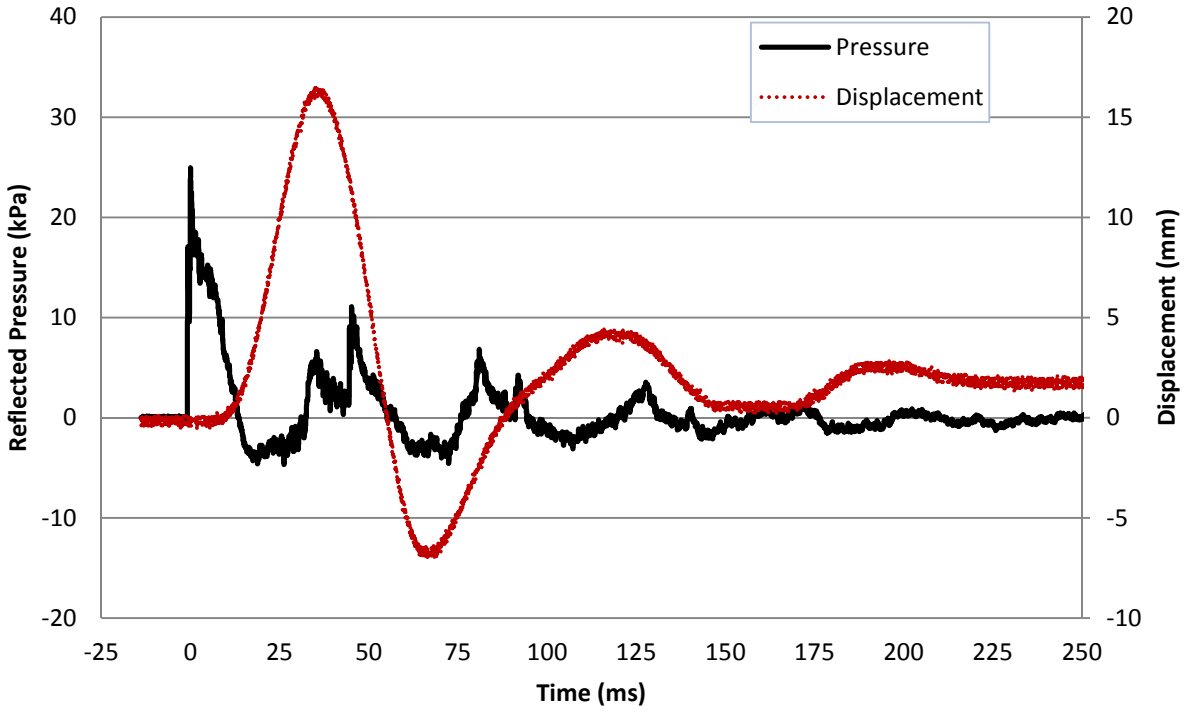

Figure 3.39: Reflected Pressure and Mid-Height Displacement Time History for Test URM-3-3

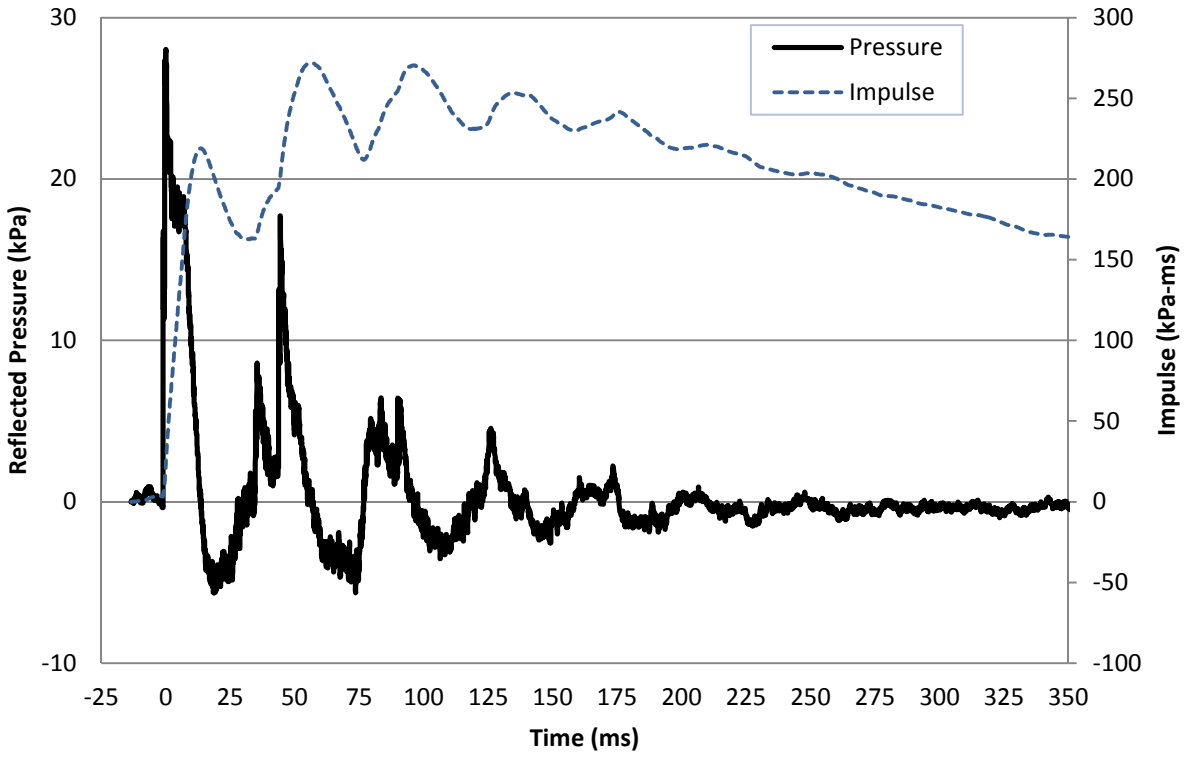

Figure 3.40: Reflected Pressure and Impulse Time History for Test URM-3-4

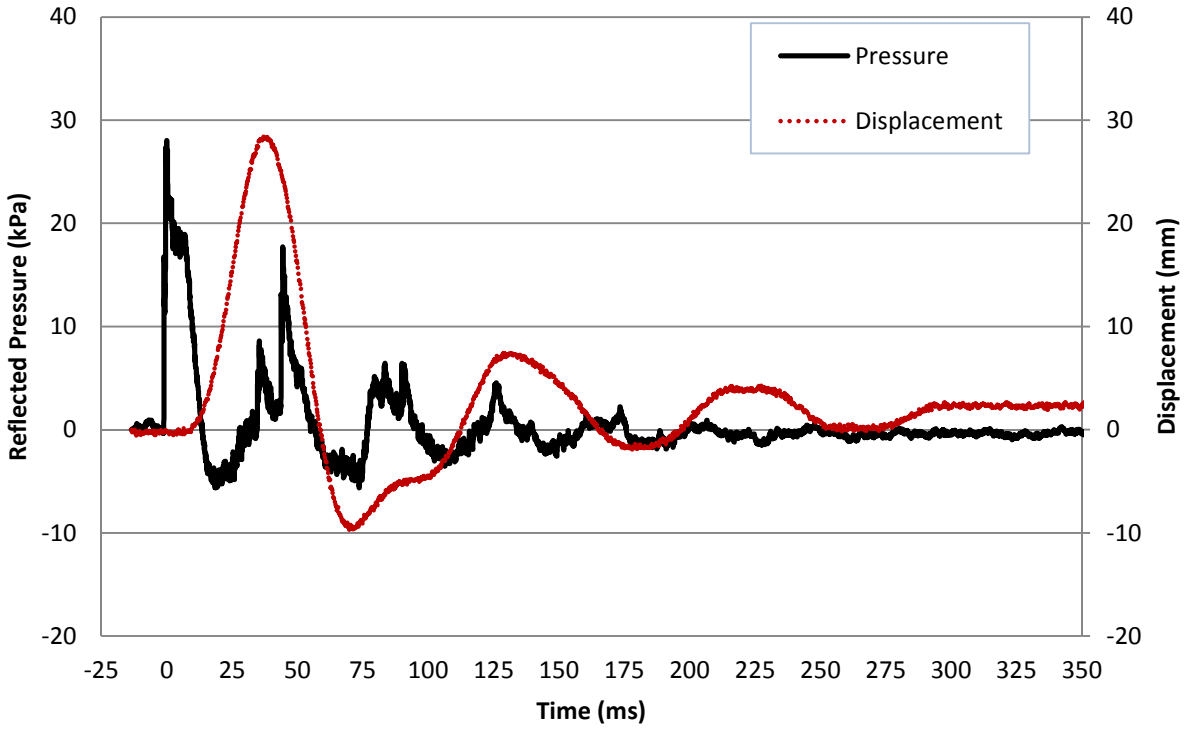

Figure 3.41: Reflected Pressure and Mid-Height Displacement Time History for Test URM-3-4

a)

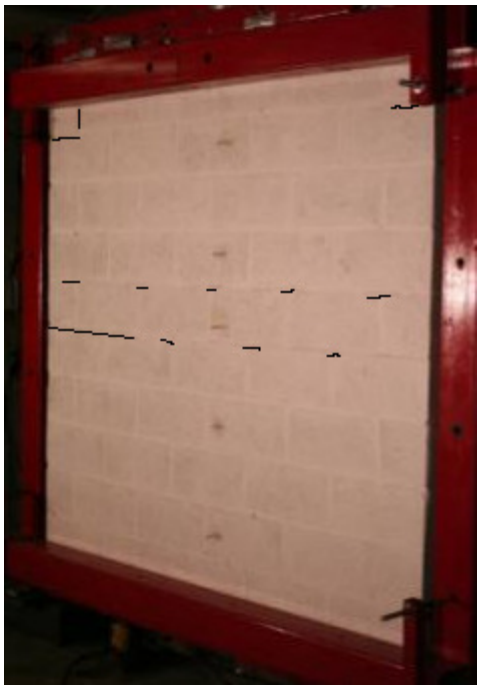

b)

c)

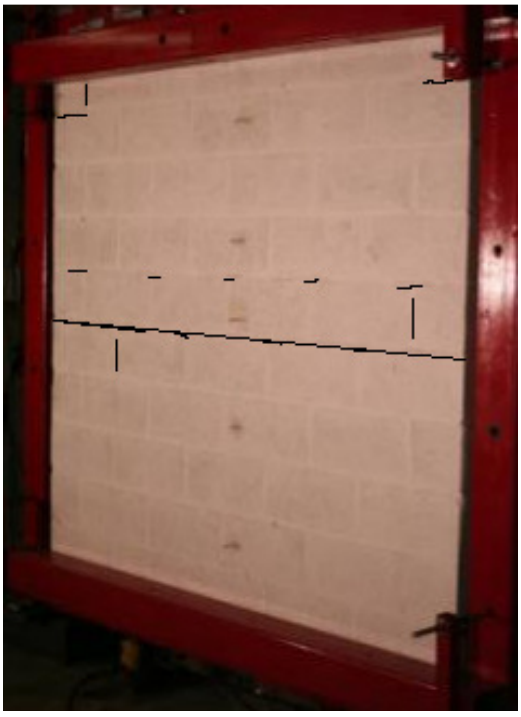

d)

Figure 3.42: Load-Bearing Wall URM-3: a) After Shot 4; b) After Shot 4- Failure of Top Left Concrete Masonry Unit; c) After Shot 5- Extended Crack Pattern; d) After Shot 7- Global Collapse

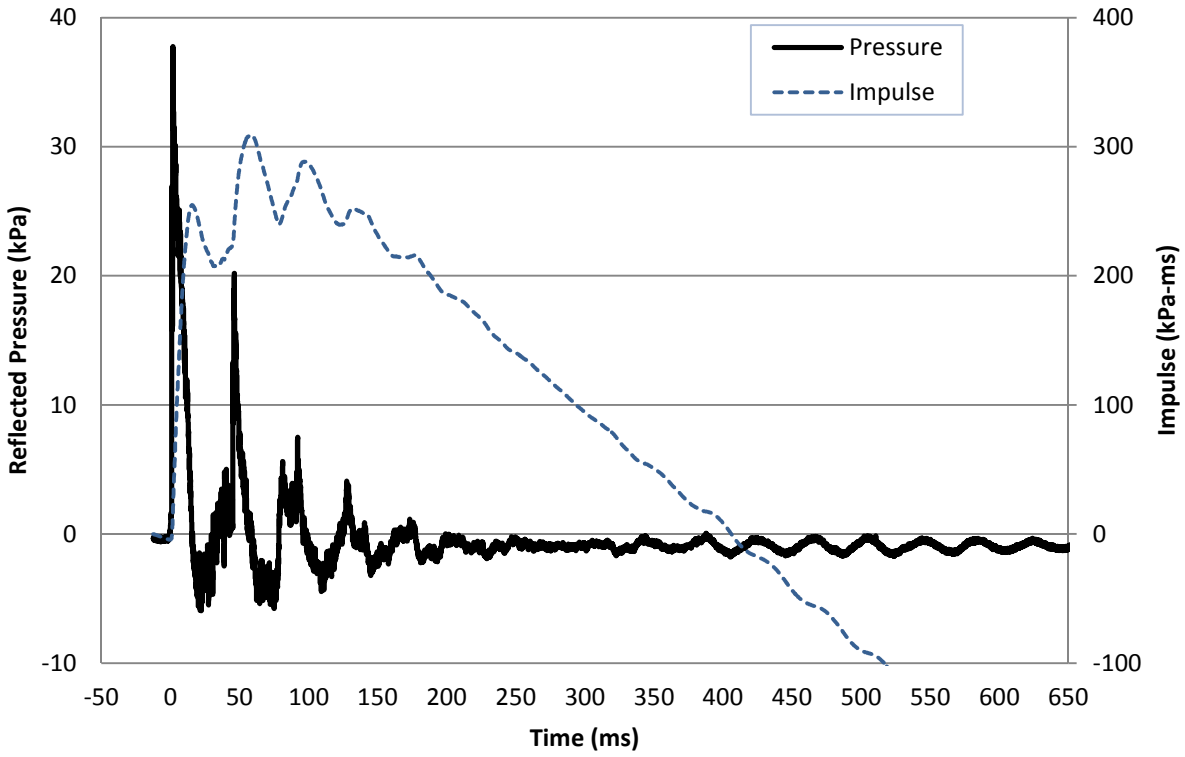

Figure 3.43: Reflected Pressure and Impulse Time History for Test URM-3-5

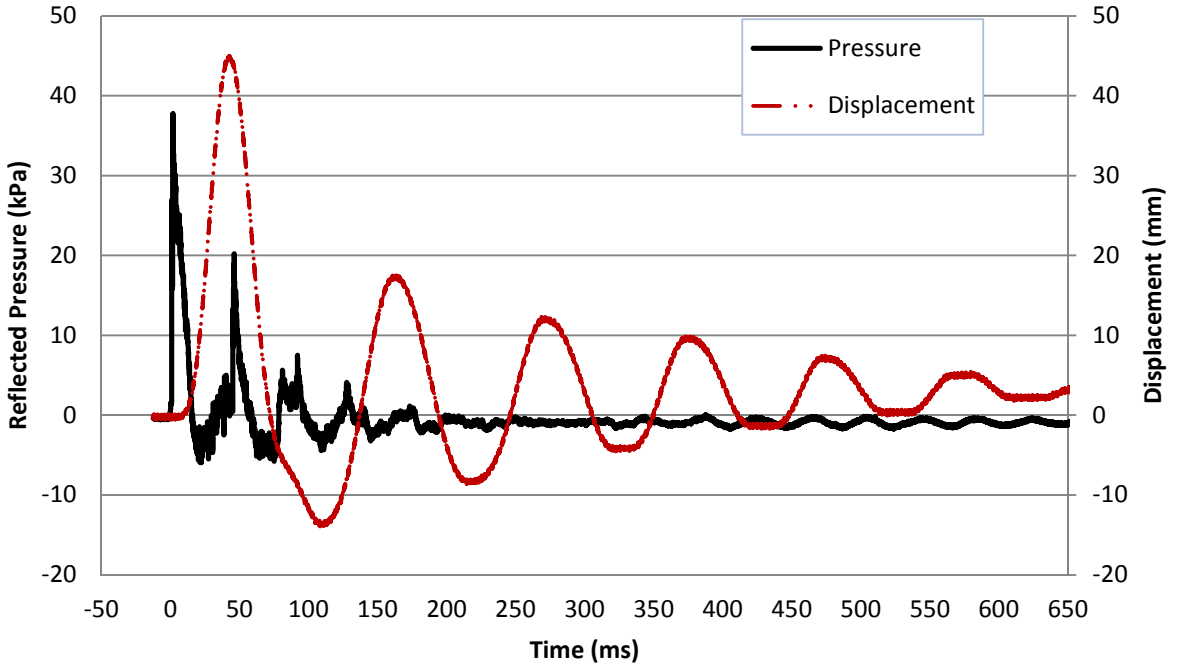

Figure 3.44: Reflected Pressure and Mid-Height Displacement Time History for Test URM-3-5

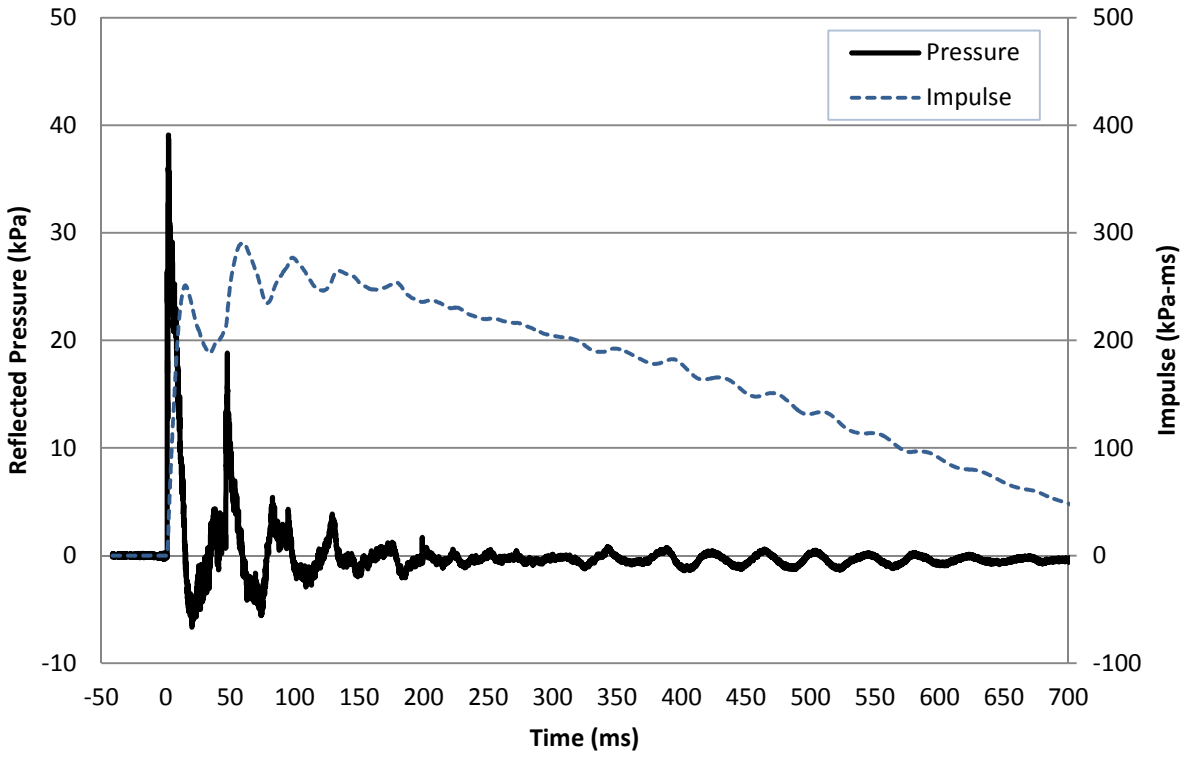

Figure 3.45: Reflected Pressure and Impulse Time History for Test URM-3-6

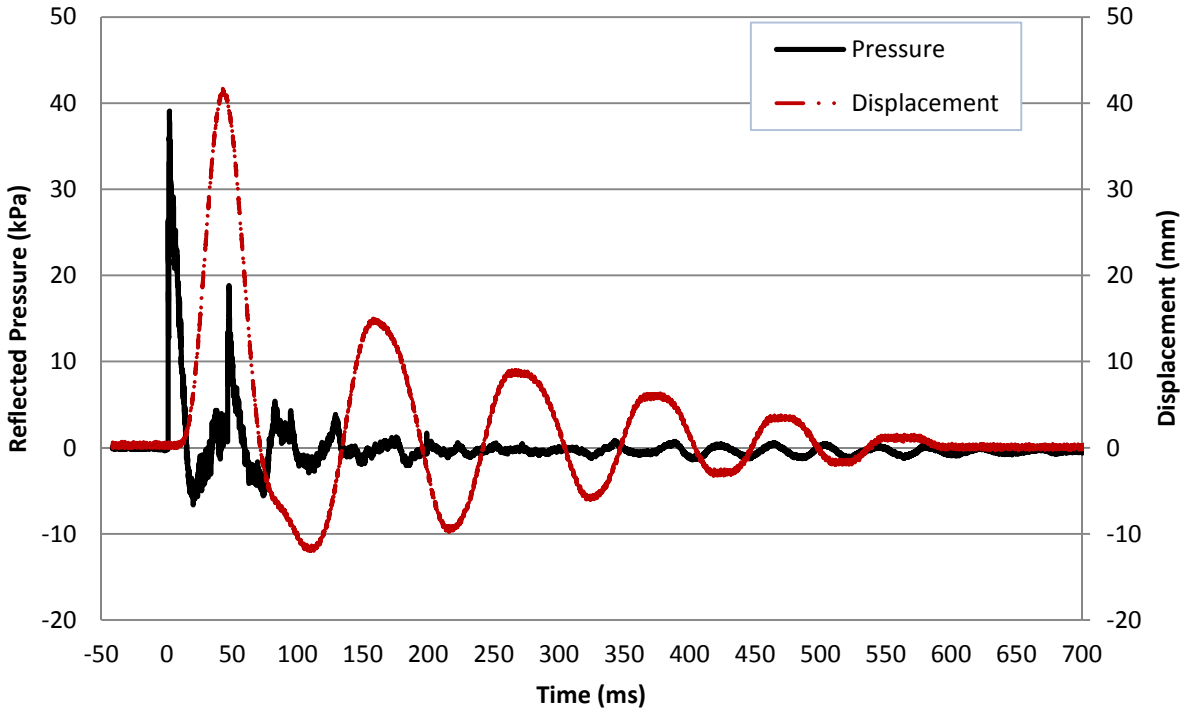

Figure 3.46: Reflected Pressure and Mid-Height Displacement Time History for Test URM-3-6

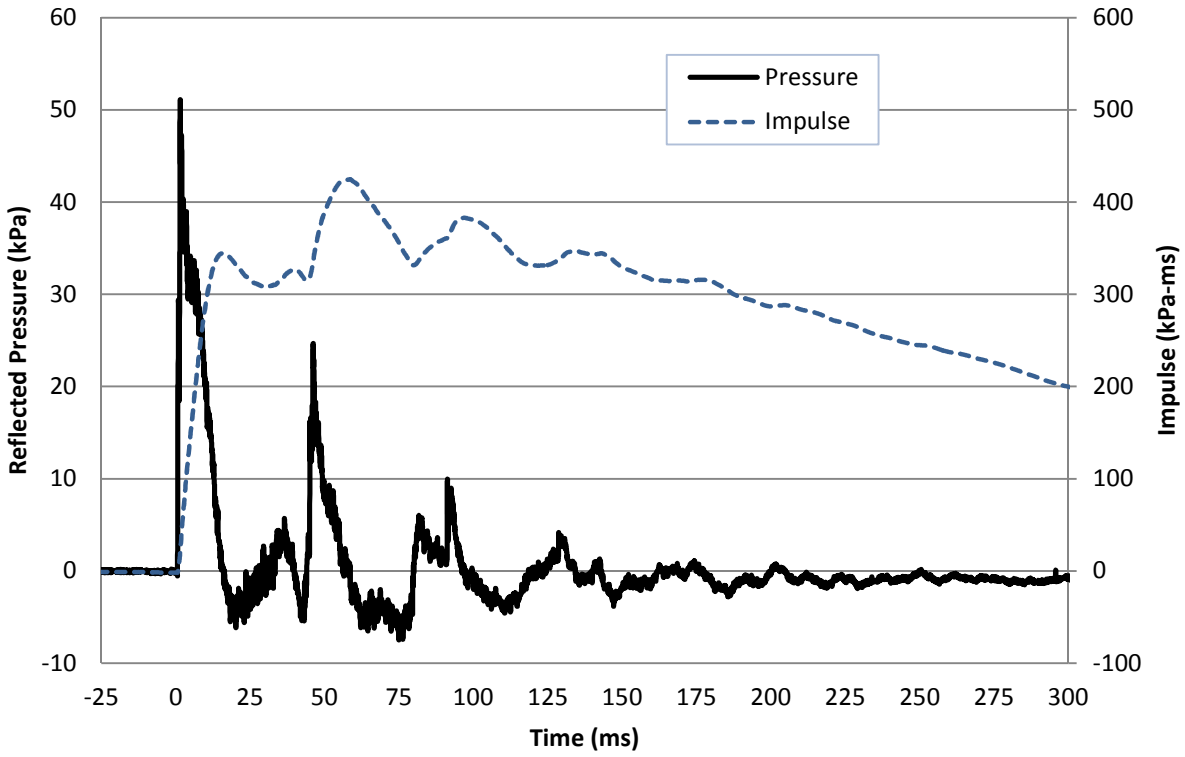

Figure 3.47: Reflected Pressure and Impulse Time History for Test URM-3-7

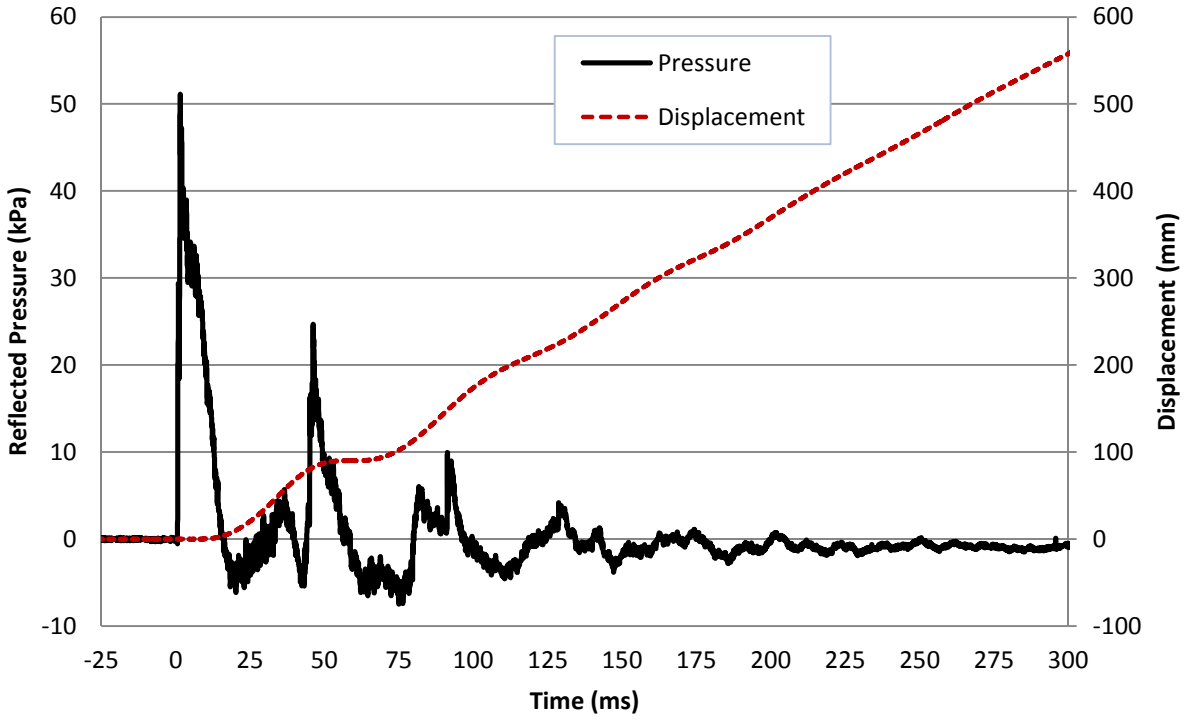

Figure 3.48: Reflected Pressure and Mid-Height Displacement Time History for Test URM-3-7

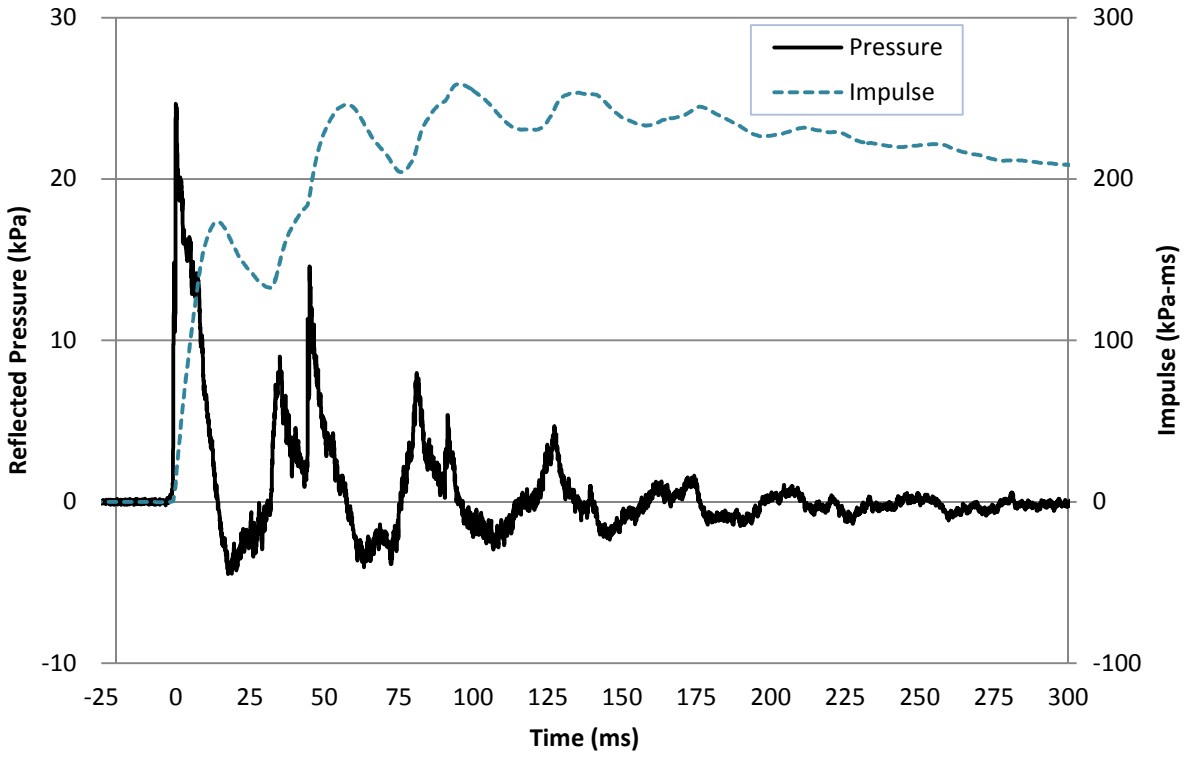

Figure 3.49: Reflected Pressure and Impulse Time History for Test URM-4-1

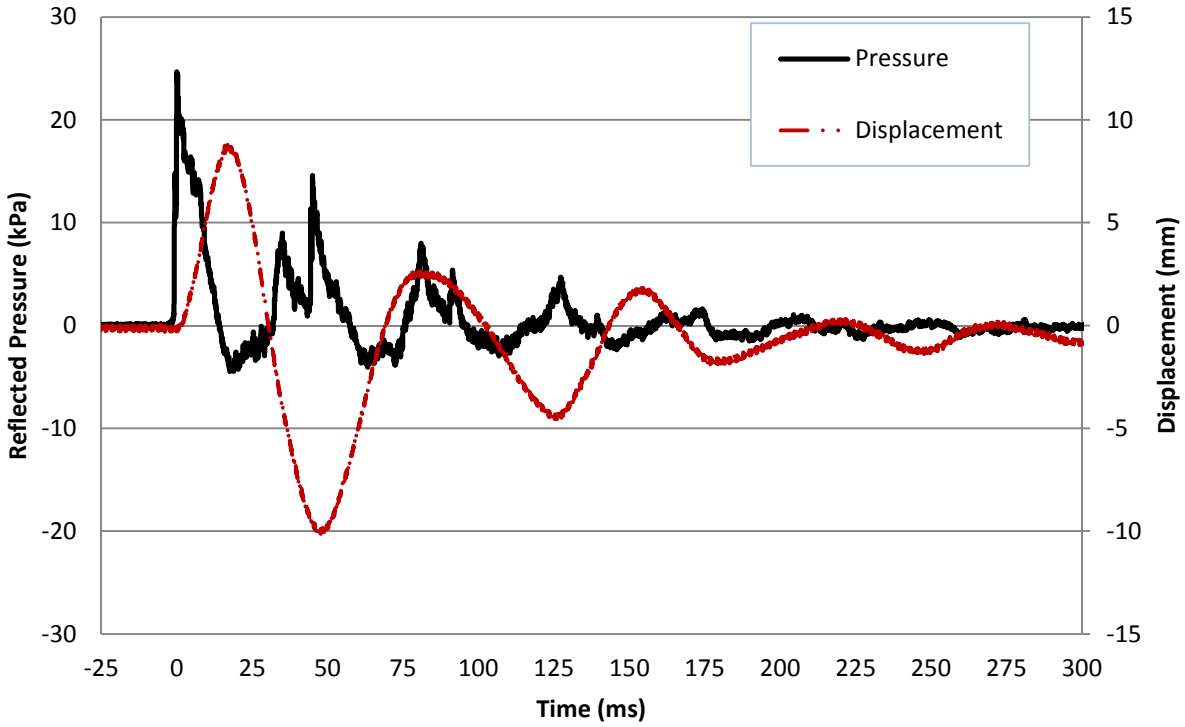

Figure 3.50: Reflected Pressure and Mid-Height Displacement Time History for Test URM-4-1

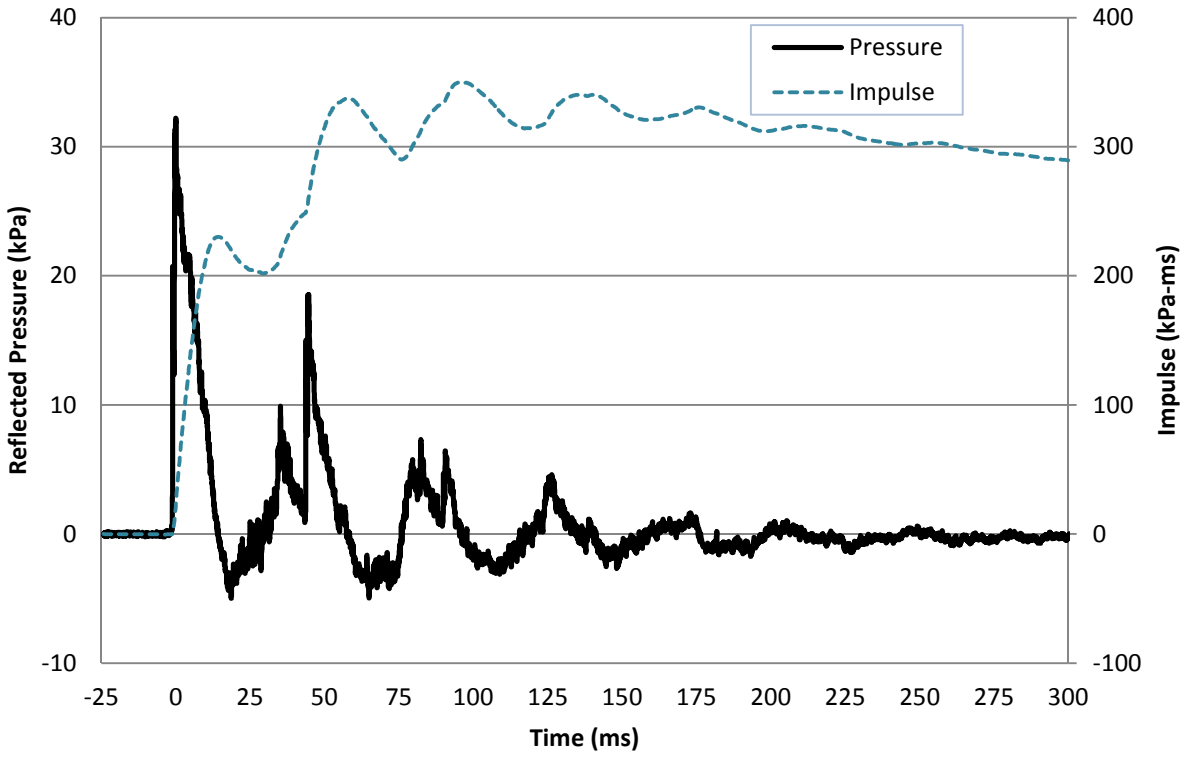

Figure 3.51: Reflected Pressure and Impulse Time History for Test URM-4-2

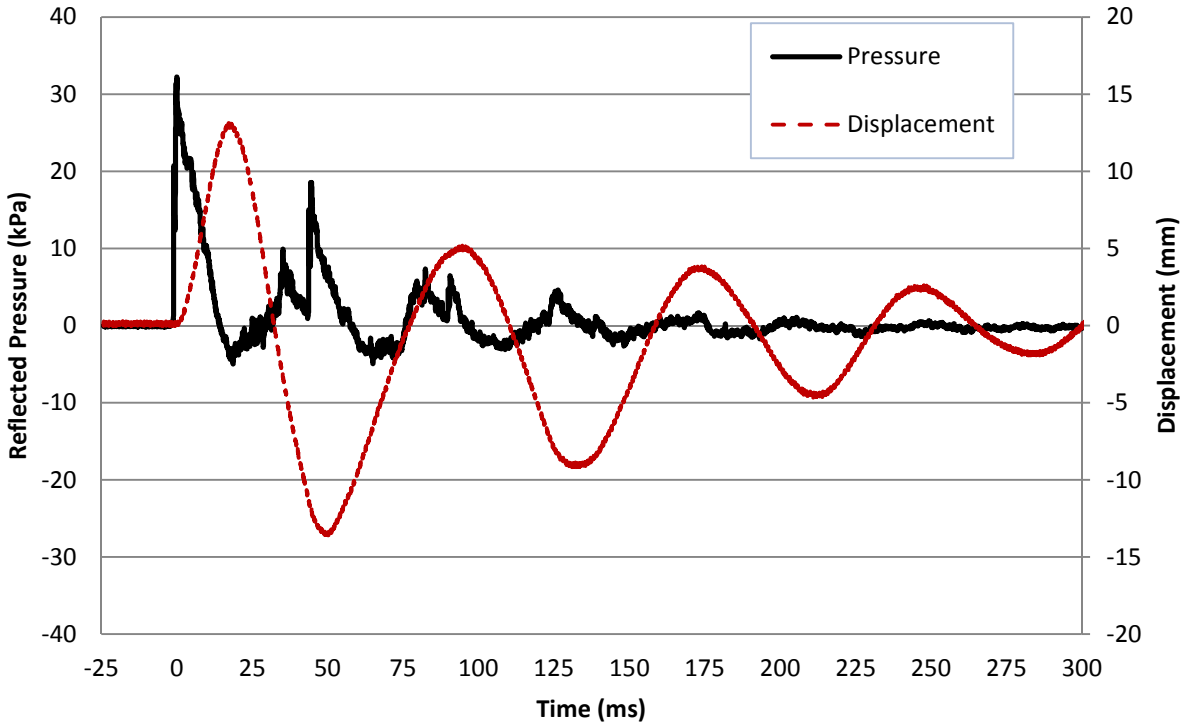

Figure 3.52: Reflected Pressure and Mid-Height Displacement Time History for Test URM-4-2

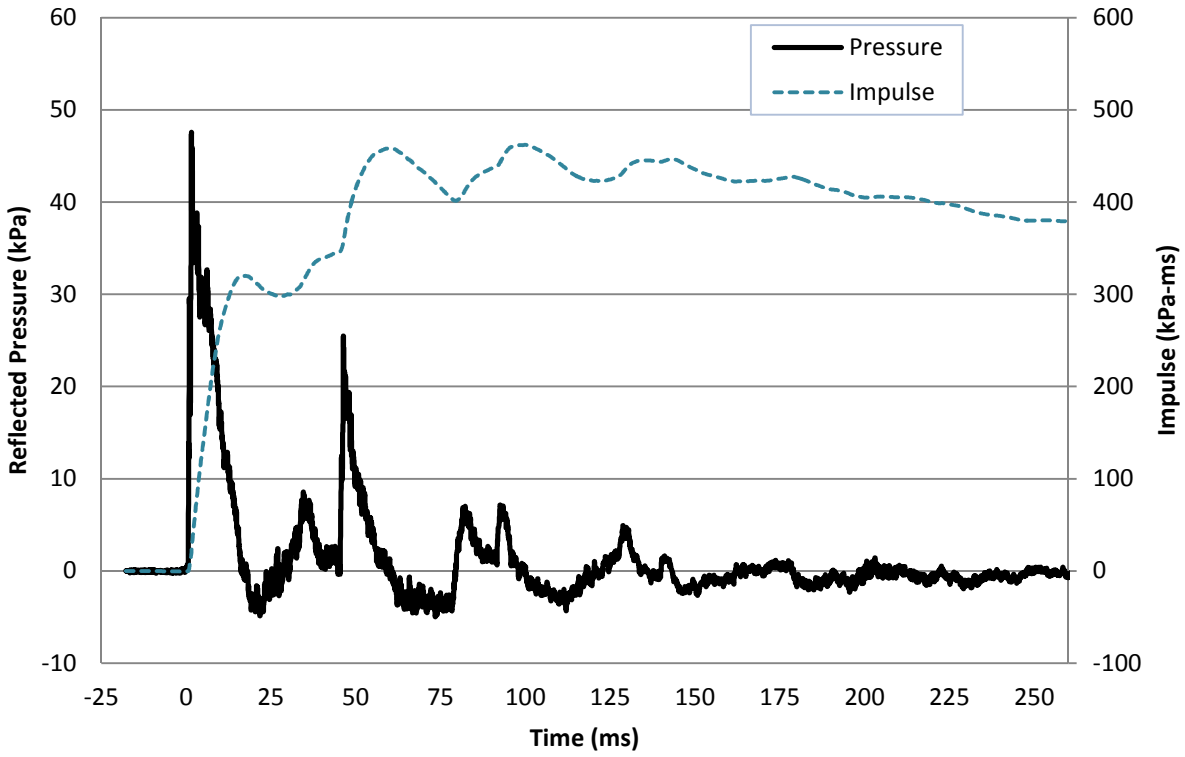

Figure 3.53: Reflected Pressure and Impulse Time History for Test URM-4-3

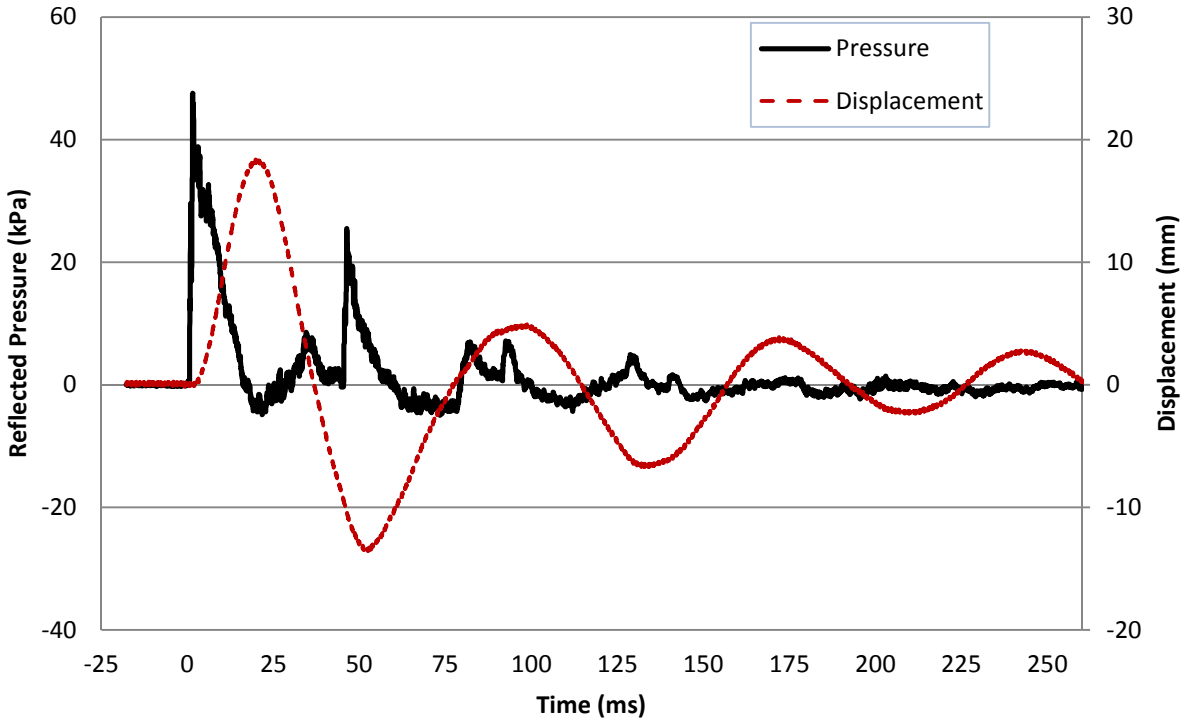

Figure 3.54: Reflected Pressure and Mid-Height Displacement Time History for Test URM-4-3

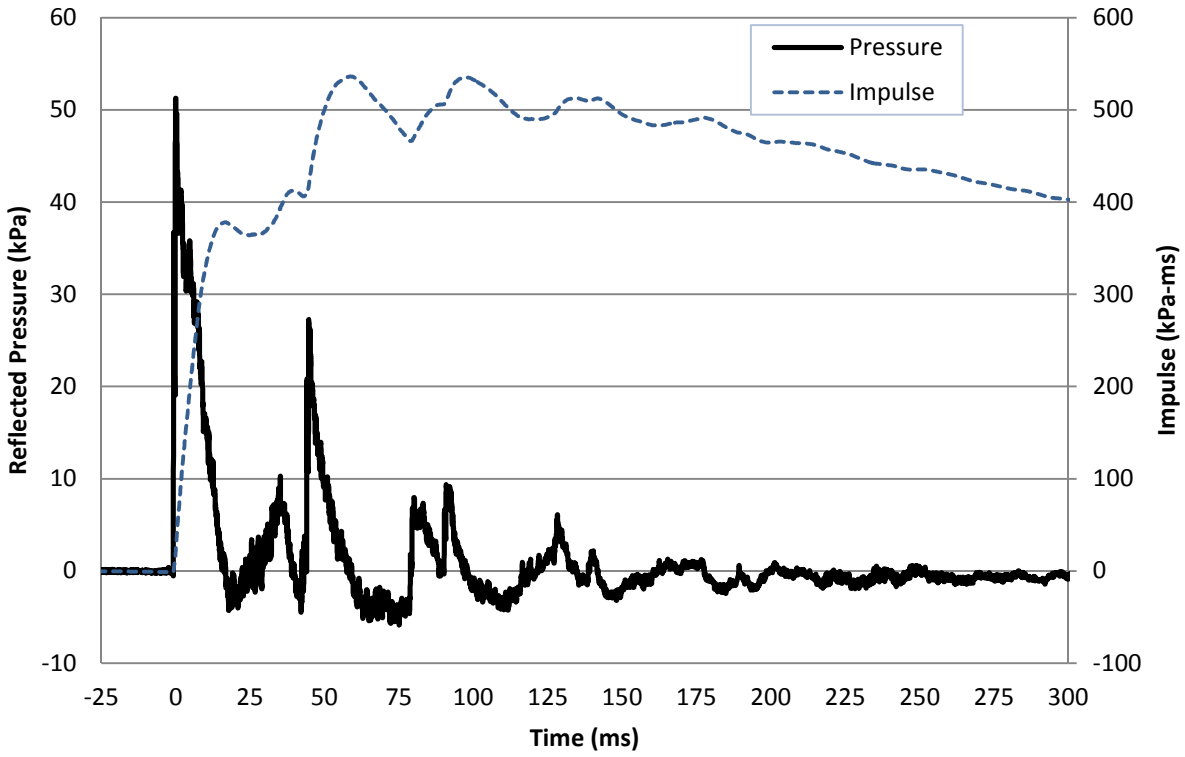

Figure 3.55: Reflected Pressure and Impulse Time History for Test URM-4-4

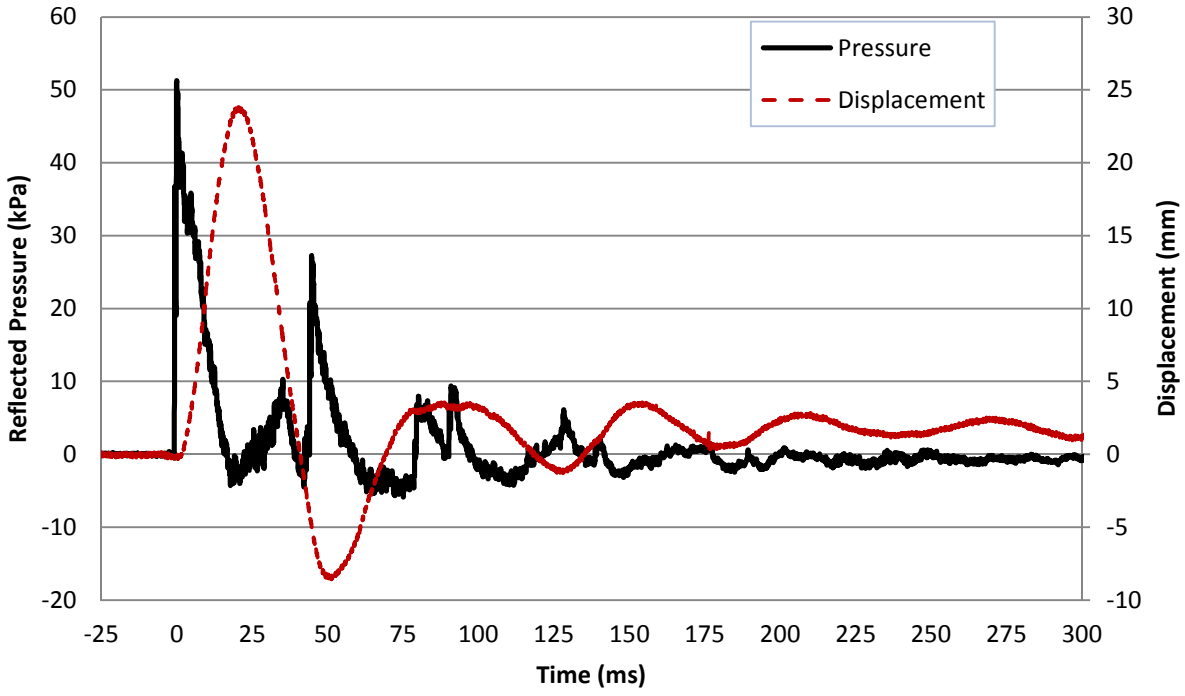

Figure 3.56: Reflected Pressure and Mid-Height Displacement Time History for Test URM-4-4

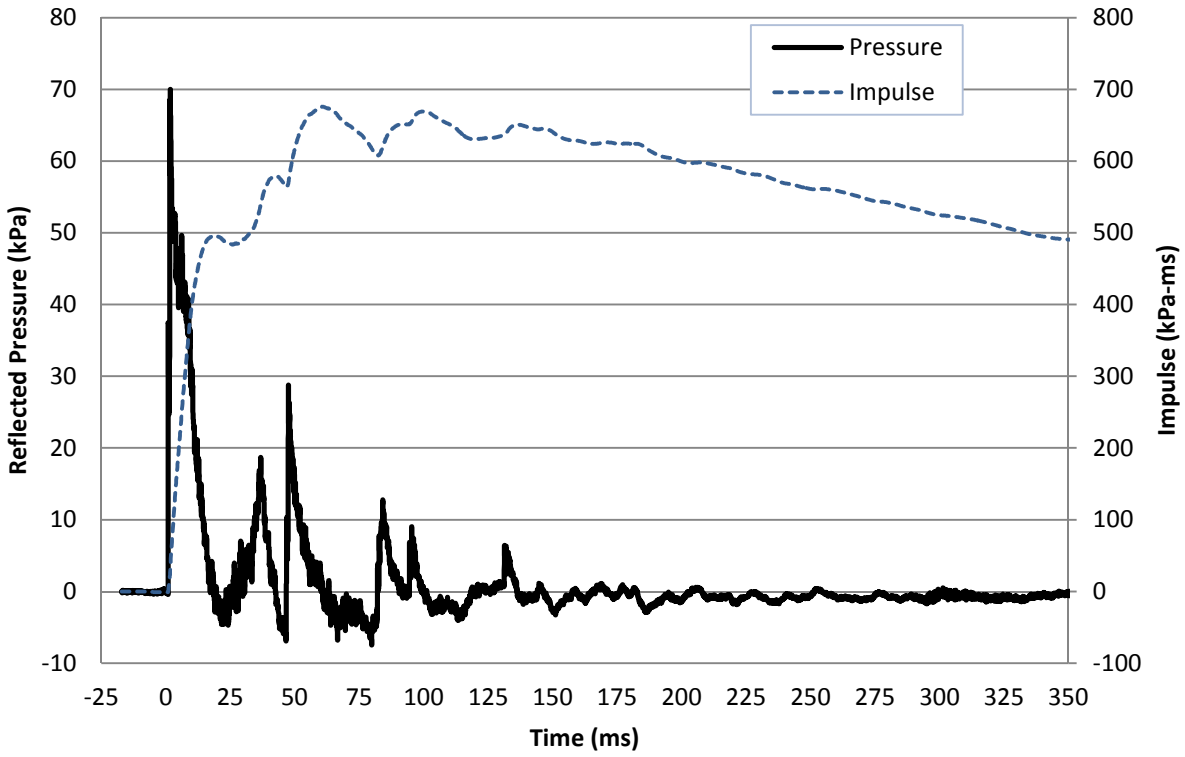

Figure 3.57: Reflected Pressure and Impulse Time History for Test URM-4-5

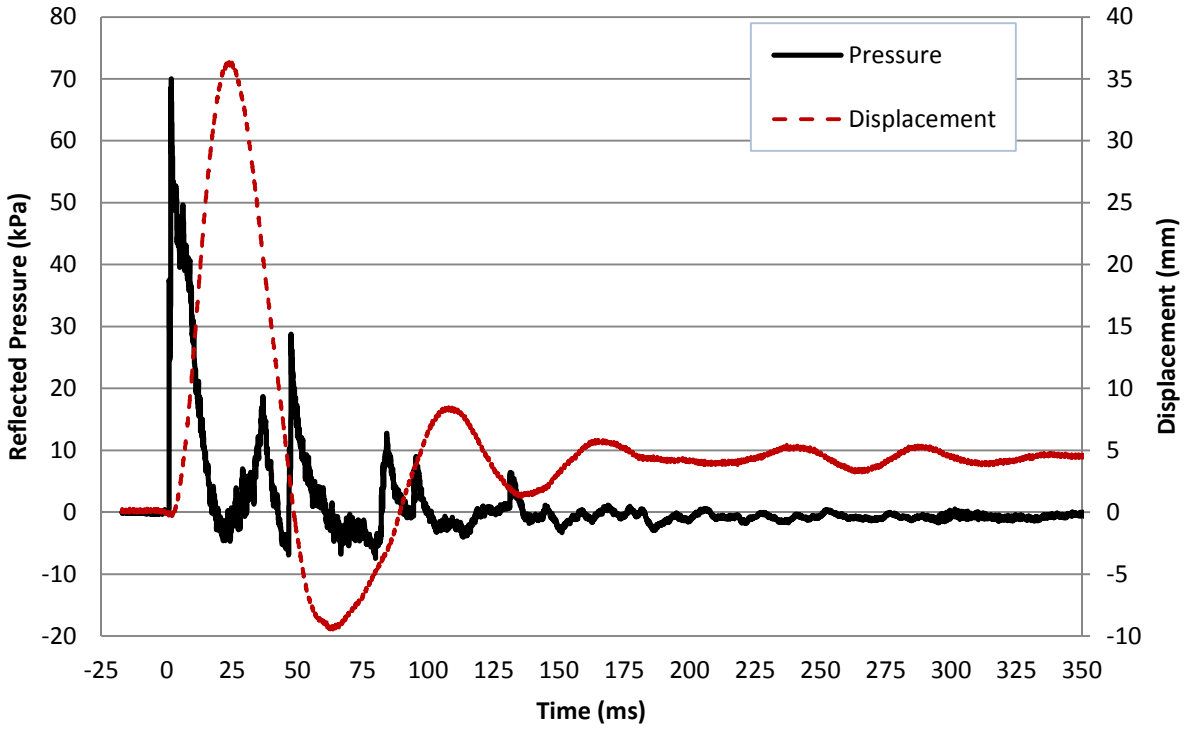

Figure 3.58: Reflected Pressure and Mid-Height Displacement Time History for Test URM-4-5

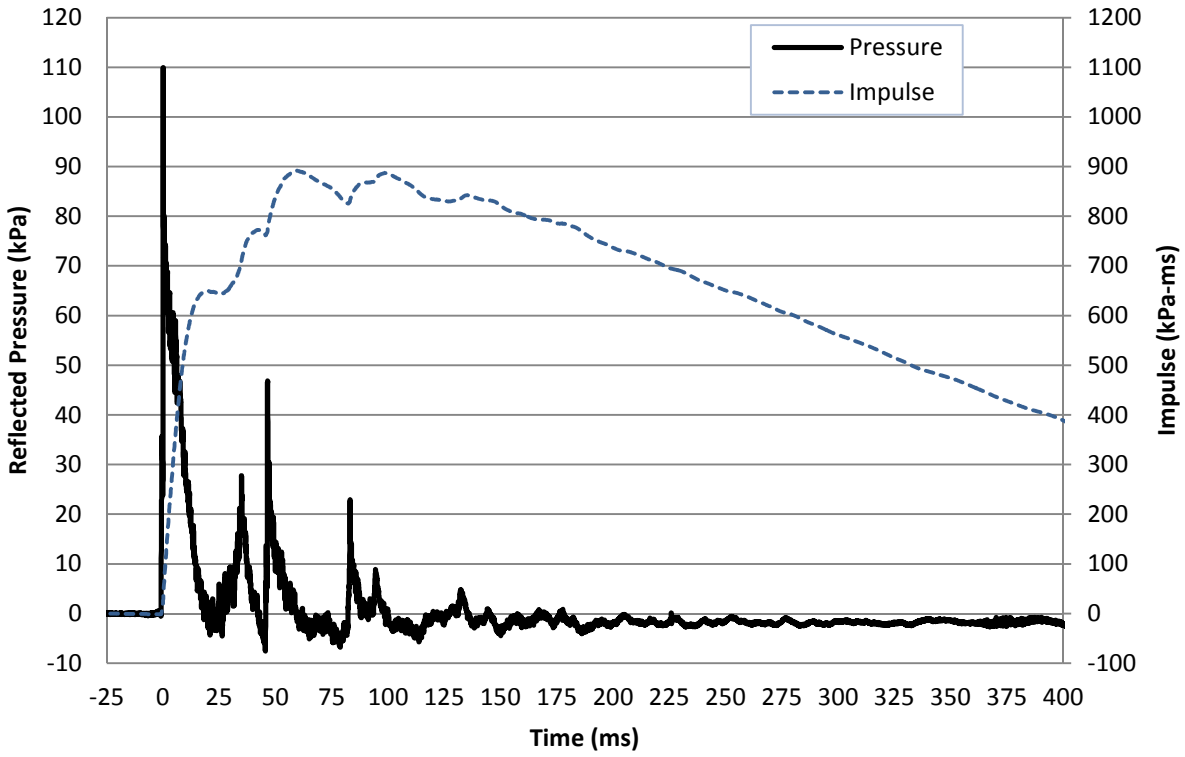

Figure 3.59: Reflected Pressure and Impulse Time History for Test URM-4-6

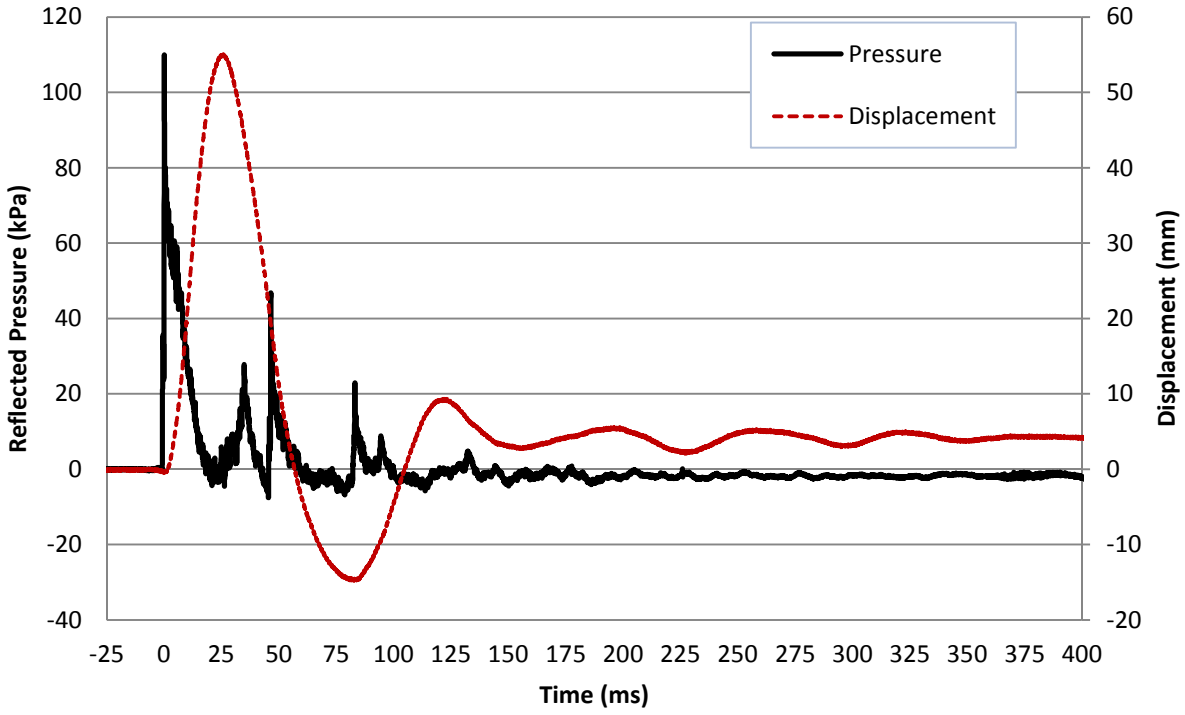

Figure 3.60: Reflected Pressure and Mid-Height Displacement Time History for Test URM-4-6

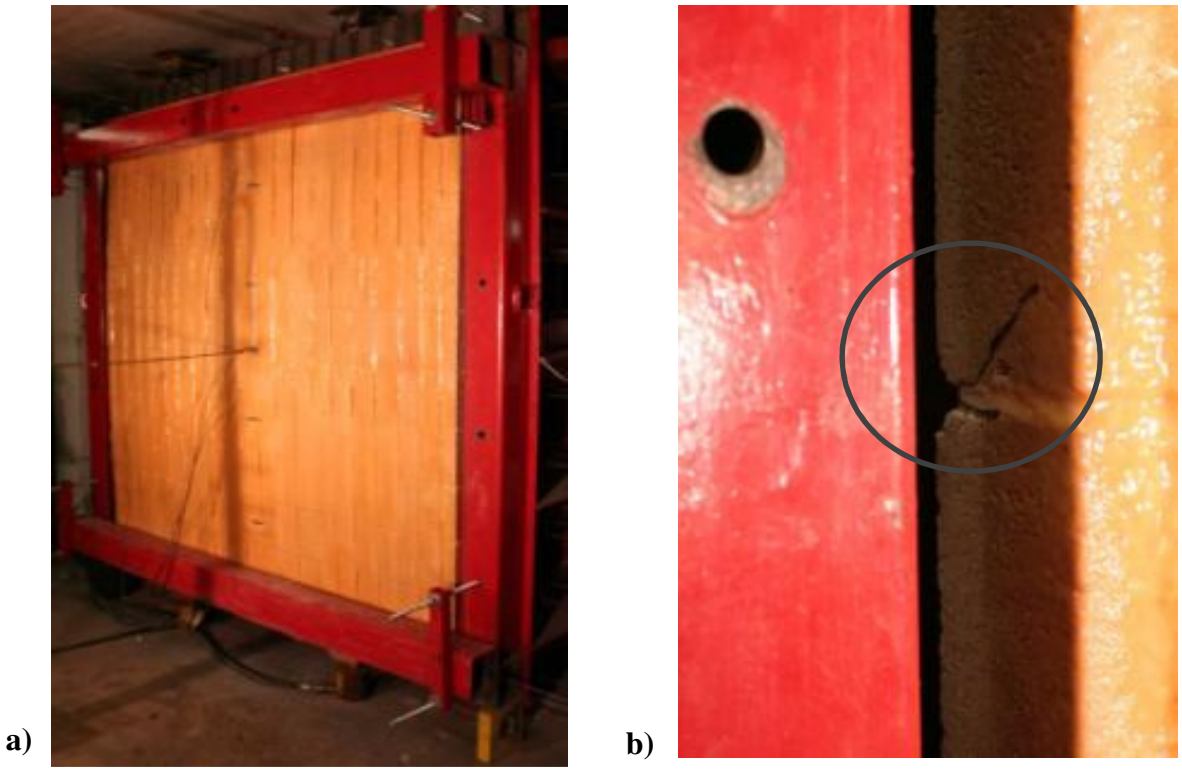

Figure 3.61: Retrofitted Load-Bearing Wall URM-4: a) After Shot 6; b) Tension Cracks Developed Near the Middle Mortar Joint after Shot 6

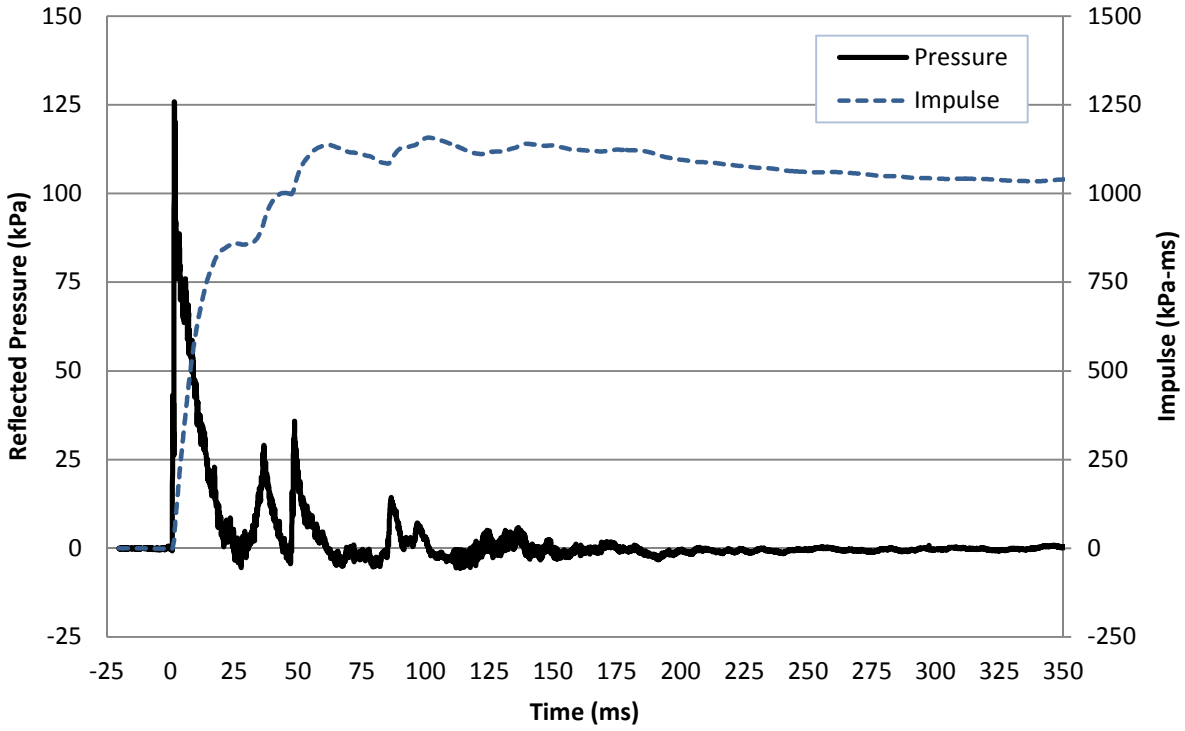

Figure 3.62: Reflected Pressure and Impulse Time History for Test URM-4-7

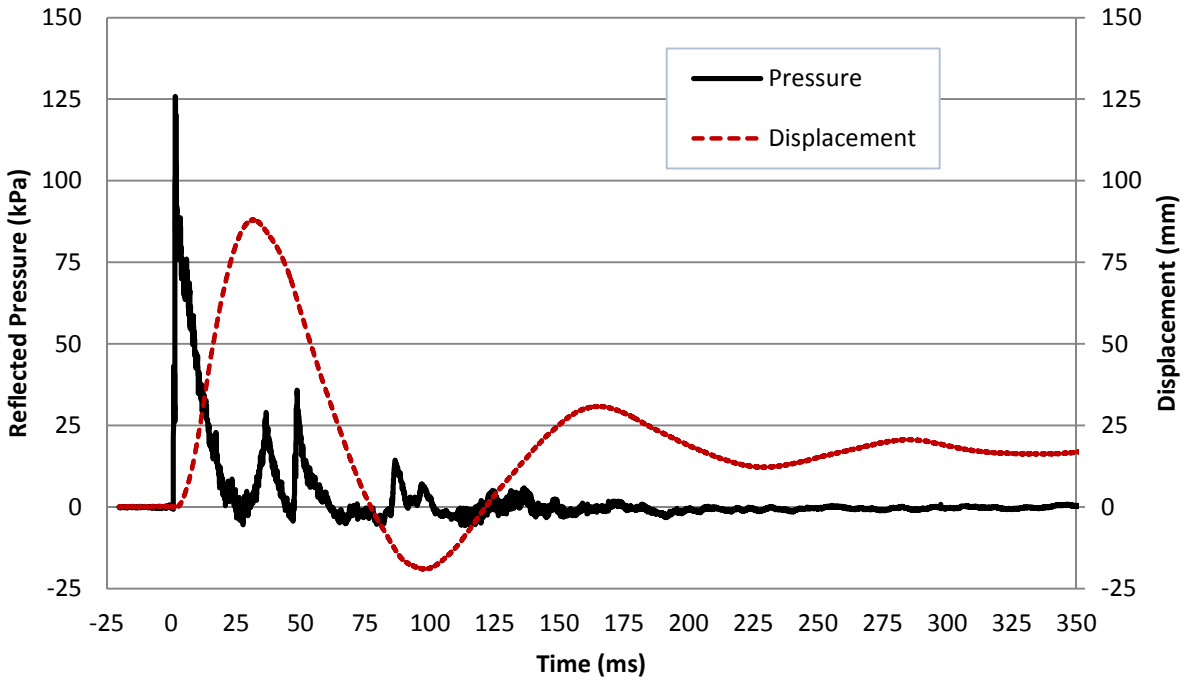

Figure 3.63: Reflected Pressure and Mid-Height Displacement Time History for Test URM-4-7

a) b)

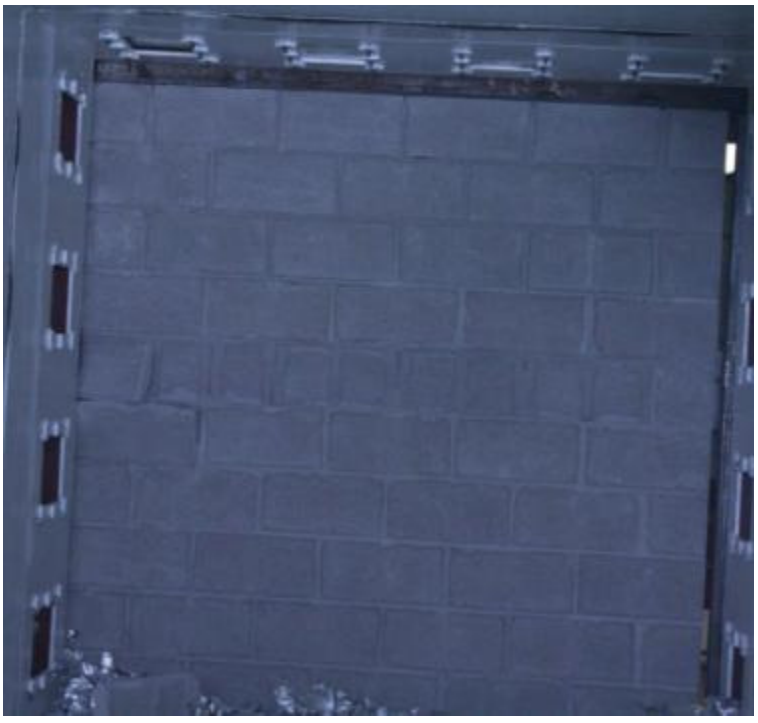

Figure 3.64: Retrofitted Load-Bearing Wall URM-4: a) After Shot 7; b) View of the Compression Face of Wall- Failure of Concrete Masonry Unit Block Face Shells in the Middle Two Courses after Shot 7

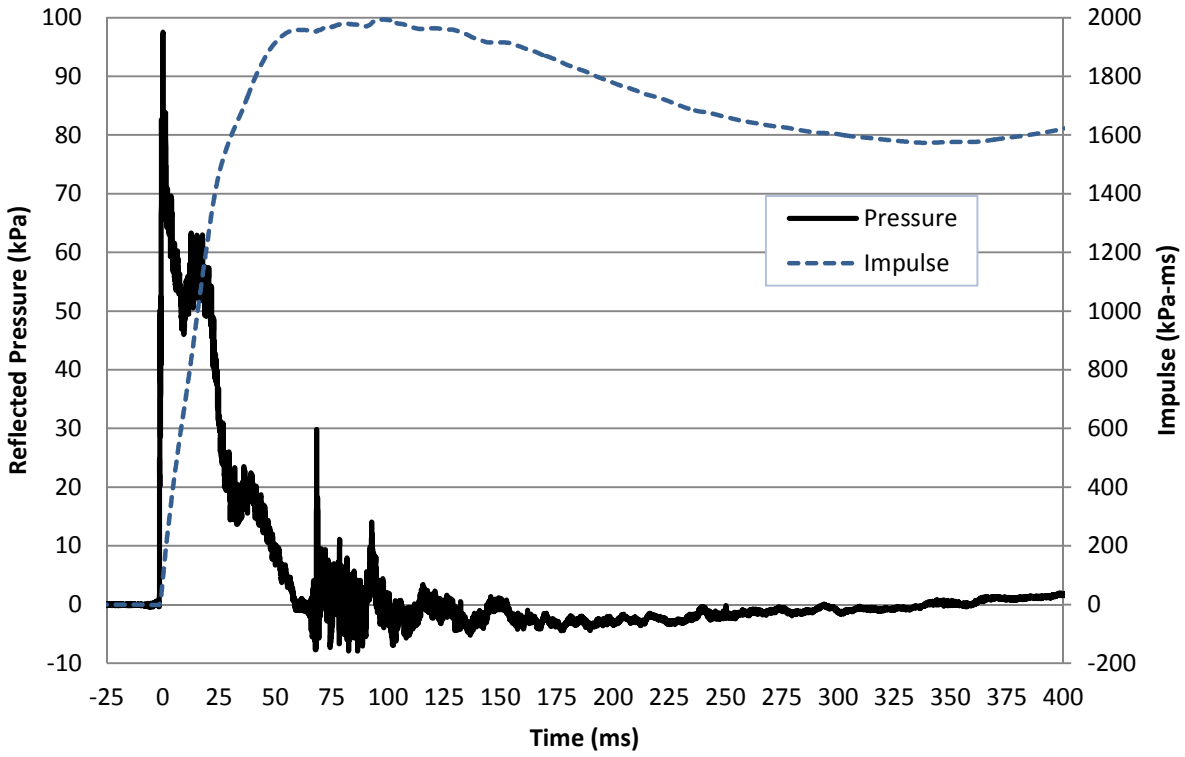

Figure 3.65: Reflected Pressure and Impulse Time History for Test URM-4-8

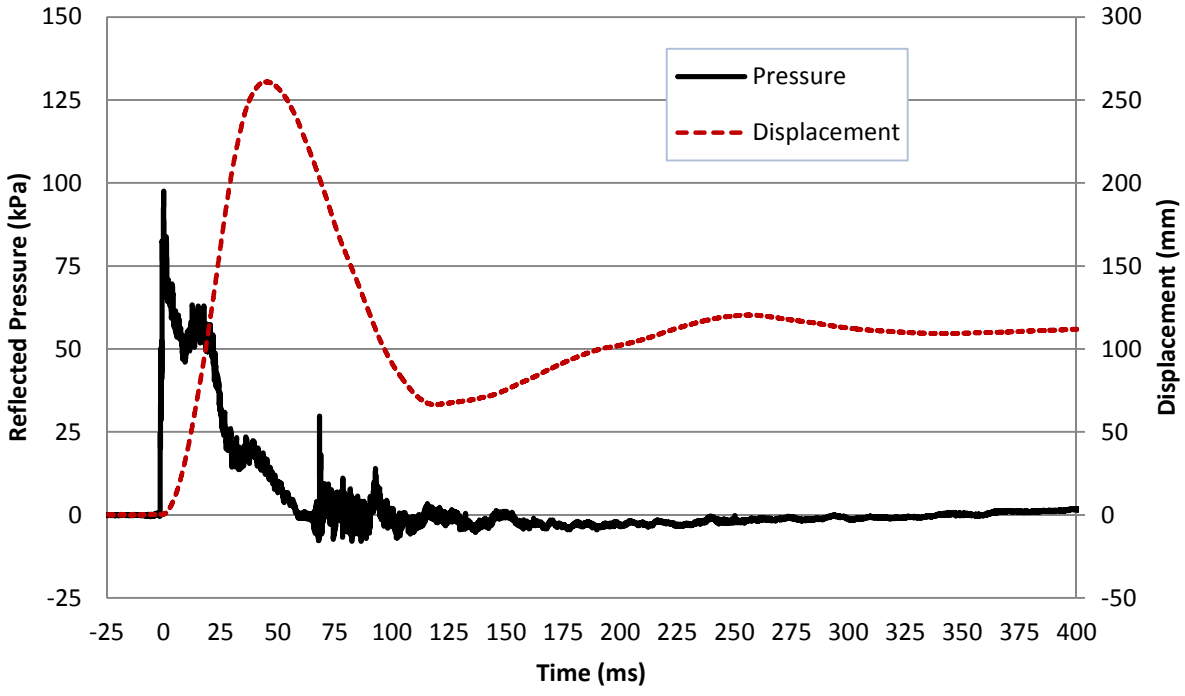

Figure 3.66: Reflected Pressure and Mid-Height Displacement Time History for Test URM-4-8

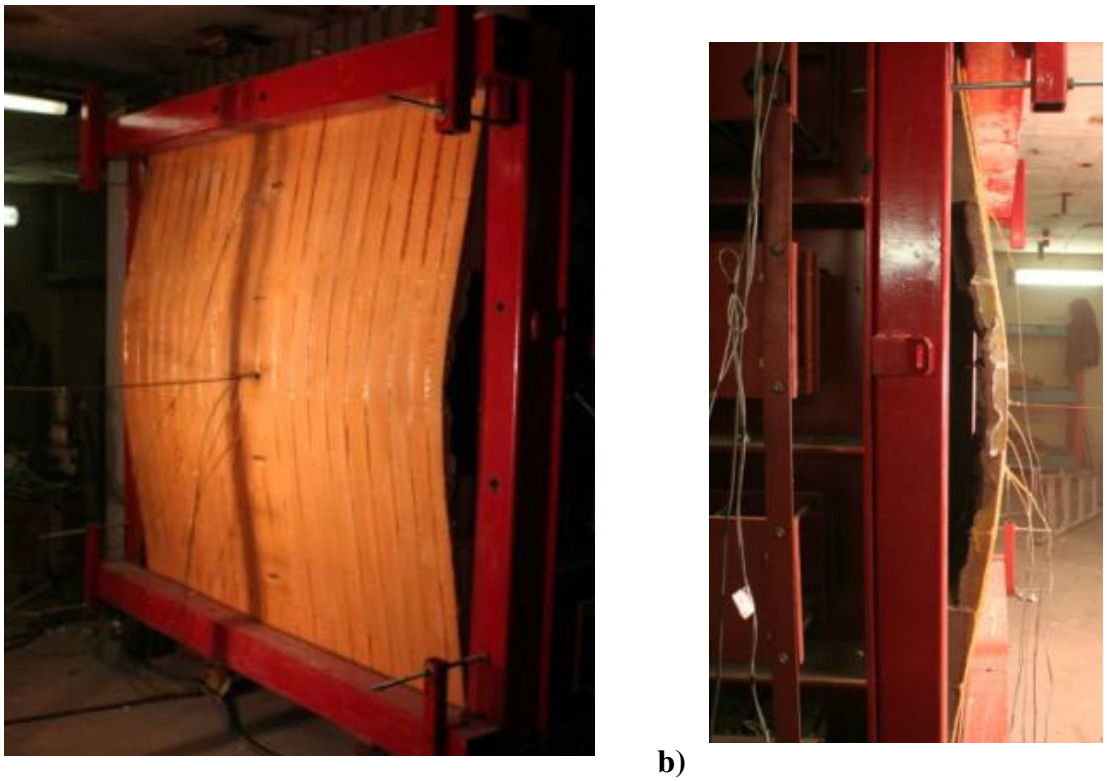

a) b)

Figure 3.67: Retrofitted Load-Bearing Wall URM-4: a) Deflected Shape of Wall URM-4 after Shot 8; b) Deflected Shape of Wall URM-4 after Shot 8 (Side View)

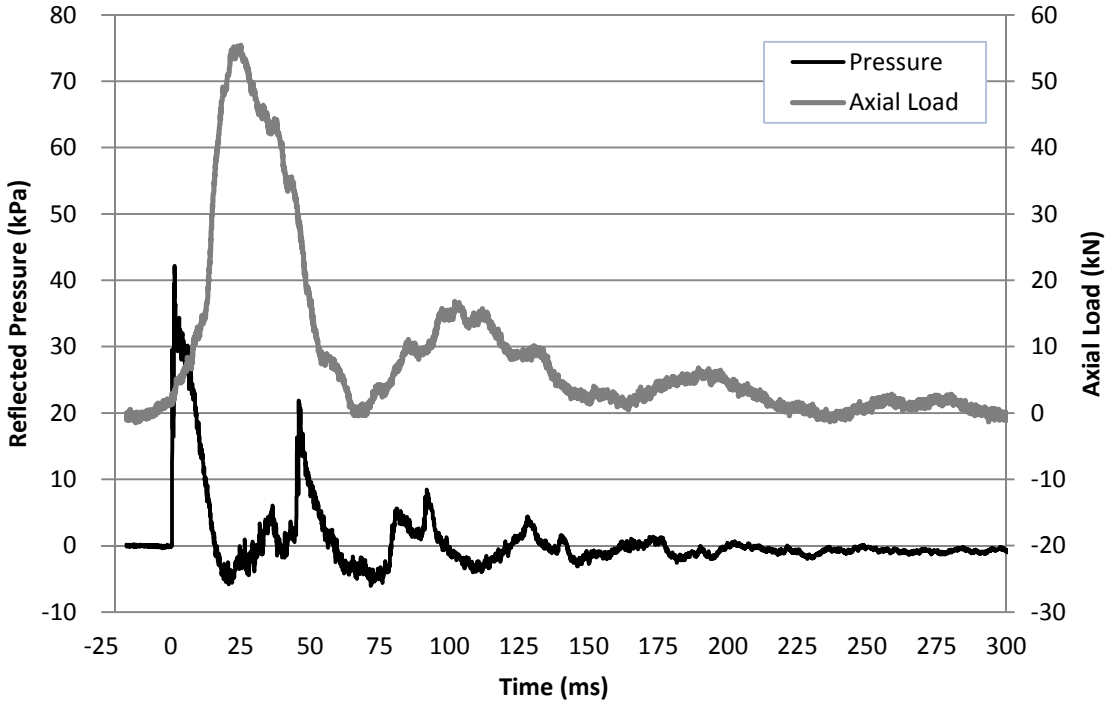

Figure 3.68: Axial Load Time History for Test URM-2-6

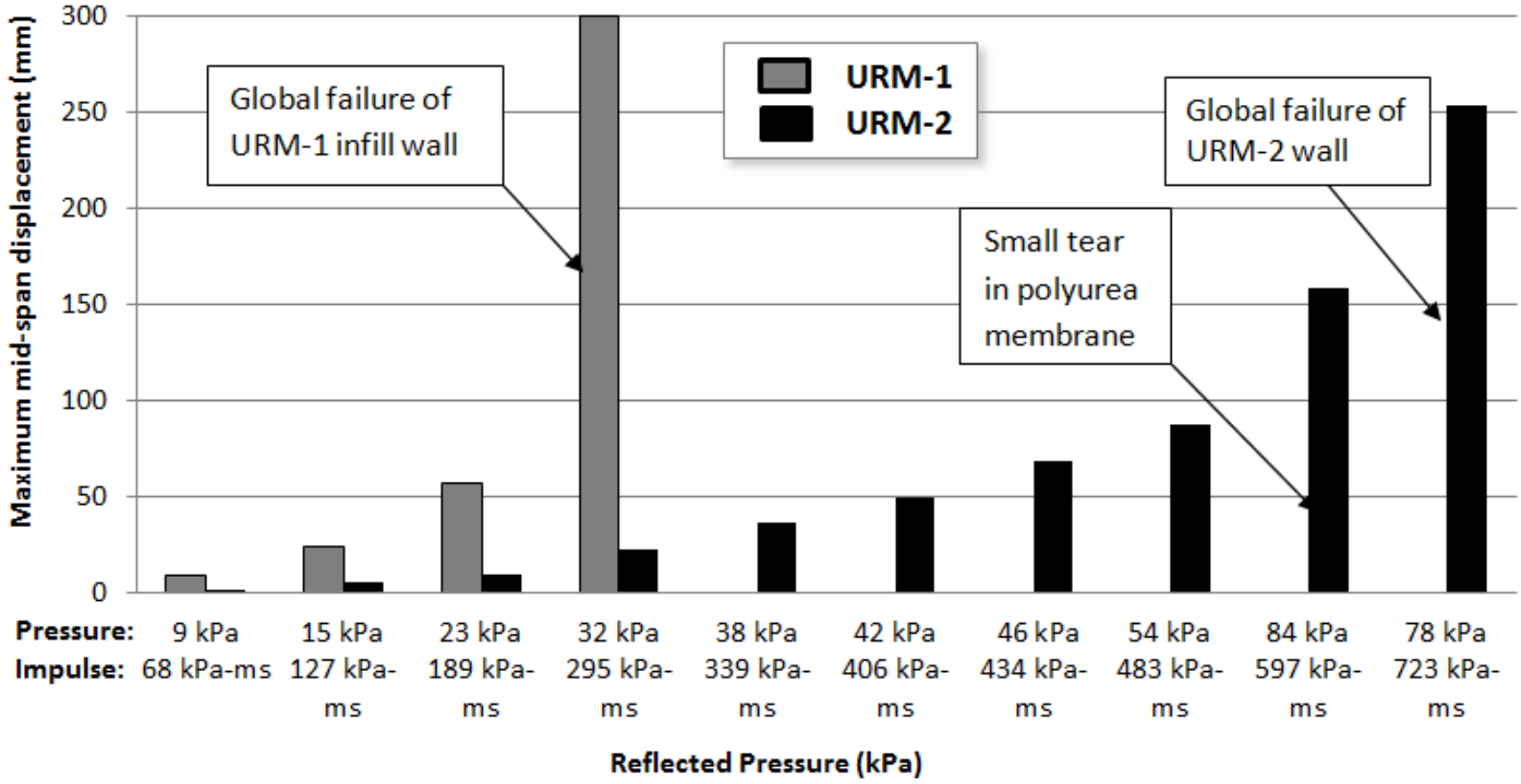

Figure 3.69: Maximum Mid-Height Displacement Comparison for URM-1 and URM-2 Wall Specimens

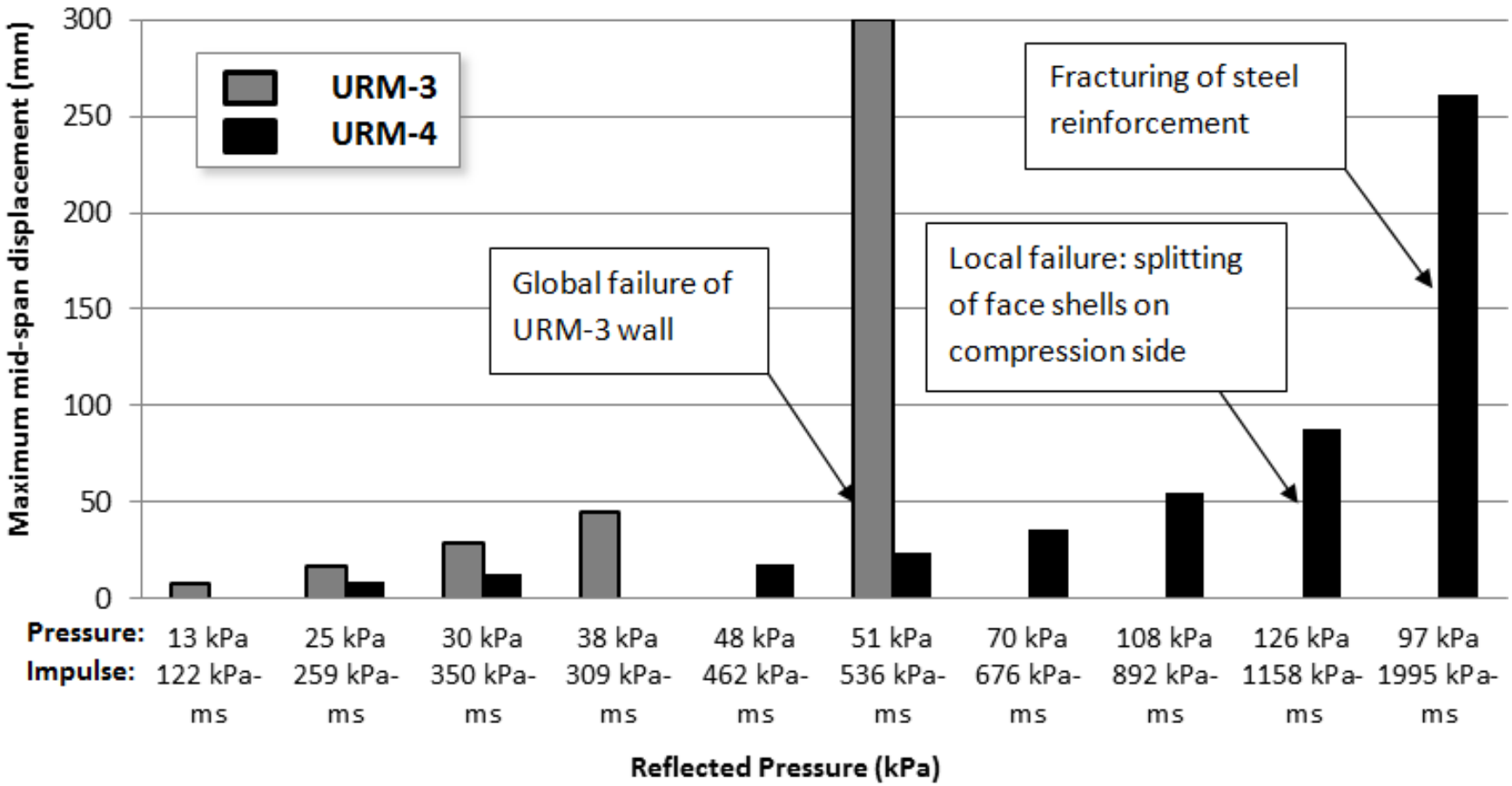

Figure 3.70: Maximum Mid-Height Displacement Comparison for URM-3 and URM-4 Wall Specimens

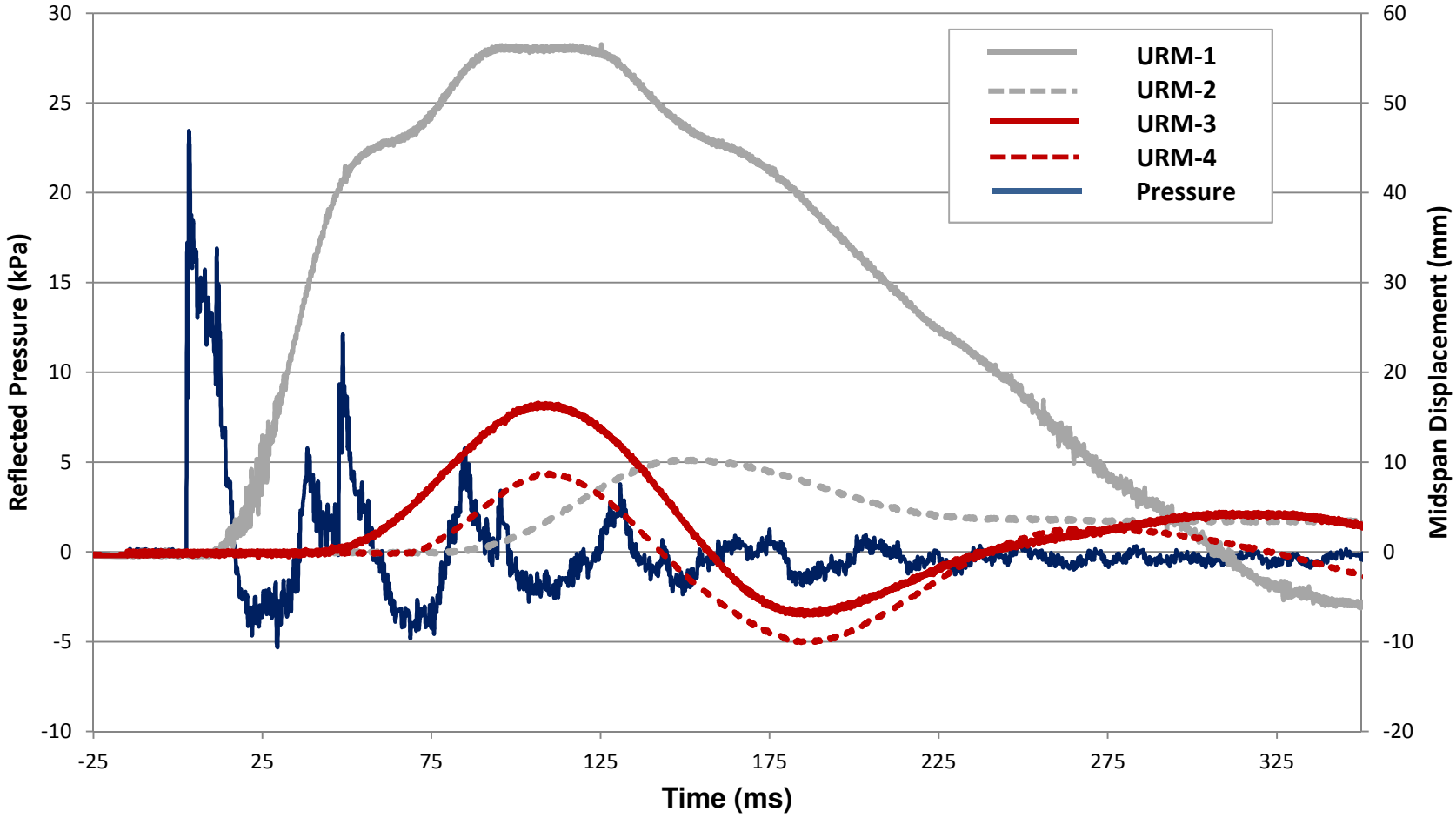

Figure 3.71: Mid-Height Displacement Time History Comparison of URM Wall Specimens Subjected to 23 kPa Peak Reflected Pressure over 17 ms Positive Phase Duration

CHAPTER 4

Analytical Results

4.1 General

An analytical model was developed to predict mid-height displacement time histories for each URM wall specimen tested under different levels of blast loading. The computed results were compared with those recorded experimentally to validate the analytical approach. This chapter describes the procedure for developing the analytical model as well as the comparisons made with the test results.

4.2 Dynamic Analysis

Mid-height displacement time histories were produced using an equivalent single-degree-of freedom model. From a design point of view, it was considered that only peak displacements are of concern, therefore the descending branch of the mid-height displacement time history was not generated. The effect of repeated loading on the strength of the specimens was considered negligible.

4.2.1 Single-Degree-of-Freedom (SDOF) Analysis

Although there are detailed and complex methods available for performing non-linear multiple-degree-of freedom dynamic analysis, an approximate Single-Degree-of-Freedom (SDOF) method was adopted in this study for the idealization of the one-way masonry wall system. This method, first suggested by Biggs (1964), is deemed to yield acceptable results.

A structural system, subjected to an external forcing function, can be represented as a SDOF mass-spring system shown in Figure 4.1. The response of the system can be written as

$$m\ddot{u}(t) + ku(t) = AP(t) \qquad [4.1]$$

where m is the mass of the structural system, $\ddot{u}(t)$ is the time dependent acceleration of the system mass, k is the stiffness, $u(t)$ is the time dependent displacement of the system mass, A is the surface area exposed to blast waves, and $P(t)$ is the time dependent forcing function.

In the above equation, the damping is ignored due to the short duration of the structural response (Biggs, 1964). Replacing $ku(t)$, the spring force, with a non-linear resistance term, $R(u)$, the above equation becomes

$$m\ddot{u}(t) + R\big(u(t)\big) = AP(t) \qquad [4.2]$$

In order to solve the above equation of motion, UFC-03-340-02 (2008) recommends the use of the average acceleration method due to its unconditional stability.

4.2.2 Equivalent Single-Degree-of-Freedom Approach

A multi-degree of freedom system can be converted into a single-degree of freedom system by using the equivalent Single-Degree-of-Freedom (SDOF) approach. This common method for member analysis, uses certain transformation factors, denoted by K, in order to convert the mass and the applied load of a real system into an equivalent SDOF model of a single point of interest that has a single direction of motion (Biggs, 1964).

The first step in idealizing the system into an equivalent SDOF system is to assume a displacement shape function, ϕ. Figure 4.2 shows the displacement shape for a member with simply supported boundary conditions subjected to uniformly distributed loading. The shape function changes with the member behaviour. A plastic hinge formation would automatically change the displacement shape of the system (Figure 4.2).

The mass factor, denoted by K_M, transforms a system with a distributed mass into a lumped-mass system and it can be obtained from the following equation

$$K_M = \frac{\int_0^L m\phi^2(x)dx}{mL} \qquad [4.3]$$

where m is the mass per unit length of the member, L is the member length, and $\phi(x)$ is the assumed shape function of the member.

The load factor, denoted by K_L, transforms a distributed force, and stiffness into an equivalent single point load. The load factor is determined from the following equation

$$K_L = \frac{\int_0^L p(x)\phi(x)dx}{pL} \quad [4.4]$$

where $p(x)$ is the load function.

The equation of motion for the equivalent SDOF system can then be written as

$$K_M m\ddot{u}(t) + K_L R\big(u(t)\big) = K_L A P(t) \quad [4.5]$$

or if only one factor is used

$$K_{LM} m\ddot{u}(t) + R\big(u(t)\big) = F(t) \quad [4.6]$$

where k_{LM} is a load-mass factor, defined as the mass factor divided by the load factor and $F(t)$ is the external loading.

Common transformation factors have been tabulated for one-way and two-way flexure members, with variable support conditions and subjected to either distributed or point loading. These factors are provided as design aids in Biggs (1964).

4.2.3 Resistance Curve Formulation

The non-linear resistance term, $R\big(u(t)\big)$, also referred to as the static resistance function, required to solve the equation of motion, is a function of the total statically applied load and the resulting displacement. The resistance function is dependent on the dynamic strength of materials under high strain-rate loading and also describes the transition between different member responses (i.e. transition from elastic to plastic behavior). The following sections will describe in detail the procedures used to formulate resistance curves for each URM wall specimen.

4.2.3.1 URM-1 Resistance Curve Formulation

For the URM-1 wall specimen, a composite resistance function was generated based on initial flexural resistance, followed by arching resistance. URM-1 wall specimen was built as an infill wall, with no tension face retrofit, and with a reduced (6 mm only) top edge gap between the wall and the surrounding frame. Mechanical shear restraints were provided to prevent out-of-plane movement. Figure 4.3 shows the resistance curve for URM-1 that was used in the SDOF model to predict mid-height displacements. The procedure used to formulate the static resistance function for URM-1 wall specimen is described below.

Flexural Resistance

Initially, the wall resists the out-of-plane blast loading through flexure governed by the tensile capacity of the masonry mortar bed joint. When the tensile capacity of the mortar joint is reached, a crack initiates at mid-height of the wall. This crack propagates and the wall does not experience global failure until it becomes unstable; in other words, until the line of action of the wall's weight above the mortar joint falls outside of the wall. This translates to a displacement equal to half the wall thickness (45 mm displacement).

Figure 4.4 shows the flexural component of the resistance function for the URM-1 wall specimen. The displacement (Δ_u) at maximum resistance, the maximum flexural resistance (F_u), and the stiffness (k_e) are computed from the following equations respectively:

$$\Delta_u = \frac{F_u}{k_e} \quad [4.7]$$

$$F_u = \frac{8M_e}{H} \quad [4.8]$$

$$k_e = \frac{384EI_e}{5H^3} \quad [4.9]$$

where M_e is the uncracked sectional moment $[Nmm]$, Δ_u is the displacement corresponding to maximum resistance $[mm]$, E is the modulus of elasticity of masonry $[MPa]$, I_e is the moment of inertia of the gross, uncracked section $[mm^4]$, and H is the wall height $[mm]$. In Figure 4.4, Δ_{max} represents half of wall thickness$[mm]$.

Arching Resistance

Figure 4.5 shows the arching mechanism in a gapped URM wall. During flexure the wall deflects and the top edge gap between the wall and the surrounding frame gets reduced. After the top edge gap is closed, arching is activated and the wall starts pushing on the top and bottom rigid supports, until the ultimate compressive strength of mortar is achieved.
Figure 4.6 shows the arching component of the resistance function of the URM-1 wall specimen. Drysdale et al. (1994) derived a series of equations that were used in the arching resistance function formulation.

When the flexural resistance is ignored, the wall has zero resistance until the top edge gap between the wall and the surrounding frame gets closed (Figure 4.5). This translates into an initial displacement due to closing of the gap that can be computed from the following equation

$$\Delta_g = \frac{gH}{4\gamma t} \qquad [4.10]$$

where Δ_g is initial displacement due to closing of the gap $[mm]$, g is the initial gap between the URM wall and the surrounding frame $[mm]$, t is masonry wall thickness $[mm]$ and γ is a factor approximately equal to 0.9 (Drysdale et al., 1994).

The displacement corresponding to the ultimate arching resistance, Δ_u, is computed as follows

$$\Delta_u = \Delta_g + \Delta_{go} \qquad [4.11]$$

where Δ_{go} is the additional displacement due to axial shortening $[mm]$. Axial shortening occurs when the wall pushes on the top and bottom rigid supports and compresses the mortar to the point of ultimate compressive strength, leading to partial crushing and shortening of the member.

The displacement due to axial shortening of the wall is computed from Eqn. 4.12

$$\Delta_{go} = \frac{g_o H}{4\gamma t} \qquad [4.12]$$

where g_o is the total reduction in wall height due to axial load shortening $[mm]$ and it can be computed by multiplying the strain in masonry (e_m) with the wall height (H)

$$g_o = \epsilon_m H = \frac{f_{mortar}}{E_m} H = \frac{0.85 f'_{mortar}}{850 f'_m} H \quad [4.13]$$

where f_{mortar} is the stress in the mortar $[MPa]$, $E_m$is the modulus of elasticity of masonry $[MPa]$, f'_{mortar} is the ultimate compressive strength of mortar $[MPa]$ and f'_m is the ultimate compressive strength of the masonry wall $[MPa]$.

The maximum deflection that can be achieved during arching is calculated from Eqn. 4.14:

$$\Delta_{max} = \gamma t \quad [4.14]$$

The arching resistance is computed for simply supported boundary conditions as follows

$$F_u(arching) = \frac{8C}{H}(\gamma t - \Delta_u) \quad [4.15]$$

where C is the thrust force corresponding to ultimate state conditions. Assuming rectangular stress distribution (Figure 4.5), the thrust force can be determined from Eqn. 4.16:

$$C = 0.85 f'_{mortar}(1 - \gamma) t b \quad [4.16]$$

where $(1 - \gamma)$t is the depth of the compression block (Figure 4.5) and b is masonry wall width $[mm]$. The depth of the compression block is always smaller than the flange width for all the available CMU units; therefore Eqn. 4.16 applies to ungrouted masonry walls as well.

4.2.3.2 URM-2 Resistance Curve Formulation

Wall URM-1 was built in a similar manner as the URM-2 wall specimen, with an additional 3 mm polyurea membrane retrofit. A composite resistance curve was formulated for wall URM-2 to reflect initial flexural behavior, followed by arching after the top edge gap gets closed, and last, membrane action. In the initial stages of loading, the wall resists out-of plane loading through tensile capacity of the mortar and, after cracking, through the

additional tension component from the polyurea membrane. At this stage, the wall starts pushing on the top and bottom rigid supports causing the activation of the arching mechanism that adds to the total moment resistance of the wall. After the mid-height displacement of the wall reaches a value equal to the maximum deflection computed from Eqn. 4.14, arching ceases and the wall behaves like a membrane until rupture.

The following section describes the components that contribute to the static resistance function of the URM-2 wall specimen.

Flexural Response

Figure 4.7 describes the flexural component of the resistance function for the URM-2 wall specimen. The resistance at the point of crack initiation (F_e), and the corresponding displacement (Δ_e) and stiffness (k_e) are computed as follows

$$\Delta_e = \frac{F_e}{k_e} \quad [4.17]$$

$$F_e = \frac{8M_e}{H} \quad [4.18]$$

$$k_e = \frac{384EI_e}{5H^3} \quad [4.19]$$

where M_e is the uncracked cross-section moment capacity $[Nmm]$, I_e is the moment of inertia of the gross uncracked section $[mm^4]$, and E is the modulus of elasticity of masonry $[MPa]$. The ultimate resistance (F_u) and corresponding displacement (Δ_u) and stiffness (k_u) are computed as follows

$$\Delta_u = \frac{F_u}{k_u} \quad [4.20]$$

$$F_u = \frac{8M_u}{H} \quad [4.21]$$

$$k_u = \frac{384EI_{cr}}{5H^3} \quad [4.22]$$

where M_u is the ultimate moment capacity computed from force equilibrium using a rectangular stress block approximation $[Nmm]$, and I_{cr} is the moment of inertia of the cracked cross-section $[mm^4]$.

After reaching ultimate state, the resistance remains constant until a displacement equal to the thickness of the wall is achieved (Figure 4.7).

Arching Resistance

In order to determine the contribution of arching action to the total static resistance function, three computational scenarios were investigated.

In the first scenario, arching is assumed to take place after the top edge gap between the URM wall and the surrounding frame has been closed. This assumption is valid if the polyurea membrane is not present. However, since the polyurea has compressive resistance at high strain rates (Sarva et al., 2007), the polyurea that filled the top edge gap between the URM wall and the steel frame instantly activates arching.

The second scenario assumes that the polyurea promotes instant arching. The wall starts pushing on the polyurea layer at the top and against the rigid bottom support until it reaches the ultimate compressive strength of the mortar, then the resistance decreases until the arch height is reduced to zero.

In the third scenario, the wall develops instant arching until the ultimate compressive strength of the mortar is achieved (partial crushing of mortar), then the resistance drops until the top edge gap between the URM wall and the surrounding frame is closed. At this point a secondary arching mechanism occurs as the wall pushes against the top rigid support. When partial crushing of the mortar occurs from secondary arching, the resistance drops again. Axial shortening was not considered for the secondary arching mechanism.

Membrane Action

Overlapping the polyurea on to the supportive frame sets up membrane behavior that commences after the wall reaches a mid-span displacement equal to the thickness of the wall.

Figure 4.8 shows the geometry of parabolic membrane deflection. The length of the membrane, s, can be computed from the following equation:

$$s = \sqrt{4\Delta^2 + \left(\frac{H}{2}\right)^2} + \frac{H^2}{8\Delta}\ln\left[\frac{2\Delta + \sqrt{2\Delta^2 + \left(\frac{H}{2}\right)^2}}{\frac{H}{2}}\right] \quad [4.23]$$

The mid-height displacement can be related to the rotation at supports:

$$tan\theta = \frac{4\Delta}{H} \Leftrightarrow \theta = \tan^{-1}\left(\frac{4\Delta}{H}\right) \quad [4.24]$$

In a pure membrane response, the polyurea is uniformly strained along its height. Using this assumption and applying Hooke's law:

$$\epsilon = \frac{s - H}{H} \quad [4.25]$$

Knowing the strain, the stress can be obtained from the material stress-strain relationship presented in Chapter 2. For the elastic range the stress can be computed as follows:

$$\sigma = E\epsilon \quad [4.26]$$

The tension in the polymer strip per unit width of wall can be computed by multiplying the stress by the thickness of the polymer:

$$T = \sigma t \quad [4.27]$$

Knowing the rotation at supports and the tension in the polymer strip, the vertical and horizontal support reaction are computed:

$$R_v = Tcos(\theta) \quad [4.28]$$

$$R_h = Tsin(\theta) \quad [4.29]$$

The horizontal support reaction is related to the applied lateral pressure as described by Eqn. 4.30:

$$R_h = \frac{pH}{2} \quad [4.30]$$

The total lateral force can then be computed as follows:

$$F = 2R_h b \quad [4.31]$$

where b is the width of the wall.

The following computational procedure was developed and used to formulate the static resistance-displacement function:

a) select a deflection value, Δ
b) compute length of membrane, s, from Eqn. 4.23
c) obtain strain in membrane, ϵ, from Eqn. 4.25
d) knowing the material stress-strain relationship, obtain the stress, σ
e) determine the tension in the polymer strip, T, from Eqn. 4.27
f) compute rotation, θ, from Eqn. 4.24
g) compute horizontal reaction, R_h, from Eqn. 4.29
h) compute lateral pressure, p, from Eqn. 4.30
i) compute total resisting force, F from Eqn. 4.31
j) plot $\Delta - F$

Since the polyurea is sprayed on top of the URM wall, stress concentrations form at the mortar joints. Davidson et al. (2004) observed that the membrane strains only half the block height on each side of the middle mortar joint, with little or no strain at the other mortar joints. In other words, the wall is assumed to deflect as a rigid body and only about 200 mm of the membrane is strained. In the case of a 2 m high wall, only 10% of the height is strained. However, during this experimental study, high speed video observations show the wall deflecting in a parabolic manner, unlike a rigid body. Although the highest membrane stress concentrations are at the middle mortar joint, the polyurea membrane also stretches across the other mortar joints. The percentage of the membrane that is active is variable, less than 10% for small deflections and higher than 10% for larger deflections. To simplify calculations, it was assumed that only 10% of the membrane is strained and that

the wall deflects in a parabolic manner. The previously mentioned procedure for developing resistance curve for a membrane is still valid, however Eqn. 4.25 was modified as follows:

$$\epsilon = \frac{s - H}{10\%H} \qquad [4.32]$$

Localized strains at the mortar joint would lead to higher stresses. The membrane will also reach its ultimate strength at smaller displacements.

Figure 4.9 shows the total resistance function for URM-2 wall specimen that considers flexural resistance and contribution of arching, when arching is assumed to commence only after the top edge gap between the URM wall and the surrounding steel frame is closed. After a displacement value equal to the thickness of the wall is achieved, pure membrane response is assumed to commence.

Figure 4.10 shows the total resistance function for URM-2 wall specimen that considers flexural resistance and the contribution of arching, when arching starts instantaneously.

Figure 4.11 shows the total resistance function for URM-2 wall specimen when arching starts instantaneously and secondary arching occurs after closing of the top edge gap between the URM wall and the surrounding frame.

The above resistance curves were used in a SDOF model to predict mid-height displacements. Figures 4.12, 4.13 and 4.14 show the maximum experimentally recorded mid-height displacements versus the maximum SDOF predicted displacements for all the three scenarios. The first scenario (Figure 4.12), overestimates mid-height displacements as it completely ignores the contribution of polyurea to arching. The second scenario (Figure 4.13), assumes a system that is too rigid and underestimates mid-height displacements. The third scenario (Figure 4.14) provides the best prediction for mid-height displacements hence it was selected as being the most suitable for the SDOF model.

4.2.3.3 URM-3 Resistance Curve Formulation

URM-3 wall specimen was built as a load-bearing wall, with no retrofit on the tension face and with a tight contact between the wall specimen and the surrounding frame. Mechanical

shear restraints were placed across the top and bottom of the wall to prevent out-of-plane movement. The resistance curve for URM-3 wall specimen was developed considering flexural resistance as well as axial load arching (Oswald and Zehrt, 2010). The flexural capacity of an unreinforced masonry wall is based on the tensile capacity of the mortar as well as any precompression due to supported dead load. Axial load arching occurs after the flexural response and the member begins deflecting as a rigid body. Figure 4.15 shows the static resistance function developed for URM-3 wall specimen. Since flexural resistance and axial load arching do not occur simultaneously, the resistance function was not determined using superposition.

Flexural Resistance

The static resistance function for the initial flexural response was generated using the procedure developed by Moradi et al. (2008). This procedure is valid only for URM walls, constructed from hollow blocks with ungrouted cells, supporting axial loading and subjected to one-way bending with a constant lateral load over the wall height. This method neglects the tensile strength of the mortar joint.

Take for example the URM wall shown in Figure 4.16. As the wall starts deflecting, the crack forms at the middle mortar joint and it propagates through the wall's thickness until the concrete fails in compression or the wall becomes unstable. Moradi et al. (2008) derived the following equation to predict displacement during crack growth

$$\Delta = \frac{t}{6} + \frac{y}{3} - \frac{(3-2\alpha)ph^2}{12W + 24P} \qquad [4.33]$$

where t is the wall thickness, y is the crack length, α is the degree of fixity expressed as a percentage, p is the applied uniform pressure on the wall, h is the wall height, W is the weight of the wall, and P is the axial loading applied at the top.

Moradi et al. (2008) also expressed the mid-height displacement as a function of the deflection at point of cracking of the middle mortar joint

$$\Delta = \beta\Delta_{cr} \qquad [4.34]$$

where Δ_{cr} is the mid-height deflection at the onset of cracking of the middle mortar joint, and the β factor is a ratio of the curvature of the central section of the wall during crack development, ϕ_{crG}, and the curvature of the central section of the wall at onset of crack, ϕ_{cr}, as shown

$$\beta = \frac{\phi_{\mathrm{crG}}}{\phi_{\mathrm{cr}}} = \frac{R_{crG}t^2}{R_{cr}(t-y)^2} \quad [4.35]$$

where

$$R_{crG} = R_{cr} = P + \frac{W}{2} \quad [4.36]$$

The mid-height deflection at the onset of crack is computed from the following equation

$$\Delta_{cr} = \frac{(5-4\alpha)ph^4}{384E_mI} \quad [4.37]$$

where $E_m$is the modulus of elasticity of the URM wall and I is the moment of inertia of the gross section.

The following procedure was used to develop the static resistance function:

a) At the onset of cracking, $y = 0$, compute Δ_{cr} from Eqn. 4.37
b) Equate Δ from Eqn. 4.33 to Δ_{cr} from Eqn. 4.37 and solve for the lateral pressure, p; convert into equivalent force, F.
c) During crack development, incrementally choose a crack length, y
d) For each crack length, compute Δ from Eqn. 4.34
e) Compute lateral pressure, p, from Eqn. 4.33; convert to equivalent force, F
f) Plot $\Delta - F$ curve

Axial Load Arching Resistance

After the ultimate flexural resistance is achieved and the supports underwent significant rotation, the axial load is being resisted at the unloaded face near the supports and near the loaded face at mid-height as shown in Figure 4.17.

The resulting axial force couple, provides a total resisting force, F_{al}, that can be computed from the following equation

$$F_{al} = \frac{8P}{H}(t - \Delta_u) \qquad [4.38]$$

where Δ_u is the deflection at the beginning of axial load arching that can be assumed as the deflection at ultimate flexural resistance $[mm]$, and P is the applied axial load $[N]$. The above equation ignores the wall weight in computing the total resisting force.

The resistance function for the URM-3 wall specimen shown in Figure 4.15 follows the same slope as the flexural resistance function determined using the method developed by Moradi et al. (2008). The peak resistance is computed from Eqn. 4.38 where the displacement corresponding to the ultimate flexural resistance, Δ_u, is computed from Eqn. 4.34.

4.2.3.4 URM-4 Resistance Curve Formulation

URM-4 wall specimen was constructed in a similar manner to the URM-3 wall specimen, with the addition of the smooth steel wires and a polyurea layer retrofit. Figure 4.18 shows the total static resistance function developed for the URM-4 wall specimen. Superposition was used to account for flexural and arching resistance in the initial stages of loading and membrane response was considered after large displacements were achieved.

Flexural Resistance

A part of the total applied out-of-plane loading is being resisted through flexure. The tensile stresses are being resisted by the smooth steel wires as well as the polyurea membrane. Precompression from axial loading contributes to flexural resistance as well.

The same procedure for determining flexural resistance that was used for the URM-2 wall specimen could also be used for URM-4. However, a computer software developed by Jacques et al. (2012) was considered a better option for developing static resistance-displacement function for flexural response. The program generates moment-curvature relationship obtained from sectional analysis using the neutral axis depth and strains found from strain compatibility. Knowing flexural rigidities and the plastic hinge length, the

moment-rotation relationship is established and sequentially the total lateral force versus mid-height displacement.

Arching Resistance

Arching is also contributing to the total resistance-displacement function for the URM-4 wall specimen. Since the URM-4 wall specimen had no gap between the wall and the surrounding rigid steel test frame, arching begins instantaneously; the wall undergoes axial shortening until the mortar reaches its ultimate compressive strength and then the arching resistance drops until a mid-span displacement equal to γt is achieved (Eqn. 4.14). The procedure for determining the axial resistance is similar to that described for wall URM-1; however, another component needs consideration: contribution of steel in compression. Since the smooth steel wires are welded to flat plates and bolted to the custom-made steel testing frame with polyurea sprayed on top, they are restrained against any vertical movement. As the wall pushes on the top rigid support, the smooth steel wires are also being compressed, that leading to an increase in arching resistance.

The compressive force in the smooth steel wires can be computed as

$$C_{steel} = \epsilon_m E_{steel} A_{steel} \qquad [4.39]$$

where C_{steel} is the compressive force in steel wires, $[N]$, ϵ_m is the strain in masonry corresponding to ultimate mortar compressive strength, E_{steel} is the modulus of elasticity for the steel wires $[MPa]$ and A_{steel} is the total cross sectional area of the steel wires $[mm^2]$. The above formula can only be used if the steel does not yield prior to maximum arching resistance. The flexural response curve in Figure 4.18 shows an elastic behaviour of the specimen at a displacement corresponding to the peak arching resistance, therefore Eqn. 4.39 is applicable.

The location of the compressive force in smooth steel wires is shown in Figure 4.19. Taking summation of moments about O:

$$M_o = C_{arch}(\gamma t - \Delta) + C_{steel}\left[t - \frac{(1-\gamma)t}{2} - \Delta\right] \qquad [4.40]$$

The mid-height displacement, Δ, is the displacement due to axial shortening and it is computed from Eqn. 4.12.

The total lateral resistance force in $[N]$ for simply supported boundary conditions is computed as follows:

$$F = pH = \frac{8M_o}{H} \qquad [4.41]$$

where p is the lateral pressure as shown in Figure 4.19.

Membrane Action

After the wall reaches a displacement equal to the thickness of the wall, membrane action commences. The procedure described in *Section 4.2.3.2* was used to generate the static resistance-displacement function for the URM-4 wall specimen when undergoing membrane behaviour.

The assumptions used in determining the resistance-displacement function are as follows:

a) The membrane is a composite of polyurea and smooth steel wires
b) The polyurea and the smooth steel wires are analysed separately and superposition is used to obtain the total resistance function.
c) The polyurea membrane is strained only along 10% of the total height
d) The smooth steel wires are uniformly strained along the wall's height
e) The smooth steel wires yielded during flexural response, therefore the stresses in steel are constant
f) The steel contributes to the static resistance-deflection function until it ruptures, then the polyurea continues to resist the out-of-plane loading on its own until the rupture point.

4.2.4 Strain Rate and Selected Dynamic Increase Factors (DIF)

Strain rate material increase factors of 1.17 for smooth steel wires strength and 1.19 for concrete masonry block wall strength were used in the SDOF model as recommended by the US Department of the Army, the Navy, and the Air Force Structures to Resist the

Effects of Accidental Explosions (TM 5-1300 1990) design manual for a strain rate of $10^{-4}/msec$. Figure 4.20 and Figure 4.21 show the strain rate versus the dynamic increase factors for concrete and steel respectively. A strain rate material factor of 1.0 was used for the strength of polyurea.

4.3 Analytical Results

A SDOF numerical analysis software, developed by Jacques et al. (2012) was used for generating mid-height displacements time histories using the average acceleration method. The software allowed for input of the resistance curves developed in the previous section and individual pressure time histories to reflect each shot performed on the URM wall specimens. A time step of 10^{-5} seconds was selected for the numerical integration. A 2000 mm width of the wall by 2000 mm height tributary area was used for determining the total resisting force applied at mid-height. This tributary area is identical to the surface area of all the URM wall specimens. The system mass of the URM wall was 560 kg. Table 4.1 and Table 4.2 provide a summary of the experimental versus SDOF predicted mid-height displacements. Individual time histories for SDOF predicted versus experimentally recorded mid-height displacements are shown in Figures 4.24 through 4.54. Pressure-impulse (PI) diagrams, shown in Figures 4.55 through 4.60, were generated for each test performed on each specimen using the same software developed by Jacques et al. (2012).

4.3.1 Experimental versus Predicted Displacements

Table 4.1 provides a summary of the maximum predicted and the experimentally recorded mid-height displacement for the different pressure impulse combinations applied to each wall specimen. Figures 4.22 and 4.23 show the predicted maximum displacements plotted against the experimentally recorded maximum displacements. The SDOF predicted and the experimentally recorded displacement time histories with the corresponding reflected pressure time history for all the tested URM wall specimens are shown in Figures 4.24 to 4.52.

The SDOF model generally predicts the maximum mid-height displacement for all the URM wall specimens with reasonable accuracy.

4.3.1.1 Predicted Maximum Displacements

The predicted maximum mid-height displacements versus the experimentally recorded maximum mid-height displacements are compared in Figures 4.22 and 4.23. Table 4.2 provides the ratios of experimentally recorded versus predicted mid-height maximum displacements for different ranges of experimentally recorded maximum mid-height displacements. The table also provides statistical information to validate the accuracy of the SDOF model. In Table 4.2, a displacement ratio greater than unity indicates that the SDOF model is computing displacements that are less than the experimentally recorded mid-height displacements.

An average displacement ratio of the experimentally recorded versus predicted mid-height displacements (d_{EXP}/d_{SDOF}) for all the 25 tests performed on all the URM wall specimens was 1.028 with a standard deviation of 0.284 and a coefficient of variation of 0.276. Overall, the SDOF model under-predicts the displacements on average by only 3%. For experimentally recorded maximum mid-height displacements smaller or equal to 10 mm, the model over-estimates deflections by almost 20%, with an average of 0.806, a standard deviation of 0.540 and a coefficient of variation of 0.670 for 6 tests. This high standard deviation and coefficient of variation is attributed to the sensitivity of the model to smaller displacements and possibly other sources of error such as settling of the supports, movement of the shock tube and sensitivity of the displacement gauges. In a moderate range, when the experimentally recorded maximum mid-height displacements are between 10 mm and 75 mm, the displacement ratios have a mean of 1.119 with a standard deviation of 0.165 and a coefficient of variation of 0.147 for 16 tests. With higher displacements, the above mentioned sources of error become negligible. For experimentally recorded displacements higher than 75 mm, the SDOF model overestimates displacements with a displacement ratio average of 0.984 and a corresponding standard deviation of 0.178 and a coefficient of variation of 0.181 for 3 tests. Difficulty arises in predicting very large displacements when a SDOF model is used. The mid-height displacement is hard to predict after the formation of a collapse mechanism and also due to the difficulty of predicting post-ultimate state resistance. However, the statistical information shown in Table 4.2 shows that up to just before the collapse of the specimen, there was a good prediction of the maximum mid-height displacements.

4.3.1.2 Predicted Time to Maximum Displacements

Figures 4.24 to 4.52 show the predicted mid-height displacement and the experimentally recorded time histories overlaid on the same plot with the corresponding experimentally recorded reflected pressure time histories for all the tests performed on the URM wall specimens under shock tube induced blast loading.

The displacement measurements for all the tests conducted on specimens URM-1, URM-2 and URM-3 were recorded using wire transducers. The displacement measurements for tests conducted on specimen URM-4 were recorded using Linear Variable Displacement Transducers (LVDT). The difference between using wire transducers and LVDT's arises mainly from the prediction of time to maximum displacement. Figure 4.53 shows the mid-height displacement time history for test URM-3-3 recorded using a wire transducer and Figure 4.54 shows the mid-height displacement time history of test URM-4-2 recorded using a LVDT gauge. A direct comparison was not produced since the two different types of gauges were not used for the same location and the same applied pressure profile. When the wire transducer was utilized, the experimentally recorded and the predicted SDOF mid-height displacements do not follow the same slope nor do they start increasing at the same time. In reality, the displacement should start increasing as soon as the pressure is applied. This is shown in the SDOF predicted displacement time history. The wire transducer gauges shows a time lag of approximately 10 ms before the gauge starts reading any change in displacement. Due to the fact that the wire transducers were installed at a far distance from the specimens and as soon as the wall started to deflect, they would be pushed, there would be a small time when the wire is loose, before it starts being in tension and read displacements. The test data presented in Chapter 3, shows that this lag is relatively constant for all the tests performed with the wire transducers displacement gauges. When LVDT's were used as in the case of URM-4 wall specimen, this lag is not present. The experimentally recorded and the SDOF predicted mid-height displacement time histories are shown to start at the same time and to follow a similar slope.

The time to maximum displacement and the maximum displacement are two dependent variables since a higher displacement would yield longer time to maximum displacement.

The time to maximum displacement is generally under predicted even in the case when LVDT gauges were used due to the gauge sensitivity that results in a lag time.

It was concluded that wire transducers are good at predicting the maximum displacements; however, when the time to maximum displacement is of importance, then only LVDT's should be chosen to experimentally measure displacements.

4.3.2 Pressure-Impulse Iso-Damage Curves

Pressure-impulse diagrams, based on maximum mid-height displacement, were generated for each shock tube test performed on each wall specimen. These curves, shown in Figures 4.55 to 4.60, were developed using the SDOF model developed by Jacques et al. (2012) that changes the pressure and impulse values until the predicted maximum displacement is equal to a pre-selected value. This pre-selected value was chosen to be the same as the experimentally recorded maximum mid-height displacement. The shock wave pressure-time history was approximated as a triangular distribution. The predicted PI diagrams for each test were plotted with the experimentally recorded pressure and impulse combinations that resulted in the selected maximum mid-height displacement. The predicted PI curves generally overestimate maximum mid-height displacements since the curves fall under the experimentally recorded pressure impulse combination for each test. Since the analytical method requires the solution of the SDOF equation of motion, the level of accuracy for predicting iso-damage PI curves is comparable to the accuracy of the analytical results presented in *Section 4.3.1*.

4.4 Summary

The SDOF model used for determining the maximum mid-height displacements for the URM wall specimens under shock wave loading accurately predicts the experimental results presented in Chapter 3. The model is most accurate for displacements higher than 10 mm. For small displacements, even 1 mm difference would create an error of at least 10% (in the case of experimentally recorded displacements smaller than 10 mm).

Table 4.1: Pressure, Impulse, Experimentally Recorded Maximum Displacements and SDOF Predicted Displacements

	Shock Wave Properties		Experimental	SDOF	
	P_r (kPa)	I_r (kPa-ms)	d_{EXP} (mm)	d_{SDOF} (mm)	$\frac{d_{exp}}{d_{SDOF}}$
URM-1-1	6.1	53.1	9.1	5.47	1.66
URM-1-2	13.7	150.9	23.8	19.47	1.22
URM-1-3	23.4	179.3	56.5	48.36	1.17
URM-1-4	30.7	265.1		Global Failure	
URM-2-1	8.7	68.2	2.2	4.41	0.50
URM-2-2	14.6	128.7	6.4	8.9	0.72
URM-2-3	23	188.5	10.3	12.94	0.80
URM-2-4	32	294.5	23	22.27	1.03
URM-2-5	37.5	338.5	36.9	27.96	1.32
URM-2-6	42.1	406.3	50	40.47	1.24
URM-2-7	46.1	433.8	69.2	60.33	1.15
URM-2-8	53.9	483.3	88.4	102.44	0.86
URM-2-9	84.4	597.2	158.9	174.18	0.91
URM-2-10	78.1	723.4		Global Failure	
URM-3-1	6.1	49	1.1	4.06	0.27
URM-3-2	13.2	121.9	8.2	11.68	0.70
URM-3-3	24.7	193.3	16.6	18.62	0.89
URM-3-4	28	271.9	28.6	28.41	1.01
URM-3-5	37.7	309.2	45	40.8	1.10
URM-3-6	39	290.8	41.7	37.21	1.12
URM-3-7	51	414.6		Global Failure	
URM-4-1	24.6	258.8	8.8	8.95	0.98
URM-4-2	32.2	350.3	13.1	11.78	1.11
URM-4-3	47.5	462	18.4	16.69	1.10
URM-4-4	51.3	536.2	23.8	20.16	1.18
URM-4-5	69.7	675.8	36.4	29.64	1.23
URM-4-6	107.7	891.9	55.1	44.4	1.24
URM-4-7	125.7	1157.5	88.1	74.78	1.18
URM-4-8	97.3	1995		Global Failure	

Table 4.2: Summary of Experimentally Recorded and SDOF Predicted Maximum Displacement Ratios

	d_{EXP}/d_{SDOF}			
d_{EXP}	<10	10-75	>75	All
Number	6	16	3	25
Maximum	1.664	1.319	1.178	1.664
Minimum	0.271	0.796	0.863	0.271
Mean	0.806	1.119	0.984	1.028
Standard Deviation	0.540	0.165	0.178	0.284
Coefficient of Variation	0.670	0.147	0.181	0.276

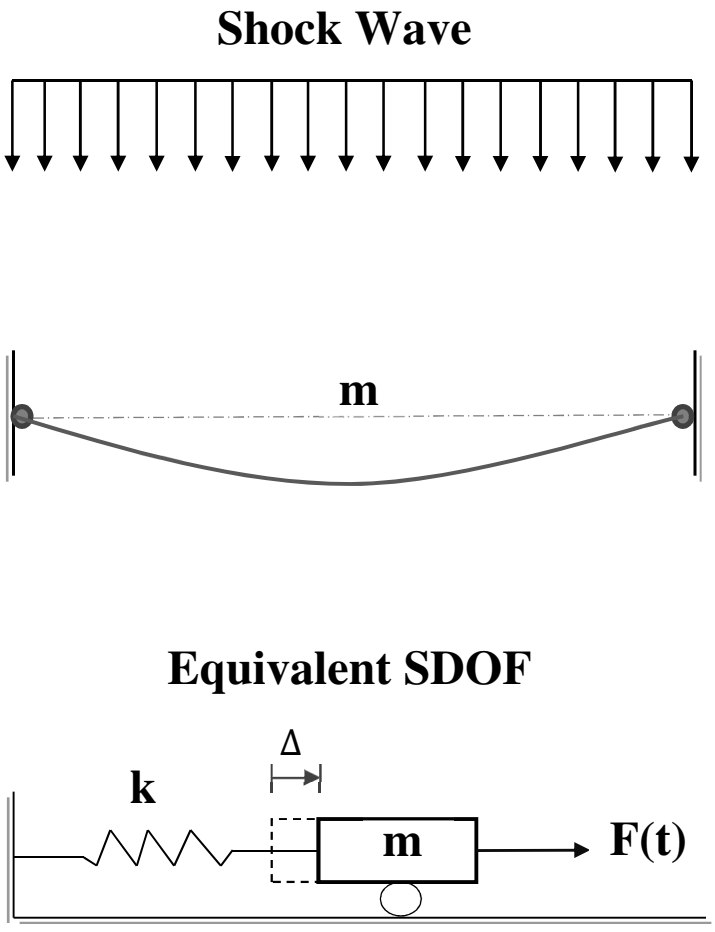

Figure 4.1: Equivalent Single-Degree-of-Freedom System

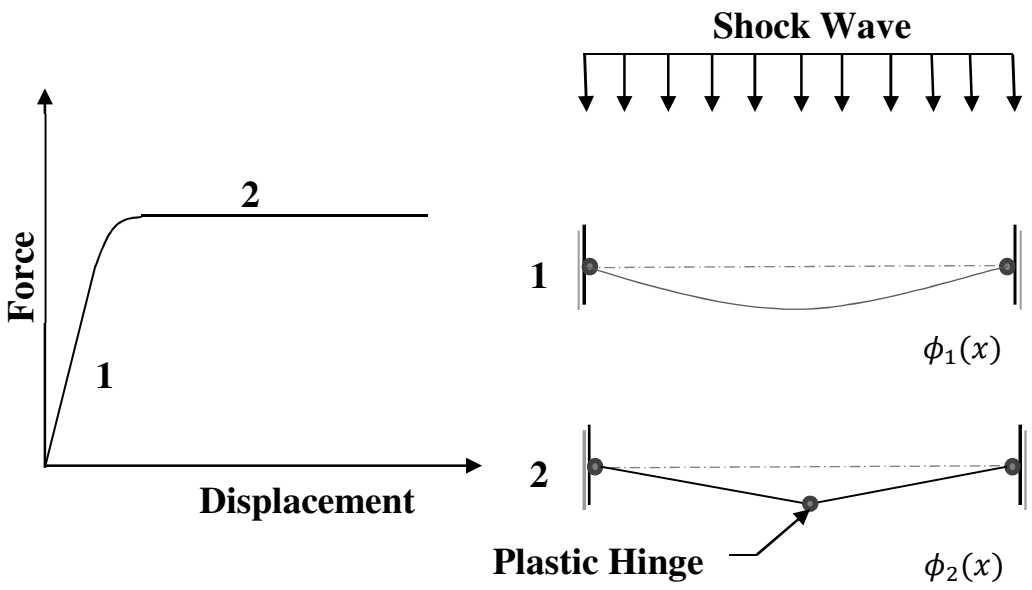

Figure 4.2: a) Force Displacement Curve for Member with Simply Supported Boundary Conditions; b) Progression of Damage through Two Mode Shapes

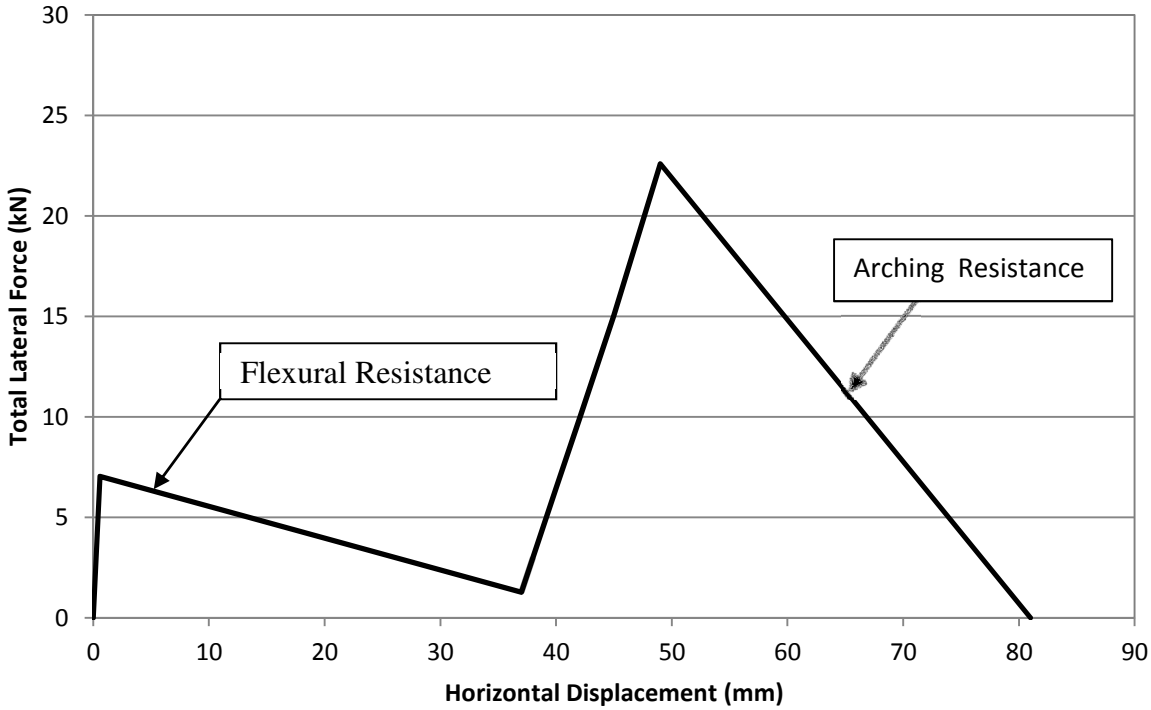

Figure 4.3 Resistance Function for Wall URM-1

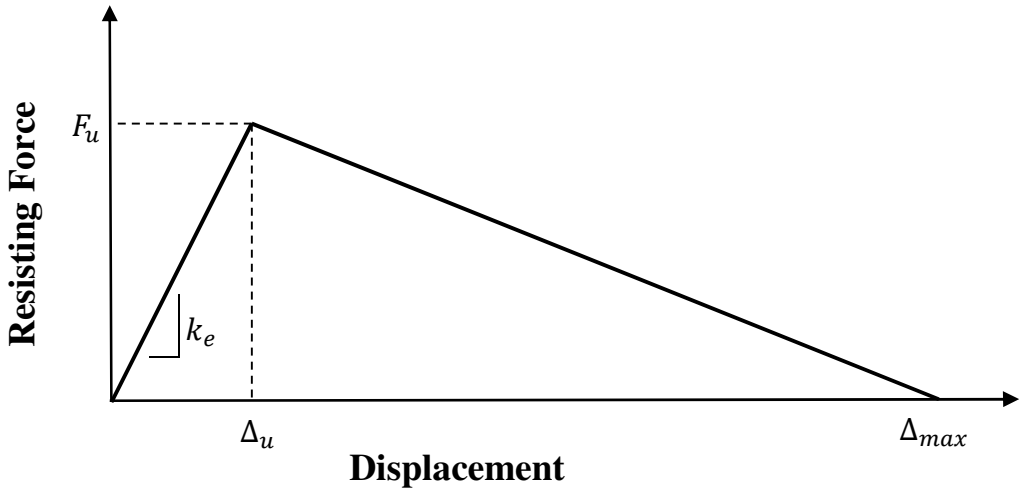

Figure 4.4: Flexural Resistance Component for Wall URM-1

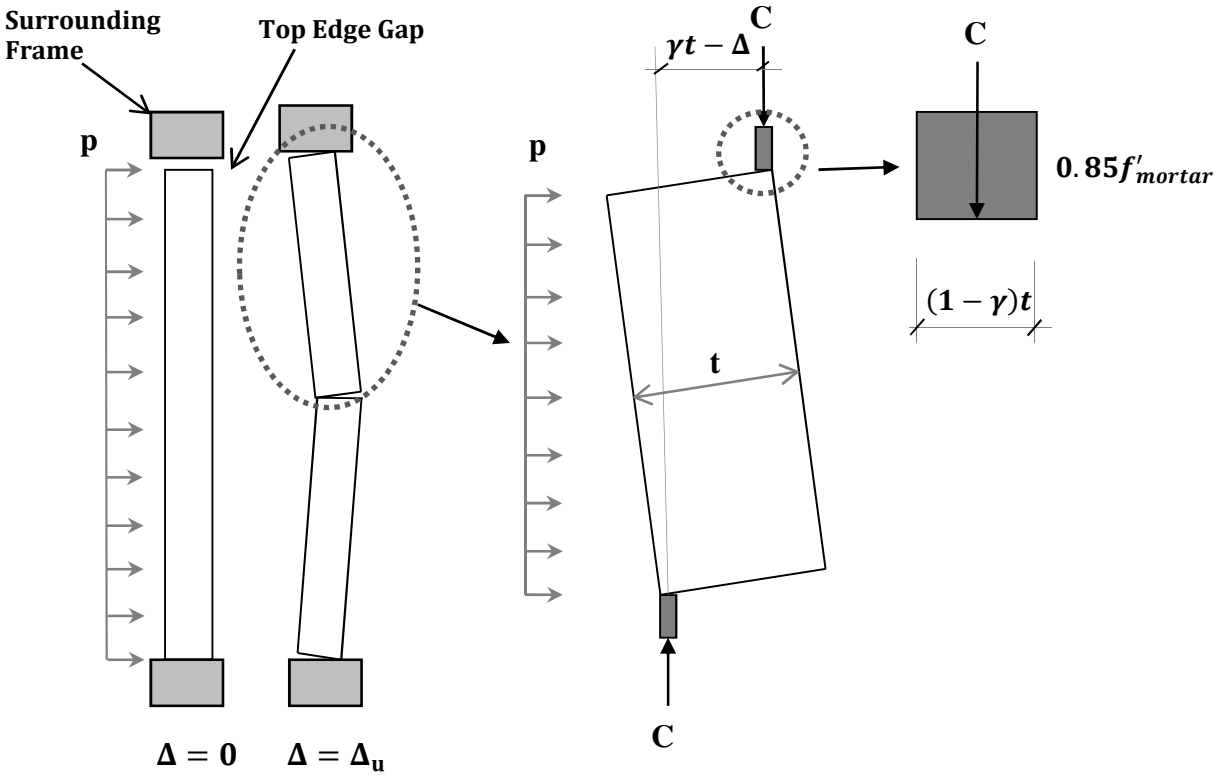

Figure 4.5: Maximum Arching Resistance

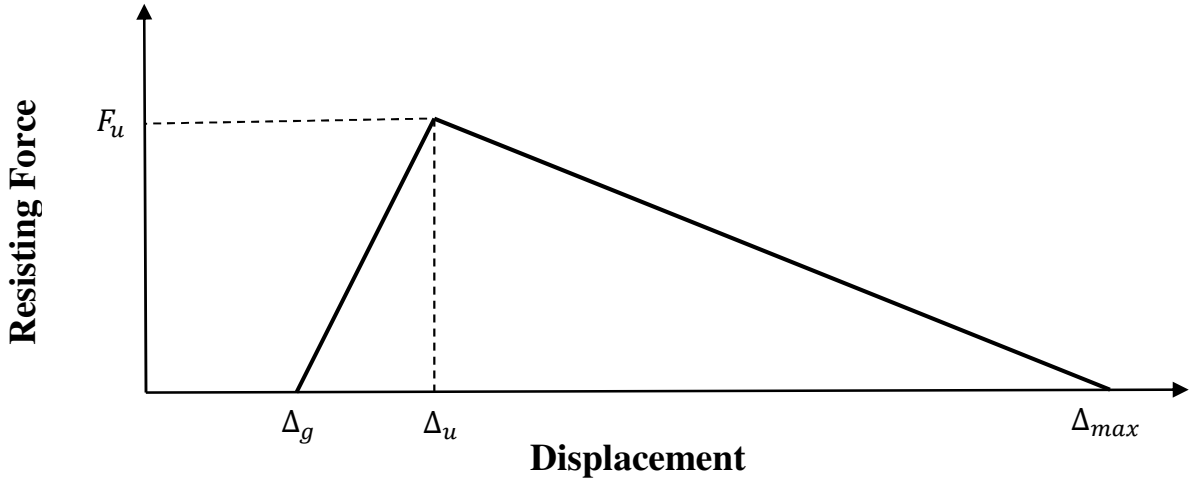

Figure 4.6: Arching Resistance Component for Wall URM-1

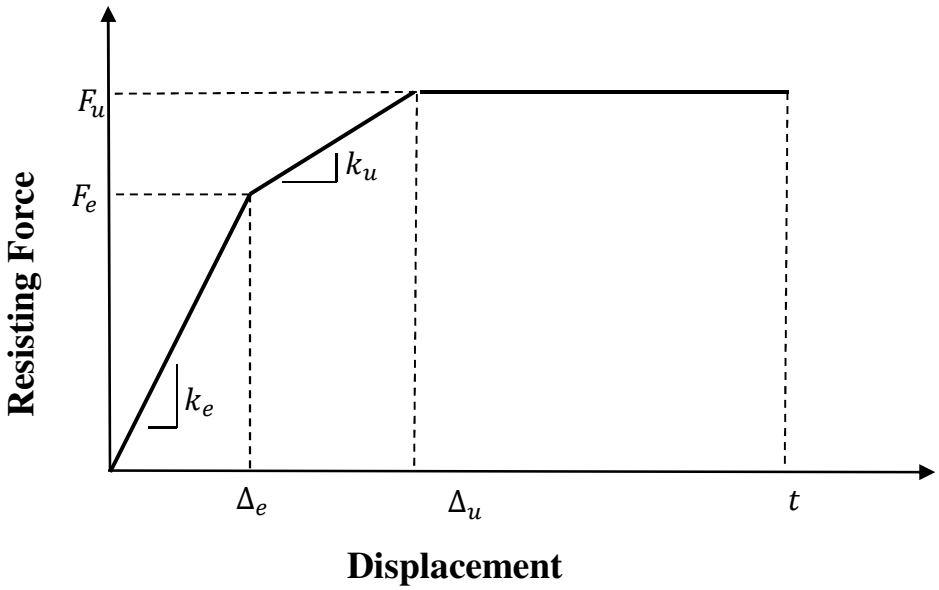

Figure 4.7: Flexural Component of the Resistance Curve for the URM-2 Wall Specimen

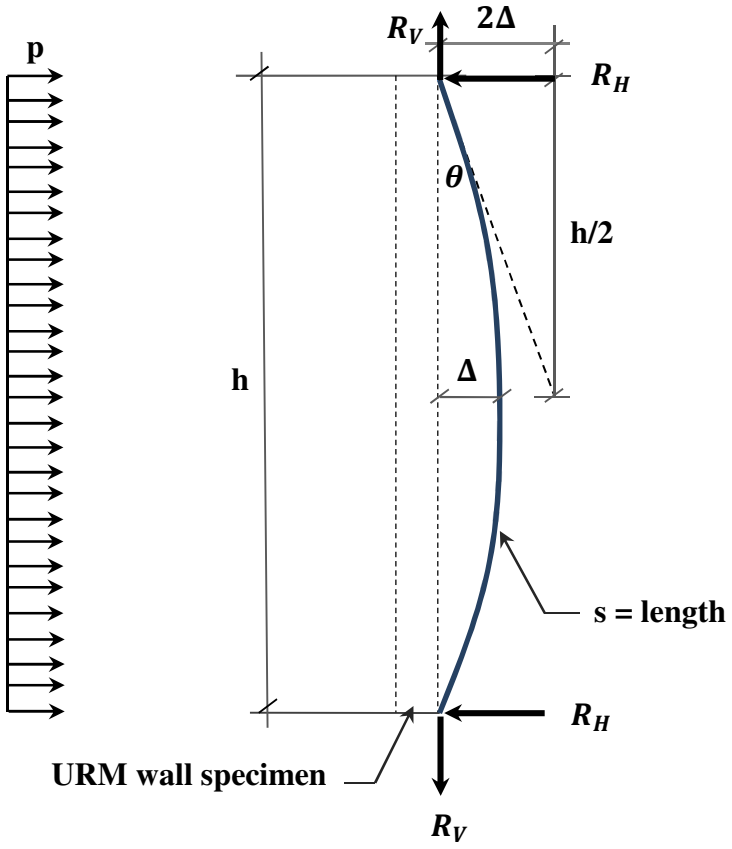

Figure 4.8: The Geometry of Parabolic Membrane Deflection

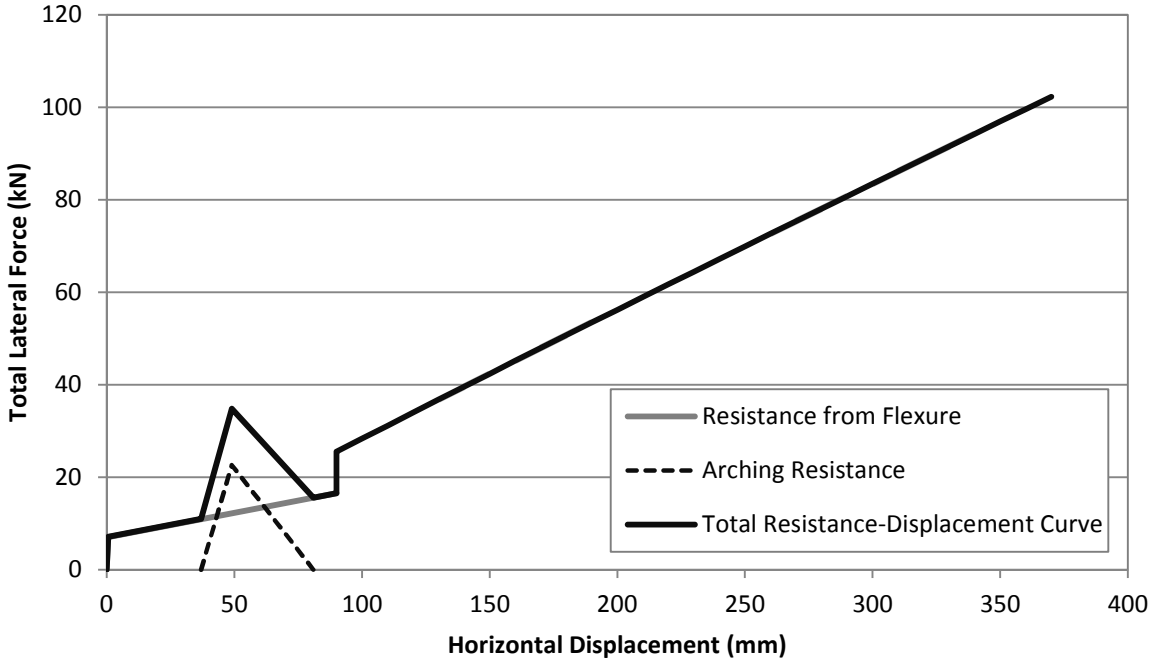

Figure 4.9 Resistance Curve for Wall URM-2 (Gapped Arching)

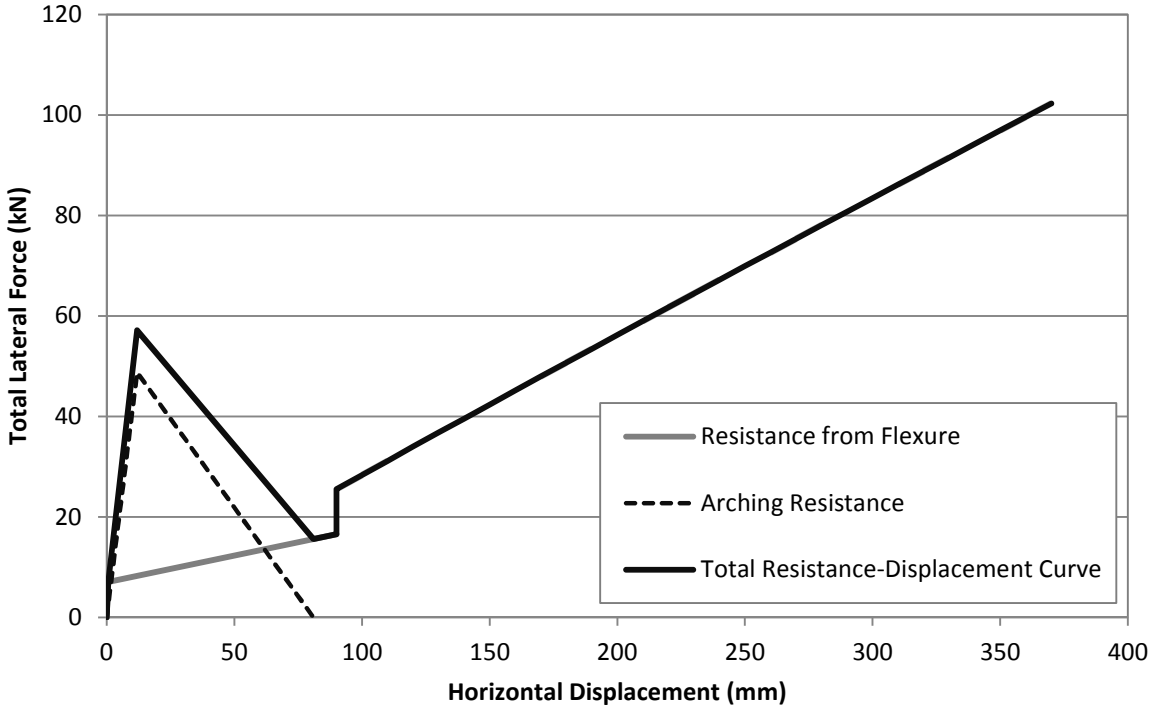

Figure 4.10: Resistance Curve for Wall URM-2 (Instant Arching)

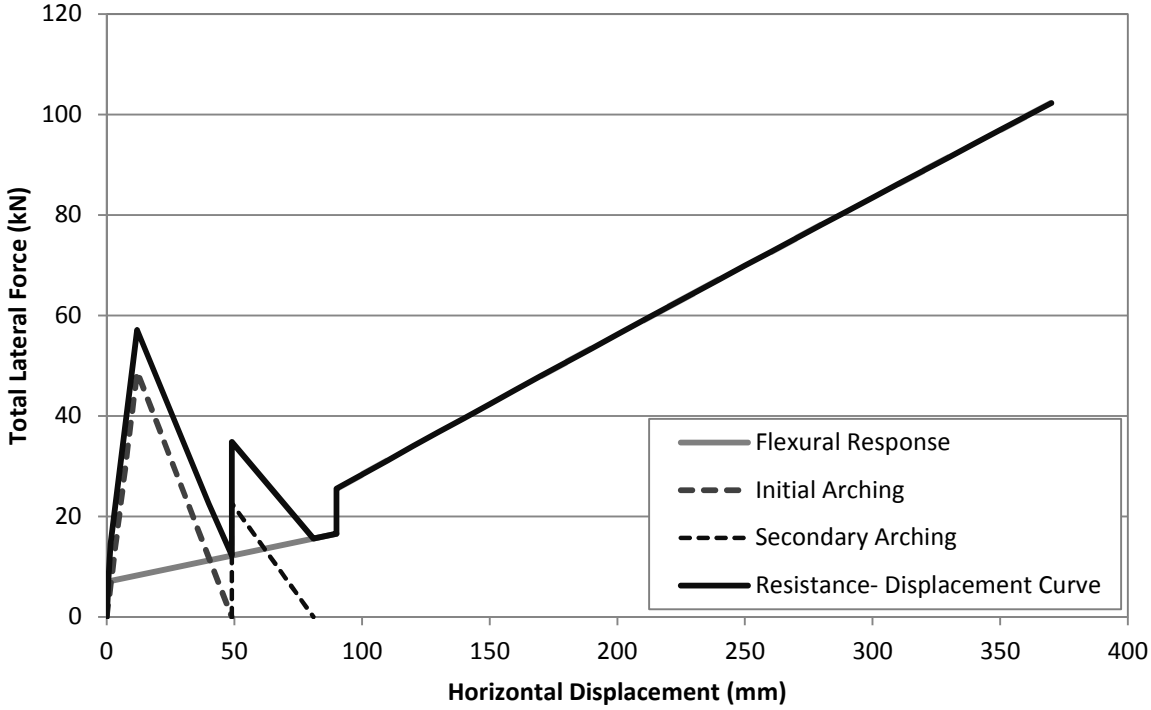

Figure 4.11: Resistance Curve for Wall URM-2 (With Initial and Secondary Arching)

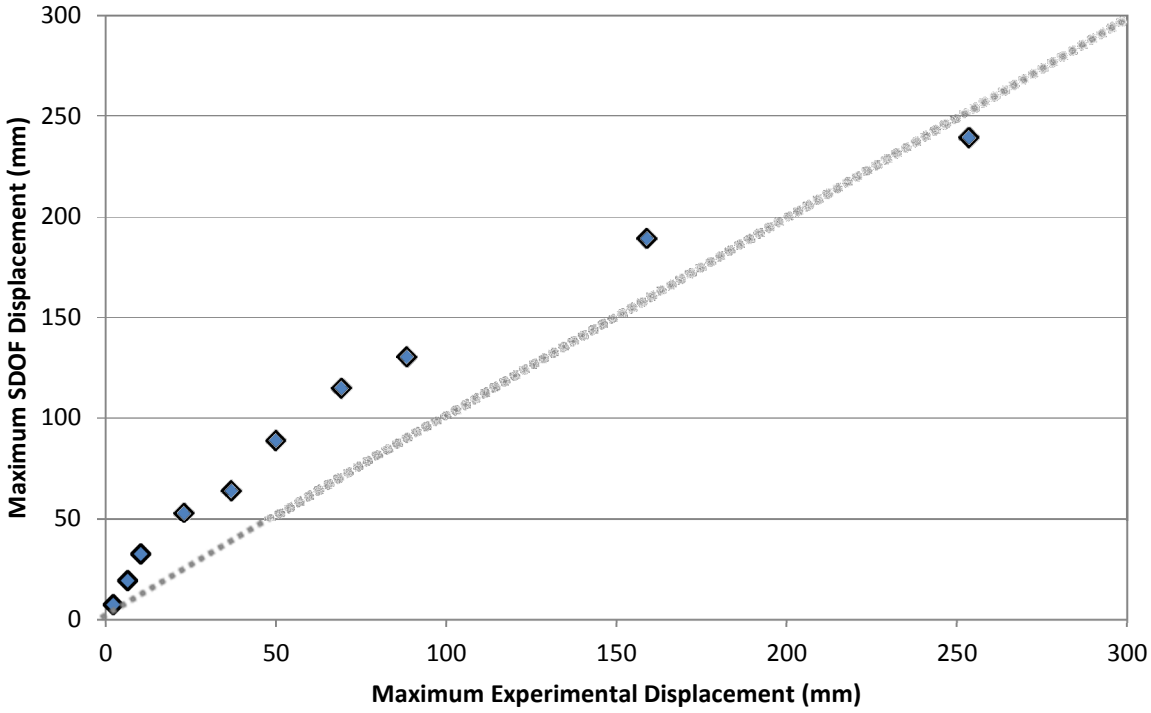

Figure 4.12: Maximum Experimental Displacement versus Maximum SDOF Displacement for Wall URM-2 (Gapped Arching)

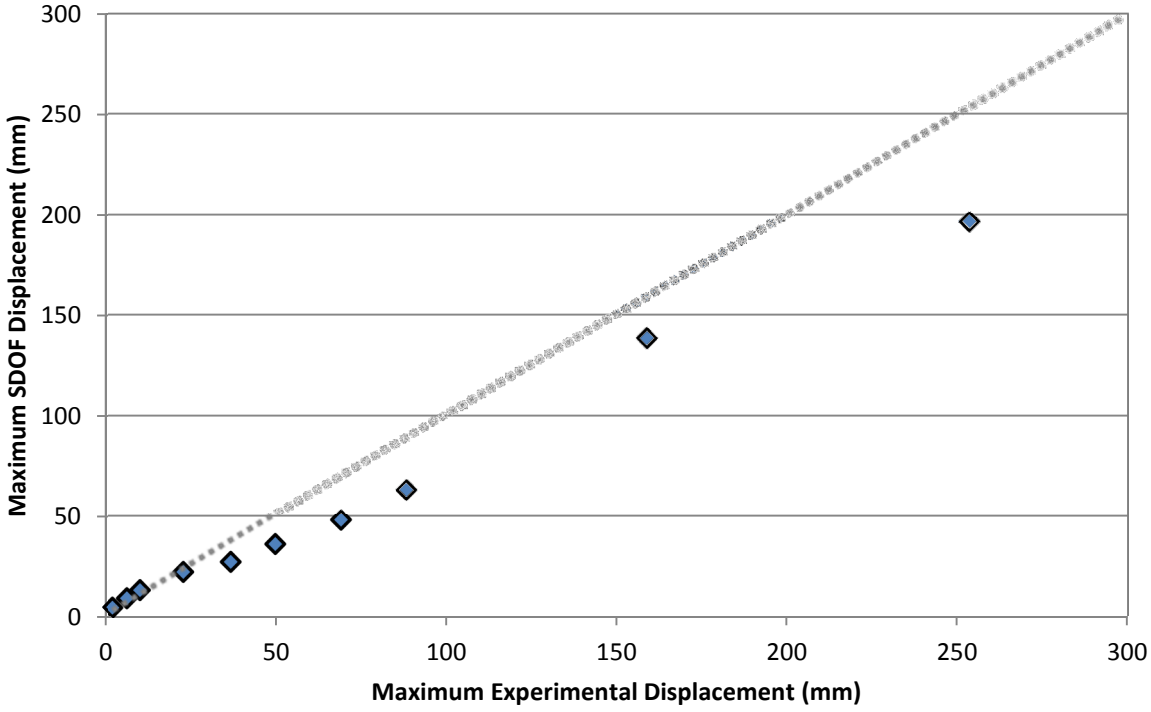

Figure 4.13: Maximum Experimental Displacement versus Maximum SDOF Displacement for Wall URM-2 (Instant Arching)

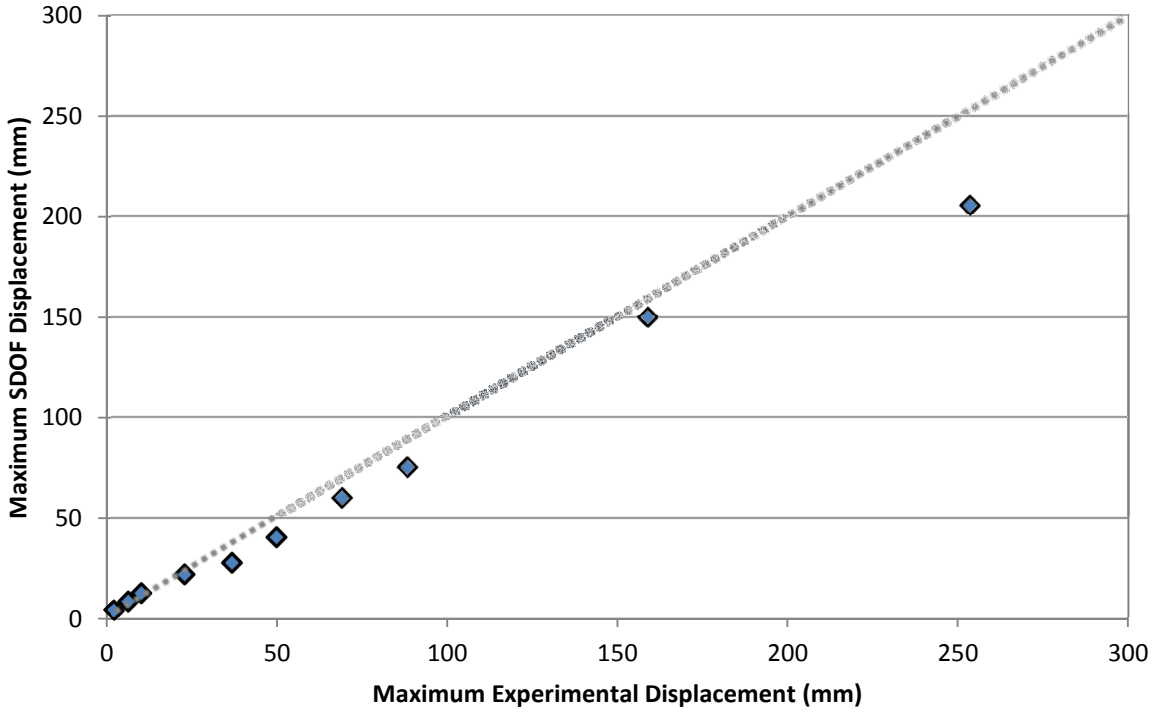

Figure 4.14: Maximum Experimental Displacement versus Maximum SDOF Displacement for Wall URM-2 (With Initial and Secondary Arching)

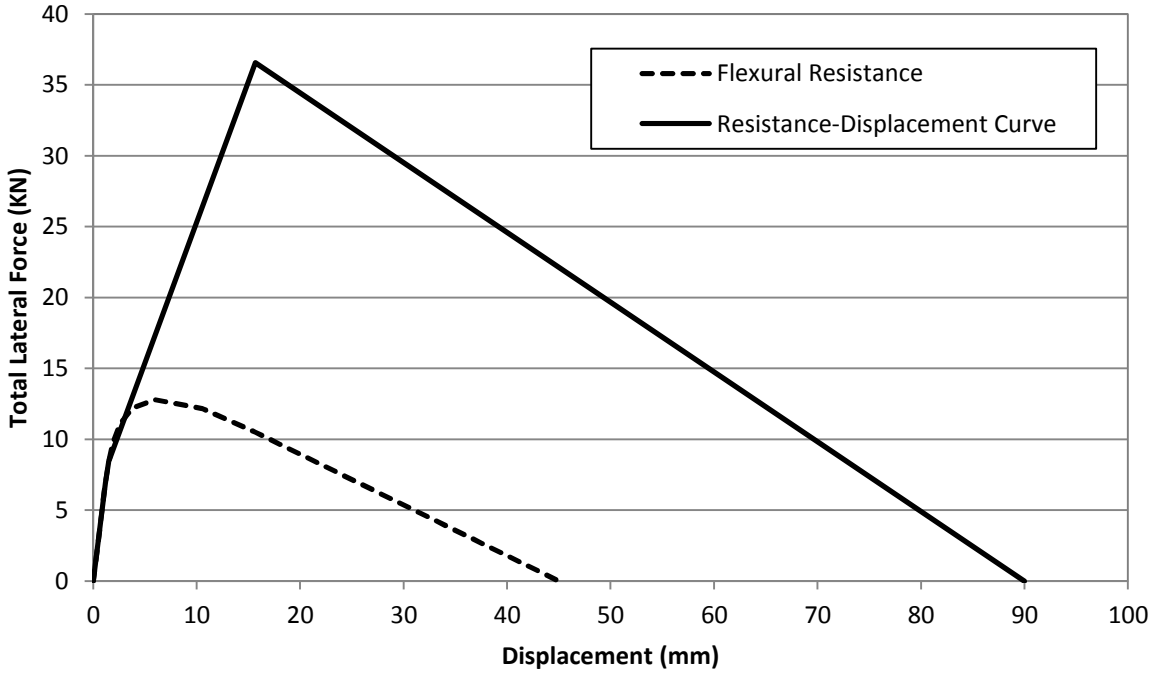

Figure 4.15: Resistance Function for Wall URM-3

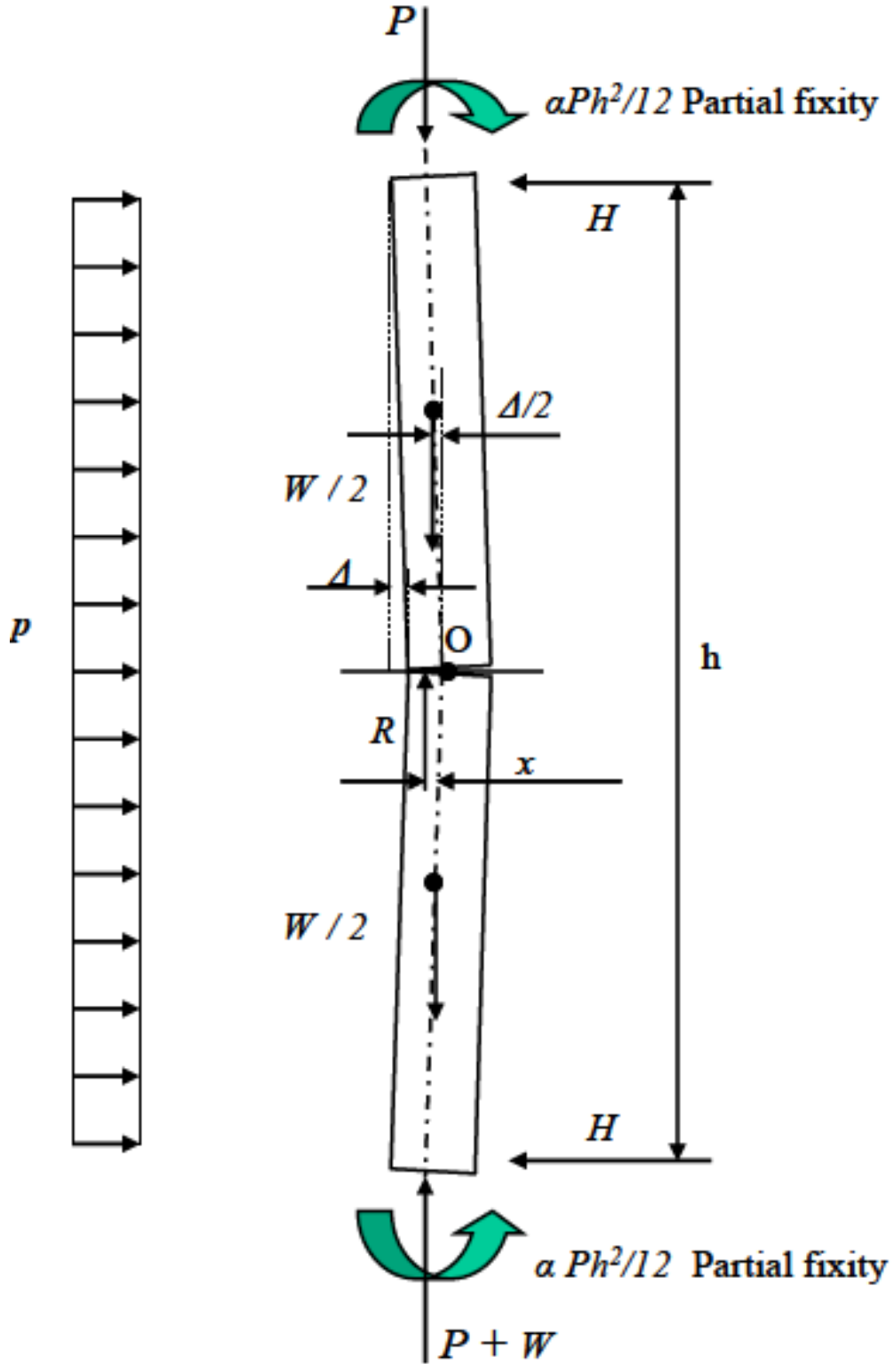

Figure 4.16: Free Body Diagram of Wall (Moradi et al., 2008)

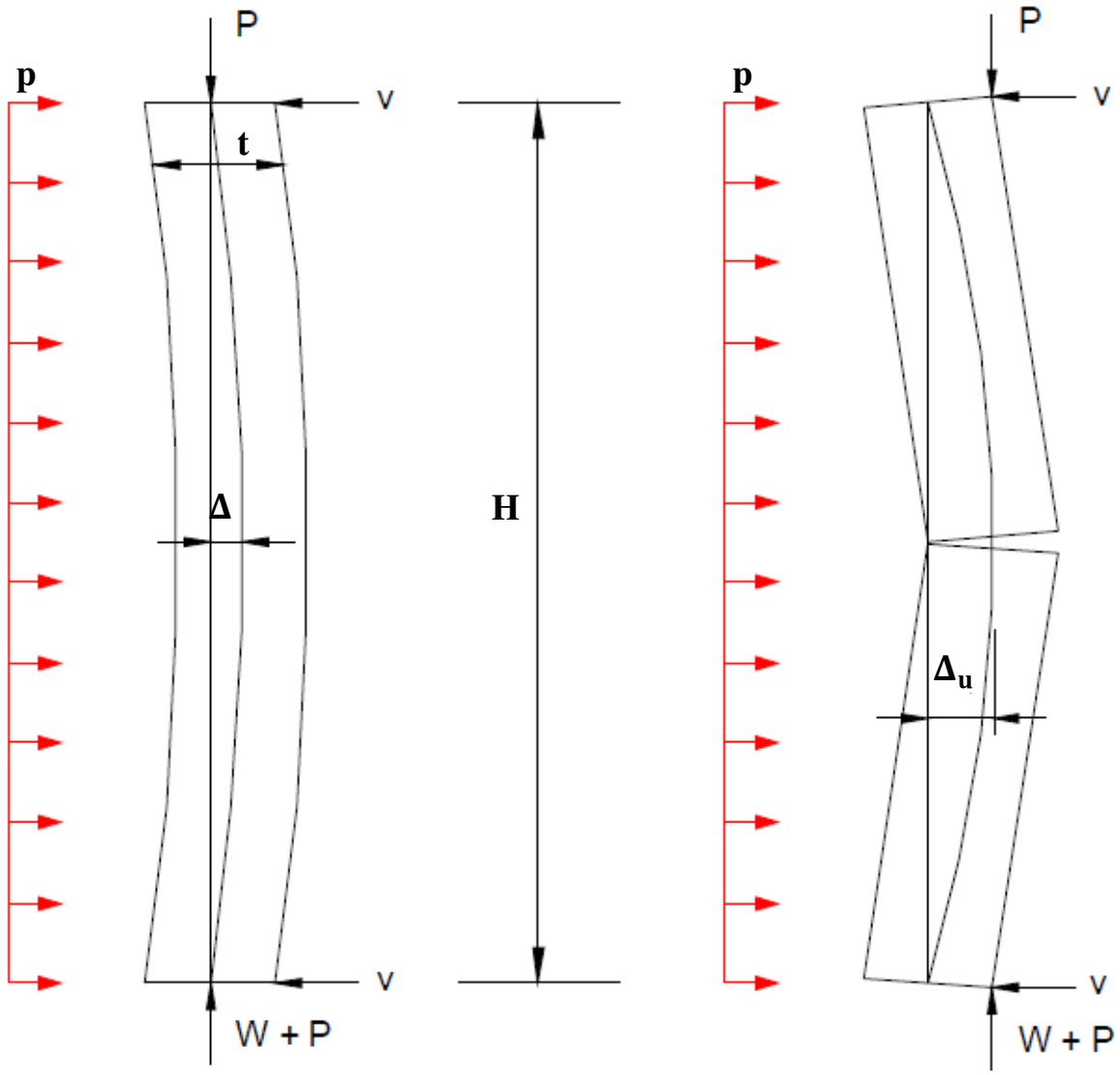

Figure 4.17: a) Flexural Response; b) Axial Load Arching

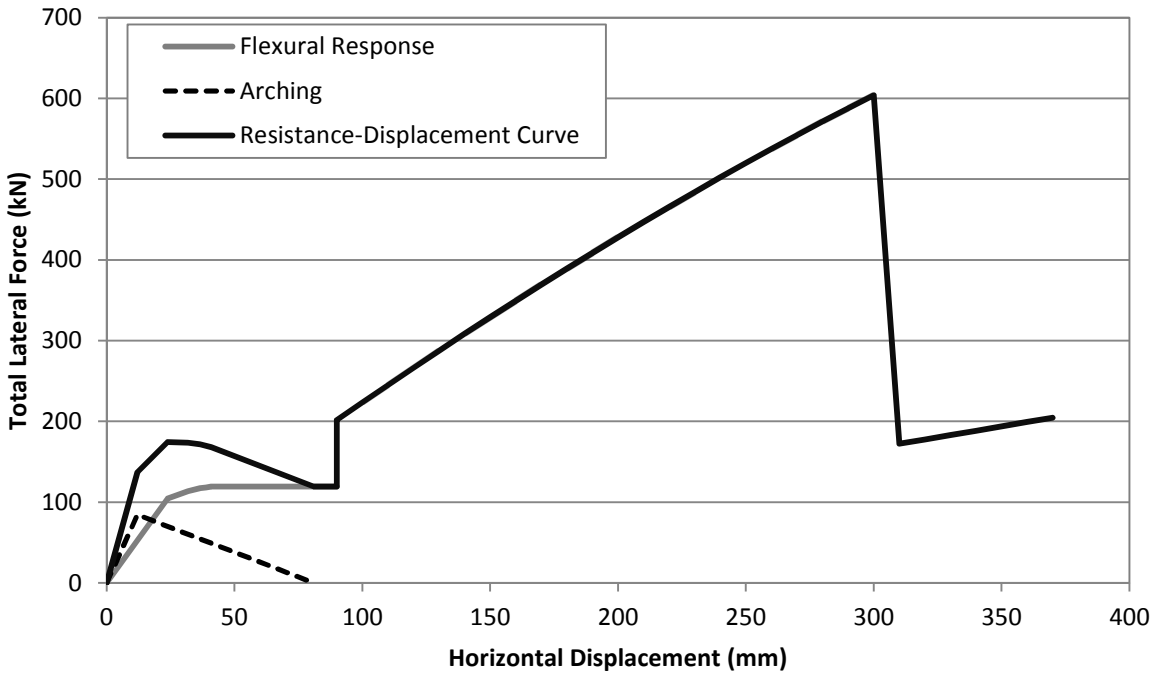

Figure 4.18: Resistance Function for Wall URM-4

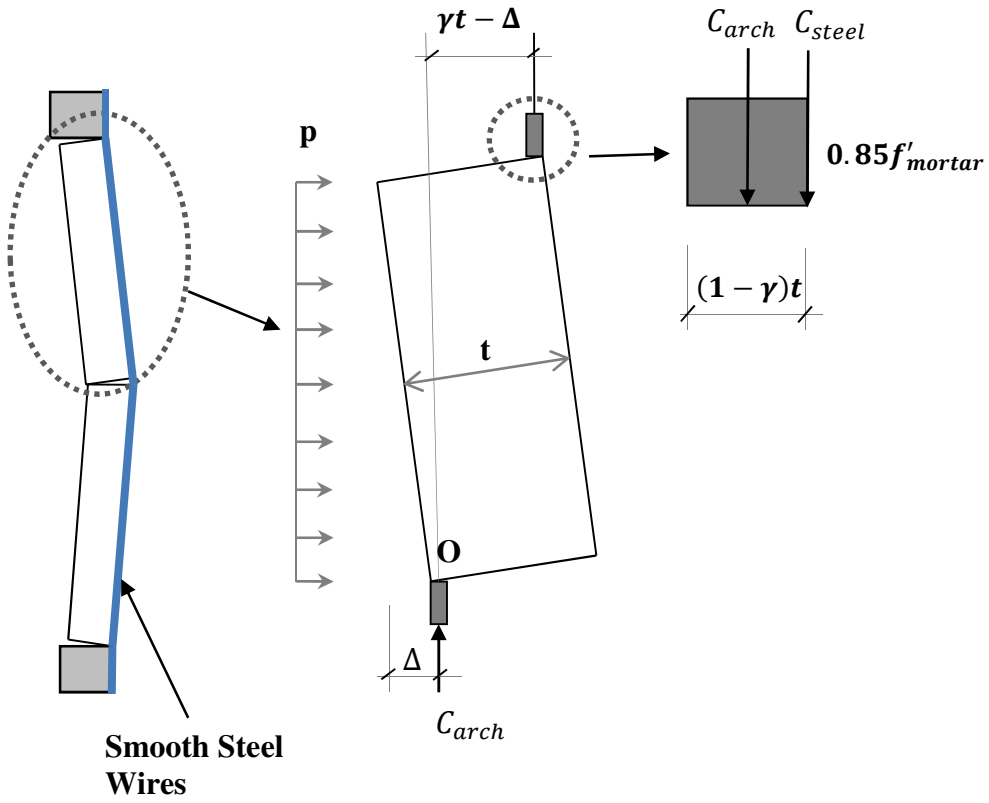

Figure 4.19: Compression of Smooth Steel Wires in URM-4 Wall Specimen

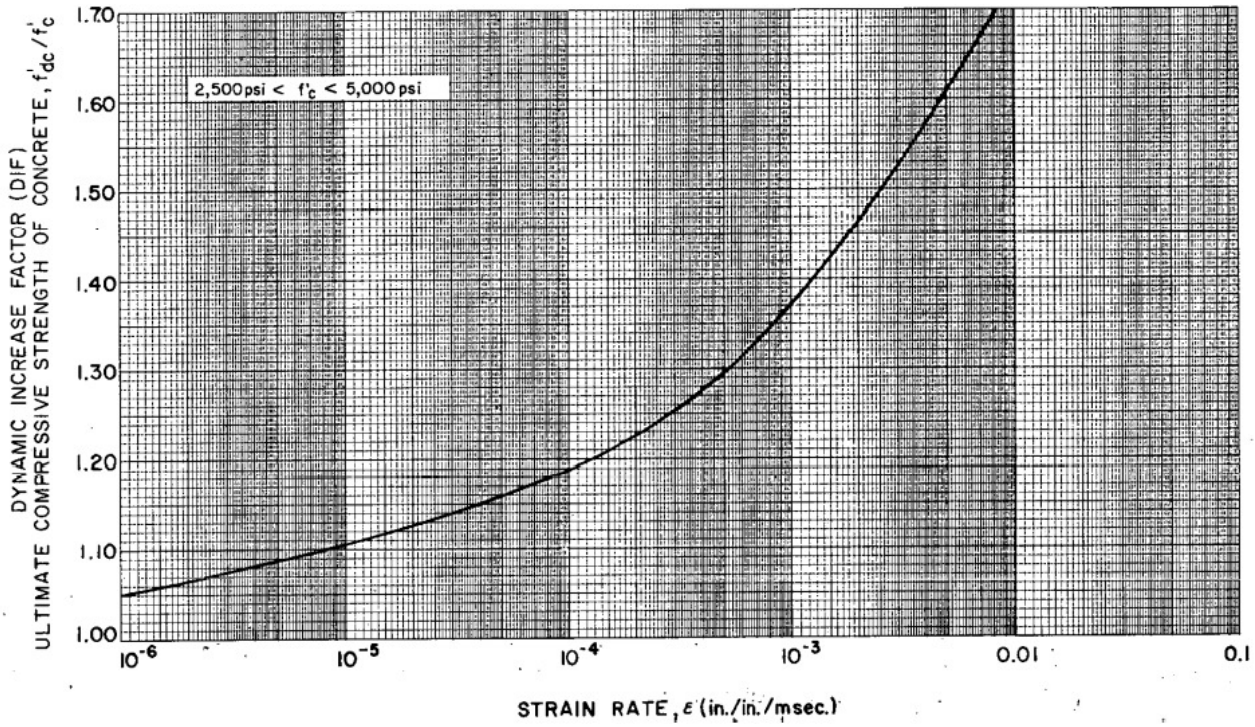

Figure 4.20: Dynamic Increase Factor for Concrete Reproduced from the US Department of the Army, the Navy, and the Air Force Structures to Resist the Effects of Accidental Explosions (TM-5-1300 1990)

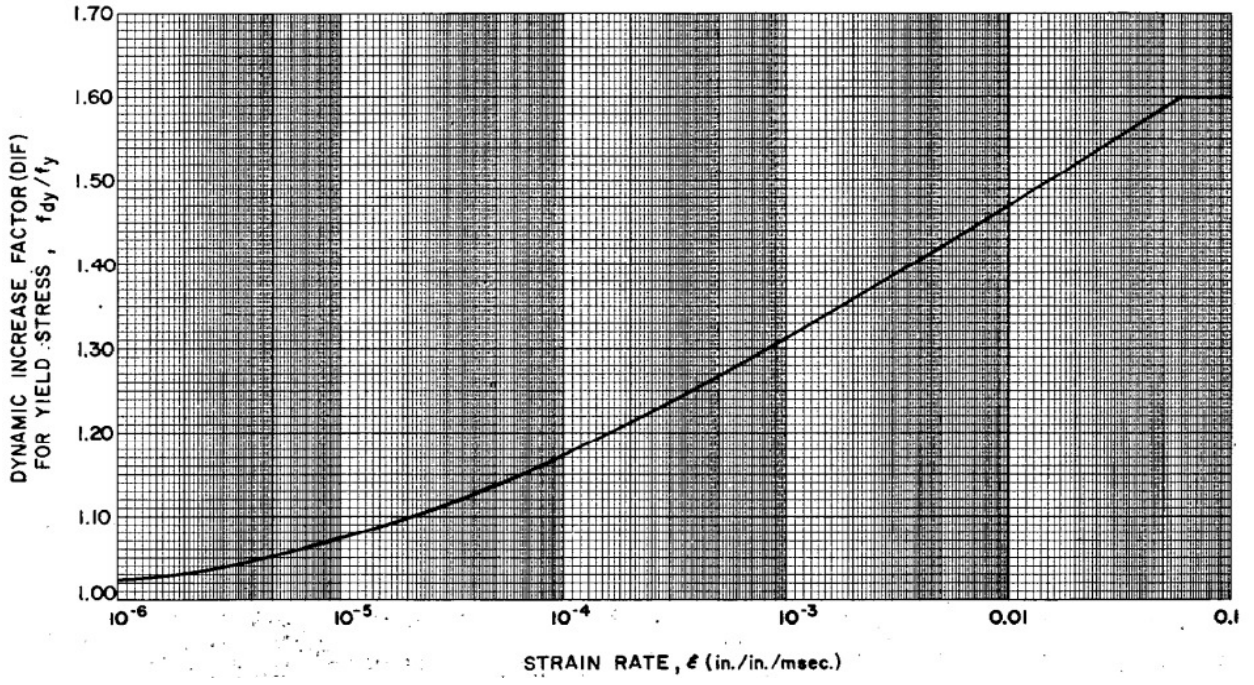

Figure 4.21: Dynamic Increase Factor for Concrete Reproduced from the US Department of the Army, the Navy, and the Air Force Structures to Resist the Effects of Accidental Explosions (TM-5-1300 1990)

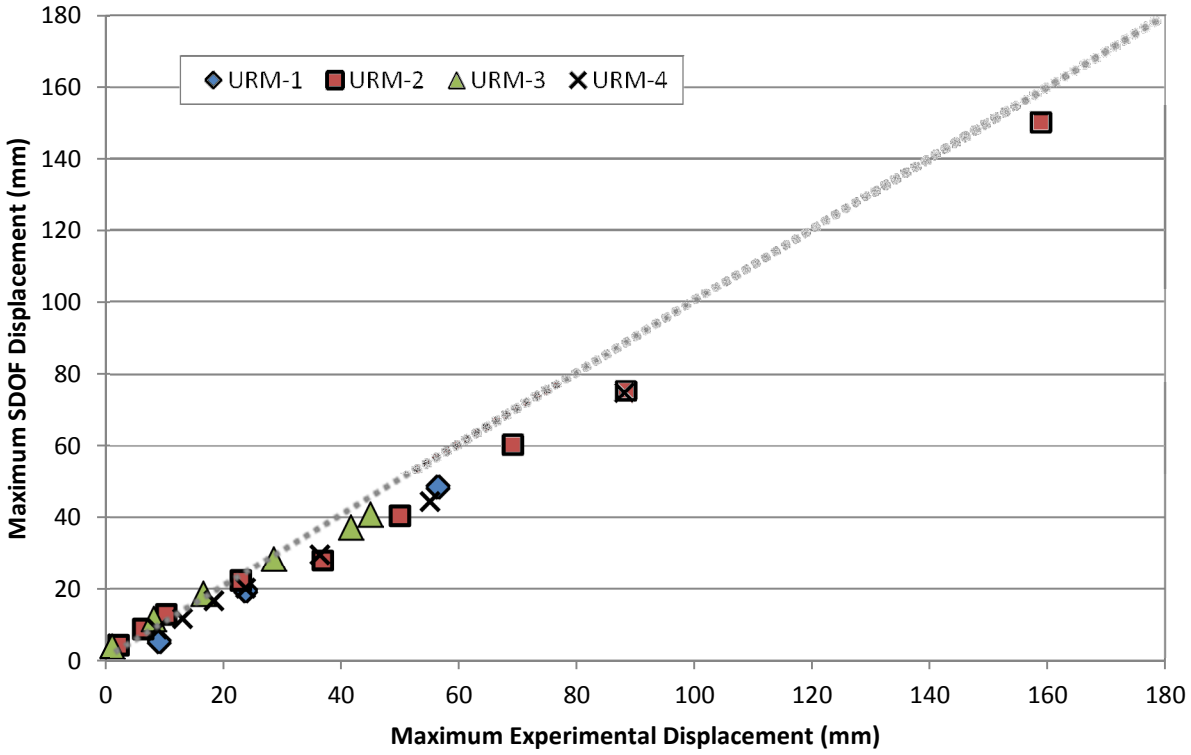

Figure 4.22: Maximum Experimental Displacement versus Maximum SDOF Displacement for all Wall Specimens

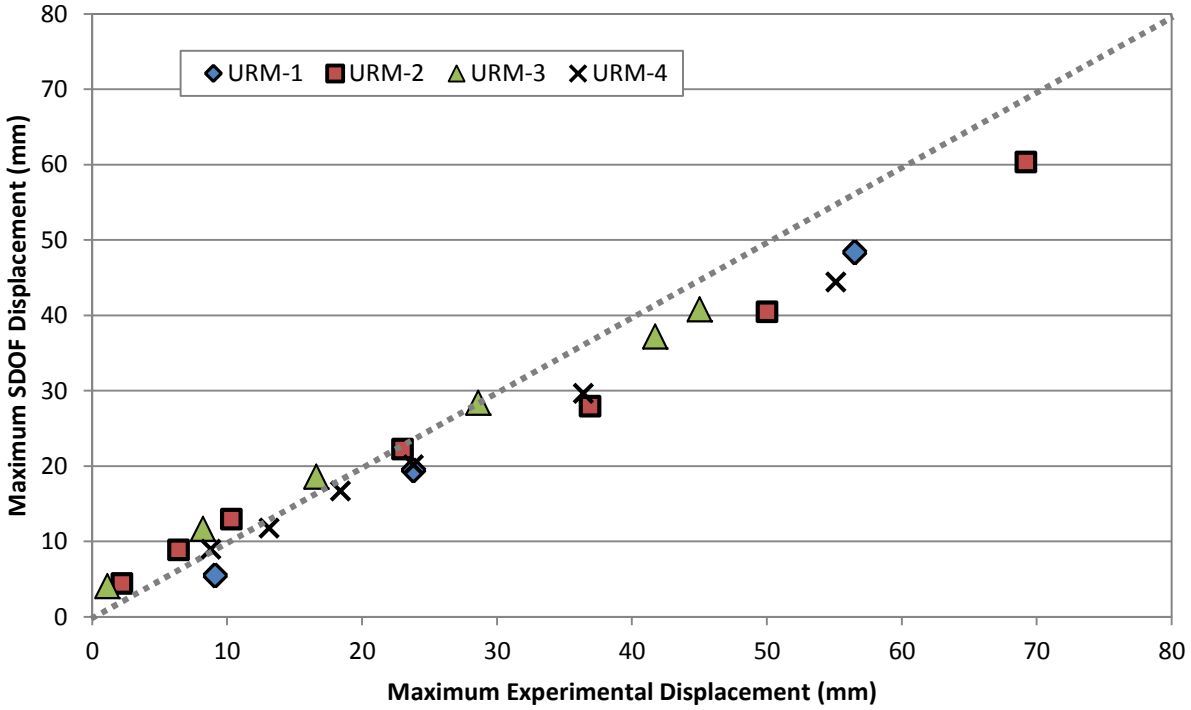

Figure 4.23: Maximum Experimental Displacement versus Maximum SDOF Displacement for all Specimens (Displacements Smaller than 80 mm)

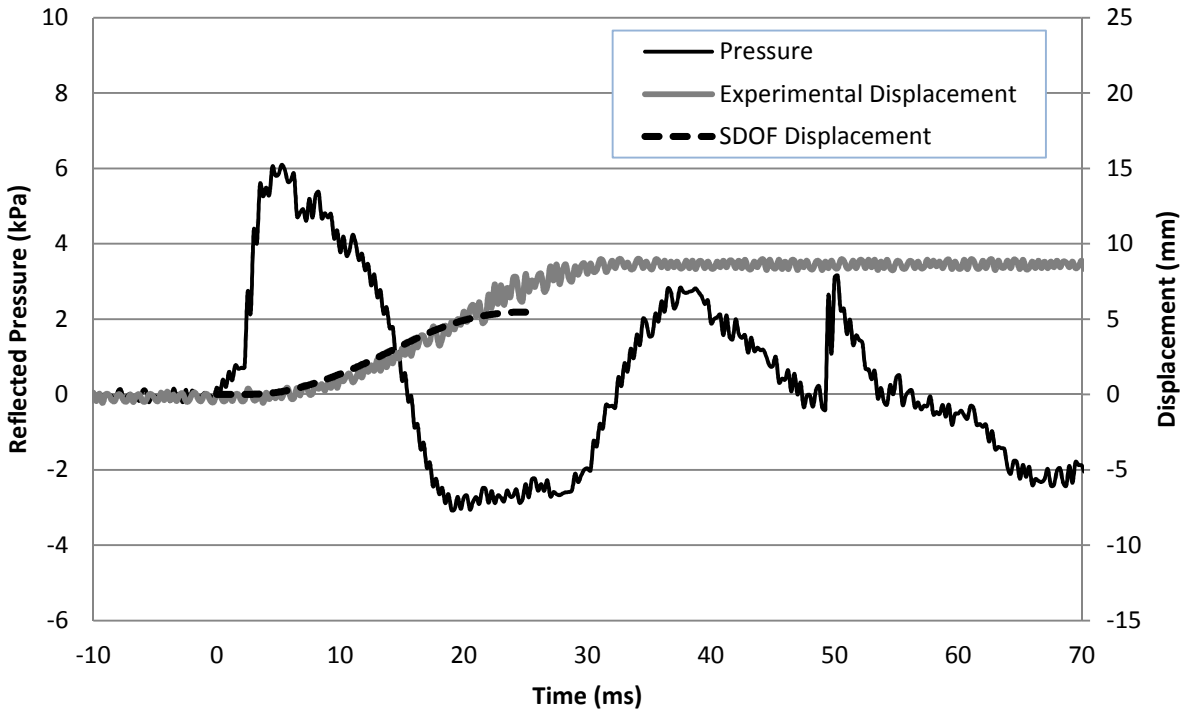

Figure 4.24: Experimentally Recorded and SDOF Predicted Mid-Height Displacement Time History for Test URM-1-1

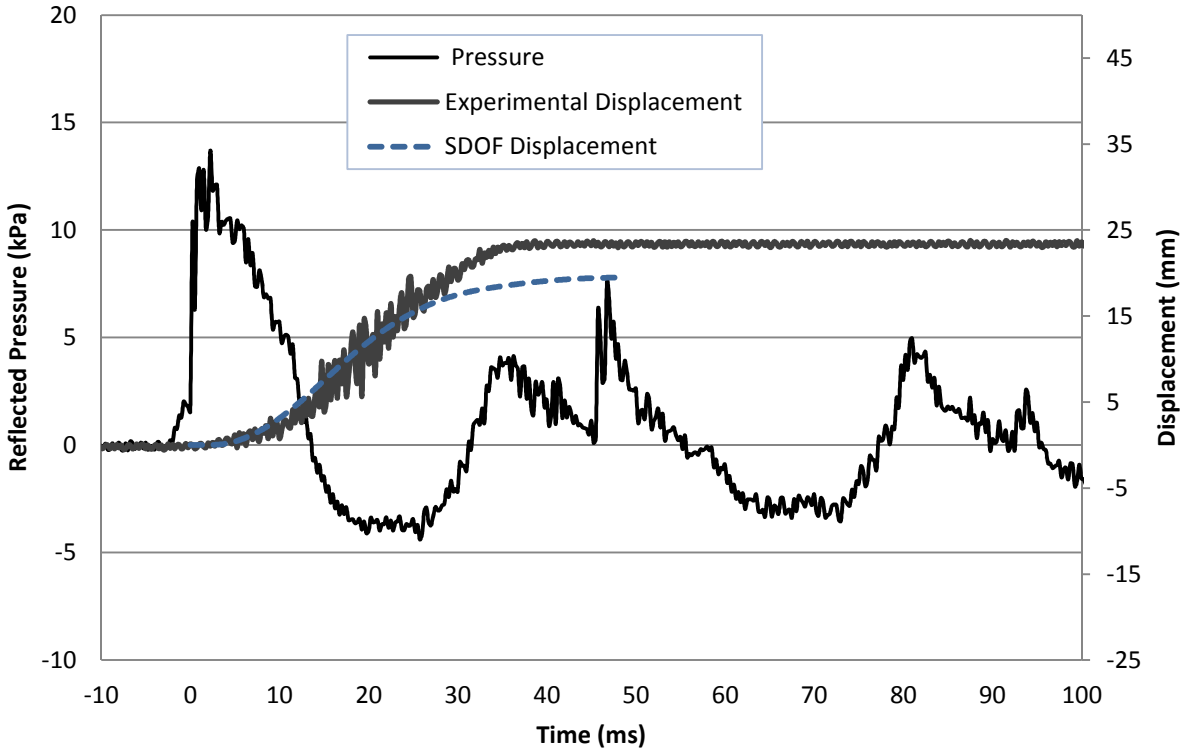

Figure 4.25: Experimentally Recorded and SDOF Predicted Mid-Height Displacement Time History for Test URM-1-2

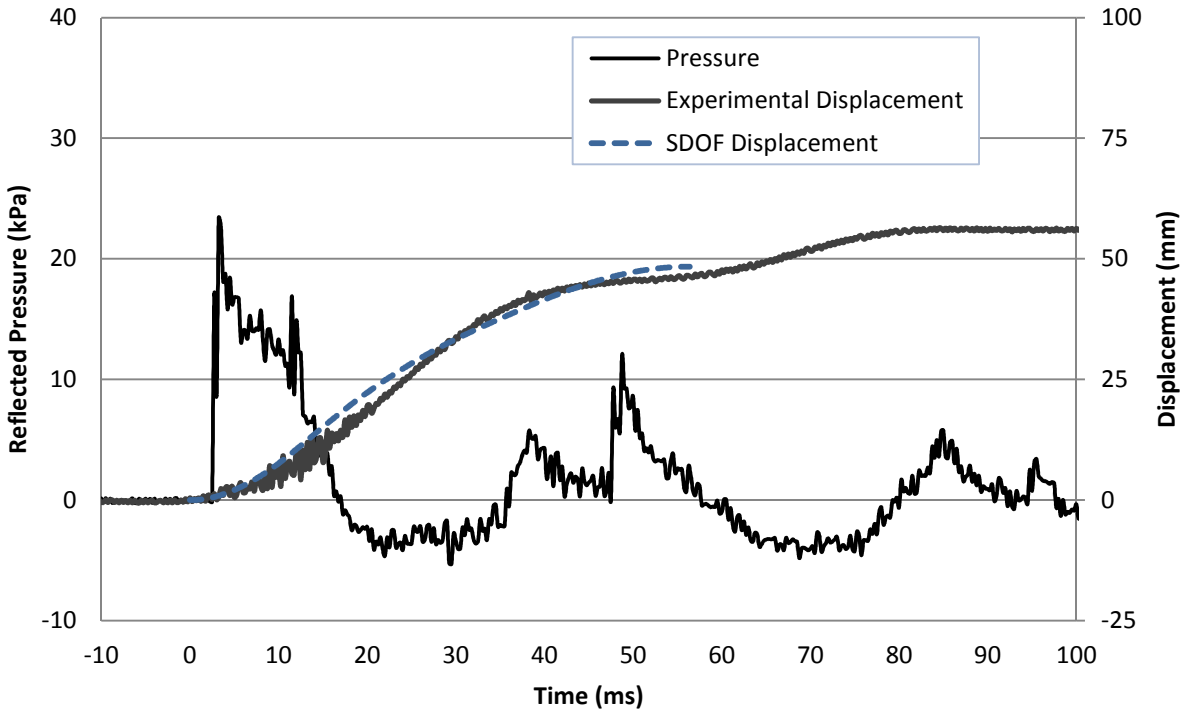

Figure 4.26: Experimentally Recorded and SDOF Predicted Mid-Height Displacement Time History for Test URM-1-3

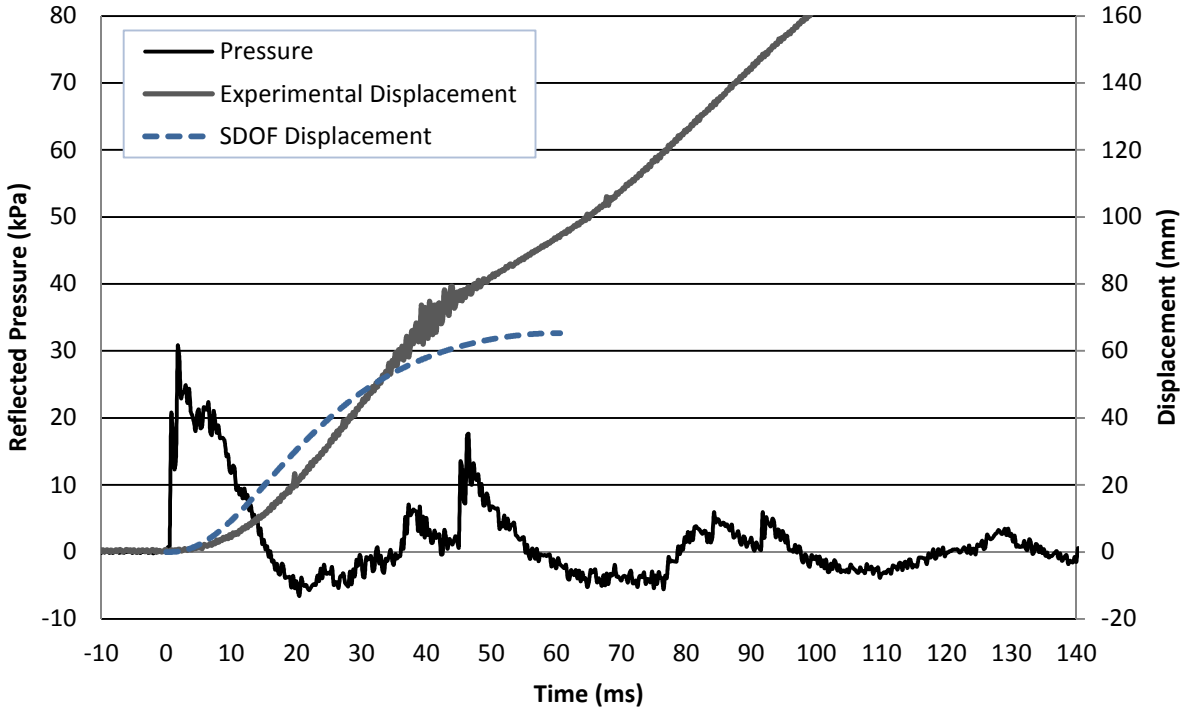

Figure 4.27: Experimentally Recorded and SDOF Predicted Mid-Height Displacement Time History for Test URM-1-4

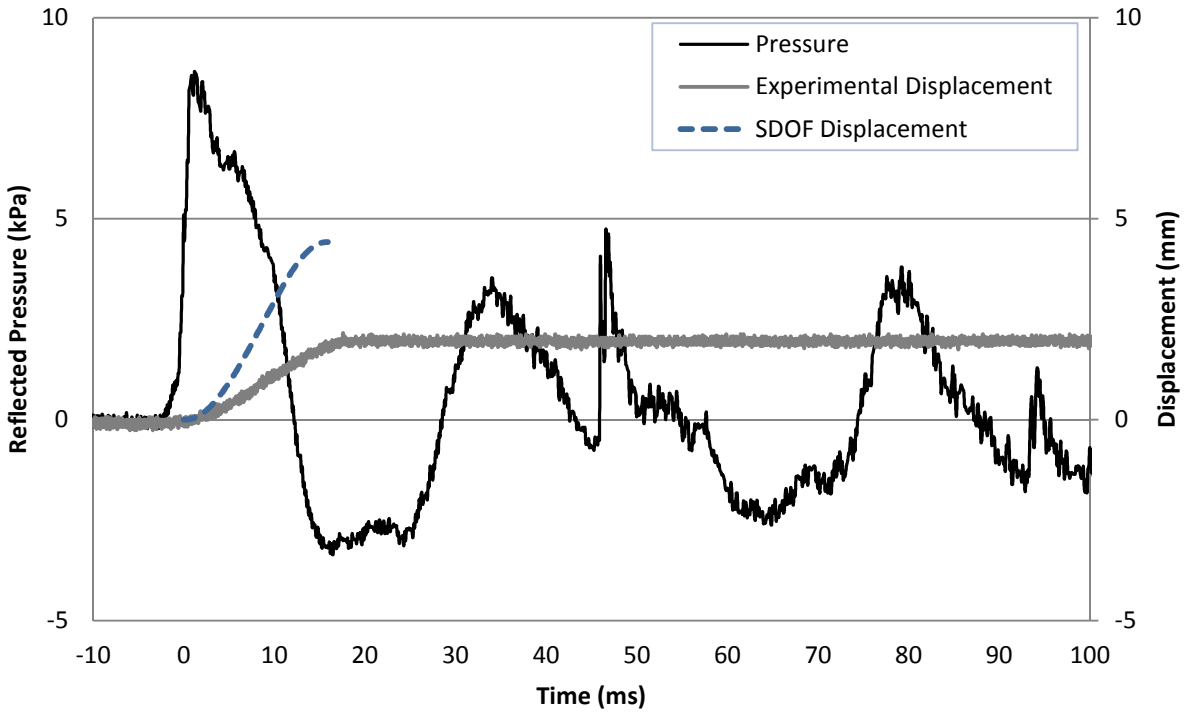

Figure 4.28: Experimentally Recorded and SDOF Predicted Mid-Height Displacement Time History for Test URM-2-1

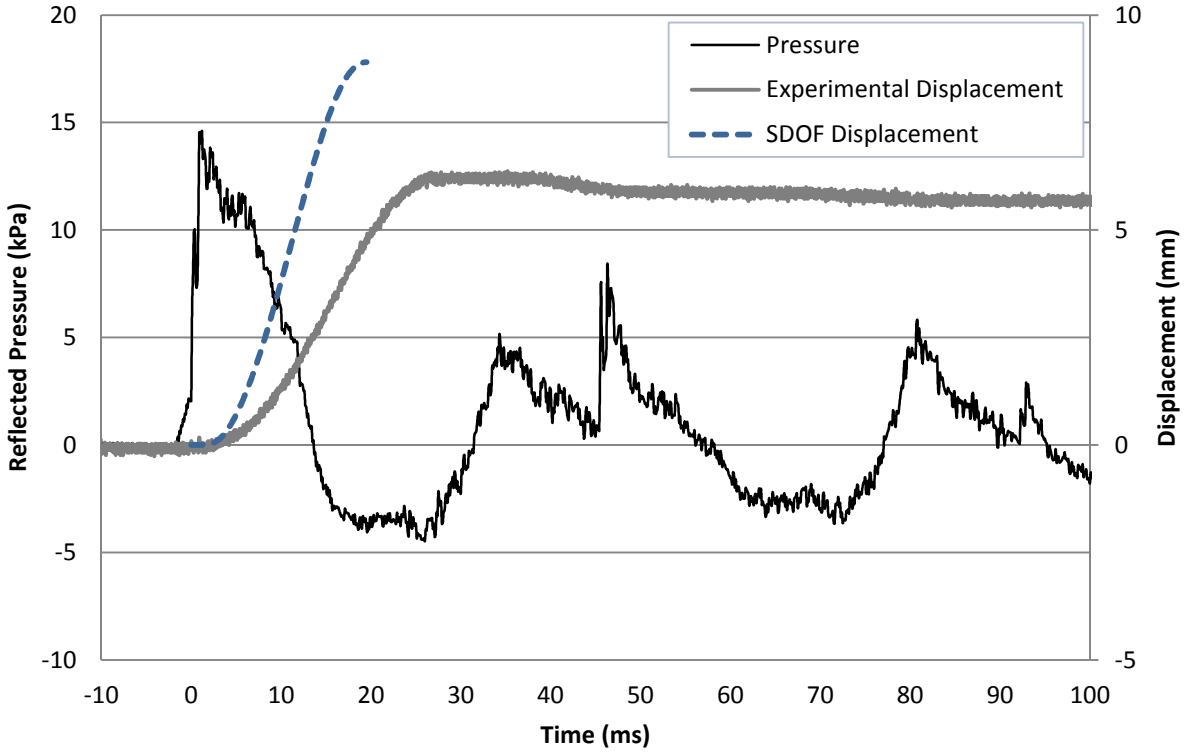

Figure 4.29: Experimentally Recorded and SDOF Predicted Mid-Height Displacement Time History for Test URM-2-2

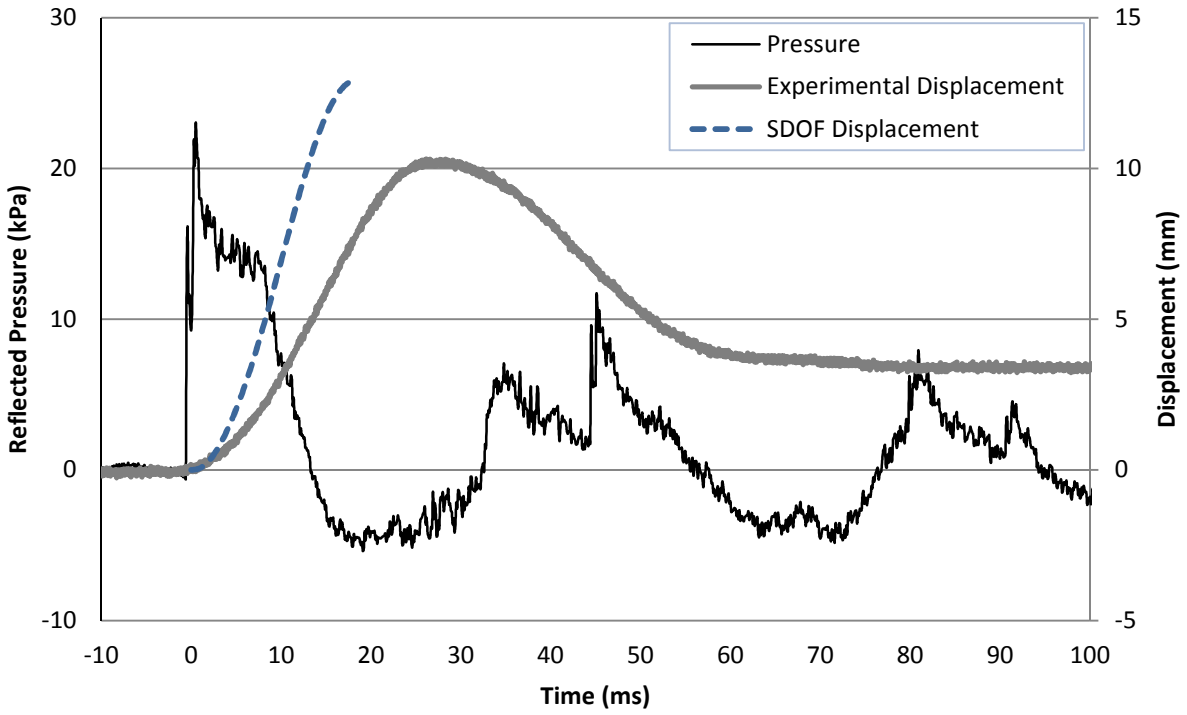

Figure 4.30: Experimentally Recorded and SDOF Predicted Mid-Height Displacement Time History for Test URM-2-3

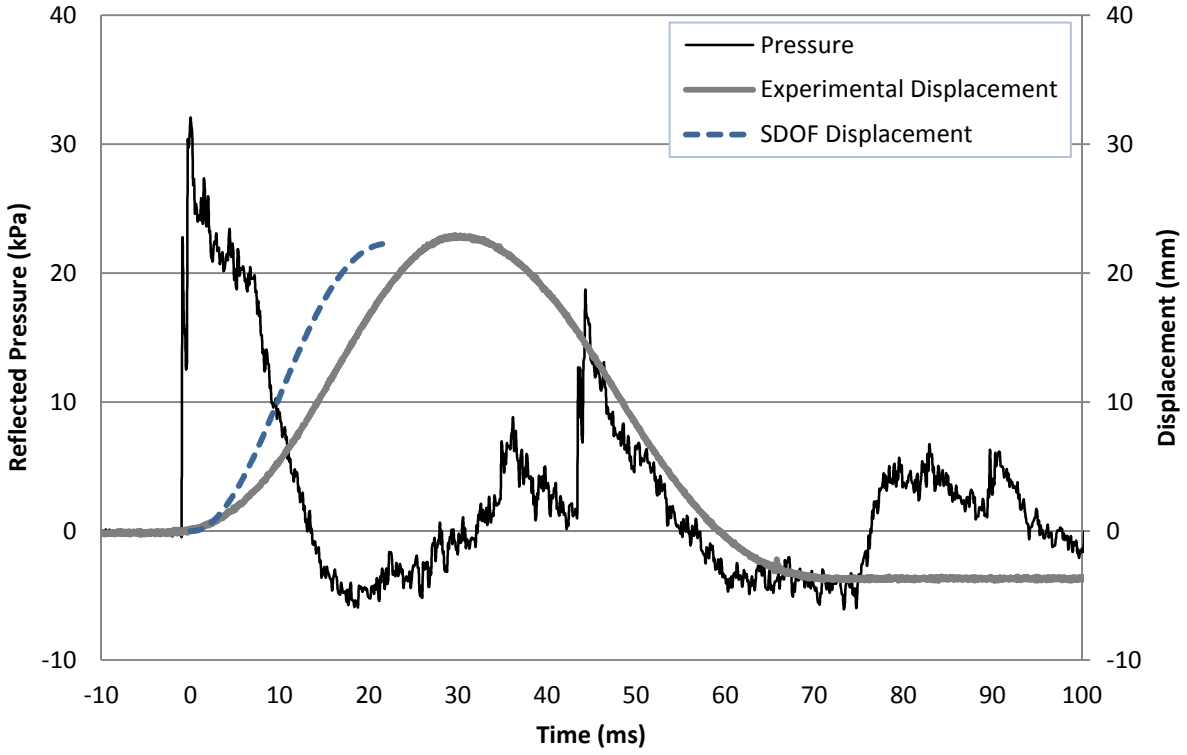

Figure 4.31: Experimentally Recorded and SDOF Predicted Mid-Height Displacement Time History for Test URM-2-4

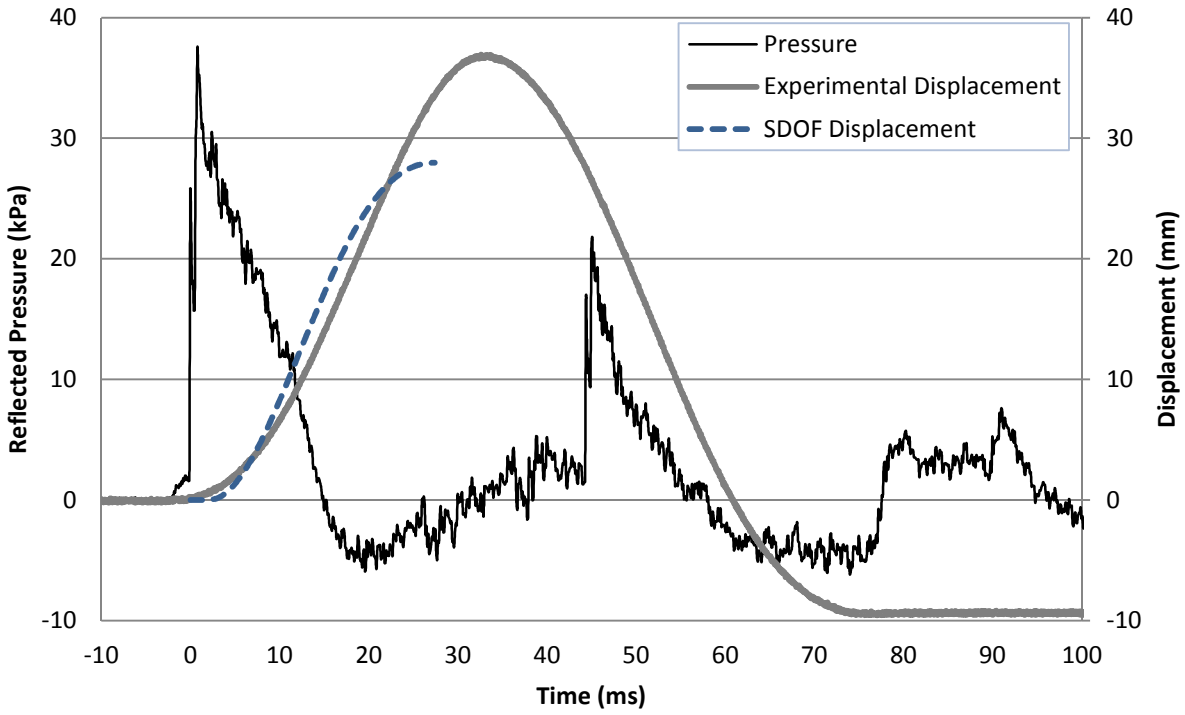

Figure 4.32: Experimentally Recorded and SDOF Predicted Mid-Height Displacement Time History for Test URM-2-5

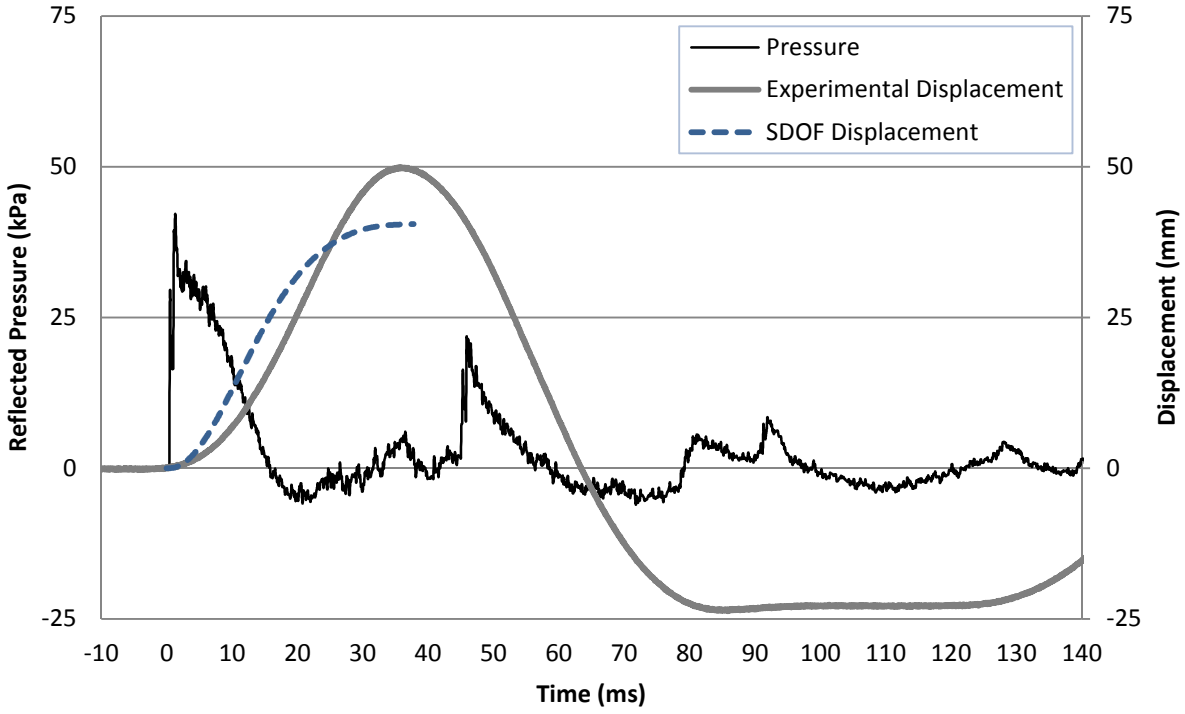

Figure 4.33: Experimentally Recorded and SDOF Predicted Mid-Height Displacement Time History for Test URM-2-6

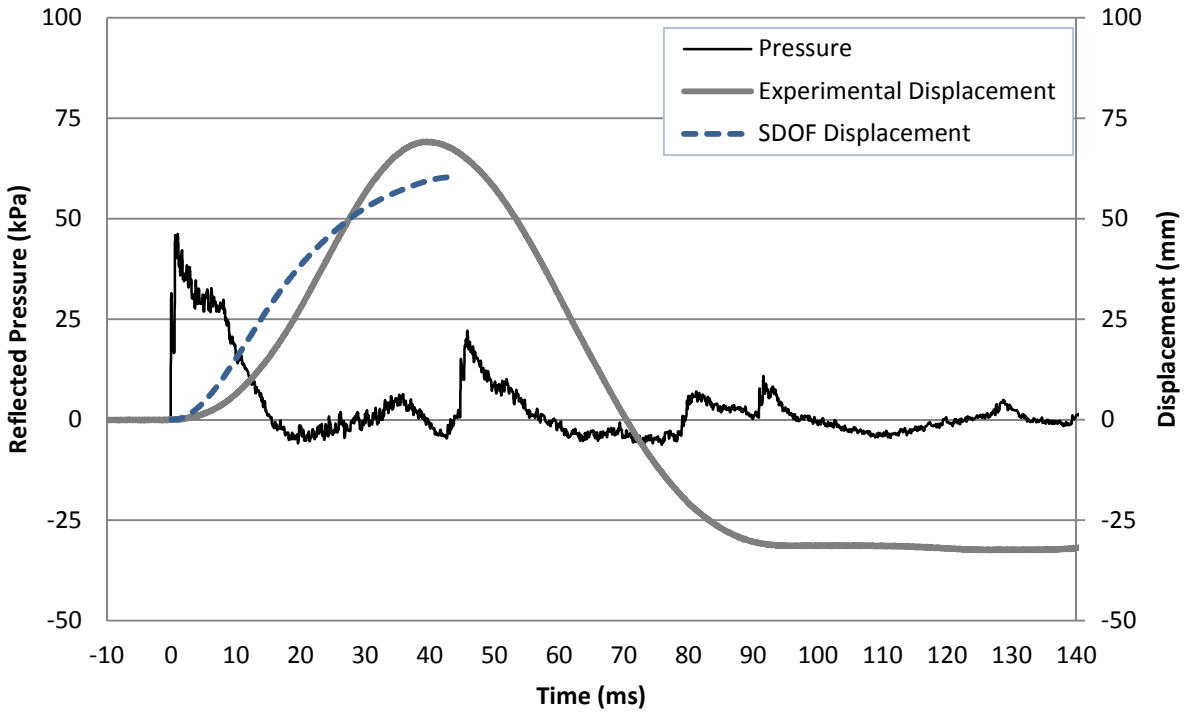

Figure 4.34: Experimentally Recorded and SDOF Predicted Mid-Height Displacement Time History for Test URM-2-7

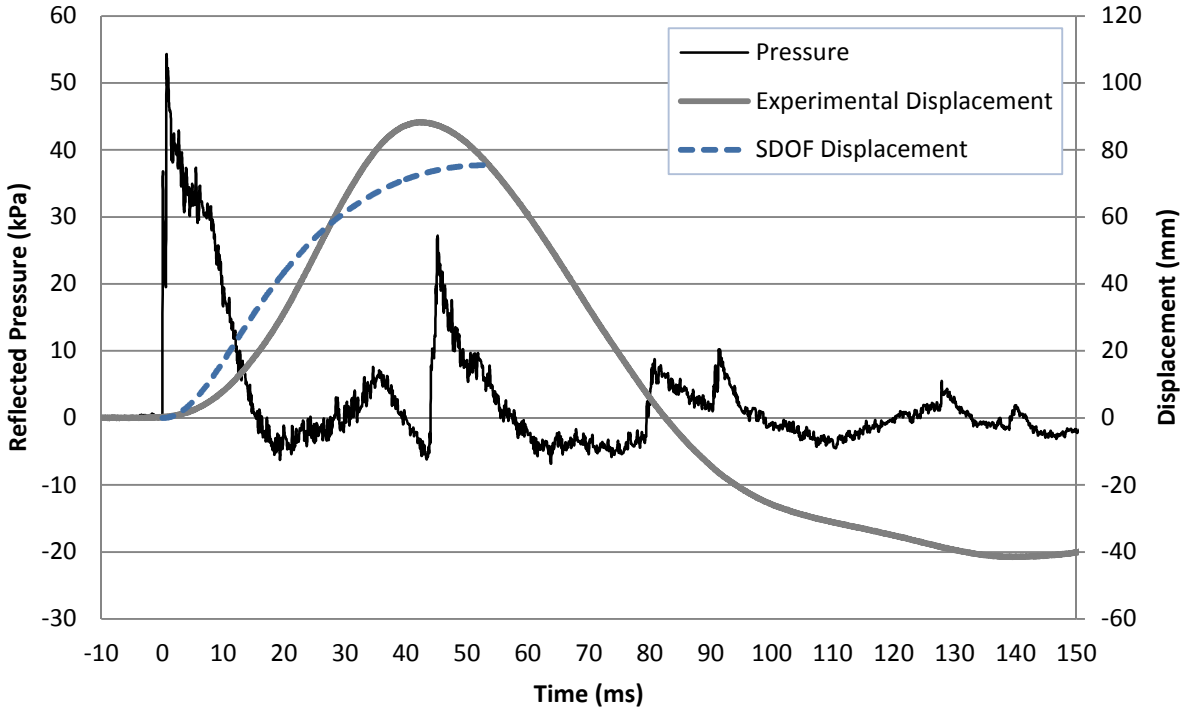

Figure 4.35: Experimentally Recorded and SDOF Predicted Mid-Height Displacement Time History for Test URM-2-8

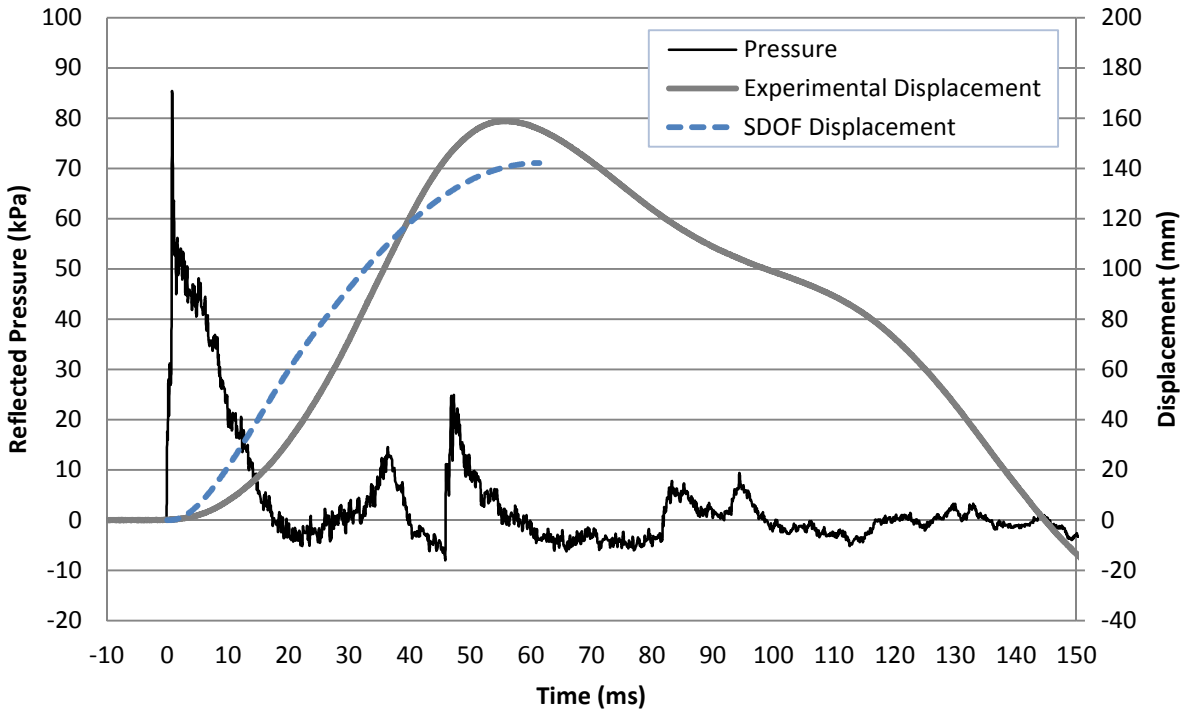

Figure 4.36: Experimentally Recorded and SDOF Predicted Mid-Height Displacement Time History for Test URM-2-9

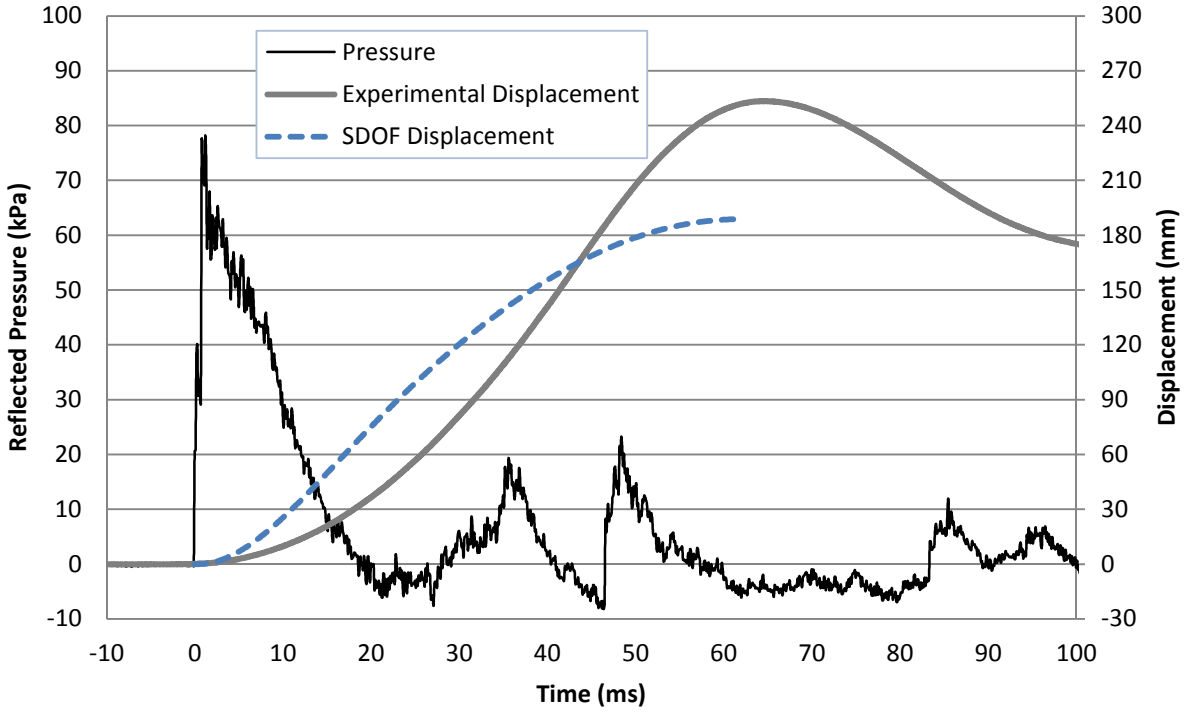

Figure 4.37: Experimentally Recorded and SDOF Predicted Mid-Height Displacement Time History for Test URM-2-10

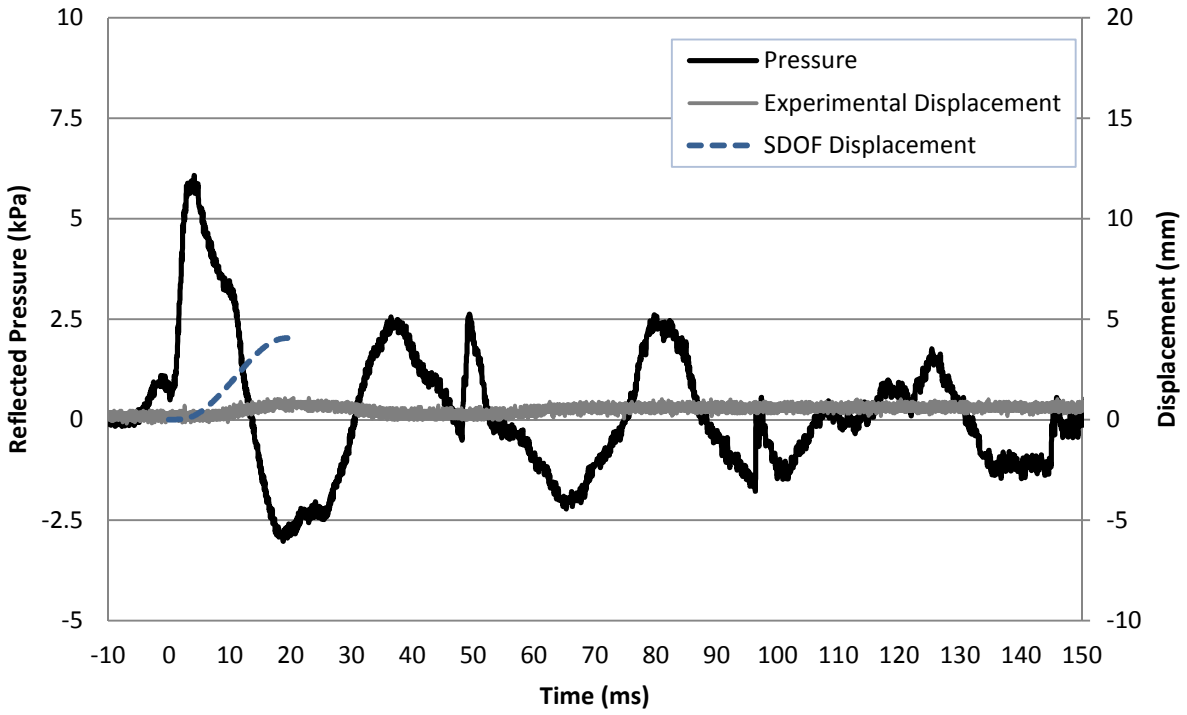

Figure 4.38: Experimentally Recorded and SDOF Predicted Mid-Height Displacement Time History for Test URM-3-1

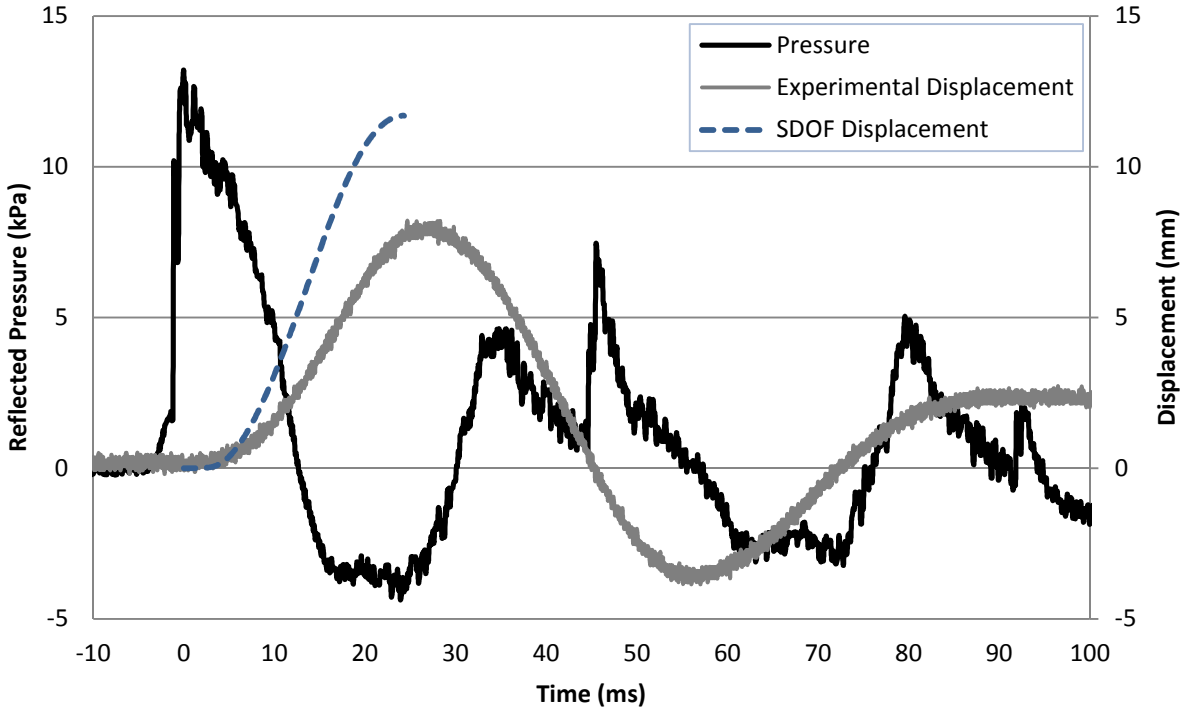

Figure 4.39: Experimentally Recorded and SDOF Predicted Mid-Height Displacement Time History for Test URM-3-2

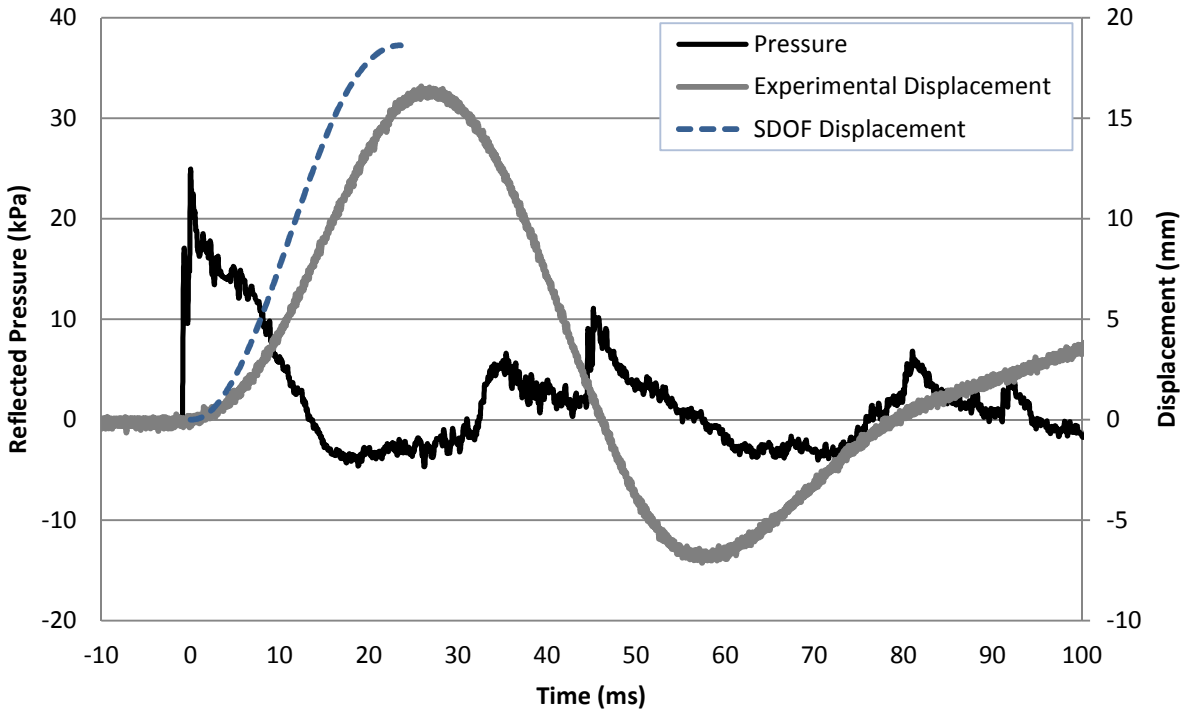

Figure 4.40: Experimentally Recorded and SDOF Predicted Mid-Height Displacement Time History for Test URM-3-3

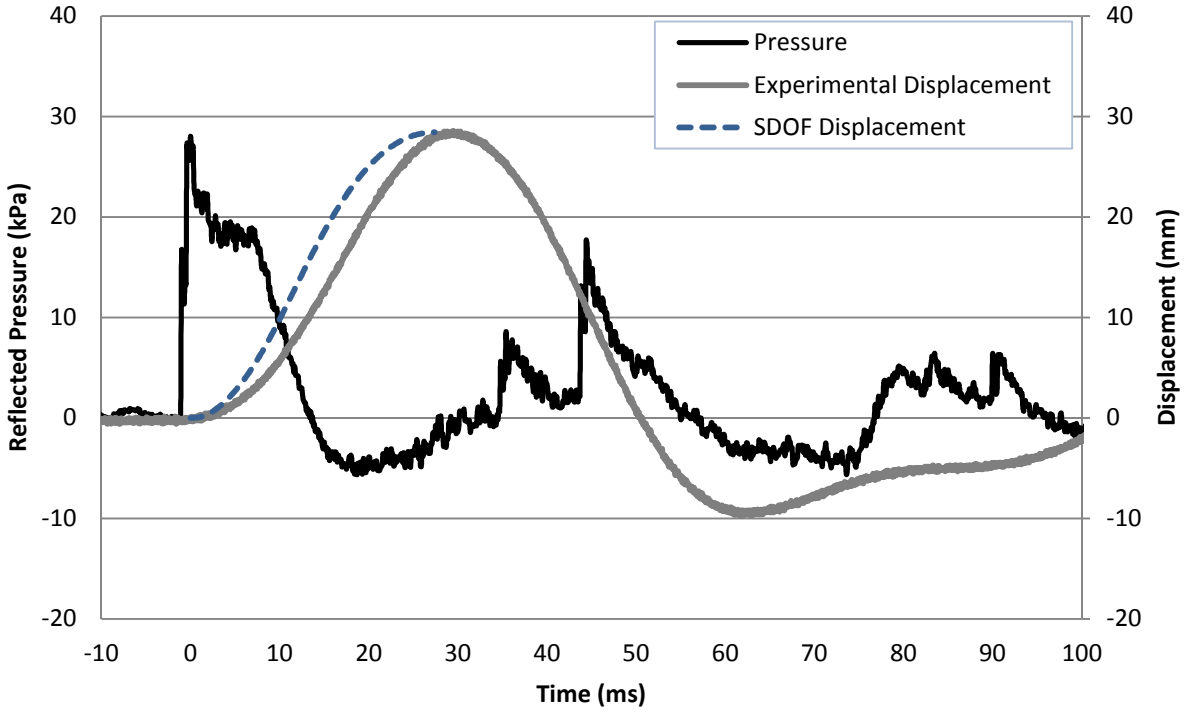

Figure 4.41: Experimentally Recorded and SDOF Predicted Mid-Height Displacement Time History for Test URM-3-4

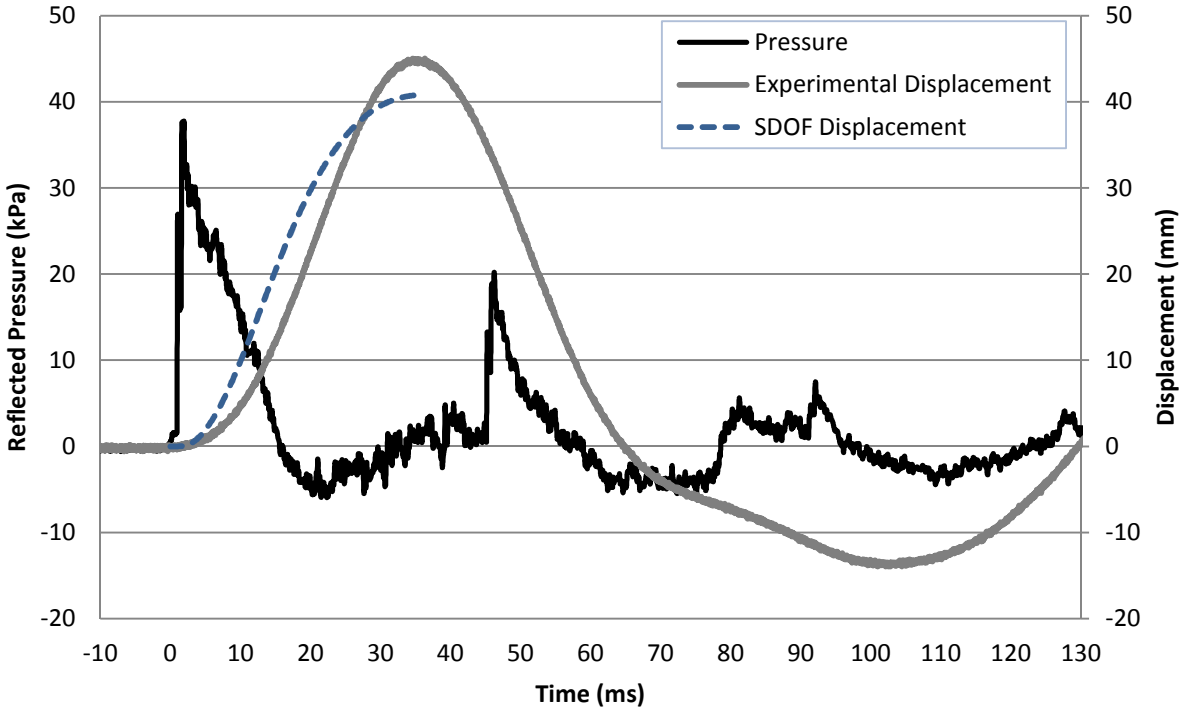

Figure 4.42: Experimentally Recorded and SDOF Predicted Mid-Height Displacement Time History for Test URM-3-5

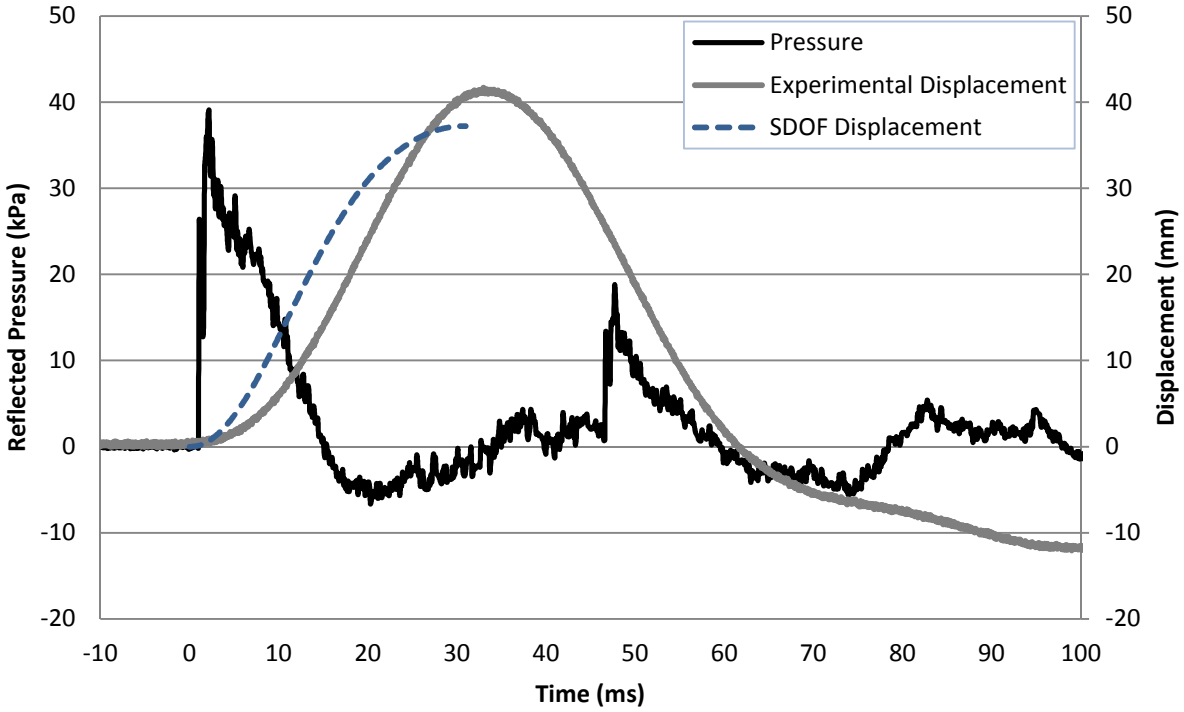

Figure 4.43: Experimentally Recorded and SDOF Predicted Mid-Height Displacement Time History for Test URM-3-6

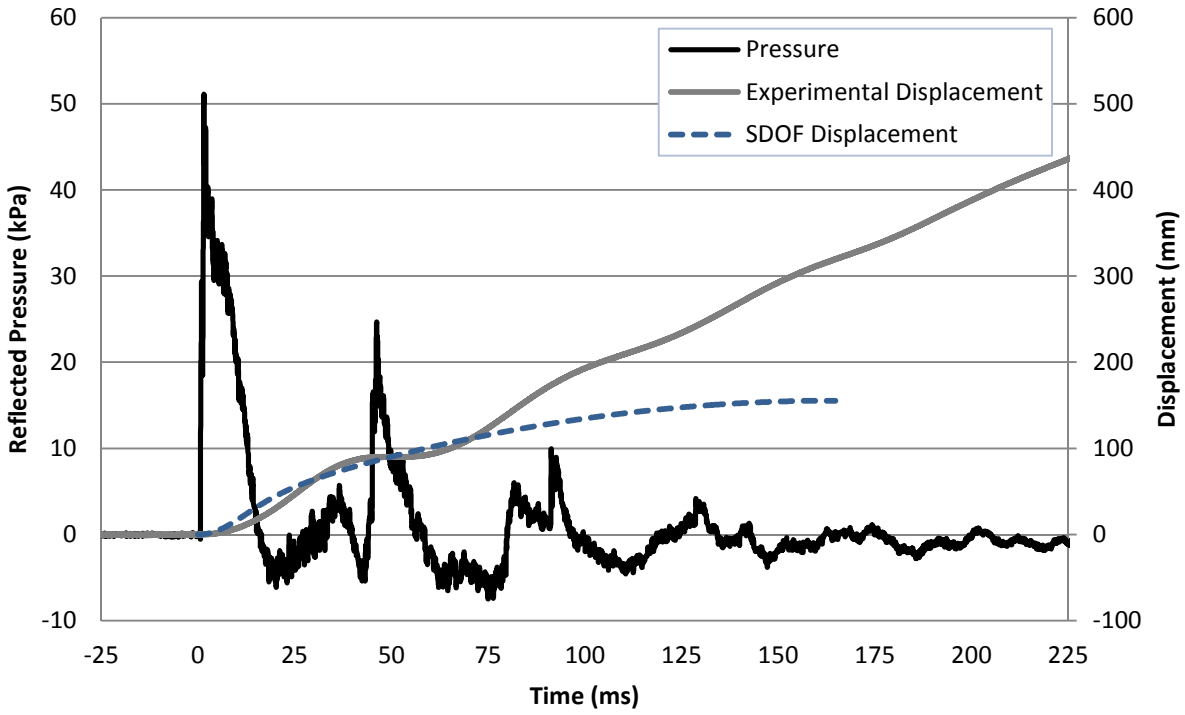

Figure 4.44: Experimentally Recorded and SDOF Predicted Mid-Height Displacement Time History for Test URM-3-7

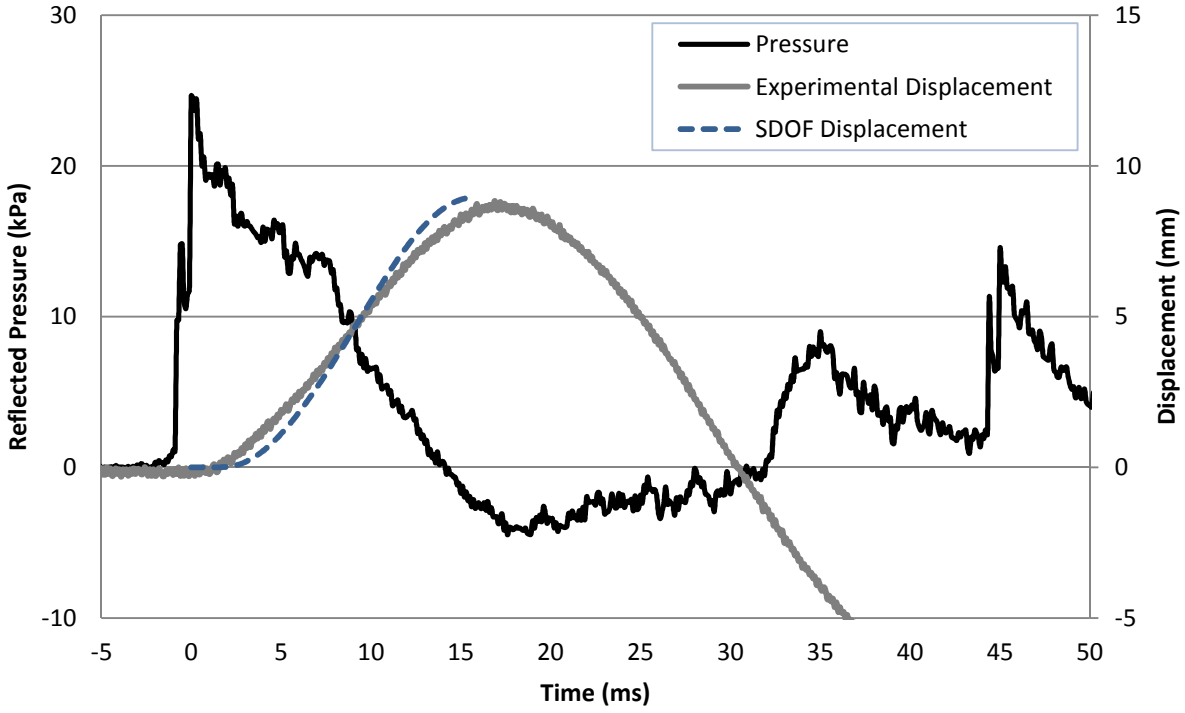

Figure 4.45: Experimentally Recorded and SDOF Predicted Mid-Height Displacement Time History for Test URM-4-1

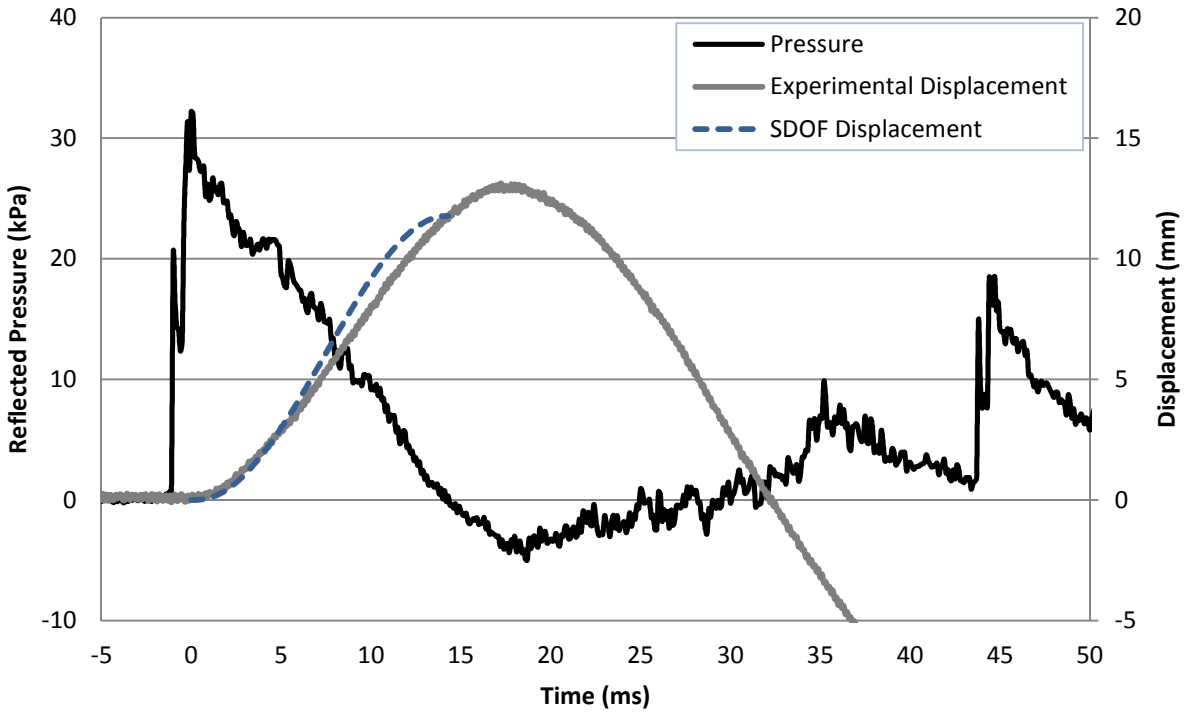

Figure 4.46: Experimentally Recorded and SDOF Predicted Mid-Height Displacement Time History for Test URM-4-2

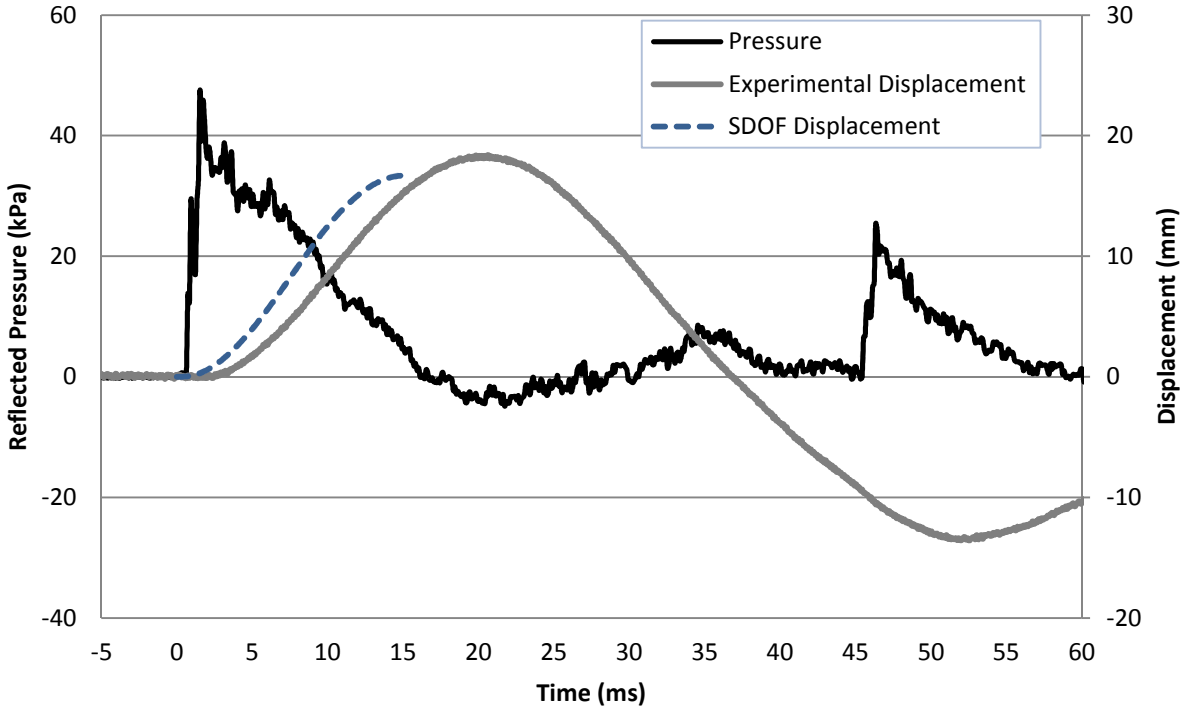

Figure 4.47: Experimentally Recorded and SDOF Predicted Mid-Height Displacement Time History for Test URM-4-3

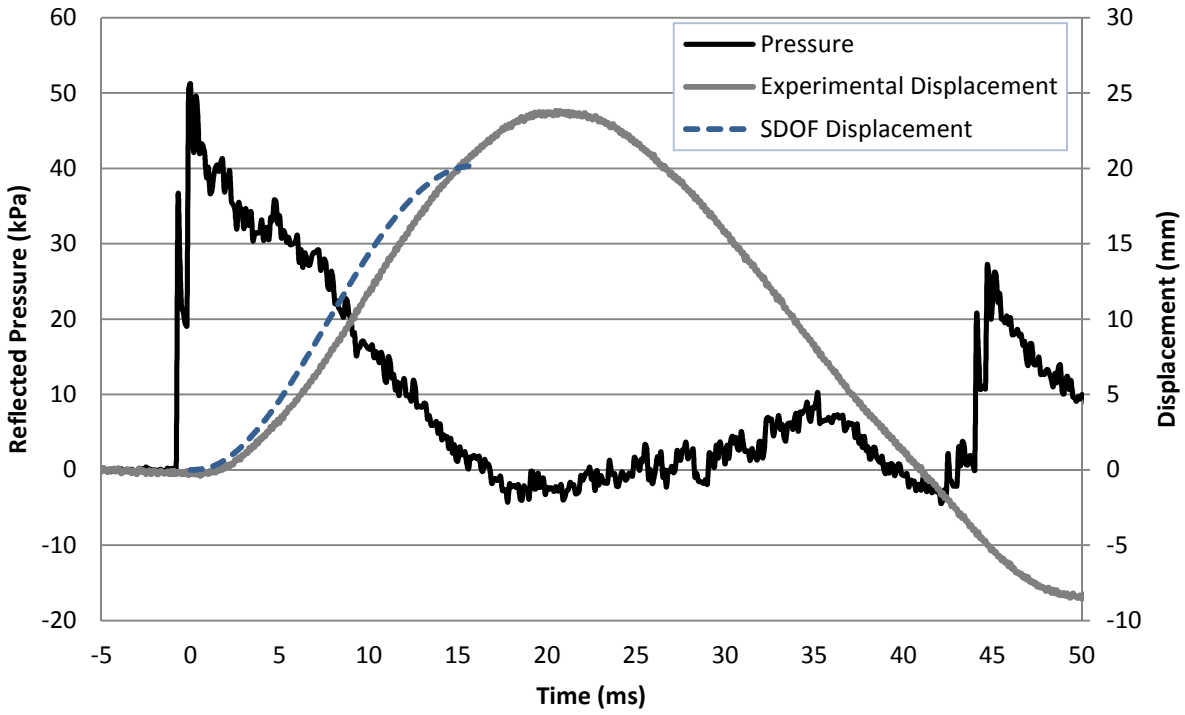

Figure 4.48: Experimentally Recorded and SDOF Predicted Mid-Height Displacement Time History for Test URM-4-4

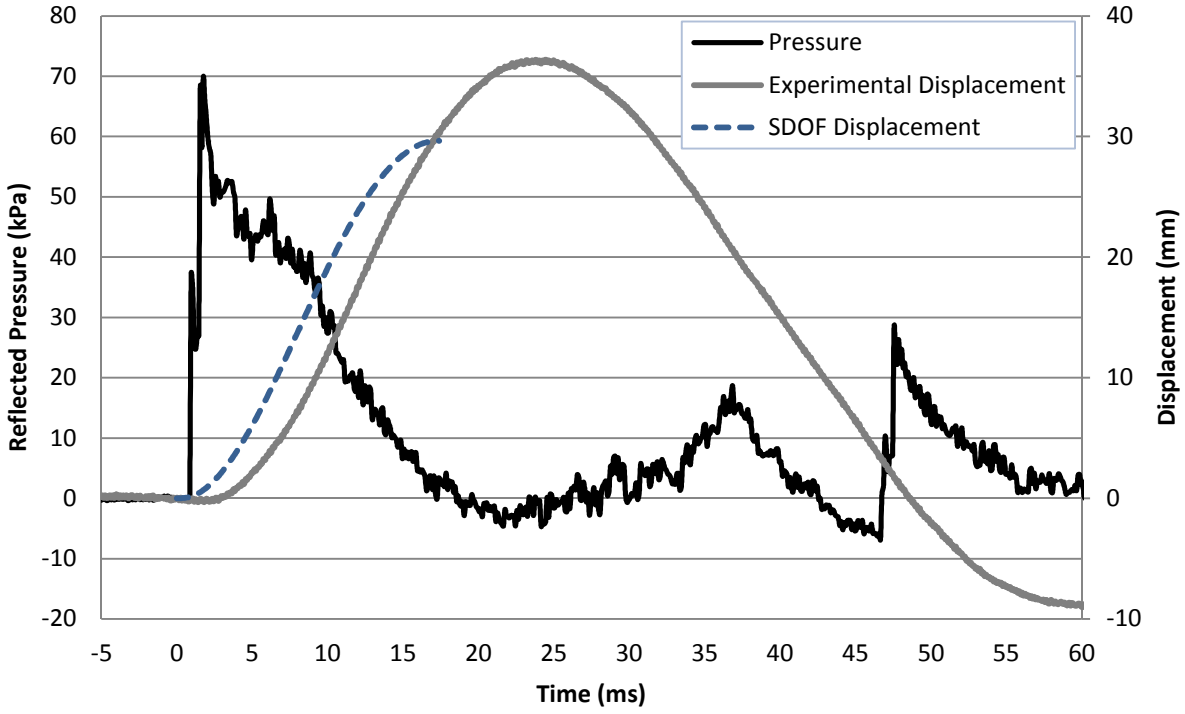

Figure 4.49: Experimentally Recorded and SDOF Predicted Mid-Height Displacement Time History for Test URM-4-5

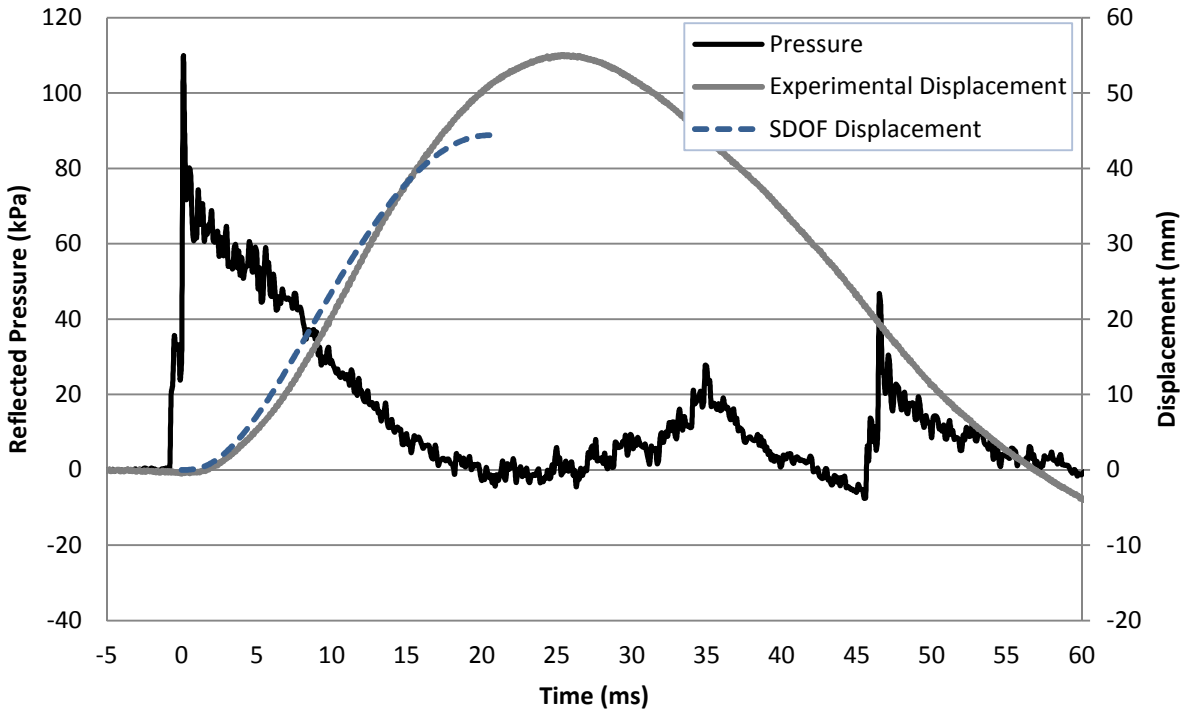

Figure 4.50: Experimentally Recorded and SDOF Predicted Mid-Height Displacement Time History for Test URM-4-6

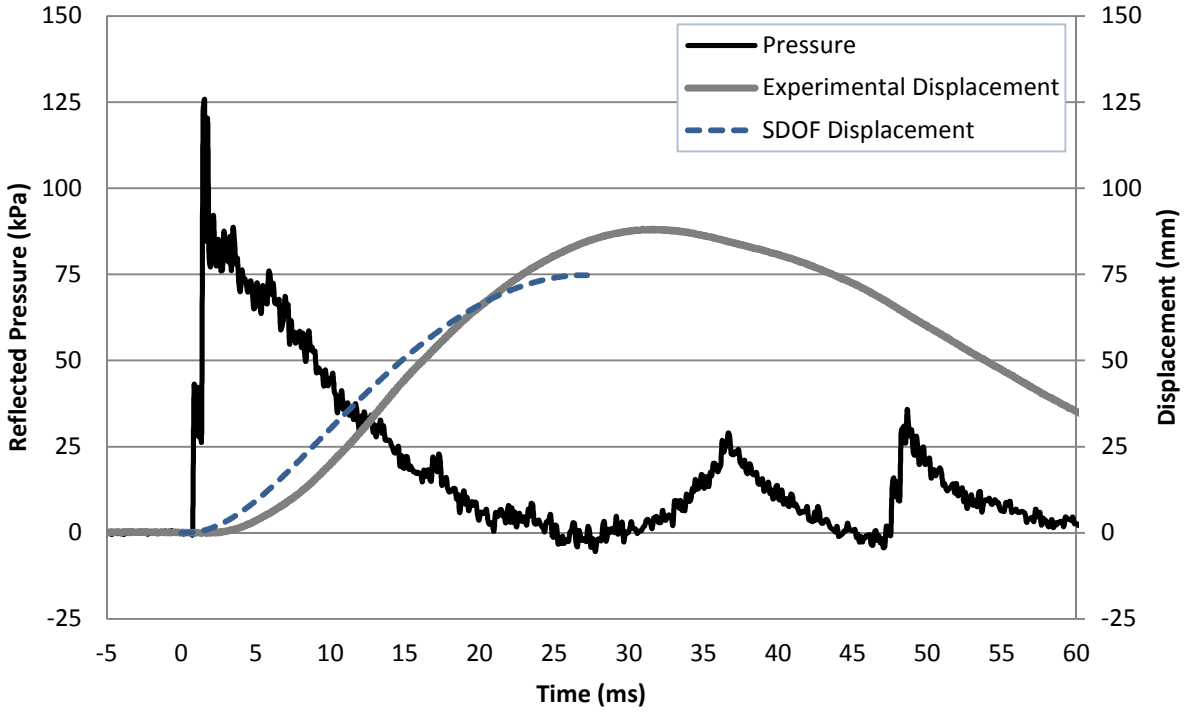

Figure 4.51: Experimentally Recorded and SDOF Predicted Mid-Height Displacement Time History for Test URM-4-7

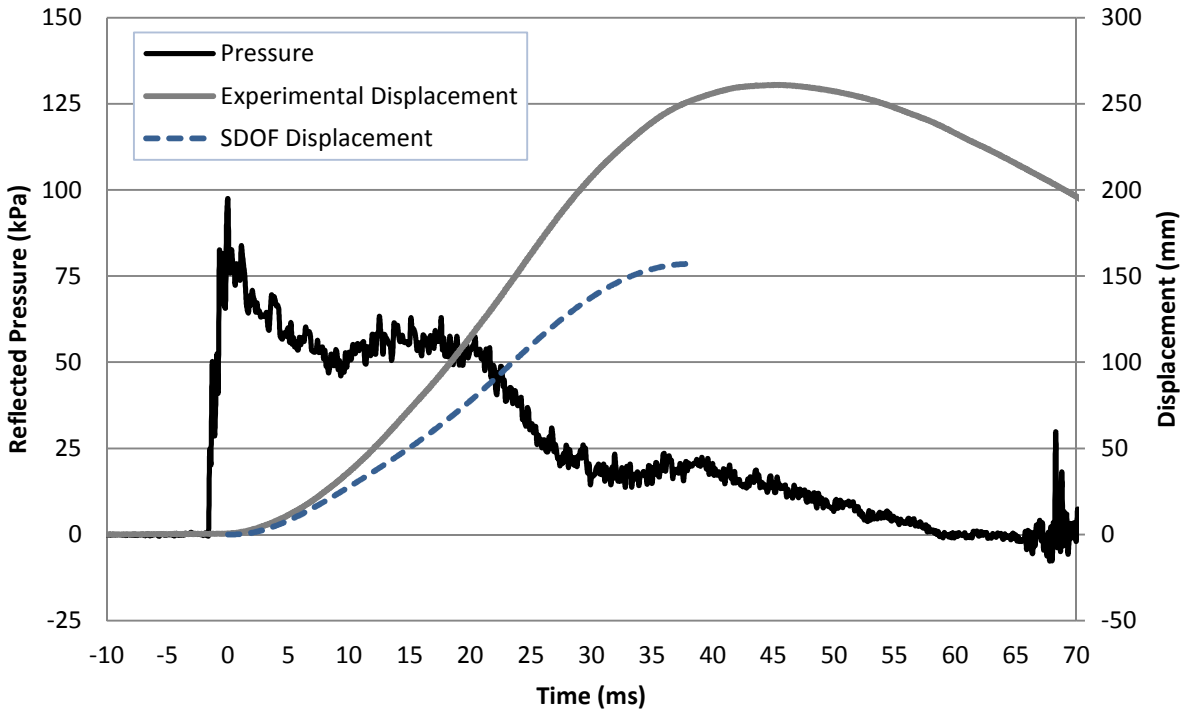

Figure 4.52: Experimentally Recorded and SDOF Predicted Mid-Height Displacement Time History for Test URM-4-8

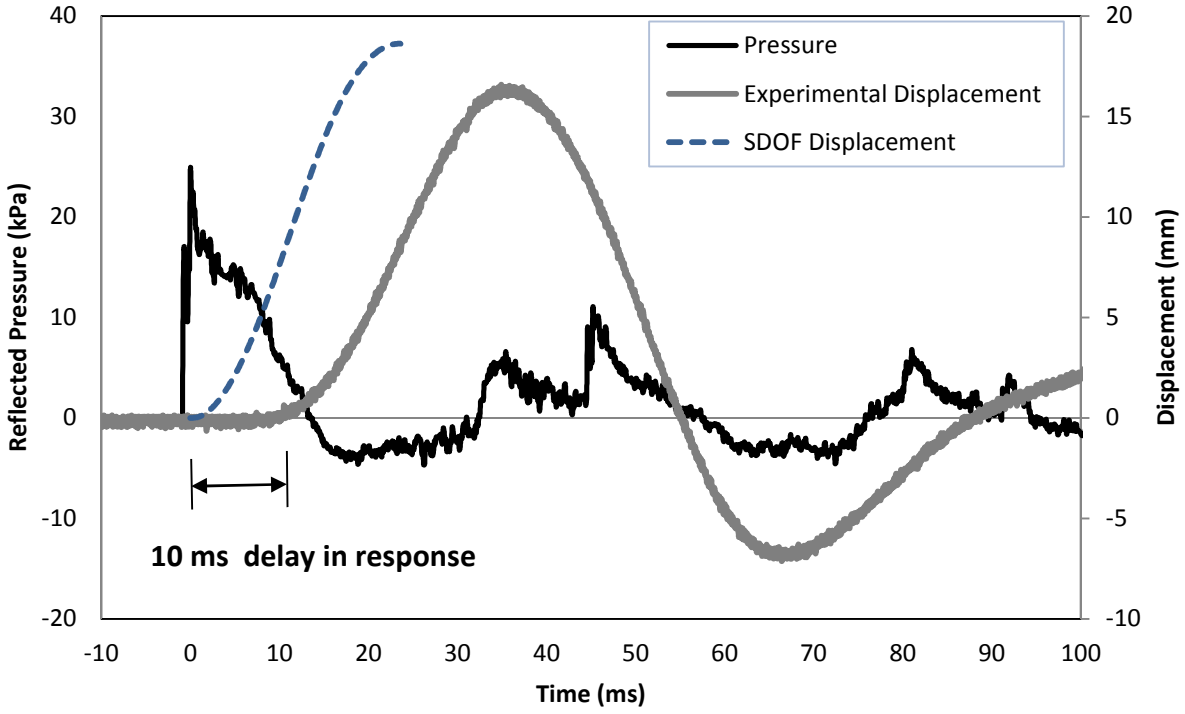

Figure 4.53: Experimentally Recorded and SDOF Predicted Mid-Height Displacement Time History for Test URM-3-3 (Wire Transducers for Measuring Mid-Height Displacements)

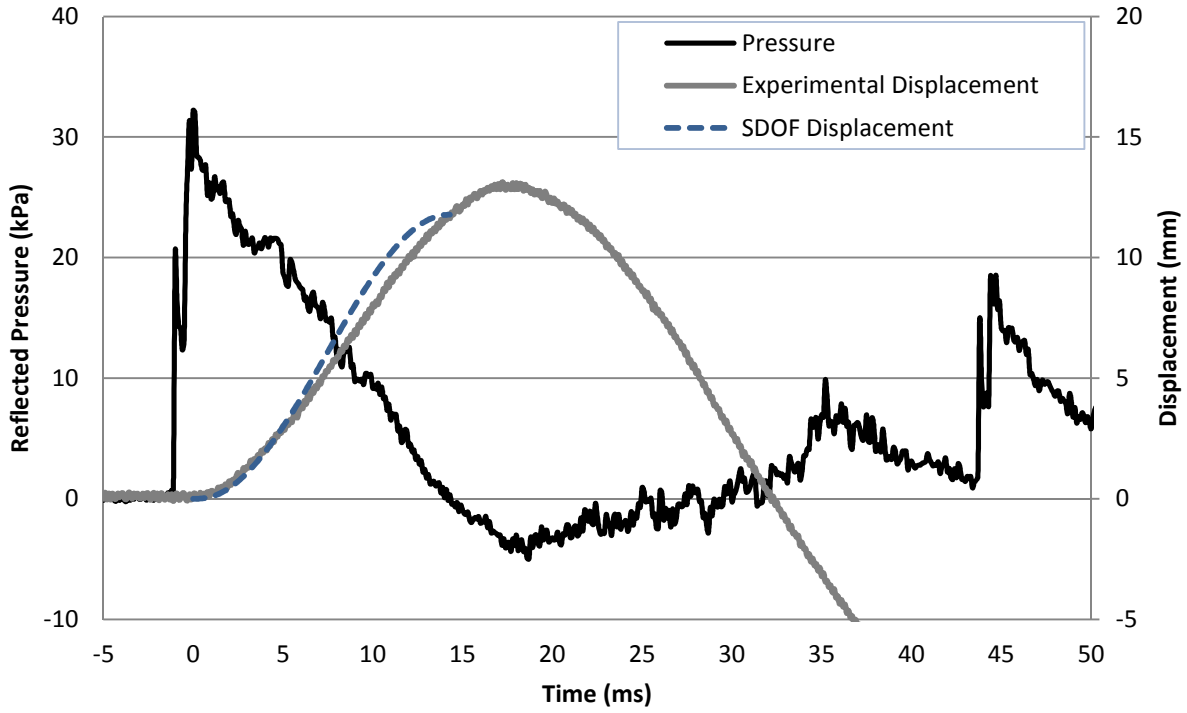

Figure 4.54: Experimentally Recorded and SDOF Predicted Mid-Height Displacement Time History for Test URM-4-2 (LVDT for Measuring Mid-Height Displacements)

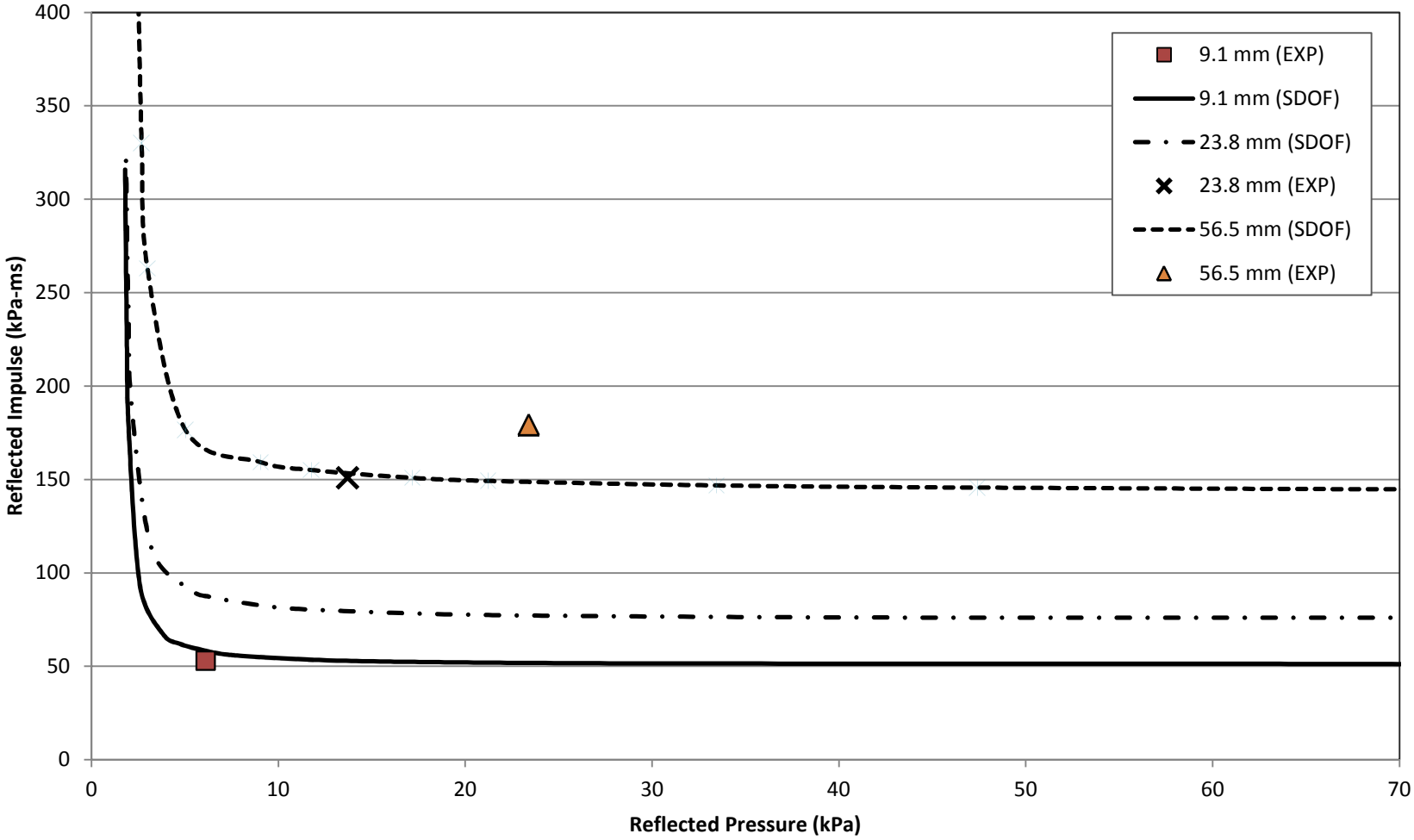

Figure 4.55: Predicted PI Diagram with Experimental Pressure-Impulse Combination Overlay for Specimen URM-1

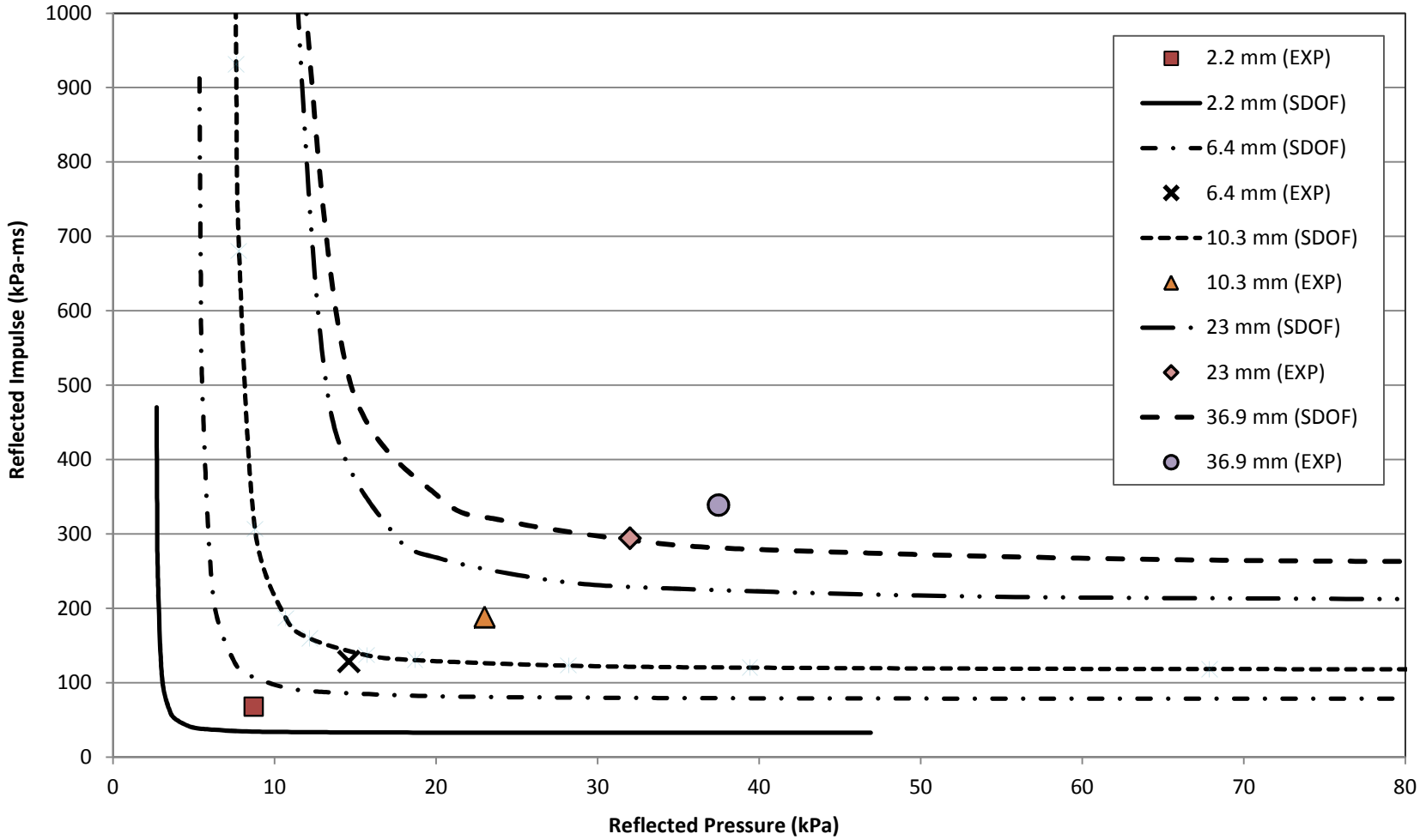

Figure 4.56: Predicted PI Diagram with Experimental Pressure-Impulse Combination Overlay for Specimen URM-2

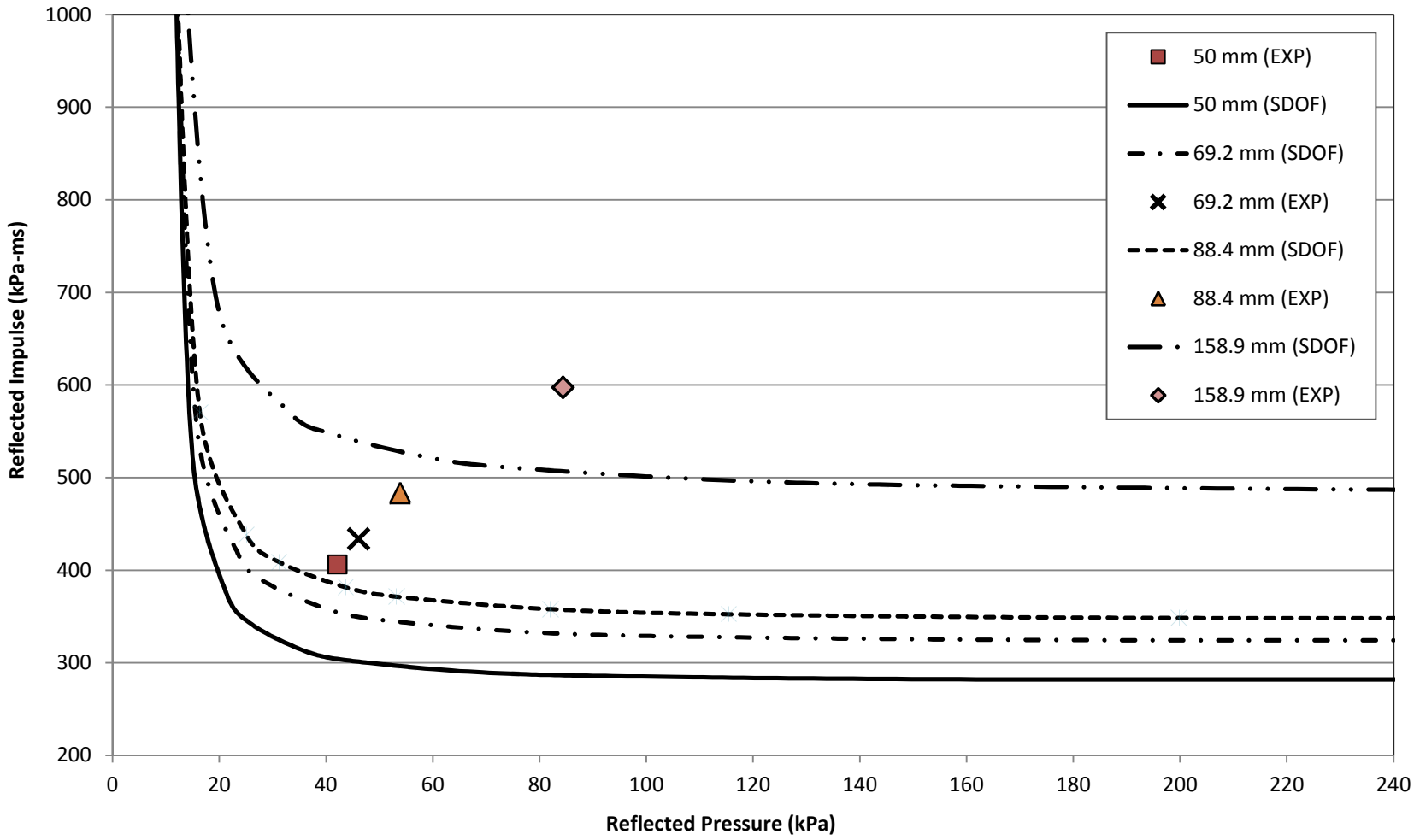

Figure 4.57: Predicted PI Diagram with Experimental Pressure-Impulse Combination Overlay for Specimen URM-2

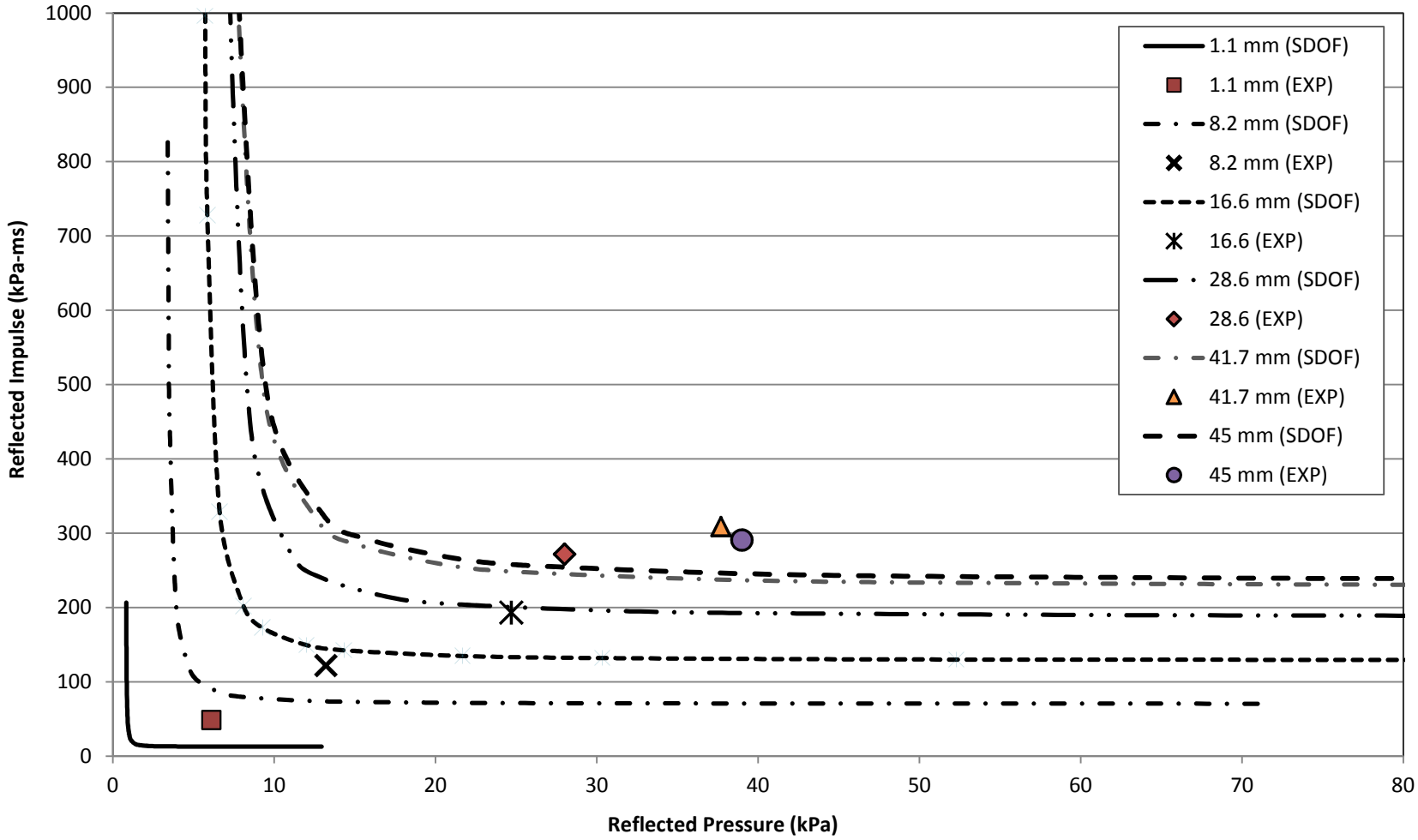

Figure 4.58: Predicted PI Diagram with Experimental Pressure-Impulse Combination Overlay for Specimen URM-3

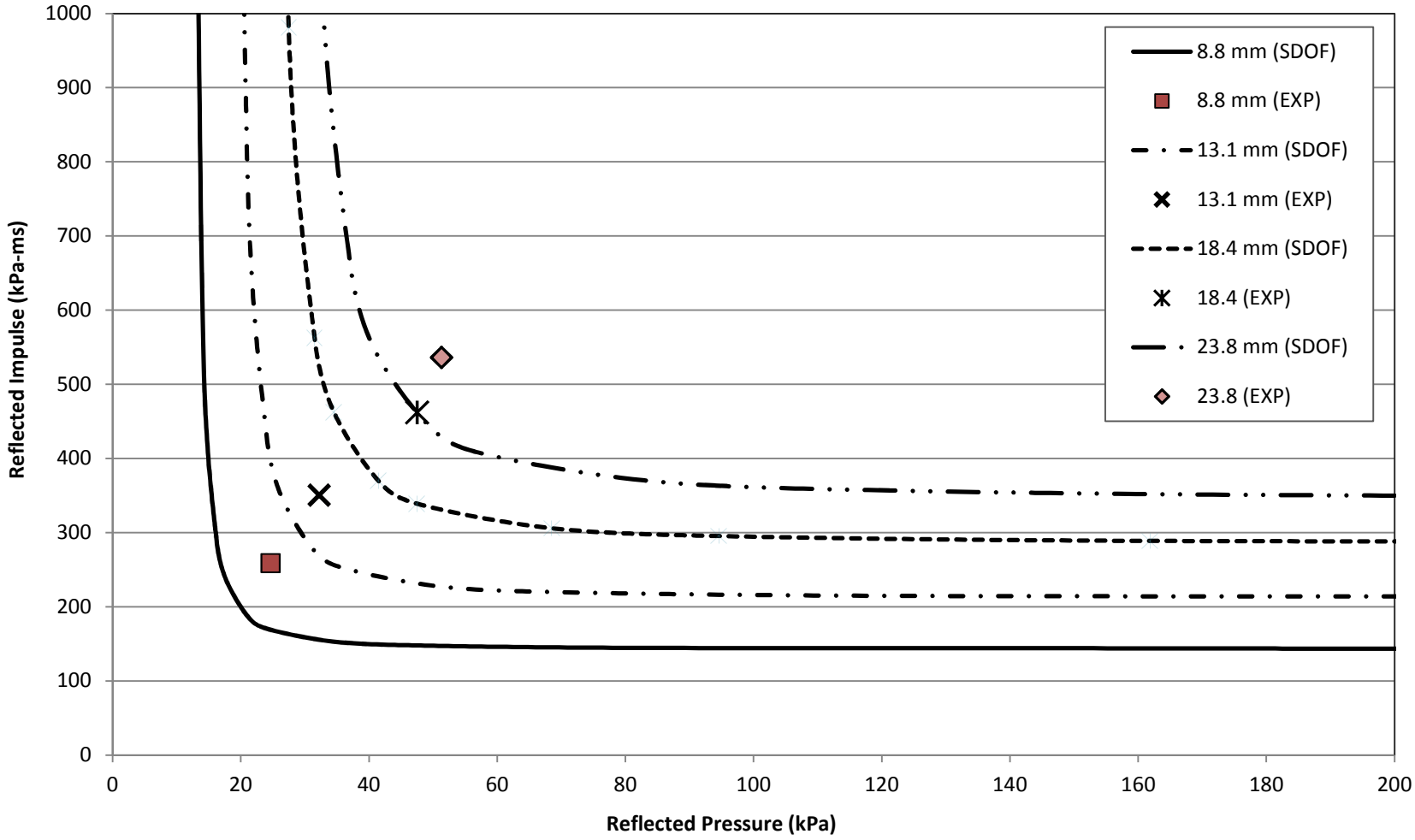

Figure 4.59: Predicted PI Diagram with Experimental Pressure-Impulse Combination Overlay for Specimen URM-4

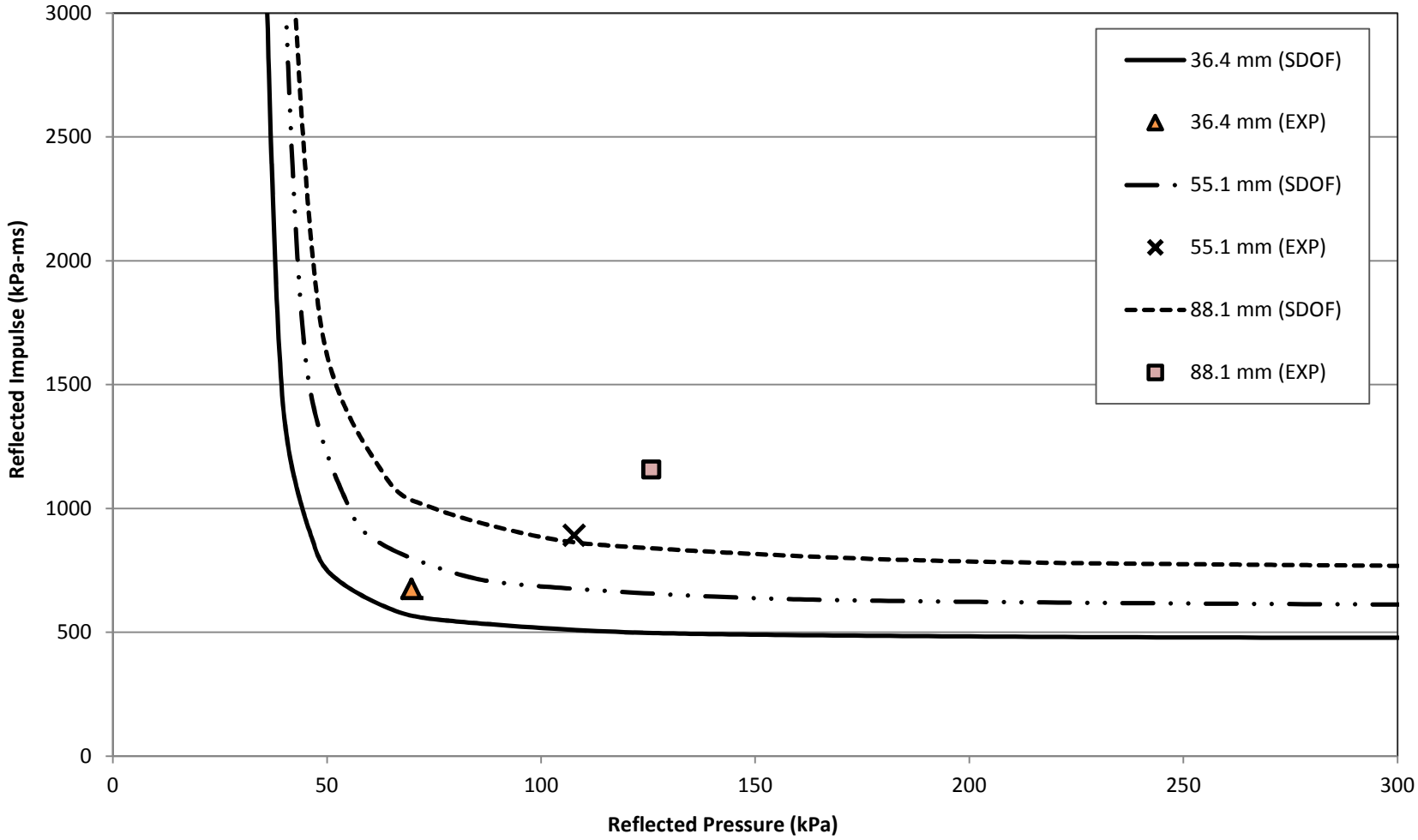

Figure 4.60: Predicted PI Diagram with Experimental Pressure-Impulse Combination Overlay for Specimen URM-4

CHAPTER 5

Conclusions

5.1 Summary

An analytical and experimental investigation was carried to examine the behaviour of retrofitted unreinforced concrete block masonry walls subjected to blast-induced shock waves. Four unreinforced masonry (URM) walls were constructed for this study and tested under shock tube induced blast loading at the University of Ottawa Shock Tube Testing Facility. Two of the URM walls were designed and built as non load-bearing, infill walls. One of the infill walls was retrofitted with a layer of spray-on polyurea. The other two URM walls were designed and built as load-bearing walls meant to represent existing building construction. One of the load–bearing walls was retrofitted with a system comprised of non deformed steel wires with a layer of polyurea sprayed over the bars and concrete masonry surface. The specimens were designed to simulate one-way action.

The shock tube driver pressures were increased incrementally to the point of wall failure. Duration of blast loading was kept constant for majority of tests. The reflected pressure and displacement time histories, strain in steel reinforcement as well as any increase in axial loading due to arching action were recorded and presented.

An equivalent single-degree-of-freedom analysis was conducted to predict the mid-height displacements for each shock tube test. Individual static resistance-displacement curves, required to solve the dynamic equation of motion, were developed for each wall specimen. The constant acceleration numerical integration method was utilized to predict mid-height displacements of the wall until the maximum displacement was reached. The numerically predicted displacements were compared to the experimentally recorded mid-height displacements for each shock tube test. Iso-damage pressure-impulse curves were also generated.

5.2 Conclusions

The following is a summary of the experimental and analytical findings presented in this thesis:

- Results indicate that reducing the top edge gap between the URM wall and the surrounding frame can increase capacity of URM wall by activating the arching mechanism.
- Arching mechanism and the addition of mechanical shear restraints changed the failure mode of the URM-1 wall specimen from a tilt-over to a hinged-arched type collapse.
- Polyurea retrofit significantly increased the blast resistance of both infill and load-bearing masonry wall specimens. In addition to increasing strength and ductility, fragmentation and flying debris due to disintegration of concrete masonry units are reduced.
- In the case of the retrofitted infill wall specimen, the increase in capacity in the initial stages of loading was attributed to the instantaneous activation of arching mechanism due to the filling of the top edge gap with polyurea. In the absence of polyurea, the wall would have no resistance until the top edge gap is closed. Polyurea maintained the cracking strength of mortar with marginal increase in flexural resistance. The increase in wall capacity after the wall experienced large deflections was due to the polyurea membrane not being uniformly strained along the entire height of the URM wall. As the wall deflected, the polyurea layer developed stresses and strains at and near the mortar joints, with the highest levels at the mid height. These regions were identified from post-experimental observations as regions where polyurea debonded from the masonry wall surface.
- For the load-bearing wall, the addition of steel reinforcement significantly increased the wall capacity by adding a tension component that enhanced the sectional moment resistance. Presence of polyurea ensured composite action between the steel and the masonry wall. Furthermore, the steel embedded in polyurea was welded on the top and bottom steel plates and hence it developed additional compression resistance. This latter action further increased the resistance of the wall.

- Polyurea proved excellent at dissipating the energy by changing the failure mode from a brittle to a ductile mode.
- The SDOF model used for determining the maximum mid-height displacements for the URM wall specimens under shock wave loading accurately predicts the experimental results. The model is most accurate for displacements higher than 10 mm.

5.3 Recommendations for Future Research

The following recommendations are made for future research:

- Further test data is needed to quantify the effectiveness of polyurea in activating the arching action. Walls with different size gaps need to be tested to investigate the effectiveness of polyurea in filling the top edge gap.
- Performance of polyurea on two-way behavior of infill walls need to be investigated.
- For load-bearing URM walls, the amount of reinforcing steel used for retrofitting need to be quantified by further testing. Different walls with different configurations of externally placed reinforcement will shed more light into the effectiveness of reinforced polyurea. Performance of load-bearing walls retrofitted in two orthogonal directions to activate two-way action need to be investigated.
- Surface strain characteristics of polyurea during response to blast loading require in depth study. This should be done with appropriate instrumentation, leading to results that will help map the locations of strain concentrations.
- The effect of gravity load on load-bearing masonry walls retrofitted with polyurea requires study. This should be done while incorporating sound instrumentation techniques permitting the measurement of any variations in axial load due to arching.
- The strain rate effect on polyurea in both tension and compression need to be established.
- Difficulties associated with the application of polyurea along the edges and support regions need to be resolved through further experimental research.

References

American Society of Civil Engineers (1999). *Structural Design for Physical Security: State of the Practice,* ASCE Structural Engineering Institute, Reston, VI.

Baker, W. E., Cox, P. A., Westine, P. S., Kulesz, J. J., and Strehlow, R. A. (1983). "Explosive Hazards and evaluation," *Elsevier Scientific Publishing Company*, New York, NY.

Baylot, J. T., Bullock, B., Slawson, T. R., Woodson, S. C. (2005). "Blast Response of Lightly Attached Concrete Masonry Unit Walls." *Journal of Structural Engineering*, ASCE, 131 (8), 1186-1193.

Biggs, J.M. (1964). *Introduction to Structural Dynamics*. McGraw-Hill, New York, NY.

Broekaert, M. (2002). "Polyurea spray coatings-The technology and latest developments". Huntsman International LLC, Belgium.

Connell, J. D. (2002). "Evaluation of Elastomeric Polymer for Retrofit of Unreinforced Masonry Walls Subjected to Blast," MS Thesis, University of Alabama at Birmingham, Birmingham, AL.

Crawford, J. E. (2002). "Modelling blast-resistant protection systems composed of polymer and fabric." *TMS 2002 Fall Meeting*, The Minerals, Metals and Materials Society, Columbus, OH.

Crawford, J.E. (2006). "Protective Designs for Blast and Impact Effects." *4th World Conference on Structural Control and Monitoring*, San Diego, CA.

CSA (2004). *Connectors for Masonry*, CSA Standard A370-04. Canadian Standards Association, Mississauga, Ontario.

Davidson, J. S. , Porter, J. R., Dinan, R. J., Hammons, M.I., Connell, J. D. (2004). "Explosive Testing of Polymer Retrofit Masonry Walls." *Journal of Performance of Constructed Facilities*, American Society of Civil Engineers, 18(2), 100-106.

Davidson, J. S. (2005). "Failure Mechanisms of Polymer-Reinforced Concrete Masonry Walls Subjected to Blast." *Journal of Structural Engineering*, American Society of Civil Engineers, 131 (8), 1194-1205.

Dinan, R. J., Fisher, J. W., Hammons, M. I., Porter, J. R. (2003). "Failure mechanisms in unreinforced concrete masonry walls retrofitted with polymer coatings." *Proceedings of the 11th International Symposium on Interaction of the Effects of Munitions with Structures*, Mannheim, Germany.

Drysdale, R.G., Hamid, A. A., Baker, L. R. (1994). *Masonry Structures: Behaviour and Design*. Prentice Hall, Eaglewood Cliffs, NJ.

Gabrielsen, B. L., Wilton, C. (1973). "Shock Tunnel Tests of Preloaded and Arched Wall Panels," Report #AD-764 263 prepared for the Defence Civil Preparedness Agency, URS Research Company, Distributed by National Technical Information Service, U.S. Department of Commerce, Springfield, VA.

Gabrielsen, B. L., Wilton, C., Kaplan, K. (1975). "Response of Arching Walls and Debris from Interior Walls Caused by Blast Loading," Final Report Prepared for the Defence Civil Preparedness Agency, Scientific Services, Inc., Redwood City, CA.

Glanville, J. I., Hatzinikolas, M. A., Ben-Omran, H. A. (1996). *Engineered Masonry Design.* Winston House Enterprises, Winnipeg, Manitoba.

Hrynyk, T. D., Myers, J. J. (2008). "Out-of-plane behaviour of URM arching walls with modern blast retrofits: experimental results and analytical model." *Journal of Structural Engineering*. ASCE, 134 (10), 1589-1597.

Hyde , D. (1992). "conWep – Application of TM 5-1300." *U.S. Army Engineer Waterways Experiment Station*, Vicksburg, MA, USA.

IMI Technology Brief 02.13.02 (2010). *Hybrid Masonry Design*. International Masonry Brief, Annapolis, MD.

Johnston, C. F., Slawson, T. R., Cummins, T. K., Davis, J. L. (2004). "Concrete masonry unit walls retrofitted with fibre reinforced elastomeric systems for blast loads." *24th Army Science Conf.*, Orlando, FL.

Jacques, E. , Lloyd, A. , Saatcioglu, M. (2012). "Predicting reinforced concrete response to blast loads." *Canadian Journal of Civil Engineering*, 39, 1-18.

Knox, K. J., Hammons, M. I. Lewis, T. T., Porter, J.R. (2000). "Polymer materials for structural retrofit," Force Protection Branch, Air Expeditionary Forces Technology Division. Air Force Research Laboratory, Tyndall AFB, FL.

Line-X Franchise Development Corporation (2010). "Technical Data Sheet PAXCON PX-3350," Product Manufactured Data Sheet.

Lloyd, A., Saatcioglu, M., Nistor, I., and Palermo, D. (2009). "New shock tube testing facilities for simulated blast loading of structural and non-structural components." *2nd International Workshop on Performance, Protection & Strengthening of Structures under Extreme Loading*, Japan.

McDowell, E. L., McKee, K. E., Sevin, E. (1956). "Arching Action Theory of Masonry Walls." *Journal of Structural Division*, Proceedings of ASCE, 915, 1-18.

Moradi, L. G., Davidson, J. S., Dinan, R. J. (2008). "Resistance of membrane retrofit concrete masonry walls to lateral pressure." *Journal of Performance of Constructed Facilities*. 22(3), 131-142.

Moradi, L. G., Davidson, J. S., Dinan, R. J. (2009). "Response of bonded membrane retrofit concrete masonry walls to dynamic pressure." *Journal of Performance of Constructed Facilities*. 23(2), 72-80.

Oswald, C. J., Zehrt, W. (2010). "Update to UFC 3-340-02 for Blast Resistant Design of Masonry Components." *Structures to Resist the Effects of Accidental Explosions*, United States of America Department of Defense, Washington, D.C.

Piepenburg, D., Martinez, R., Del Frate, R., Morrill, K. (2002). "Blast resistance upgrade for glazing, window frame, and wall systems- Non-load bearing in-fill walls with blast retrofits applied to the wall, window frame and glaze." Rep. No. SAIC-03/1001, Science Applications International Corporation, Alexandria, VA.

Piepenburg, D., Martinez, R., Del Frate, R., Morrill, K. (2003). "Blast resistance upgrade for glazing, window frame, and wall systems- Load bearing walls with blast retrofits applied to the wall, window frame and glaze." *Rep. No. SAIC-03/1003*, Science Applications International Corporation, Alexandria, VA.

Sarva, S., Deschanel, S., Boyce, M. C., Chen, W. (2007). "Large deformation rate dependent stress-strain behaviour of polyurea and polyurethane." Research project supported by the Office of Naval Research through grant NO. N000014-04-10469.

Slawson, T. R., Coltharp, D. R., Dennis, S. T., Mosher, R. (1999). "Evaluation of anchored fabric retrofits for reducing masonry wall debris hazard." *Proc., 9th International Symposium on Interaction of the Effects of Munitions with Structures*, Berlin, Germany

Smith, P. D., Hetherington, J. G. (1994). *Blast and Ballistic Loading of Structures*. Butterworth-Heinemann, Oxford, UK.

Sudame, S. (2004). "Development of Computational Models and Input Sensitive Study of Polymer Reinforced Concrete Masonry Walls Subjected to Blast," MS Thesis, University of Alabama at Birmingham, Birmingham, AL.

Thornburg, D.L. (2004). "Evaluation of Elastomeric Polymer Used for External Reinforcement of Masonry Walls Subjected to Blast," MS Thesis, University of Alabama at Birmingham, Birmingham, AL.

TM 5-1300 (1990). "Structures to Resist Effects of Accidental Explosions." *Technical Manual 5-1300, Department of the Army, Navy and Air Force*, Washington DC.

Unified Facilities Criteria (UFC) 3-340-01 (2002). *Design and Analysis of Hardened Structures to Conventional Weapons Effects*. United States of America Department of Defense, Washington, D.C.

Unified Facilities Criteria (UFC) 03-340-02 (2008). *Structures to Resist the Effects of Accidental Explosions*. United States of America Department of Defense, Washington, D.C.

Yi, J., Boyce, M. C., Lee, G. F., Balizer, E. (2006). "Large Deformation Rate-Dependent Stress-Strain Behavior of Polyurea and Polyurethane." *Polymer*," 47(1), 319-329.

Appendix A

Axial Load Data

For wall specimens URM-2, URM-3 AND URM-4, two load cells were installed between the testing frame and the ceiling of the laboratory. Steel shims were installed between bottom of testing frame and the concrete floor. Axial load was applied to the load-bearing walls, URM-3 and URM-4, by using two hydraulic jacks located between the bottom of the testing frame and the rigid floor. For the load-bearing walls, URM-3 and URM-4, steel shims were placed between the bottom of the testing frame and the hydraulic jacks. The frame was allowed to slide vertically so the load changes could be recorded. The axial load level applied to each load-bearing wall was approximately 122 kN, 61 kN from each jack.

The load cells were intended to record any axial loading that might be caused by arching of any of the walls as well as changes in load level for the load-bearing walls. Figures A-1 through A-25 contain overlaid reflected pressure and axial load time history plots. The axial load time history was taken as a summation of the two load cell readings.

The shape of the axial loading time history provides qualitative proof of the occurrence of arching action, but not a quantitative measure. As described in Chapter 2, the vertical translation was enabled by releasing the tension in the bolts connecting the test frame to the shock tube end frame; however, it is likely some of the axial load was transferred to the rods, thus leading to inaccurate load cell readings.

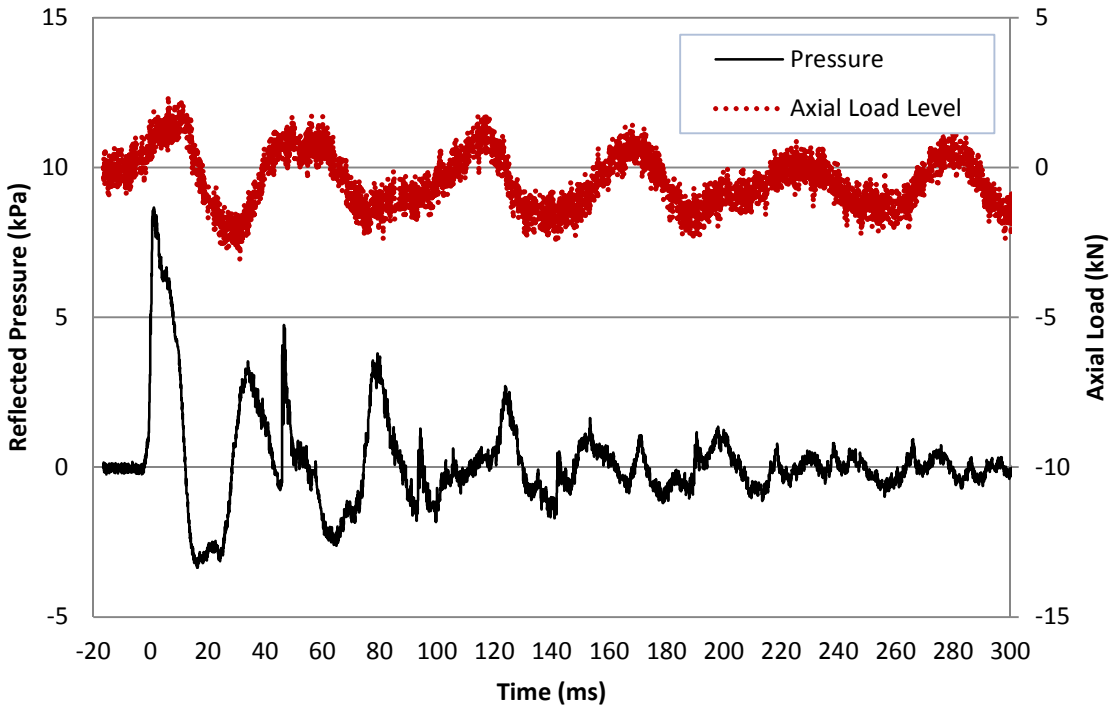

Figure A- 1: Reflected Pressure and Axial Load Time History for Test URM-2-1

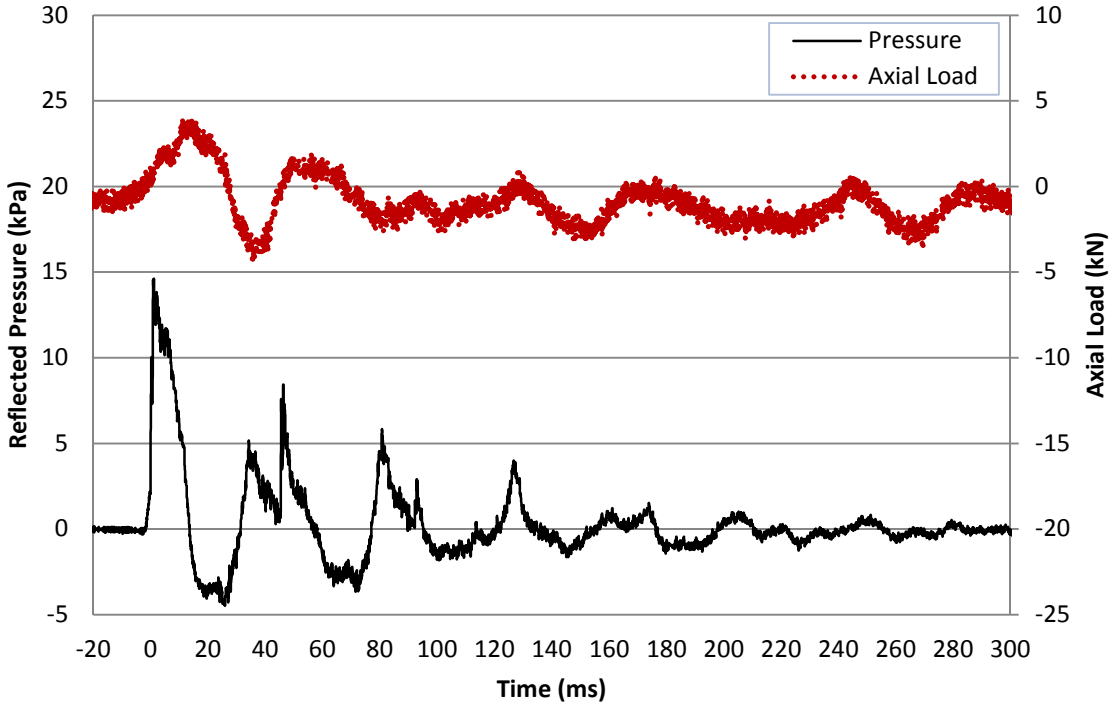

Figure A- 2: Reflected Pressure and Axial Load Time History for Test URM-2-2

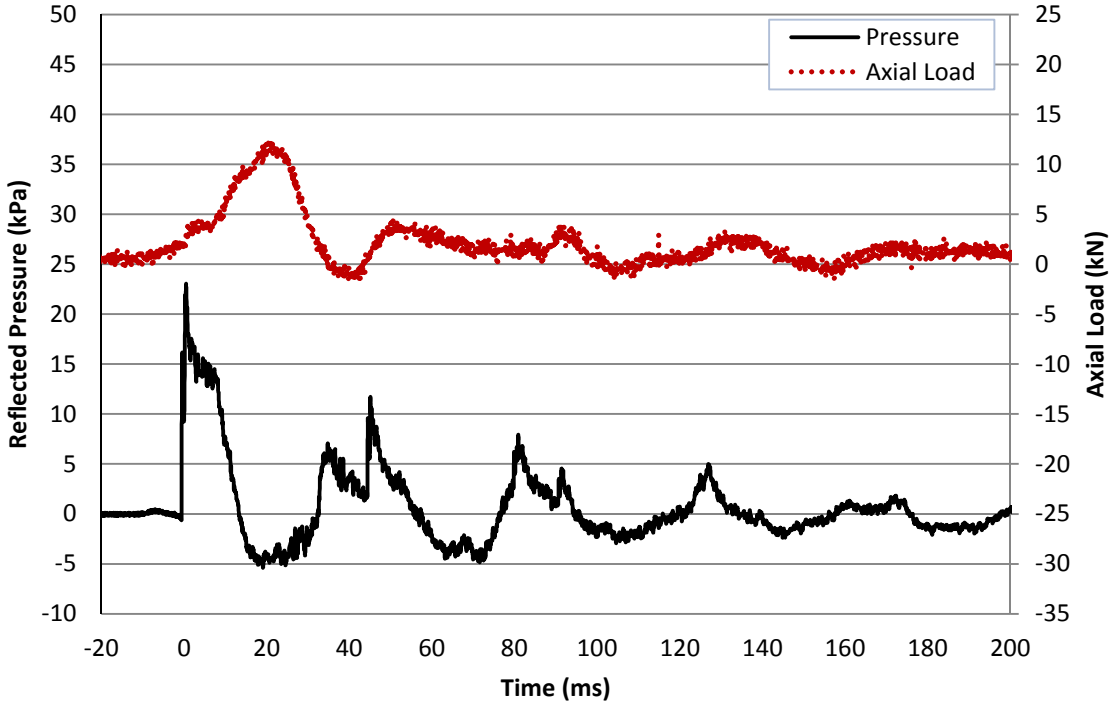

Figure A- 3: Reflected Pressure and Axial Load Time History for Test URM-2-3

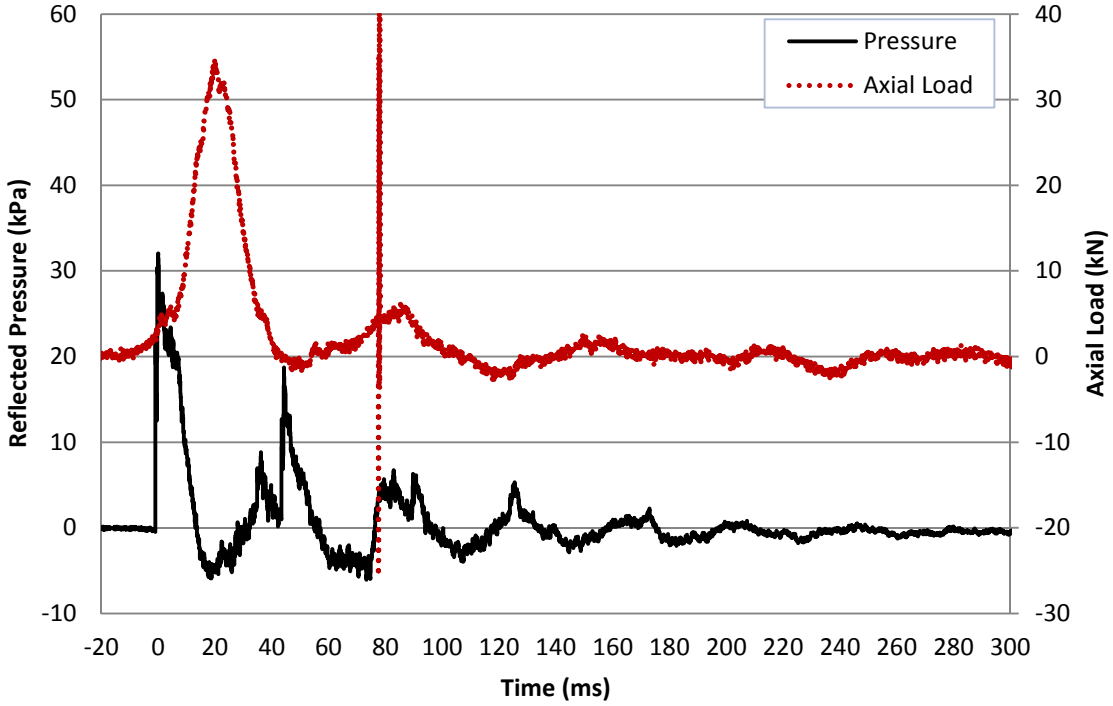

Figure A- 4: Reflected Pressure and Axial Load Time History for Test URM-2-4

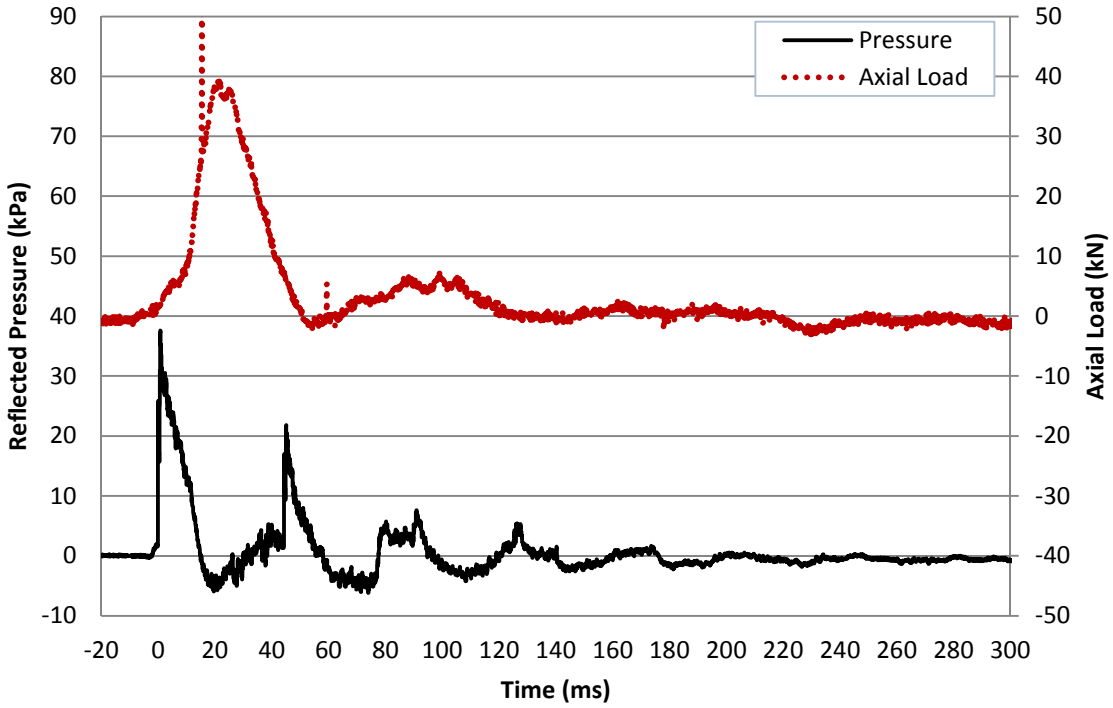

Figure A- 5: Reflected Pressure and Axial Load Time History for Test URM-2-5

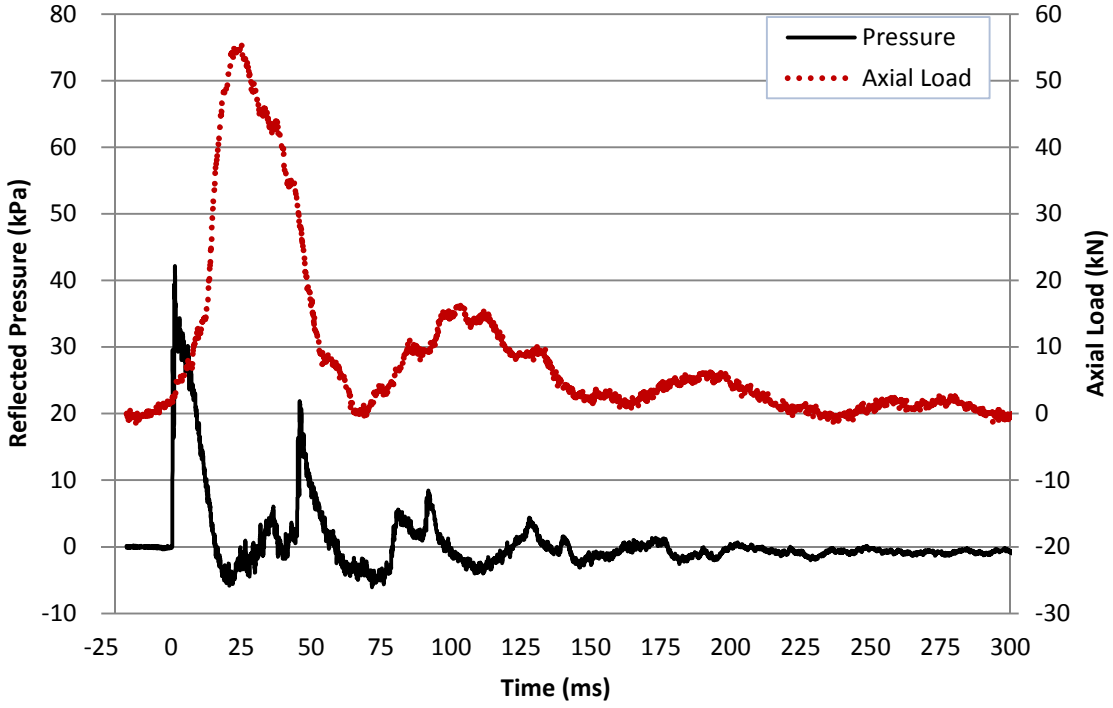

Figure A- 6: Reflected Pressure and Axial Load Time History for Test URM-2-6

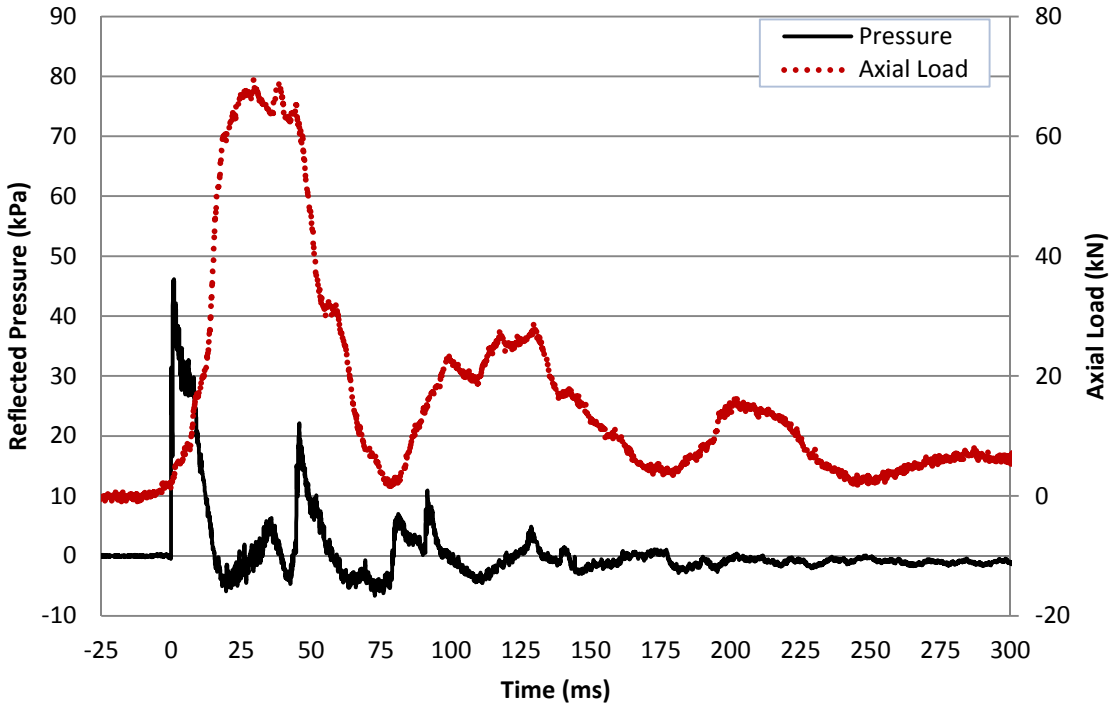

Figure A- 7: Reflected Pressure and Axial Load Time History for Test URM-2-7

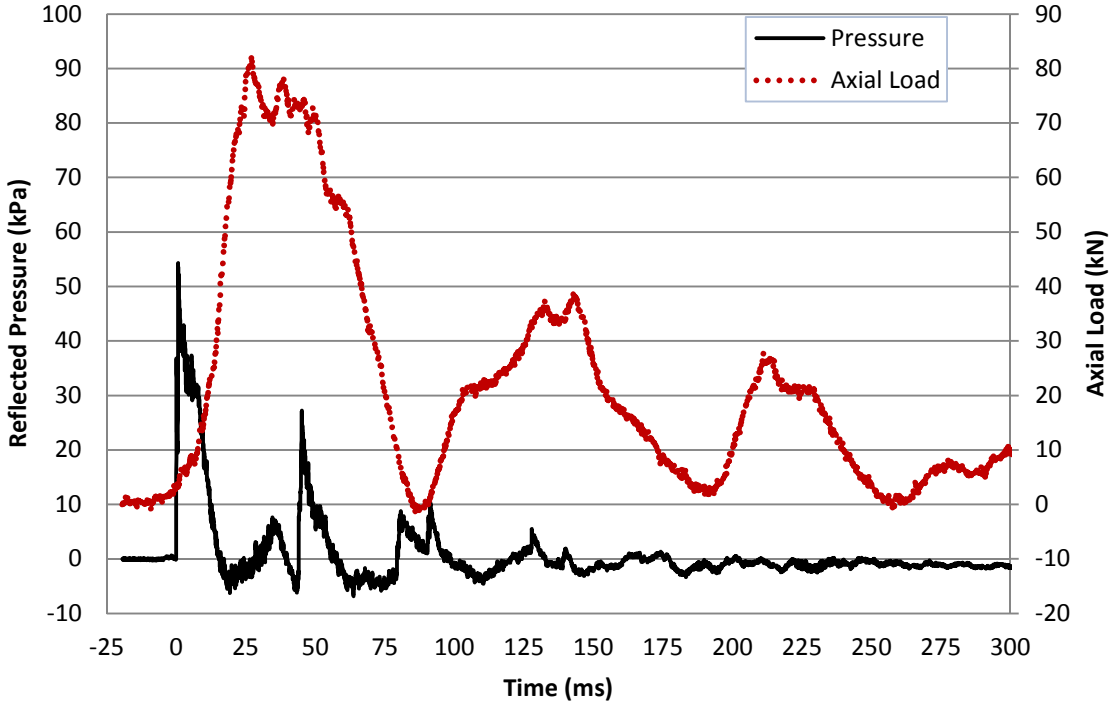

Figure A- 8: Reflected Pressure and Axial Load Time History for Test URM-2-8

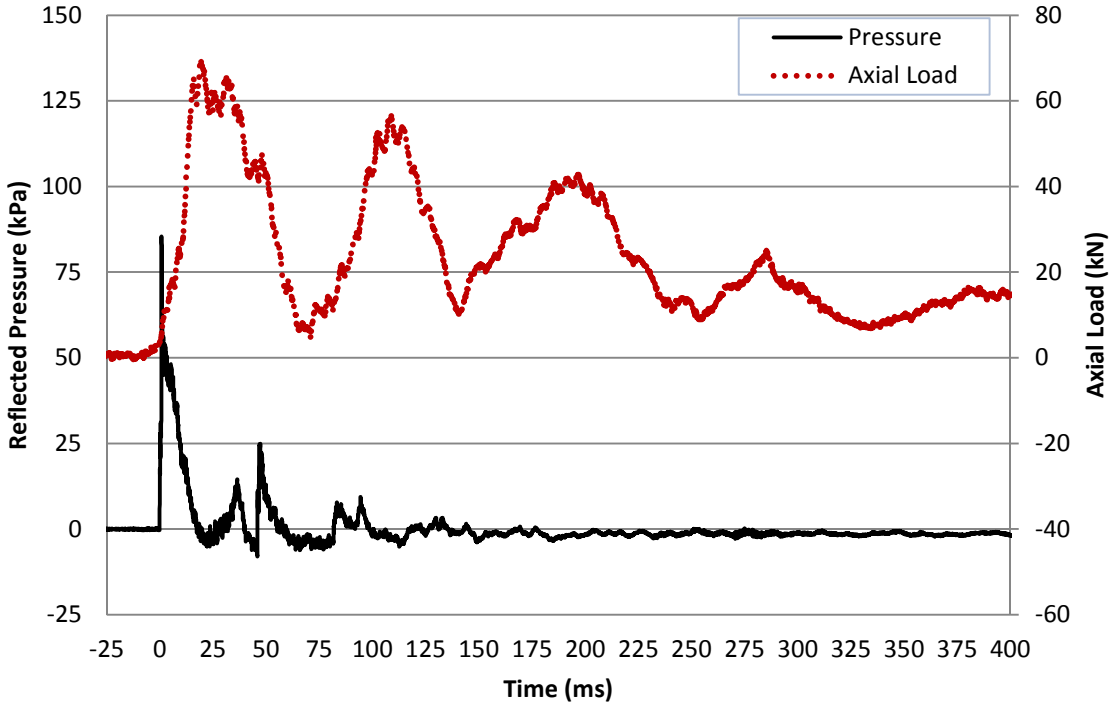

Figure A- 9: Reflected Pressure and Axial Load Time History for Test URM-2-9

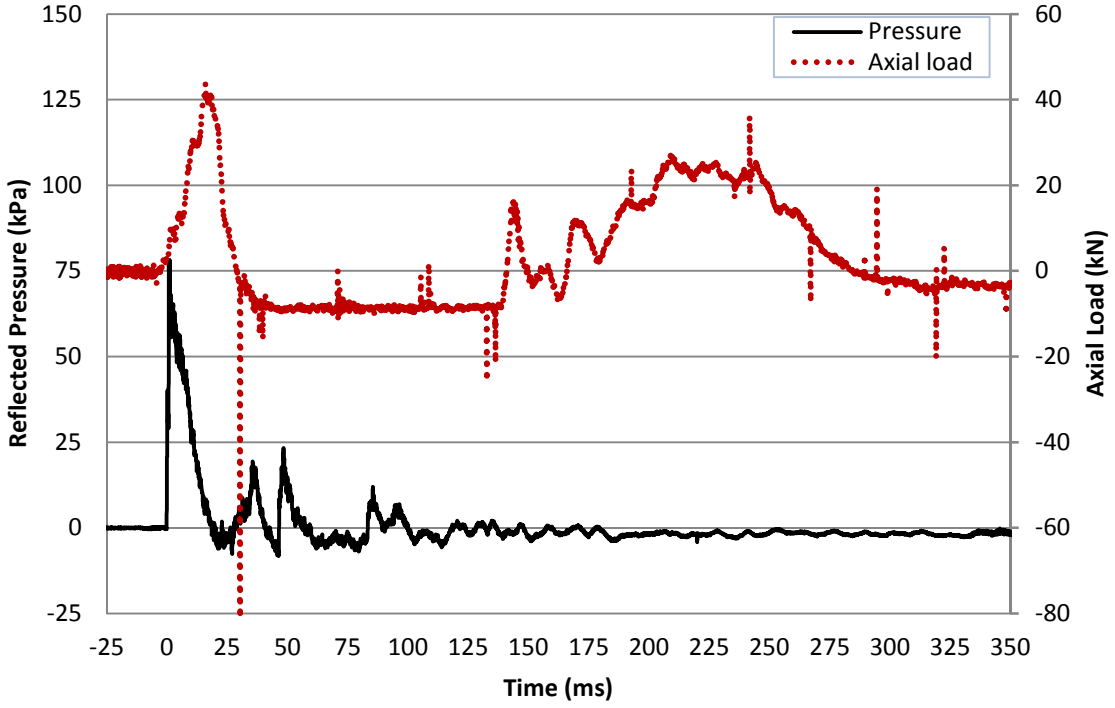

Figure A- 10: Reflected Pressure and Axial Load Time History for Test URM-2-10

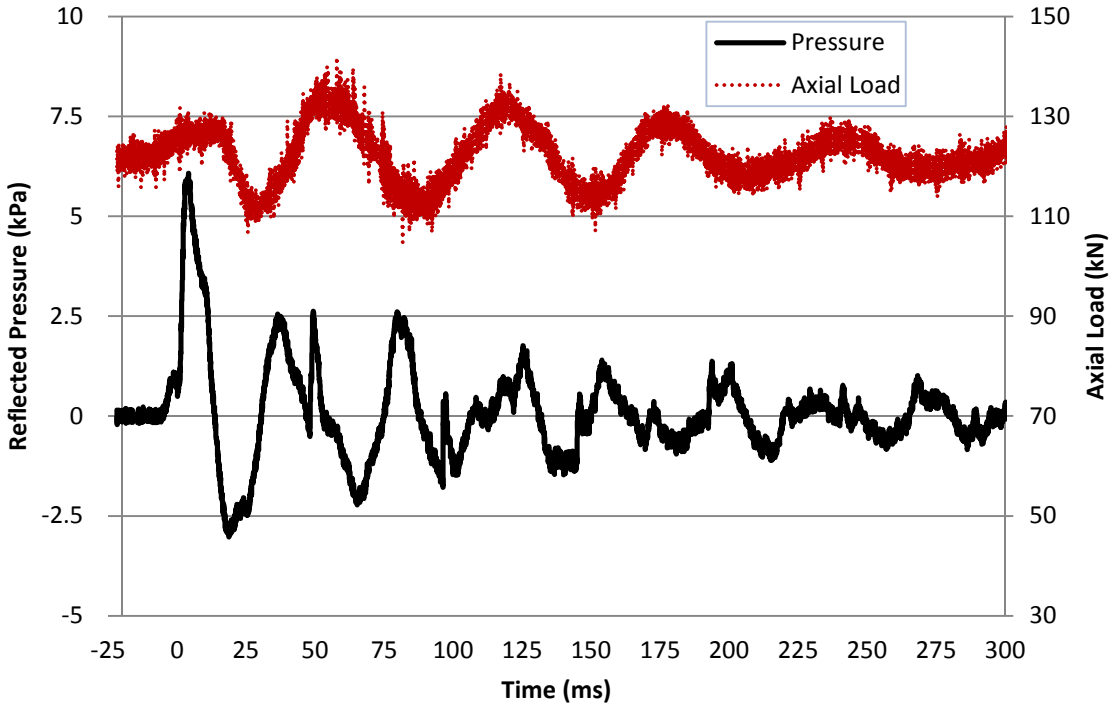

Figure A- 11: Reflected Pressure and Axial Load Time History for Test URM-3-1

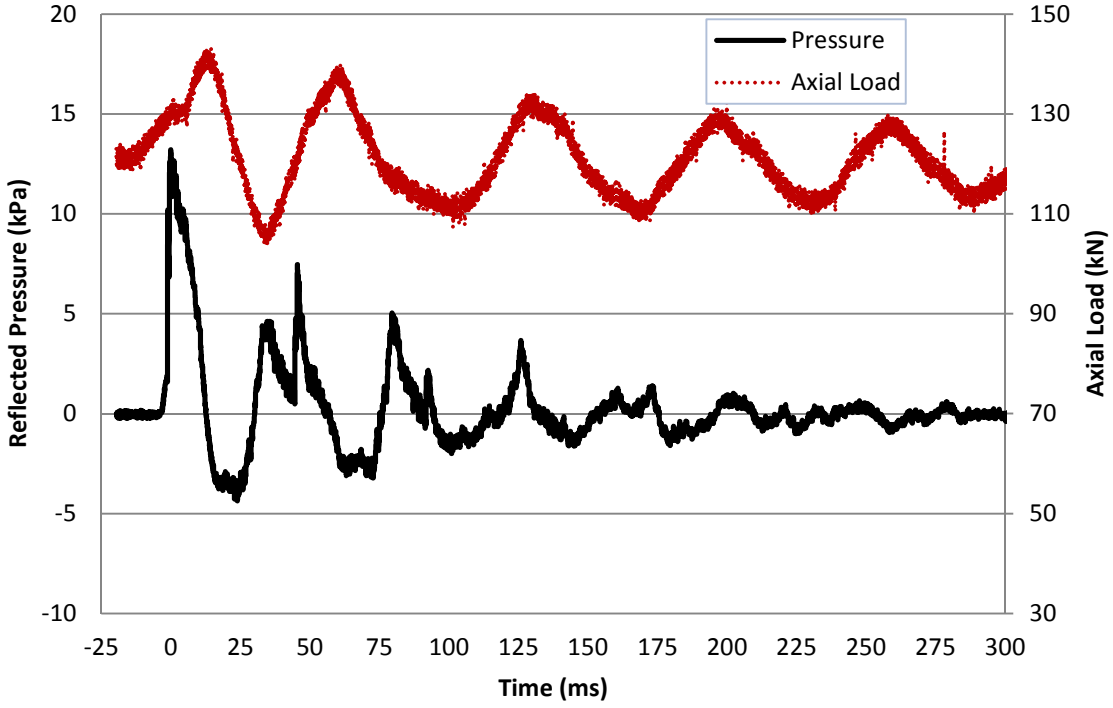

Figure A- 12: Reflected Pressure and Axial Load Time History for Test URM-3-2

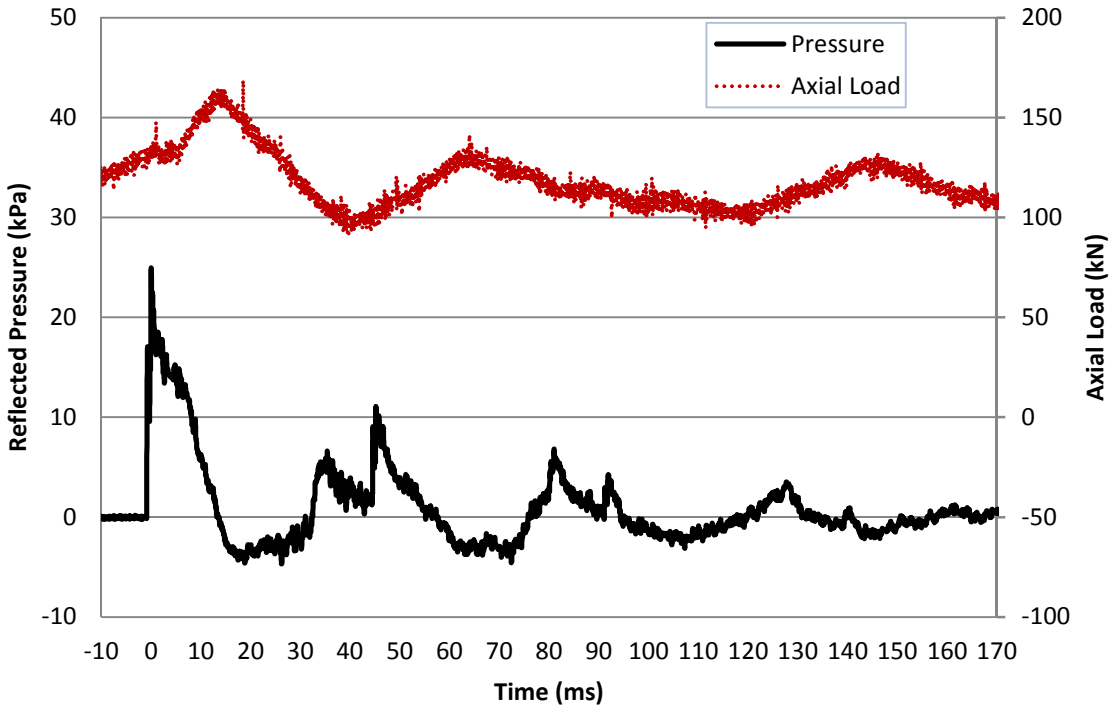

Figure A- 13: Reflected Pressure and Axial Load Time History for Test URM-3-3

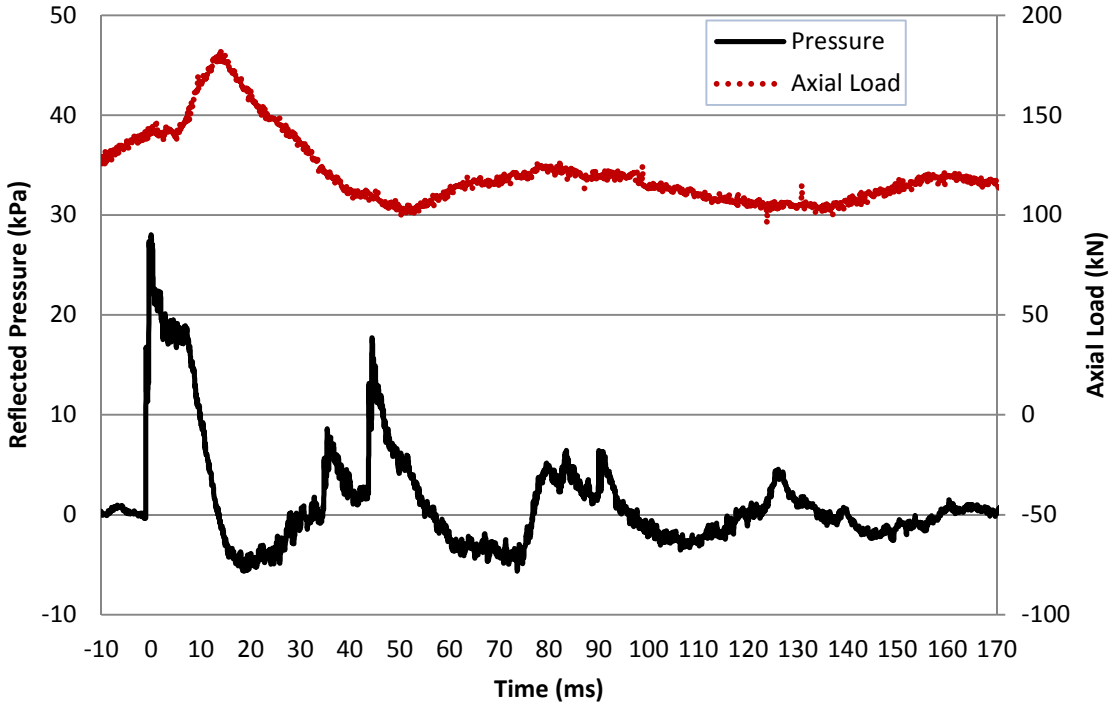

Figure A- 14: Reflected Pressure and Axial Load Time History for Test URM-3-4

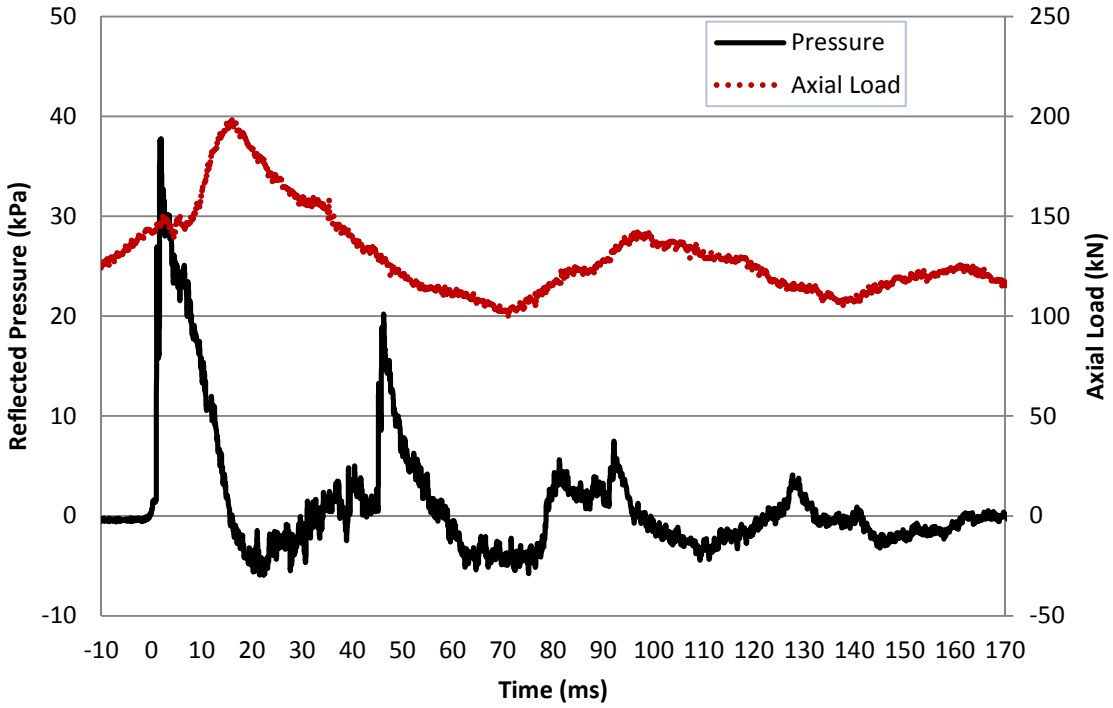

Figure A- 15: Reflected Pressure and Axial Load Time History for Test URM-3-5

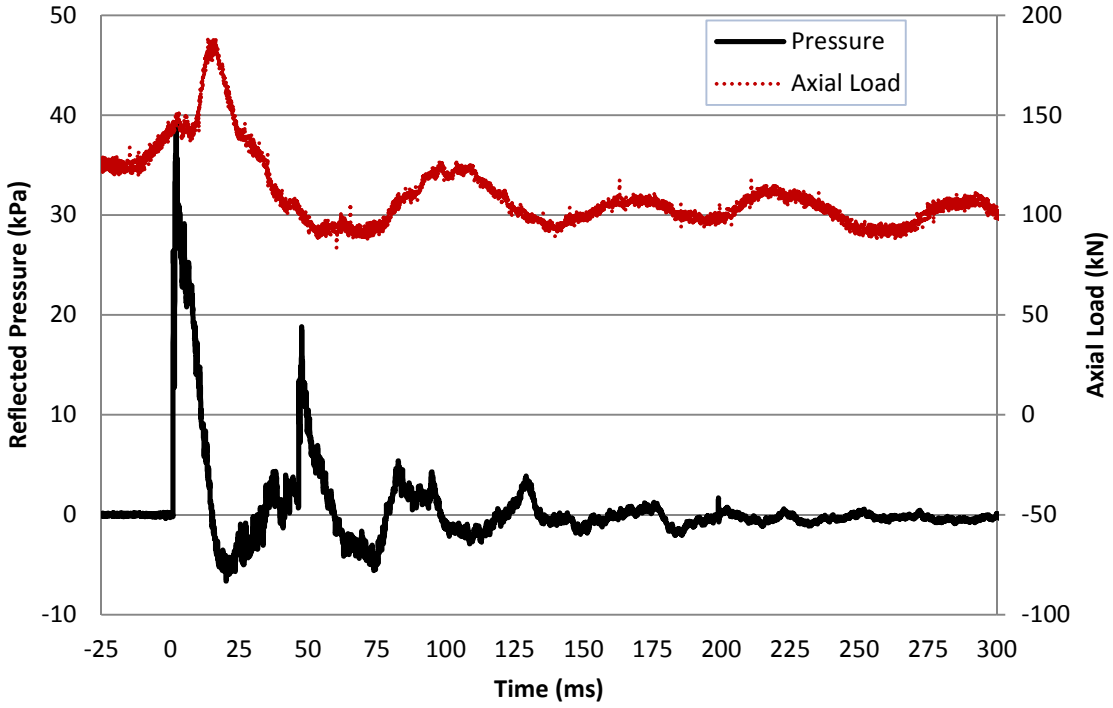

Figure A- 16: Reflected Pressure and Axial Load Time History for Test URM-3-6

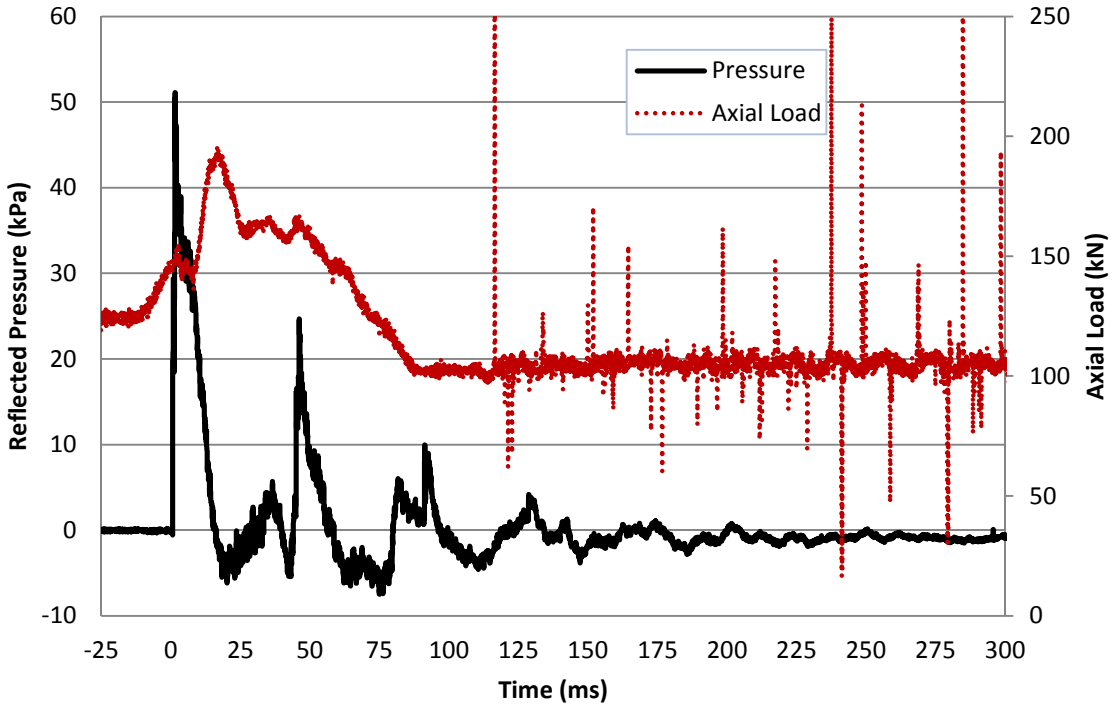

Figure A- 17: Reflected Pressure and Axial Load Time History for Test URM-3-7

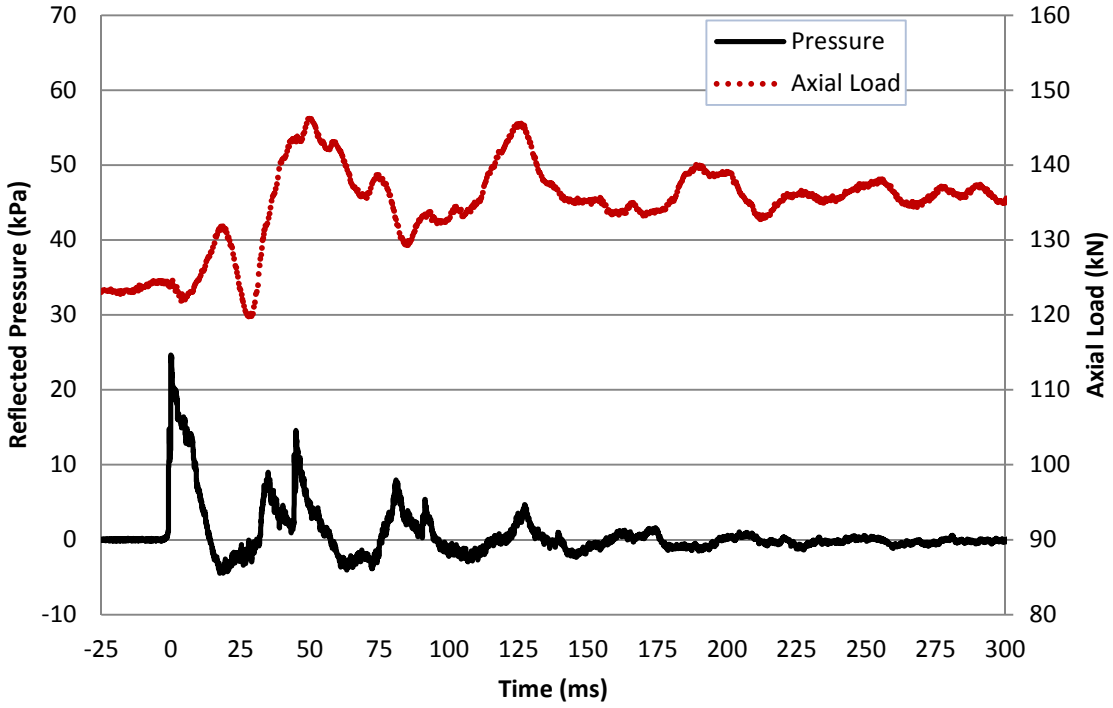

Figure A- 18: Reflected Pressure and Axial Load Time History for Test URM-4-1

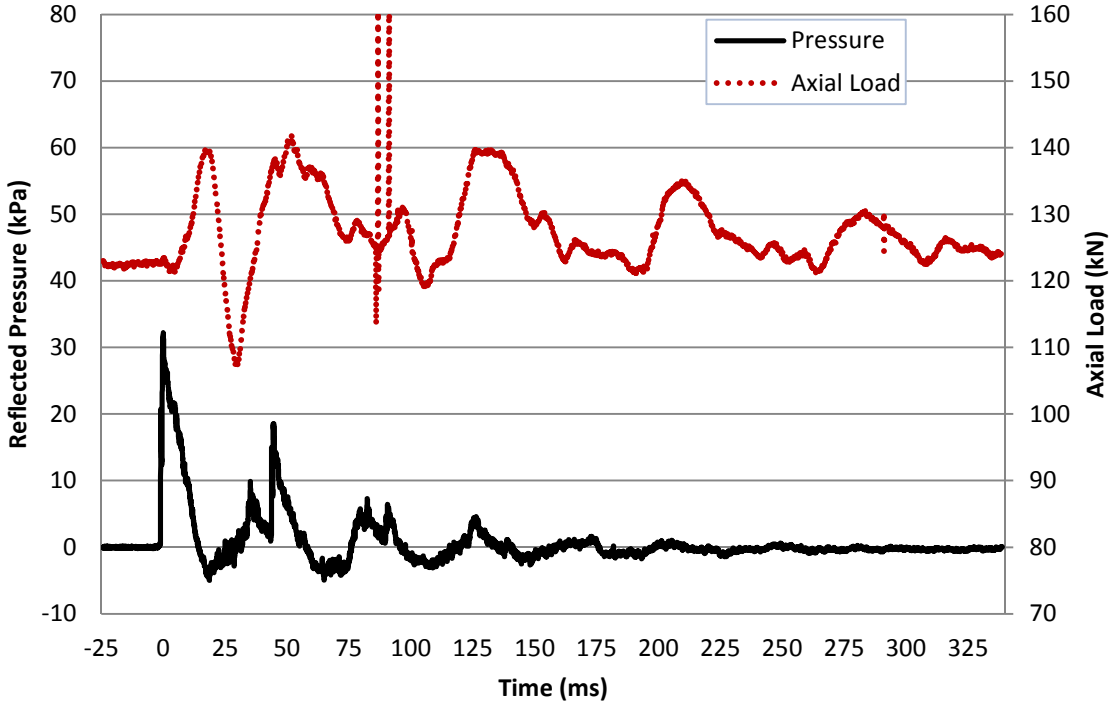

Figure A- 19: Reflected Pressure and Axial Load Time History for Test URM-4-2

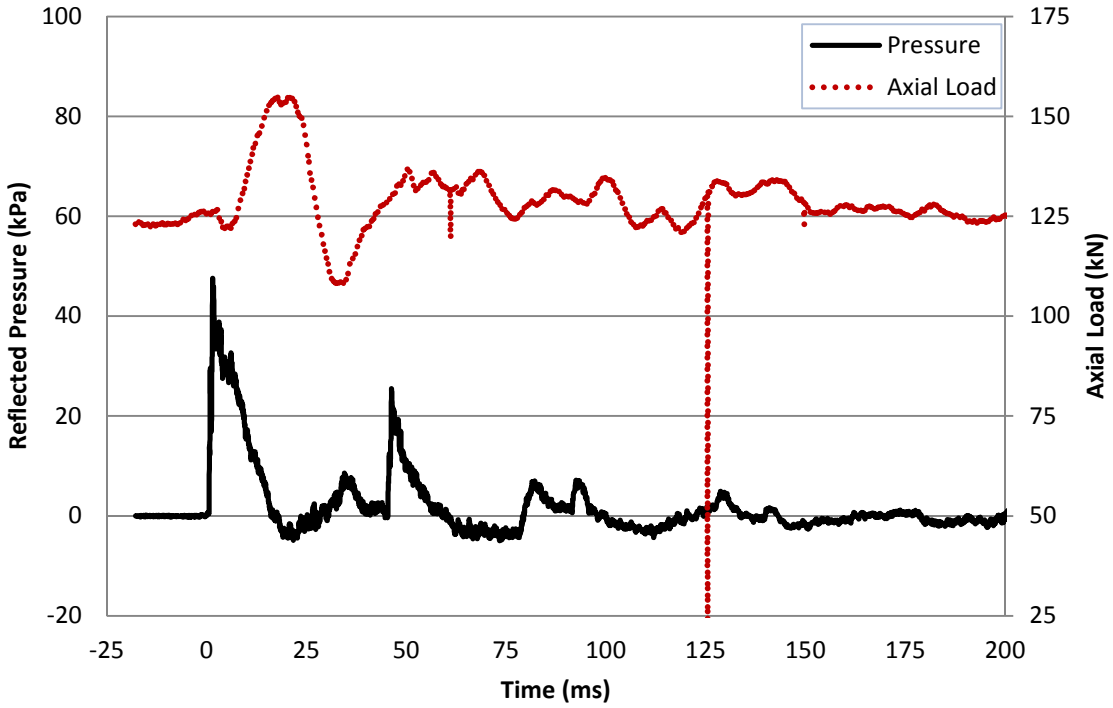

Figure A- 20: Reflected Pressure and Axial Load Time History for Test URM-4-3

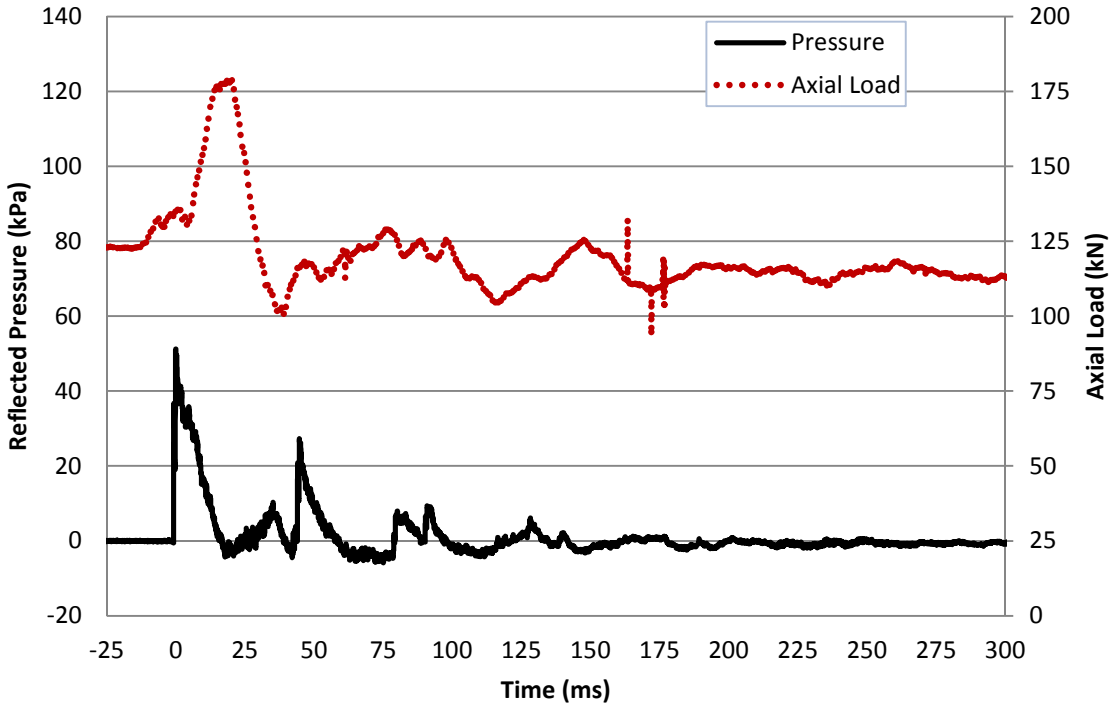

Figure A- 21: Reflected Pressure and Axial Load Time History for Test URM-4-4

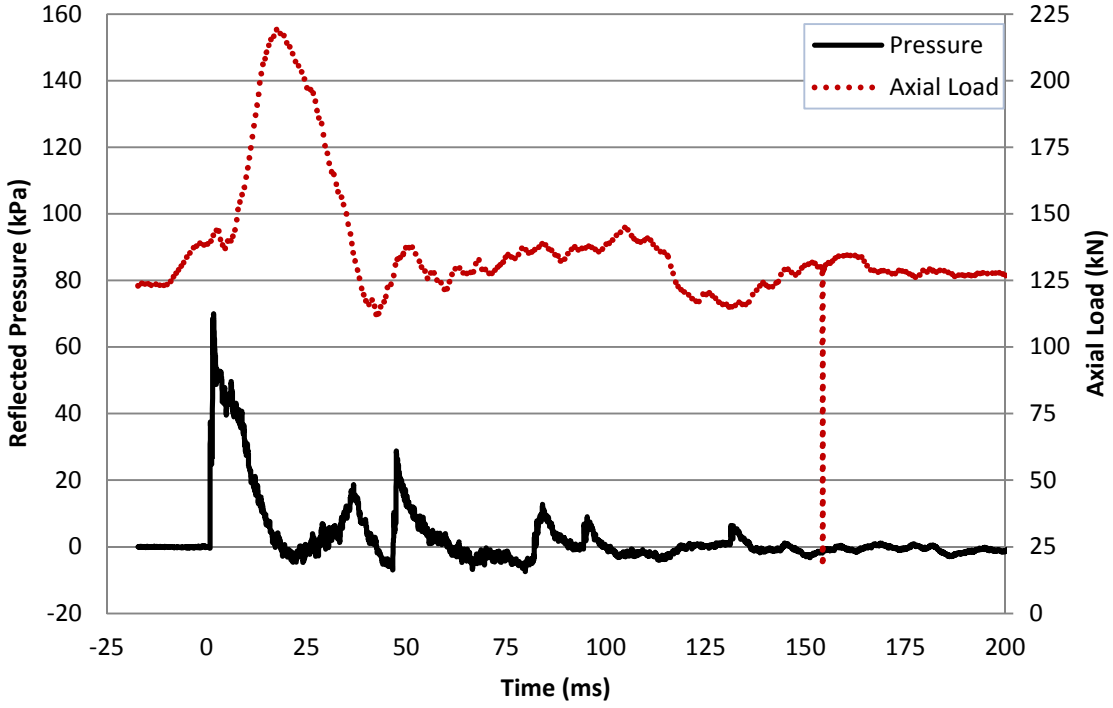

Figure A- 22: Reflected Pressure and Axial Load Time History for Test URM-4-5

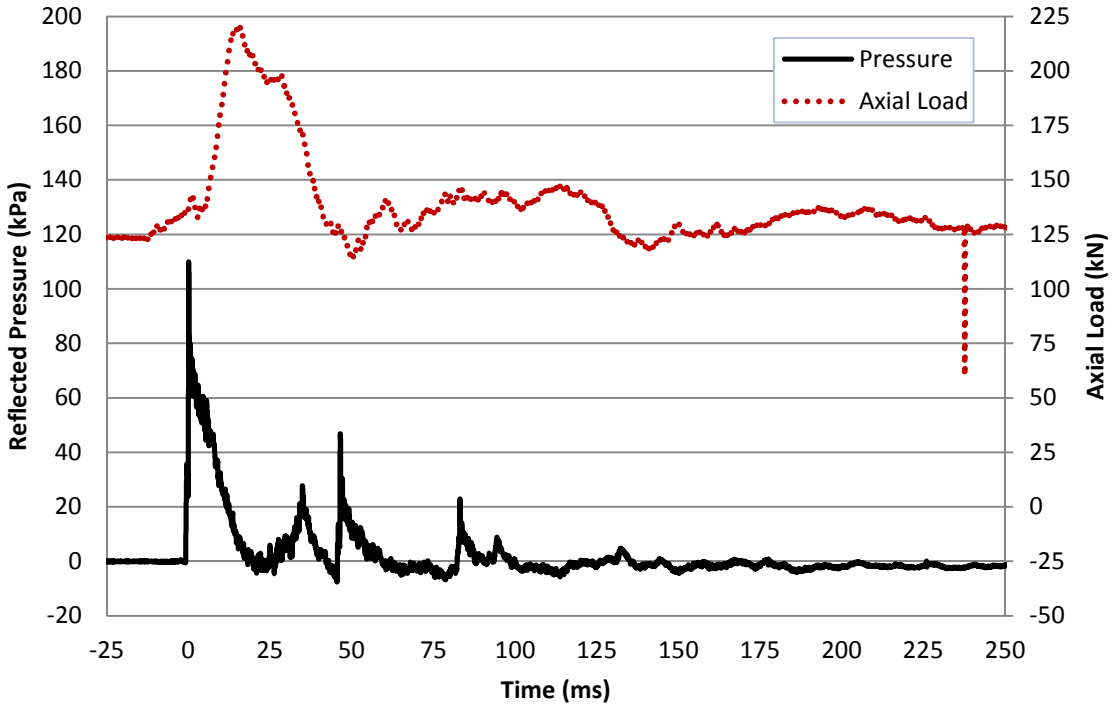

Figure A- 23: Reflected Pressure and Axial Load Time History for Test URM-4-6

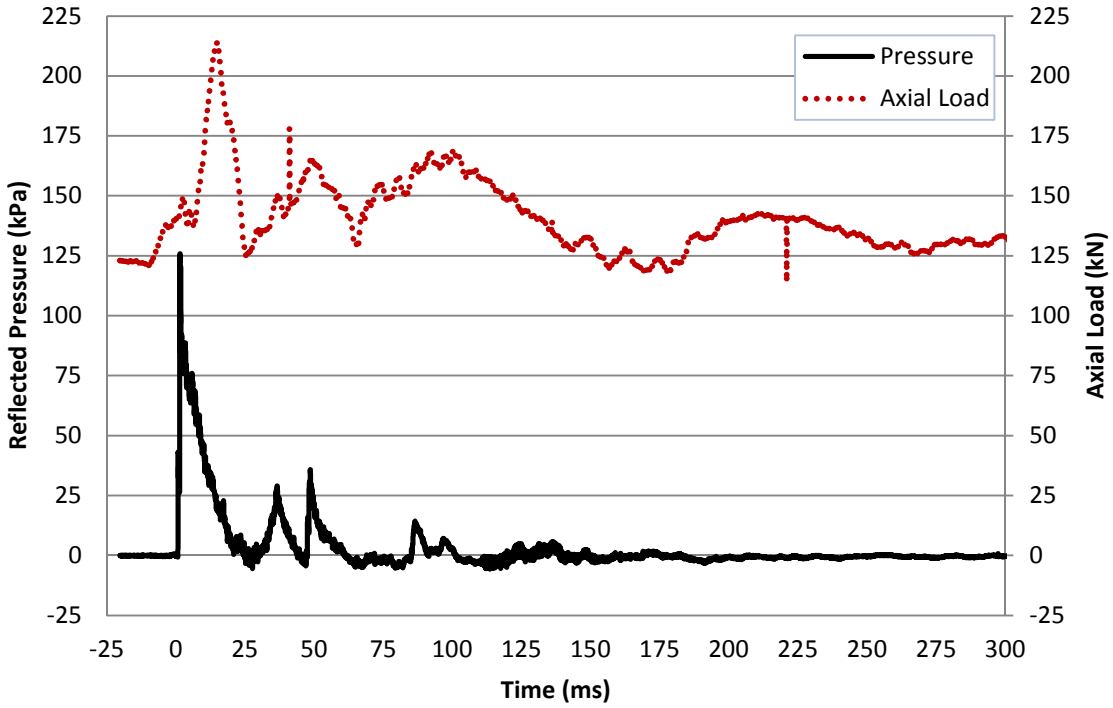

Figure A- 24: Reflected Pressure and Axial Load Time History for Test URM-4-7

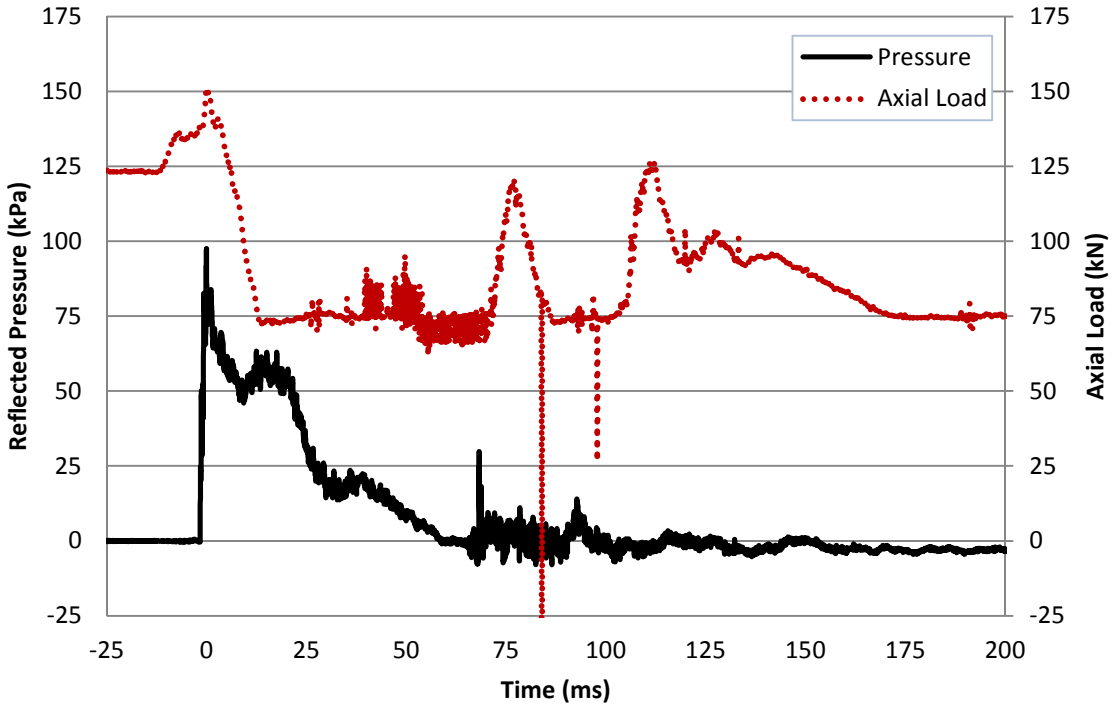

Figure A- 25: Reflected Pressure and Axial Load Time History for Test URM-4-8

Appendix B

Strain Gauge Data

The non deformed steel wires that were part of the retrofit system of wall URM-4, were instrumented with six 350 ohm linear electric resistance strain gauges, 6 mm in length as shown in Figure B-1. One strain gauge was attached at mid-height of the 5th non deformed steel wire, and the other five gauges were installed along the height of the 10th wire (counting from the left side of the wall). The strain time history plots for the shock tube tests performed on the URM-4 wall specimen are found in Figures B-1 through B-8.

Not all the strain channels were monitored during testing. S3, S4, S5 gauges were damaged during the spraying of polyurea retrofit and they could not be replaced. Gauge S6 was damaged during URM-4-5 test, gauge S1 during URM-4-7 and gauge S2 was lost during the last shock tube test, URM-4-8.

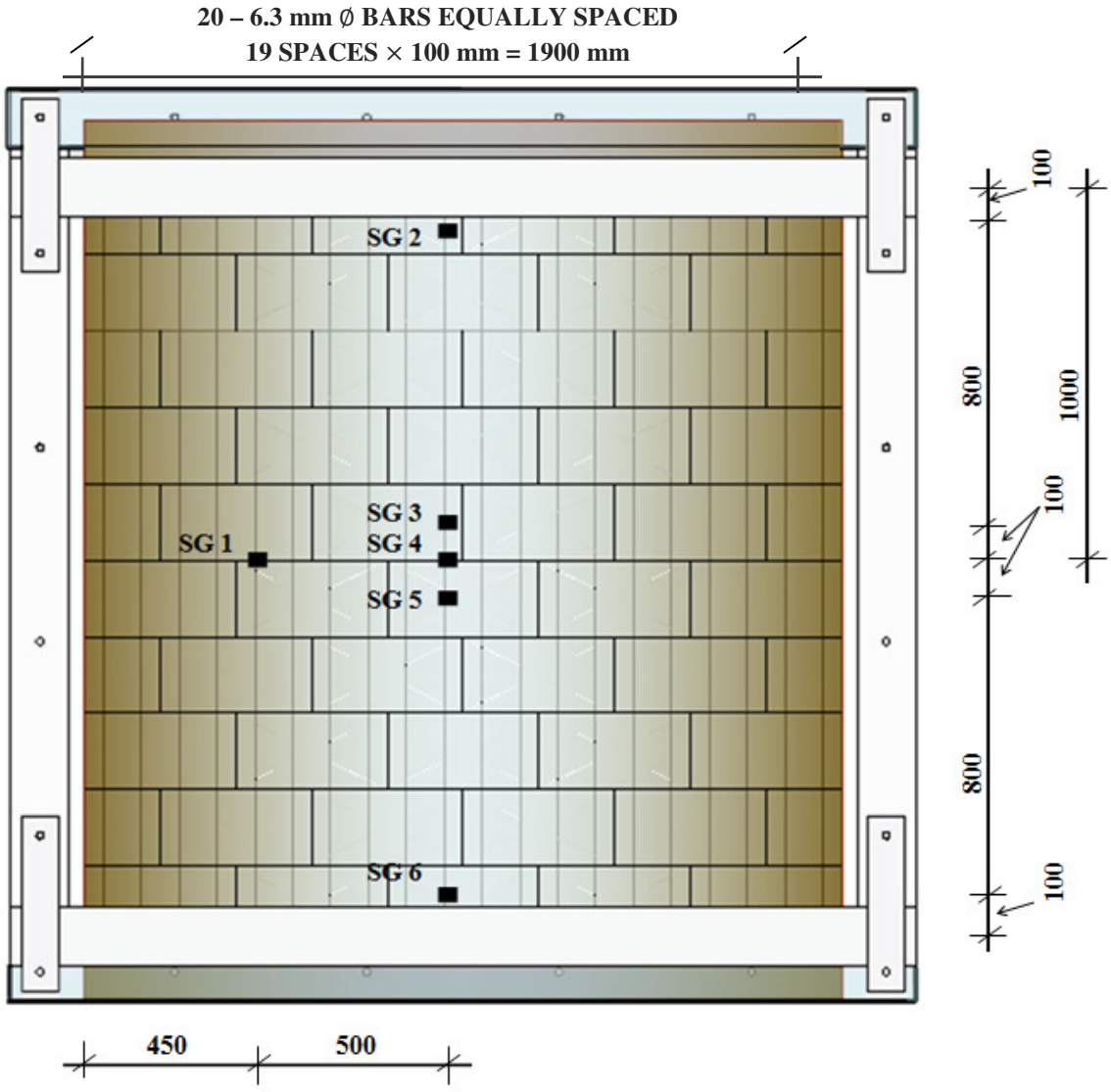

Figure B- 1: Location of Strain Gauges (Dimensions in mm)

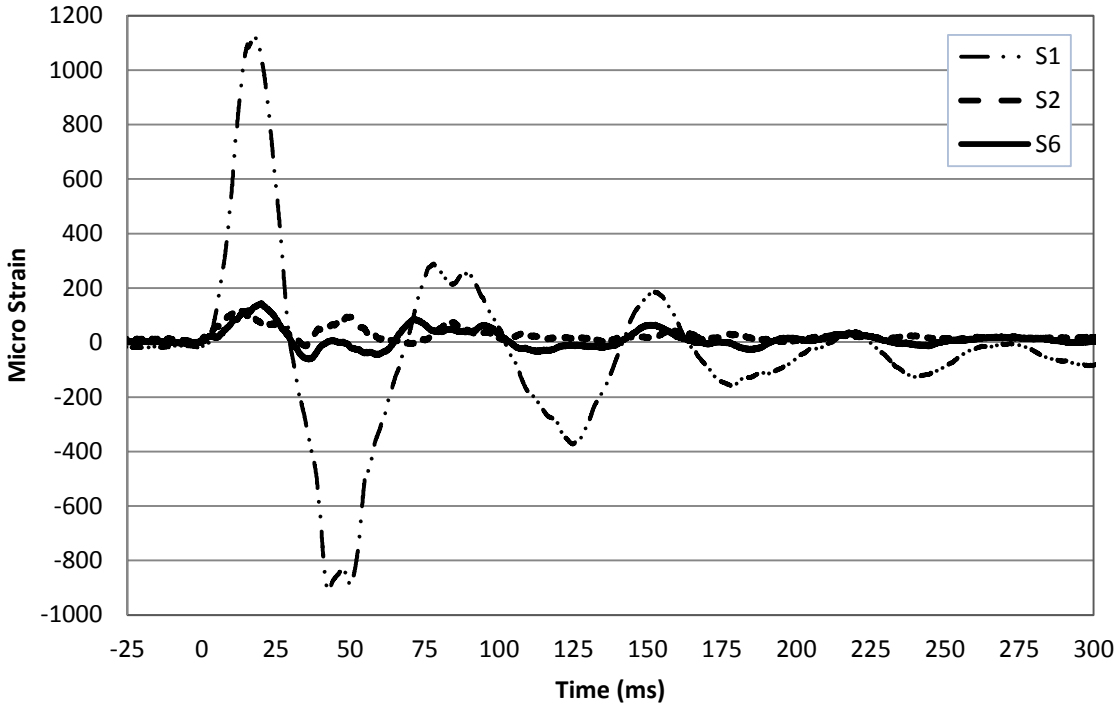

Figure B- 2: Strain Gauge Readings for Test URM-4-1

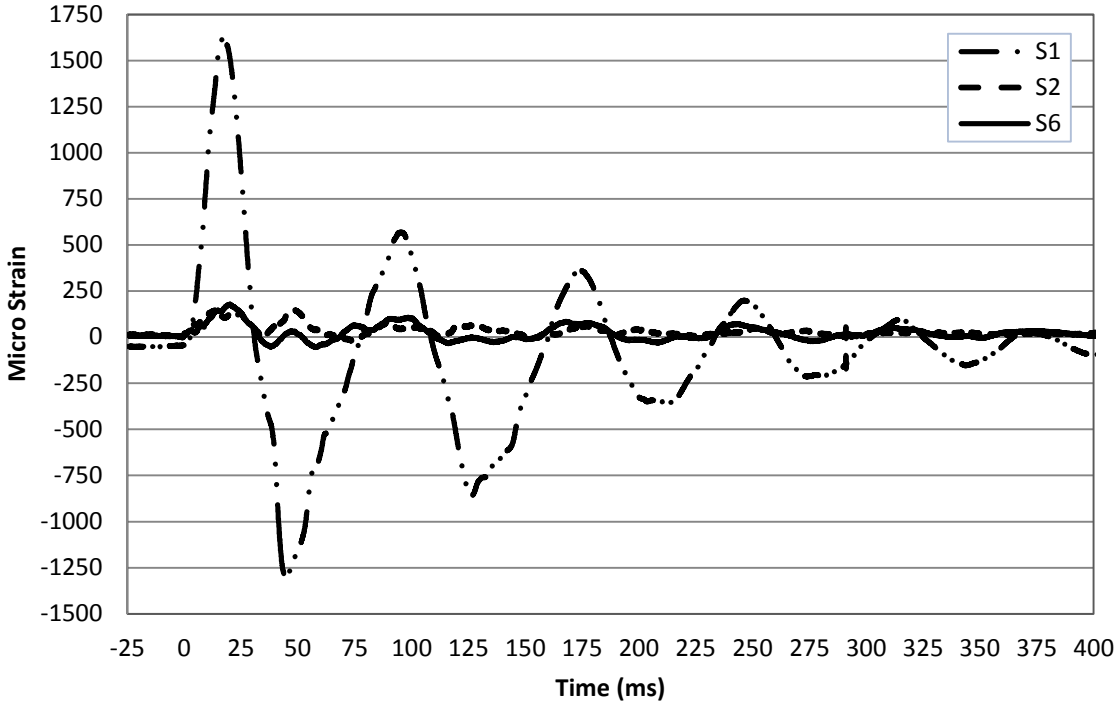

Figure B- 3: Strain Gauge Readings for Test URM-4-2

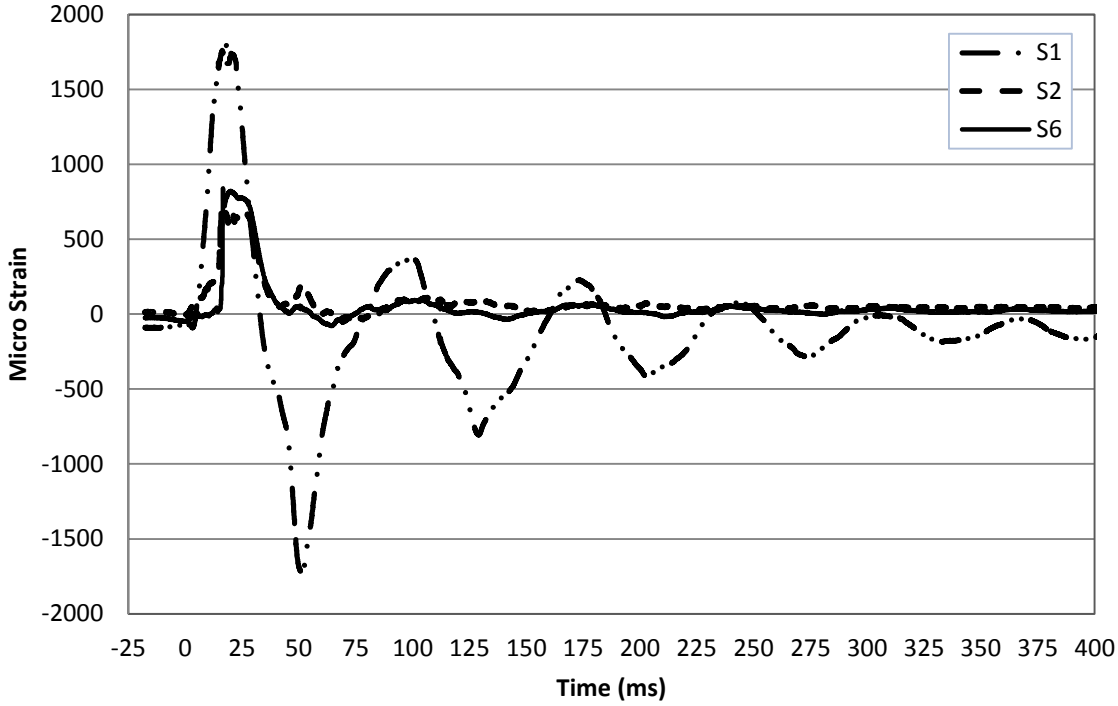

Figure B- 4: Strain Gauge Readings for Test URM-4-3

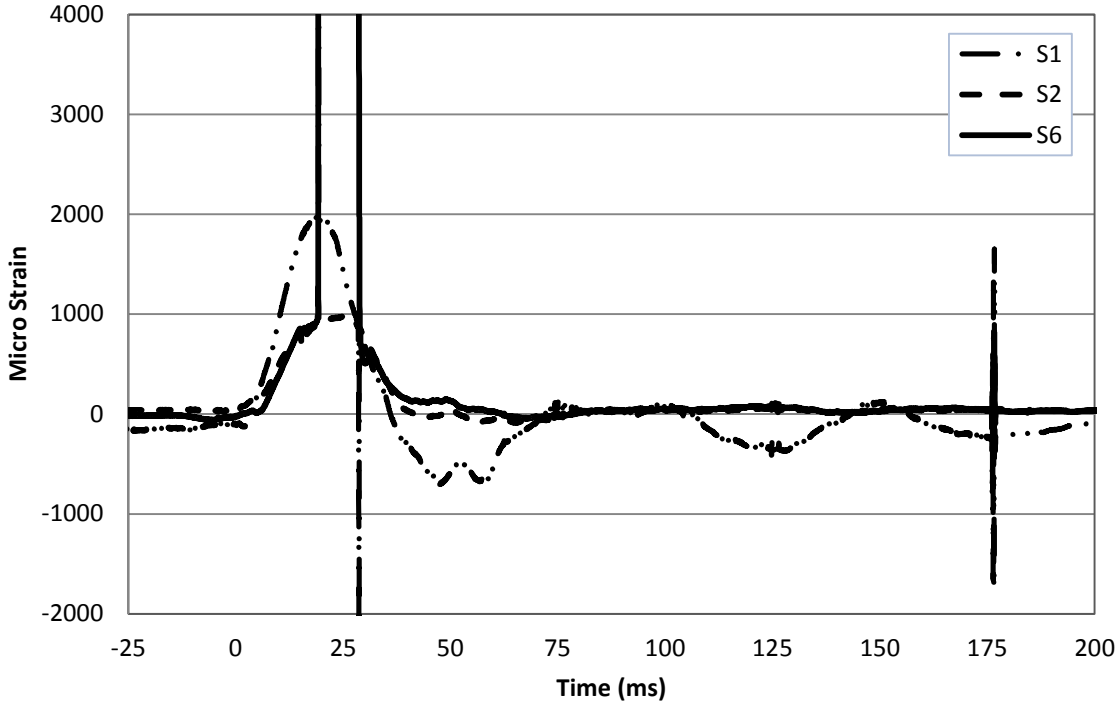

Figure B- 5: Strain Gauge Readings for Test URM-4-4

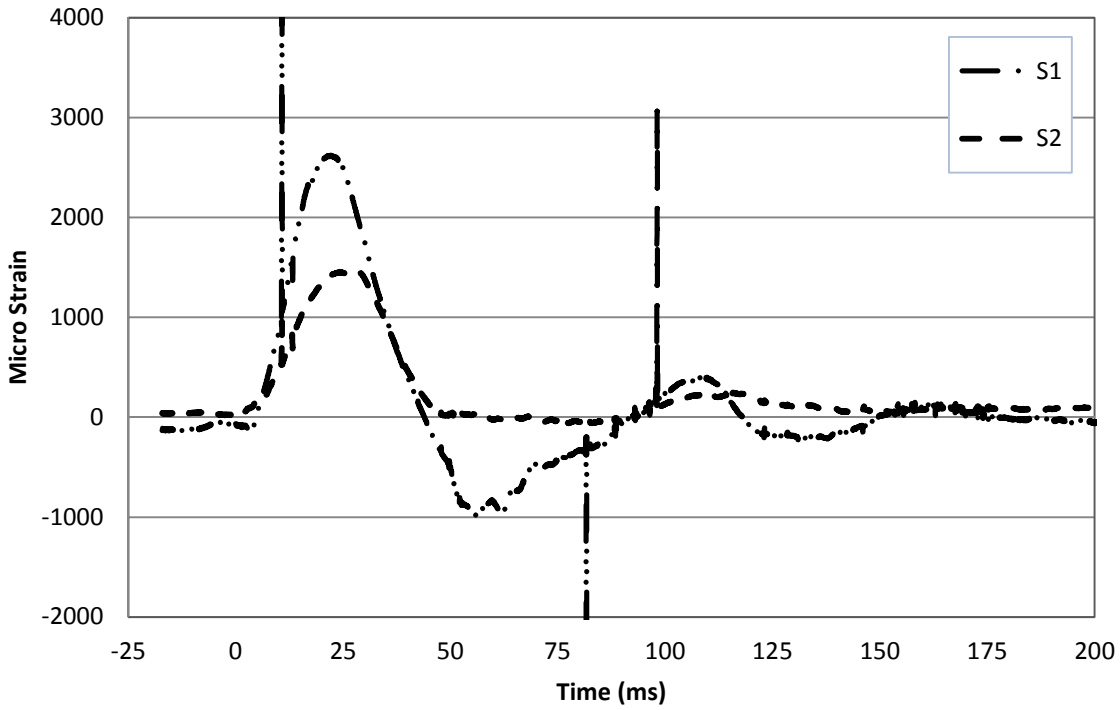

Figure B- 6: Strain Gauge Readings for Test URM-4-5

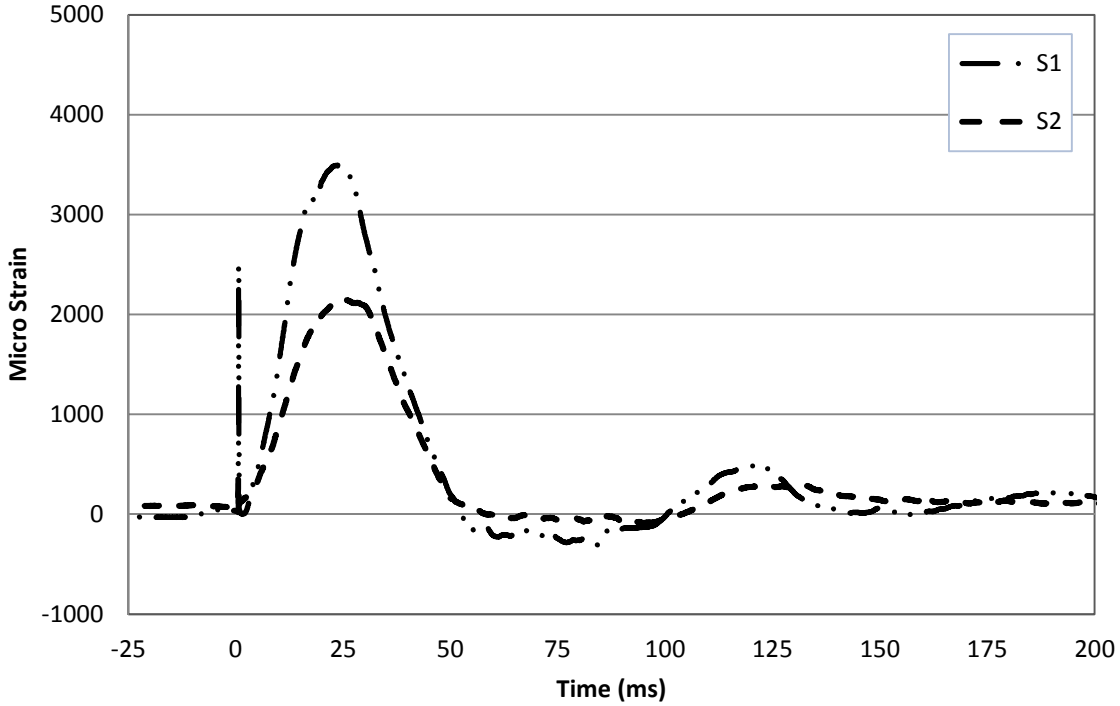

Figure B- 7: Strain Gauge Readings for Test URM-4-6

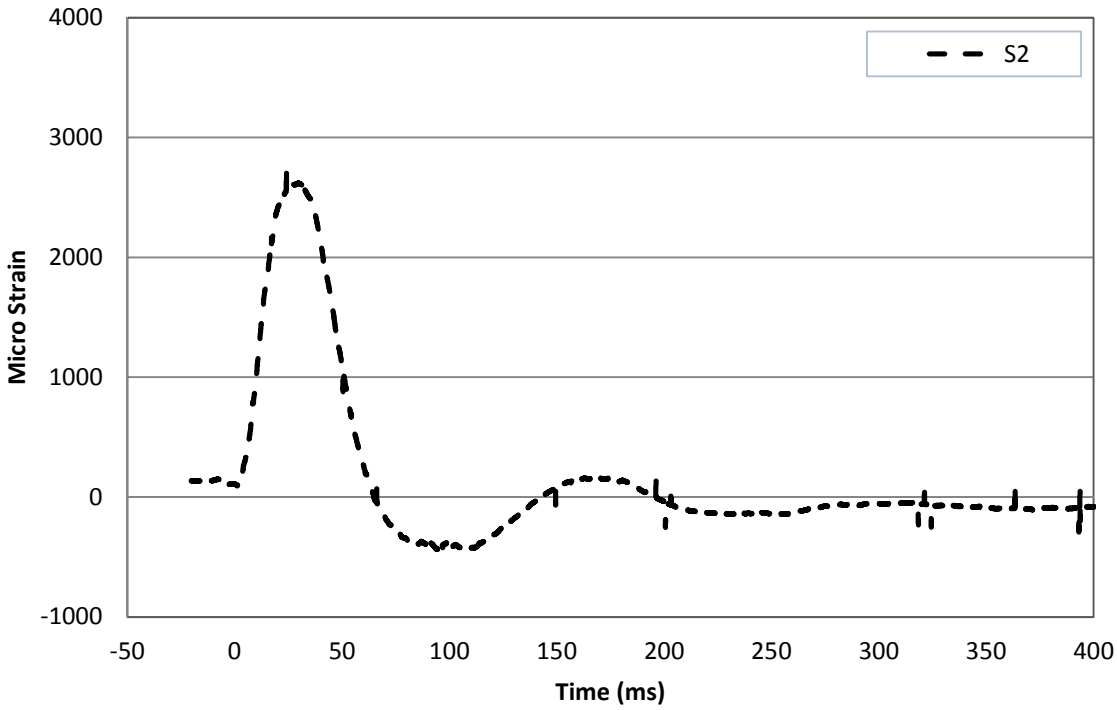

Figure B- 8: Strain Gauge Reading for Test URM-4-7